Zeitschrift: IABSE publications = Mémoires AIPC = IVBH Abhandlungen
Band: 28 (1968)

Teilband: IABSE Publications = Mémoires AIPC = IVBH Abhandlungen

Nutzungsbedingungen
Die ETH-Bibliothek ist die Anbieterin der digitalisierten Zeitschriften auf E-Periodica. Sie besitzt keine Urheberrechte an den Zeitschriften und ist nicht verantwortlich für deren Inhalte. Die Rechte liegen in der Regel bei den Herausgebern beziehungsweise den externen Rechteinhabern. Das Veröffentlichen von Bildern in Print- und Online-Publikationen sowie auf Social Media-Kanälen oder Webseiten ist nur mit vorheriger Genehmigung der Rechteinhaber erlaubt. Mehr erfahren

Conditions d'utilisation
L'ETH Library est le fournisseur des revues numérisées. Elle ne détient aucun droit d'auteur sur les revues et n'est pas responsable de leur contenu. En règle générale, les droits sont détenus par les éditeurs ou les détenteurs de droits externes. La reproduction d'images dans des publications imprimées ou en ligne ainsi que sur des canaux de médias sociaux ou des sites web n'est autorisée qu'avec l'accord préalable des détenteurs des droits. En savoir plus

Terms of use
The ETH Library is the provider of the digitised journals. It does not own any copyrights to the journals and is not responsible for their content. The rights usually lie with the publishers or the external rights holders. Publishing images in print and online publications, as well as on social media channels or websites, is only permitted with the prior consent of the rights holders. Find out more

Download PDF: 15.01.2026

ETH-Bibliothek Zürich, E-Periodica, https://www.e-periodica.ch

ASSOCIATION INTERNATIONALE DES PONTS ET CHARPENTES
INTERNATIONALE VEREINIGUNG FÜR BRÜCKENBAU UND HOCHBAU
INTERNATIONAL ASSOCIATION FOR BRIDGE AND STRUCTURAL ENGINEERING

MÉMOIRES
ABHANDLUNGEN
PUBLICATIONS

28-II

1968

PUBLIÉS PAR LE SECRÉTARIAT GÉNÉRAL À ZURICH
HERAUSGEGEBEN VOM GENERALSEKRETARIAT IN ZÜRICH
PUBLISHED BY THE GENERAL SECRETARIAT IN ZURICH

Editeur - Verleger - Publisher

Association Internationale des Ponts et Charpentes
Ecole Polytechnique Fédérale, Zurich

Internationale Vereinigung für Brückenbau und Hochbau
Eidgenössische Technische Hochschule in Zürich

International Association for Bridge and Structural Engineering
Swiss Federal Institute of Technology, Zurich

En commission pour la vente en librairie
Kommissionsverlag für den Buchhandel - Copies for sale at

Verlag Leemann Zürich

Printed in Switzerland

Préface

Le volume 28/II comprend 11 publications traitant les problèmes les plus divers mais aussi les plus actuels de l'ensemble du domaine des ponts et charpentes. Les résultats obtenus par les auteurs contribueront immédiatement à l'amélioration des prestations de l'ingénieur praticien grâce à la clarté avec laquelle les conclusions sont présentées. Nous remercions très vivement les auteurs pour leur contribution et souhaitons une large diffusion du volume 28/II de nos «Mémoires» au sein et au dehors de l'AIPC.

Zurich, en décembre 1968.

Le Président de l'AIPC:

Prof. MAURICE COSANDEY
Directeur de l'Ecole Polytechnique de l'Université de Lausanne

Les Secrétaires Généraux:

Dr sc. techn. HANS VON GUNTEN
Professeur à l'Ecole Polytechnique Fédérale, Zurich

Dr sc. techn. PIERRE DUBAS
Professeur à l'Ecole Polytechnique Fédérale, Zurich

Dr sc. techn. CHRISTIAN MENN
Coire — Zurich

Vorwort

Band 28/II umfaßt 11 Arbeiten, welche die verschiedensten, aber auch die aktuellsten Probleme auf dem Gebiet des Brücken- und Hochbaues behandeln. Die von den Verfassern erhaltenen Ergebnisse verhelfen dem praktischen Ingenieur dank der klaren Darstellung der Schlußfolgerungen zu bessern Leistungen. Wir danken den Verfassern für ihre Beiträge und hoffen, daß Band 28/II unserer «Abhandlungen» eine große Verbreitung unter den Mitgliedern und den Nichtmitgliedern der IVBH finden wird.

Zürich, im Dezember 1968.

Der Präsident der IVBH:

Prof. Maurice Cosandey
Direktor der Technischen Hochschule der Universität von Lausanne

Die Generalsekretäre:

Dr. sc. techn. Hans von Gunten
Professor an der Eidgenössischen Technischen Hochschule in Zürich

Dr. sc. techn. Pierre Dubas
Professor an der Eidgenössischen Technischen Hochschule in Zürich

Dr. sc. techn. Christian Menn
Chur — Zürich

Preface

Volume 28/II comprises 11 papers dealing with the most diverse but also the most current problems in the field of bridge and structural engineering. The results obtained by the authors directly contribute to the improvement of the work of practical engineers thanks to the clear presentation of the conclusions. We should like to express our gratitude to the authors for their contributions and hope Volume 28/II of our «Publications» will have a large distribution within and outside the IABSE.

Zurich, December 1968.

The President of IABSE:

Prof. MAURICE COSANDEY
Director of the Institute of Technology of the University of Lausanne

The General Secretaries:

Dr. sc. techn. HANS VON GUNTEN
Professor at the Swiss Federal Institute of Technology, Zurich

Dr. sc. techn. PIERRE DUBAS
Professor at the Swiss Federal Institute of Technology, Zurich

Dr. sc. techn. CHRISTIAN MENN
Chur — Zurich

Leere Seite
Blank page
Page vide

Table des matières - Inhaltsverzeichnis - Table of Contents

E. R. Bryan, W. M. El-Dakhakhni, England/Egypt, U.A.R. . . . . English 1

Projection et dimensionnement de constructions à revêtements exta-légers
Entwurf und Berechnung von Gebäuden mit leichter Verkleidung
The Design and Analysis of Buildings with Light Cladding

J. Courbon, France. . . . . Français 13

Flambement des arcs
Bogenknicken
Buckling of Arches

Hans Gesund, Donald G. Mills, Victor M. Martin, USA . . . . . English 31

Essais de rupture de poutres en béton armé soumises à l'action combinée de la torsion, de la flexion et du cisaillement
Bruchlasttests an Stahlbetonträgern unter kombinierter Beanspruchung aus Drillung, Biegung und Schub
Ultimate Strength Tests of Reinforced Concrete Beams in Combined Torsion, Bending and Shear

A. Hrennikoff, Canada. . . . . English 49

La méthode des éléments finis appliquée à des contraintes bi-dimensionnelles
Das Verfahren der Endlichen Elemente in der Anwendung auf ebene Spannungszustände
The Finite Element Method in Application to Plane Stress

K. T. Sundara Raja Iyengar, K. S. Jagadish, India. . . . . English 69

Comportement de ponts-dalles sous charges mobiles
Verhalten von Platten- und Balkenbrücken unter beweglichen Lasten
The Response of Beam and Slab Bridges to Moving Forces

Curt F. Kollbrunner, Nikola Hajdin, Schweiz/Jugoslawien . . . . . Deutsch 87

La méthode des déplacements dans la théorie des membres à parois minces et un nouveau modèle de calcul pour des membres à parois minces avec contour déformable
Die Verschiebungsmethode in der Theorie der dünnwandigen Stäbe und ein neues Berechnungsmodell des Stabes mit in seinen Ebenen deformierbaren Querschnitten
Displacement-Method in the Theory of Thin-Walled Members, and a New Calculation-Model for the Thin-Walled Bars with Deformable Contours

ALFRED KORN, USA . . . . . English 101

Une approximation des facteurs influant sur la stabilité de portiques
Näherungen für Stabilitätseinflüsse an Rahmen
The Approximation of Stability Effects on Frames

K. H. LIN, E. C. ROSSOW, S. L. LEE, USA . . . . . English 113

Stabilité de colonnes émincées à larges ailes dans le domaine plastique
Stabilität von zugespitzten Breitflanschstützen im plastischen Bereich
Inelastic Stability of Tapered Wide-Flange Columns

CH. MASSONNET, M. ŠKALOUD, J. DONEA, Belgique/Tchécoslovaquie . . . Français 137

Comportement postcritique des plaques cisaillées raidies. Deuxième partie: Répartition des contraintes et analyse de l'état limite
Verhalten von ausgesteiften Platten bei Schub im überkritischen Bereich. 2. Teil: Spannungsverteilung und Analyse des Grenzzustandes
Postbuckling Behaviour of Stiffened Plates Subjected to Pure Shear. 2nd Part: Distribution of Stress and Analysis of the Limit State

WILLIAM E. SAUL, JAAFAR K. AL-ABDULLA, USA . . . . . English 157

Dynamique non-linéaire inélastique de bâtiments à multiples étages
Nichtlineare, unelastische Dynamik von Hochhäusern
Nonlinear Inelastic Dynamics of Multi-Story Buildings

A. C. WALKER, England . . . . . English 169

Charges maximales pour piles à parois minces en U, comprimées excentriquement
Höchstlasten für dünnwandige U-Stützen unter ausmittiger Belastung
Maximum Loads for Eccentrically Loaded Thin-walled Channel Struts

The Design and Analysis of Buildings with Light Cladding

Projection et dimensionnement de constructions à revêtements extra-légers

Entwurf und Berechnung von Gebäuden mit leichter Verkleidung

E. R. BRYAN
M. Sc., Ph. D., Senior Lecturer,
University of Manchester, England

W. M. EL-DAKHAKHNI
B. Sc., Ph. D., Associate Professor,
Assuit University, Egypt, U.A.R.

Introduction

It has long been recognised that light cladding makes a contribution to the stiffness and strength of steel framed buildings but the effect has not been taken into account in design. This is probably because the cladding has been regarded as an uncertain element for structural purposes; it can be easily removed for maintenance and the methods of attachment have been variable and uncertain. In addition, steel sheets may corrode and the properties of other types of cladding may deteriorate with the passage of time. Also, no method has been available for estimating, even approximately, what the likely stiffening effect of the sheeting would be. Consequently, designers have tended to regard the effect as a "bonus" in reducing frame stresses and deflexions to values somewhat below the calculated values. In many cases, the only conscious use of the sheeting in design has been to allow the sheeting to provide lateral support to the purlins, but this must be regarded as a purely local effect which does not affect the overall behaviour of the building.

In recent years, however, a much more positive role for sheeting and decking has been adopted in the United States [1—4]. Welded floor decking has been used to provide resistance to wind and seismic forces, and light steel decking has been used for the shear diaphragms in folded plate roofs. In both these cases, design information has been based on the results of full scale tests.

In the design of industrial shed-type buildings, it has been shown [5] that the contribution of the sheeting to the frame stiffness and strength can be calculated provided that the shear behaviour of a panel of sheeting is known. In this connexion a panel is regarded as being that area of sheeting, complete

with all attachments, between two adjacent rafters and between the extreme purlins. Originally, full scale tests were carried out to determine the shear behaviour of complete panels, though it was realised that the expense and delay occasioned by such a procedure could not normally be tolerated in design practice. More recently [6], a method of calculating the shear behaviour of complete roof panels has been advanced and satisfactory agreement has been obtained with experimental results [6, 7].

Before considering in detail the shear behaviour of roof decks and the analysis of an actual building allowing for the contribution of the decking, it is important to first consider whether it is safe or even desirable to take this stiffening effect into account in design.

Safety of Clad Buildings

The prime purpose of most shed-type buildings is to act as an umbrella to protect the contents from the weather, so that much of the load on the building frames is dependent on the sheeting (i. e. dead load, wind load and snow load). If the sheeting were totally removed much of the load would also be removed. Under such conditions, it is suggested that the effect of the sheeting should be taken into account in design. If the major part of the load on the building is derived from other sources, then the argument for allowing for the sheeting is not so strong.

If cladding is to be taken into account, it must be regarded as a structural element and proper care must be taken in specifying fixings, etc. For instance, hook bolts would not suffice, but self tapping screws or fired pins would be necessary. There is also the difficulty that sheeting has traditionally been regarded as an element which can be easily removed for maintenance purposes. Hence, it could be asked whether unauthorized removal of a number of sheets in an important part of the building would endanger the structure. It might also be asked if deterioration of the sheeting could weaken the whole building rather than cause a local weakness.

The foregoing questions are quite legitimate and contain elements of truth. Undoubtedly, if the membrane strength of cladding is to be used in design, then it will be necessary to train engineers to think in terms of the whole building, rather than in terms of a framework. Nevertheless, this has been done in the unitary construction of car bodies, in the stressed skin construction of airframes and in the design of ships' hulls, so there seems no basic reason why it should not be done in the structural industry, in spite of the special problems.

Because of the varied workmanship likely to be achieved in the site fixing of cladding, it is necessary to have proper safeguards. It is also necessary to ensure that the building is safe at all stages of construction, occupation and use. It is therefore suggested that the bare steel framework must be strong

enough to withstand by itself all the design loads but that the maximum stress under this condition be allowed to approach the yield stress. After sheeting, the maximum calculated stress in the clad frame under the design loads should not exceed the present permissible working stress, and the calculated deflexions should be acceptable. By conforming to these conditions the safety of a building would be assured and economy in the design of the frame would result. It would also mean that the design reflected the true behaviour of the building rather than the hypothetical behaviour based on the bare frame.

Shear Tests on Steel Decks

In order that the method proposed for calculating the shear behaviour of panels of sheeting or decking may be assessed, the results of three sets of tests are compared with the calculated values. These tests are described more fully in references [6] and [7]. The method of calculation is given in reference [6] and illustrated by the example in the present paper.

Test 1. This test was carried out on a panel of steel sheeting 8 ft. wide $\times$ 10 ft. deep with 3 purlins (Fig. 1). The sheeting was 0.024 in. thick, the pitch of the corrugations was 4 in., the seam bolts were spaced at 12 in. centres and the sheet-purlin fasteners (self tapping screws) were spaced at various centres. Table 1 gives a comparison of the calculated and measured shear flexibilities and shear strengths.

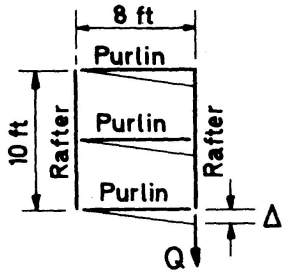


Fig. 1. Panel of sheeting in test 1.

Table 1

No. of fasteners per sheet	Shear flexibility Δ/Q in in./ton		Shear strength in tons	
	Calculated	Measured	Calculated	Measured
7	0.18	0.17	1.7	2.3—2.8
4	0.27	0.31	1.7	1.6—1.8
3	0.40	0.38	1.4	1.0—1.6

Test 2. The panel of steel sheeting was 12 ft. $\times$ 12 ft. with provision for either 3 purlins or 5 purlins (Fig. 2). The sheeting was 0.028 in. thick, the pitch of the corrugations was $6^3/_4$ in., the seam fasteners (pop rivets) were generally at 18 in. centres and the sheet-purlin fasteners (self tapping screws) were

fixed in every corrugation or alternate corrugations. Table 2 summarizes the calculated and observed behaviour.

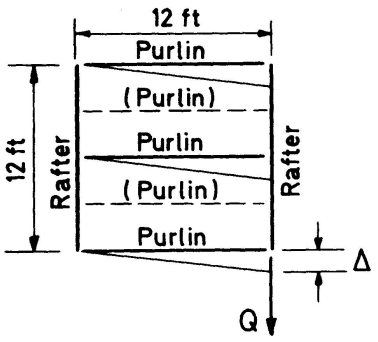


Fig. 2. Panel of sheeting in test 2.

Table 2

No. of purlins	Sheet-purlin fasteners	Shear flexibility Δ/Q in in./ton		Shear strength in tons	
		Calculated	Measured	Calculated	Measured
3	Every corrug.	0.060	0.056	3.5	3.4
	Altern. corrug.	0.359	0.328		
5	Every corrug.	0.045	0.050		
	Altern. corrug.	0.305	0.237		

Test 3. The panel was of steel sheeting 5 m wide × 3 m deep with 4 light gauge purlins (Fig. 3). The sheet thickness was 0.85 mm, the pitch of the corrugations was 125 mm, the seam fasteners (pop rivets) and the sheet-purlin fasteners (self tapping screws) were spaced at 125 mm or 250 mm centres. Table 3 summarizes the calculated and observed behaviour of the original and modified panels.

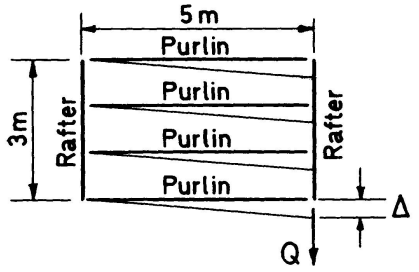


Fig. 3. Panel of sheeting in test 3.

Table 3

	Spacing of sheet-purlin fasteners	Spacing of seam fasteners	Shear flexibility Δ/Q in in./ton	
			Calculated	Measured
Original Panel	250 mm	250 mm	0.97	1.30
	125 mm	125 mm	0.91	1.36
Modified Panel	125 mm	125 mm	0.10	0.14
	250 mm	125 mm	0.14	0.15

Summary of Results. The tests show that the calculated values of the shear flexibilities of the panels tested are generally in satisfactory agreement with the measured values. The shear strengths in Tests 1 and 2, calculated on the assumption that failure occurs due to tearing at the sheet fasteners, are also in approximate agreement with the observed values. A comparison of shear strengths in Test 3 was not possible as failure did not occur in the above mode.

On the evidence of the above results, and others not quoted, it would appear that a reasonable estimate of the shear flexibility of panels of steel sheeting can be made provided that the details of construction do not differ too widely from the panels tested. Also, an estimate of the shear strength can be made assuming that failure occurs by tearing at the sheet fasteners (the usual mode).

Analysis of Clad Building

The steel framed building in question was 80 ft. wide, 309 ft. long and 50 ft. high. A diagrammatic representation of the main frames is shown in Fig. 4 and the plan of the building is given in Fig. 5. It is seen that the trans-

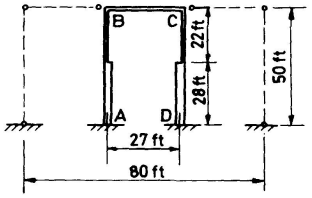


Fig. 4. Idealized steel frame.

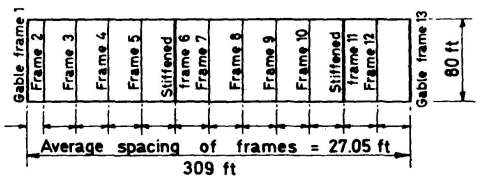


Fig. 5. Plan of roof deck.

verse strength of the building depends on the rigid portal frame ABCD in Fig. 4 and that the outer pinned frames, shown dotted, do not contribute to this strength. Referring to Fig. 5, there are rigid partition walls across the building at frames 6 and 11, so that the greatest length of building to be considered is the portion between these frames. In this portion, there are four intermediate frames and the average width of a panel of sheeting is 27.05 ft.

Bare Frame Analysis

In the bare frame analysis, the bending moments due to wind loads far exceeded those due to any other type of loading. In order to simplify the example, only wind bending moments will therefore be considered. Fig. 6 shows these calculated bending moments in the bare steel frame under working loads; the calculated sway deflexion is 2.90 in.

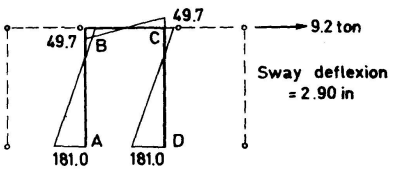


Fig. 6. Bare frame bending moments in ton-ft.

Shear Flexibility of Panel of Sheeting

The flexibility of a panel of sheeting will be due to:

1. 1.1. Bending of the corrugation profile.
   1.4. Shear strain in the panel.
   1.5. Axial strain in the purlins.
2. 2.1. Slip in the sheet/purlin fasteners.
   2.3. Slip in the seam fasteners.
3. 3.1. Twisting of the purlin/rafter connexions.

The above sub-heading numbers are those used in reference 6 where an expression for each effect was separately derived.

1.1. *Bending of the corrugation profile.* The sheet profile is shown in Fig. 7.

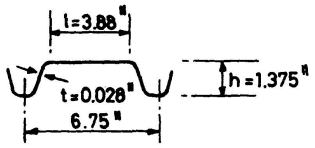


Fig. 7. Corrugation profile.

The shear flexibility due to distortion of the profile is given by

$$c_{1.1} = \frac{144\,K\,h^3\,l^2}{E\,t^3\,b^3}\,n_c\,f_1 \times 13.8,$$

where b = depth of panel = 80×12 in.
E = modulus of elasticity = 13,000 ton/in.^{2}
h = height of corrugation = 1.375 in.
l = width of flat top of corrugation = 3.88 in.
t = thickness of sheeting = 0.028 in.
K = constant of sheeting (ref. [7], table 4) = 0.145
n_c = number of corrugations per panel = 48
f_1 = reduction factor to allow for the effect of intermediate purlins (ref. [6], table 1) = 0.49
13.8 = multiplication factor to allow for fasteners in alternate corrugations (ref. [7], table 4)

hence $c_{1,1} = 1.0 \times 10^{-3}$ in./ton (1)

1.4. *Shear strain in panel.* The shear flexibility due to distortion of the panel from a rectangle to a parallelogram is given by

$$c_{1.4} = \frac{2\,a\,(1+\nu)}{b\,t\,E}\,\frac{\text{developed length of profile}}{\text{pitch of corrugations}}\,f_2,$$

where a = average width of panel = 27.05×12 in.
ν = Poisson's ratio = 0.25
developed length/pitch = 1.26 (ref. [7], table 4)
f_2 = reduction factor to allow for the effect of intermediate purlins (ref. [6], table 1) = 0.29

hence $c_{1.4} = 0.8 \times 10^{-3}$ in./ton (2)

1.5. *Axial strain in purlins.* The shear flexibility due to the tendency of the purlins to lengthen or shorten under axial stress is given by

$$c_{1.5} = \frac{2a^3}{3b^2 A E} f_3,$$

where A = cross sectional area of purlins = 2.68 in.^{2}
f_3 = reduction factor to allow for the effect of intermediate purlins (ref. [6], table 1) = 0.39

hence $c_{1.5} = 0.3 \times 10^{-3}$ in./ton (3)

2.1. *Slip in sheet/purlin fasteners.* The shear flexibility due to this cause is given by

$$c_{2.1} = \frac{2 s p}{a}\left[\frac{6}{n_p} + \frac{a^2 f_3}{b^2}\right],$$

where p = pitch of fasteners = 13.5 in.
s = slip of fastener per unit load (ref. [6]) = 0.10 in./ton
n_p = number of purlins = 13

hence $c_{2.1} = 4.2 \times 10^{-3}$ in./ton (4)

2.3. *Slip in the seam fasteners.* The shear flexibility due to seam slip is given by

$$c_{2.3} = \frac{n_{sh} s_s}{n_s},$$

where n_{sh} = number of sheet widths per panel = 14
n_s = number of seam fasteners per seam = 54
s_s = slip of seam fastener per unit load (assumed to have the same value as s) = 0.10 in./ton

hence $c_{2.3} = 25.9 \times 10^{-3}$ in./ton (5)

3.1. *Twisting of the purlin/rafter connexions.* Fig. 8 shows a typical purlin/rafter connexion at eight of the purlins; the remaining connexions were more

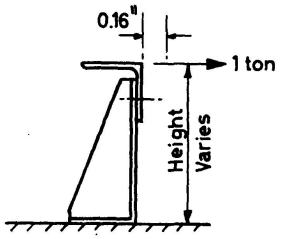


Fig. 8. Detail of purlin/rafter connexion.

flexible. From tests on other types of connexion (ref. [6]), it can be estimated that the flexibility per connexion is 0.160 in./ton.

hence $$c_{3.1} = \frac{0.160}{8} = 20.0 \times 10^{-3} \text{ in/ton}. \quad (6)$$

Total Shear Flexibility

From Eqs. (1) to (6), the total shear flexibility is given by

$$c = (1.0 + 0.8 + 0.3 + 4.2 + 25.9 + 20.0) \times 10^{-3} = 0.052 \text{ in./ton}.$$

Modified Bending Moments and Deflexions in Clad Frames

From Fig. 6, the flexibility of a bare frame is

$$k = \frac{\text{sway deflexion}}{\text{sway force}} = \frac{2.90}{9.2} = 0.315 \text{ in/ton},$$

Hence, the relative stiffness factor r is

$$r = \frac{c}{k} = \frac{0.052}{0.315} = 0.168.$$

Instead of using the type of design chart derived in reference [5], the information is tabulated. It is seen from Table 4 that for a building with 4 intermediate frames and for $r = 0.168$, the maximum value of m is 0.34. This is used in the expression

Final moment in clad frame =
Non sway moment + $m \times$ Sway moment of bare frame.

Since only wind bending moments are being considered, the non sway moment is zero and

Final moment in clad frame = $0.34 \times$ Sway moment in bare frame.

This expression applies to the two central frames of the portion considered, i.e. frames 8 and 9. The relevant factor for frames 7 and 10 is 0.24. For frames 8 and 9 the modified bending moment diagram is given in Fig. 9; the sway deflexion is 0.34 of the bare frame value.

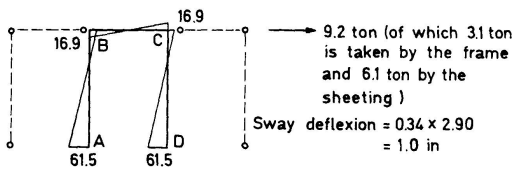


Fig. 9. Clad frame bending moments in ton-ft.

Table 4. Reduction factors to be applied to sway moments in clad buildings with 4 intermediate frames

Relative stiffness factor r	Reduction factor m to be applied	
	Intermediate frames 1 and 4	Intermediate frames 2 and 3
0.02	0.04	0.06
0.04	0.07	0.11
0.06	0.10	0.16
0.08	0.13	0.20
0.10	0.16	0.24
0.12	0.19	0.27
0.15	0.22	0.32
0.20	0.27	0.39
0.25	0.31	0.45
0.30	0.35	0.50
0.40	0.41	0.58
0.50	0.46	0.64
0.60	0.49	0.68
0.80	0.56	0.75
1.00	0.60	0.80

Forces on Roof Sheeting

Referring to Figs. 5 and 9, the force on the sheeting at frames 8 and 9 is (1—0.34) × 9.2 = 6.1 tons and the force on the sheeting at frames 7 and 10 is (1 − 0.24) × 9.2 = 7.0 tons. Hence the total shear force on the sheeting between frames 6 and 7 and between frames 10 and 11 is 13.1 tons. This represents an average shear stress in the sheeting of $13.1/80 \times 12 \times 0.028 = 0.5$ ton/in.^{2}, which is very small compared with the likely stress due to ordinary flexure of the sheet.

Ultimate Shear Strength of Panel

The strength of the panel will be calculated on the assumption that failure occurs due to

1. Tearing at the sheet/purlin fasteners.
2. Failure of the seam fasteners.

1. *Tearing at the sheet/purlin fasteners.* The normal forces on the fasteners are assumed to vary linearly along the length of a purlin as shown in Fig. 10.

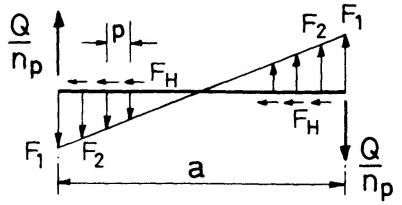


Fig. 10. Forces acting on a purlin.

The maximum normal force on a fastener, F_1, can be shown to be given by

$$F_1 = \frac{Q}{n_p\left[1+\left(\frac{a-2p}{a}\right)^2+\left(\frac{a-4p}{a}\right)^2+\cdots\right]} = \frac{Q}{13\times 4.46} = 0.017\,Q.$$

The force per fastener along the purlin, F_H, is given by

$$F_H = \frac{Q}{b}pf_3 = 0.005\,Q.$$

Hence, the maximum resultant load per fastener is

$$F_r = \sqrt{F_1^2+F_H^2} = 0.018\,Q.$$

From tests, the ultimate tearing load per fastener = 0.42 tons, so $Q = 0.42/0.018 =$ 23.4 tons which is the maximum shear strength of a panel according to this criterion.

2. *Failure of the seam fasteners.* The total shear forces on the purlins give rise to a moment Qa (Fig. 11) which is resisted by the forces on the sheeting. Hence the total shear force distribution across the sheeting is as shown in Fig. 12, the maximum value being $\frac{3}{2}Q$.

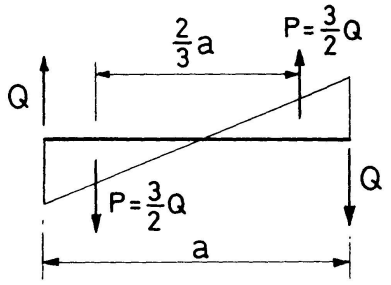


Fig. 11. Total forces acting on purlins.

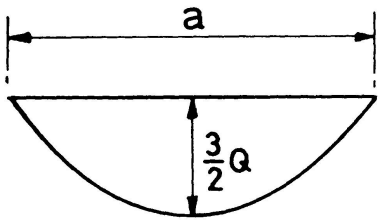


Fig. 12. Shear force distribution across sheeting.

Along the central seam there are 40 screws (ultimate tearing load 0.34 ton each) and 14 self tapping screws into the purlins (0.42 ton each) so that the maximum allowable shear force is $40\times 0.34+14\times 0.42 = 19.5$ ton. Equating this to $\frac{3}{2}Q$ gives the maximum permissible shear strength of a panel as $Q = 13.0$ ton.

From criteria (1) and (2), it is apparent that case (2) dominates. Hence the maximum shear force, under working loads, in a panel of sheeting, is slightly greater than that to cause tearing at the seam fasteners (13.1 ton cf. 13.0 ton).

Conclusions

From the calculations for a particular clad building, it is shown that the sway bending moments and deflexion may be drastically reduced by allowing

for the effect of sheeting in design. Conversely, it can be said that in analysing the given building, unless the cladding is taken into account, the calculated stresses are fictitious.

In the building considered, the seam fasteners in certain panels of roof decking are on the point of tearing the sheeting, even under working loads. Obviously this does not endanger the structure, since the steelwork has been designed on the basis of bare frames, but it could cause trouble in keeping the cladding watertight. The level of shear stress in the sheeting is so low that design of the sheeting would be determined by the ordinary flexural requirements.

By using the effect of sheeting in design it should be possible to achieve greater economy than at present without loss of safety, for the design would be based on the actual behaviour of the building rather than on the hypothetical behaviour of the bare frame.

Acknowledgements

Thanks are due to the Science Research Council for supporting the work being carried out at the University of Manchester into the stiffening effect of sheeting in buildings.

References

1. NILSON, A. H.: "Shear diaphragms of light gage steel". J. Struct. Div., Am. Soc. Civ. Engrs., 86 (ST 11), p. 111—139, November 1960.
2. LUTTRELL, L. D.: "Strength and behaviour of light gage steel shear diaphragms". Cornell Engineering Research Bulletin No. 67-1, 1967.
3. "Design of light gage steel diaphragms". American Iron and Steel Institute, New York, 1967.
4. NILSON, A. H.: "Folded plate structures of light gage steel". J. Struct. Div., Am. Soc. Civ. Engrs., 87 (ST 7), p. 215—237, October 1961.
5. BRYAN, E. R. and EL-DAKHAKHNI, W. M.: "Behaviour of sheeted portal frame sheds: theory and experiments". Proc. Instn. Civ. Engrs. vol. 29, p. 743—778, Dec. 1964.
6. BRYAN, E. R. and EL-DAKHAKHNI, W. M.: "Shear flexibility and strength of corrugated decks". J. Struct. Div., Am. Soc. Civ. Engrs. Nov. 1968.
7. BRYAN, E. R. and EL-DAKHAKHNI, W. M.: "Shear of corrugated decks: calculated and observed behaviour". Proc. Instn. Civ. Engrs. Nov. 1968.

Summary

A review is given of recent work on the diaphragm behaviour of light steel sheeting, with particular reference to shed-type buildings. The safety and desirability of taking account of the stiffening effect of sheeting in structural design is then considered.

A resume is given of three sets of shear tests on steel sheeting and decking and the results are shown to be in satisfactory agreement with the calculated values. On the basis of this agreement, a specimen calculation is made of the stiffening effect of sheeting on an actual steel framed building. The calculations show that the actual wind bending moments and transverse deflexions will be only one third of the bare frame values, and that the seam fasteners in the end panels of roof decking are stressed to the limit, even though the building was not designed to take account of the cladding.

Résumé

L'auteur commence par un bref aperçu sur les travaux récents concernant le comportement de diaphragmes en panneaux d'acier minces, où l'accent est mis sur les constructions à sheds. Puis il étudie la sécurité et l'utilité de la prise en considération de la rigidité des panneaux dans le dimensionnement d'une construction.

Il résume trois séries de tests de cisaillement faits sur des panneaux de façades et de toitures en acier. Leurs résultats se rapprochent de façon satisfaisante des valeurs calculées. Cette concordance permet de développer un calcul type pour évaluer l'effet de renforcement dû aux panneaux sur une construction d'acier à portiques. Les calculs montrent que les valeurs réelles des moments de flexion et des déplacements transversaux dus au vent se réduisent à un tiers des valeurs calculées sur le squelette nu, et que les fixations des panneaux extérieurs du toit sont sollicités à la limite, bien que le bâtiment était projété en négligeant les revêtements.

Zusammenfassung

Die Verfasser geben einen Überblick über die Scheibenwirkung von Leichtstahlplatten mit besonderer Berücksichtigung von Gebäuden mit Schirmdach (Shed-Dach).

Sicherheit und Wunsch, dem Steifigkeitseinfluß der Platten Rechnung zu tragen, werden sodann untersucht. Für drei Schubversuchssätze von Stahlplatten und -decken wird eine Zusammenfassung angegeben, und es zeigt sich, daß die Ergebnisse mit den errechneten Werten gut übereinstimmen.

Auf Grund dieser Übereinstimmung wurde eine spezielle Berechnung über den Steifigkeitseinfluß der Platte für einen gängigen Stahl-Stockwerkrahmen angestellt. Die Rechnung zeigt uns, daß die wirklichen Windbiegemomente und Querverschiebungen nur einen Drittel der Werte des baren Rahmens ausmachen und daß die Saumverbindungen in den Endfeldern der Dachplatten bis zur Grenze beansprucht sind, als ob das Gebäude ohne Verkleidung entworfen worden wäre.

Flambement des arcs

Bogenknicken

Buckling of Arches

J. COURBON
Prof., Ecole Nationale des Ponts et Chaussées, Paris

Nous exposerons deux méthodes de calcul de la poussée critique de flambement dans son plan d'un arc de section quelconque soumis à des charges verticales: la méthode des approximations successives et la méthode de l'énergie. Nous examinerons les divers types d'arcs classiques: arc encastré, arc à deux articulations, arc à une seule articulation et arc à trois articulations.

Il existe une théorie élémentaire du flambement des arcs fondée sur l'hypothèse simplificatrice qui consiste à négliger la composante horizontale du déplacement d'un point de la fibre moyenne. Cette théorie, qui ramène l'étude du flambement d'un arc à celle d'une poutre droite, n'est valable que pour des arcs très surbaissés; dès que la flèche de l'arc est notable, la théorie élémentaire donne des valeurs beaucoup trop fortes pour la poussée critique.

Il faut donc tenir compte de la composante horizontale du déplacement d'un point de la fibre moyenne. Dans ce cas, il convient de distinguer deux modes d'application des charges:

A. Charges liées à l'arc: les charges sont appliquées aux points matériels de l'arc. La ligne d'action d'une charge se déplace donc en même temps que le point d'application de la charge.

B. Charges liées a l'espace: les lignes d'action des charges sont fixes dans l'espace. Une charge appliquée initialement à un point matériel de l'arc, n'est donc plus appliquée au même point matériel de l'arc après déformation de l'arc.

Ces deux modes d'application des charges conduisent, pour un arc donné, à des valeurs légèrement différentes de la poussée critique. C'est le cas des charges liées à l'arc qui présente évidemment le plus d'intérêt pour le constructeur.

I. Etude géométrique des déformations de l'arc

1. Les fonctions considérées dans la déformation d'un arc

Les axes Ox et Oy étant rectangulaires, la fibre moyenne AB d'équation $y=y(x)$ vient, après déformation, en $A'B'$ (fig. 1). Un point matériel P de

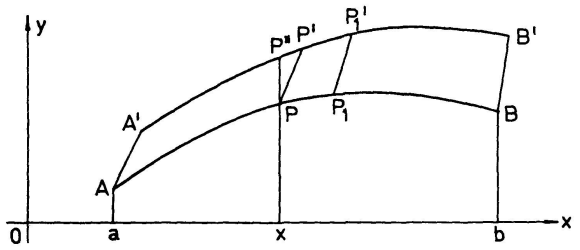


Fig. 1.

AB de coordonnées (x,y) vient, après déformation en un point P' de $A'B'$ de coordonnées $(x+\delta x,\ y+\delta y)$.

L'axe Ox fait avec la tangente en P à la fibre moyenne l'angle θ et avec la tangente en P' à la fibre moyenne déformée l'angle $\theta+\delta\theta$. Nous poserons:

$$\delta x=u, \qquad \delta y=v, \qquad \delta\theta=\varphi.$$

Enfin il existe un point P'' de $A'B'$ qui a même abscisse que P. Nous poserons $\overline{PP''}=z$.

Les fonctions u, v, φ, z sont des fonctions de x que nous considèrerons comme des infiniments petits au premier ordre. Nous allons montrer que la connaissance de la fonction v entraîne celle des fonctions u, φ, z.

a) *Calcul de la fonction u.* Un point P_1 de AB voisin de P a pour coordonnées $(x+dx, y+dy)$. Ce point vient en un point P_1' de $A'B'$ voisin de P' de coordonnées $(x+u+dx+du, y+v+dy+dv)$.

En écrivant que $PP_1=P'P_1'$ nous obtenons:

$$dx^2+dy^2=(dx+du)^2+(dy+dv)^2$$

soit en désignant par y', u' et v' les dérivées de y, u et v:

$$u'+v'y'=-\tfrac{1}{2}(u'^2+v'^2).$$

$u'+v'y'$ étant du second ordre, nous pouvons, au troisième ordre, près, remplacer dans le second membre de l'équation précédente u' par $-v'y'$. Nous obtenons ainsi:

$$u'+v'y'=-\tfrac{1}{2}(1+y'^2)v'^2. \tag{1}$$

Lorsqu'on néglige les termes du second ordre, la relation précédente se réduit à:

$$u'+v'y'=0. \tag{2}$$

Donc, si l'on se donne $v(x)$, la fonction $u(x)$ a pour expression:

$$u(x) = u(a) - \int_a^x v'(\xi)\, y'(\xi)\, d\xi \tag{3}$$

a désignant l'abscisse de l'origine A de la fibre moyenne.

b) *Calcul de la fonction* φ. Des relations:

$$\operatorname{tg}\theta = y', \qquad \operatorname{tg}(\theta+\varphi) = \frac{y'+v'}{1+u'}$$

on déduit sans difficulté, en négligeant les termes d'ordre égal ou supérieur au second, la relation:

$$\varphi = v'. \tag{4}$$

c) *Calcul de la fonction* z. Au voisinage du point P', les équations paramétriques de la fibre moyenne déformée s'écrivent:

$$X = x + u + (1+u')\,dx + \tfrac{1}{2}u''\,dx^2 + \cdots$$
$$Y = y + v + (y'+v')\,dx + \tfrac{1}{2}(y''+v')\,dx^2 + \cdots$$

Dans les expressions précédentes, dx est le paramètre variable, x et y sont les coordonnées du point P, et u, v, u', v', u'', v'' les valeurs des fonctions u, v et de leurs dérivées au point P.

Le paramètre dx du point P'' correspond à $X = x$ donc:

$$u + (1+u')\,dx + \tfrac{1}{2}u''\,dx^2 + \cdots = 0$$

d'où il résulte que, en négligeant les termes d'ordre supérieur du second:

$$dx = -u + u\,u'.$$

On en déduit immédiatement l'ordonnée Y de P'' et la valeur de $z = Y - y$. On trouve ainsi en négligeant les termes d'ordre égal ou supérieur au second:

$$z = v - u\,y'. \tag{5}$$

d) *Calcul de la variation de courbure de la fibre moyenne.* La courbure de la fibre moyenne en P est $\frac{1}{R} = \frac{d\theta}{ds}$ et la courbure de la fibre moyenne déformée en P' est $\frac{1}{R'} = \frac{d(\theta+\varphi)}{ds}$ puisque les éléments d'arc ont la même longueur. La variation de courbure est donc:

$$\delta\frac{1}{R} = \frac{d\varphi}{ds} = \frac{d\varphi}{dx}\frac{dx}{ds} = \varphi'\cos\theta.$$

Si E est le module d'Young et I le moment d'inertie de la section, le moment fléchissant résultant de la variation de courbure a donc pour valeur:

$$M = E\,I\,\delta\frac{1}{R} = E\,I\,\varphi'\cos\theta.$$

En désignant par $J = I\cos\theta$ le moment d'inertie réduit de la section et l'arc, et par D le produit EJ nous avons donc:

$$M = D\varphi' = Dv''. \tag{6}$$

Cette relation peut également être déduire des formules de Bresse, à condition de négliger les déformations dues à l'effort normal et l'effort tranchant.

2. Conditions aux limites vérifiées par le déplacement vertical

Nous définirons la déformation de l'arc par la fonction $v(x)$. Dans chaque cas particulier, cette fonction doit vérifier certaines conditions aux limites que nous allons préciser.

a) *Arc encastré.* Les axes étant choisis comme il est indiqué sur la fig. 2, la déformation est définie par la fonction $v(x)$, x étant compris entre 0 et l portée de l'arc. La fonction est nulle pour $x=0$ et $x=l$; la formule (4) montre qu'il en est de même pour la fonction $v'(x)$. Enfin $u(0)$ et $u(l)$ sont nuls. Il en résulte le cinq conditions aux limites:

$$\begin{aligned} v(0) &= 0, \qquad v(l) = 0, \\ v'(0) &= 0, \qquad v'(l) = 0, \\ &\int_0^l v'\,y'\,dx = 0 \end{aligned} \tag{7}$$

la dernière résultant de la formule (3).

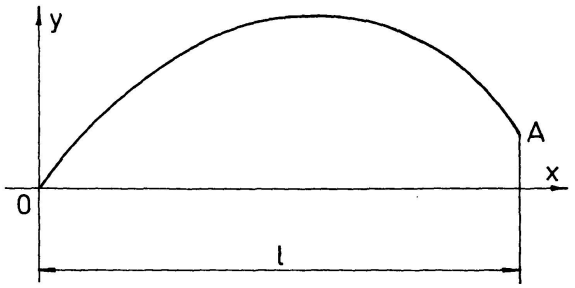


Fig. 2.

b) *Arc à deux articulations.* Les axes étant toujours ceux de la fig. 2, $v(x)$ est nul pour $x=0$ et $x=l$; il en est de même de $v''(x)$ puisque le moment fléchissant est nul aux extrémités de l'arc. Enfin $u(0)$ et $u(l)$ sont nuls. Nous avons donc les cinq conditions aux limites:

$$\begin{aligned} v(0) &= 0, \qquad v(l) = 0, \\ v''(0) &= 0, \qquad v''(l) = 0, \\ &\int_0^l v'\,y'\,dx = 0. \end{aligned} \tag{8}$$

c) *Arc à une seule articulation.* Nous choisirons deux systèmes d'axes $O_1x_1y_1$ et $O_2x_2y_2$ comme il est indiqué sur la fig. 3. La déformation est alors définie par:

$$v(x) = \begin{cases} v_1(x) & \text{pour } 0 \leqq x \leqq a_1 \quad (O_1A), \\ v_2(x) & \text{pour } 0 \leqq x \leqq a_2 \quad (O_2A) \end{cases}$$

les fonctions $v_1(x)$ et $v_2(x)$ devant satisfaire aux huit conditions aux limites:

$$\begin{aligned} &v_1(0) = 0, \qquad v_1'(0) = 0, \qquad v_1''(a_1) = 0, \\ &v_2(0) = 0, \qquad v_2'(0) = 0, \qquad v_2''(a_2) = 0, \\ &v_1(a_1) = v_2(a_2), \qquad \int_0^{a_1} v_1' y_1' dx + \int_0^{a_2} v_2' y_2' dx = 0. \end{aligned} \tag{9}$$

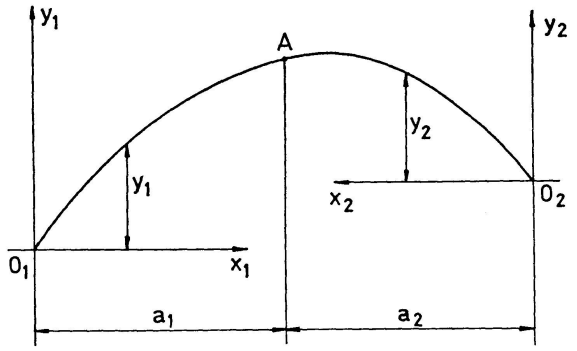


Fig. 3.

Les sept premières sont évidentes; la dernière exprime, d'après la formule (3), que le déplacement horizontal de l'articulation A est le même lorsqu'on considère cette articulation comme appartenant soit à O_1A soit à O_2A.

Les fonctions y_1 et y_2 sont les ordonnées des arcs de fibre moyenne O_1A et O_2A rapportées aux axes $O_1x_1y_1$ et $O_2x_2y_2$.

d) *Arc à trois articulations.* En conservant les axes de la fig. 3, la déformation est encore définie par:

$$v(x) = \begin{cases} v_1(x) & \text{pour } 0 \leqq x \leqq a_1 \quad (O_1A), \\ v_2(x) & \text{pour } 0 \leqq x \leqq a_2 \quad (O_2A) \end{cases}$$

les fonctions $v_1(x)$ et $v_2(x)$ devant satisfaire aux huit conditions aux limites:

$$\begin{aligned} &v_1(0) = 0, \qquad v_1''(0) = 0, \qquad v_1''(a_1) = 0, \\ &v_2(0) = 0, \qquad v_2''(0) = 0, \qquad v_2''(a_2) = 0, \\ &v_1(a_1) = v_2(a_2), \qquad \int_0^{a_1} v_1' y_1' dx + \int_0^{a_2} v_2' y_2' dx = 0. \end{aligned} \tag{10}$$

II. L'équation fondamentale vérifiée par la composante verticale du déplacement

1. Cas des charges liées à l'arc

Prenons pour origine des axes Oxy le centre de gravité de la section d'extrémité de gauche (fig. 4), et supposons l'arc *funiculaire* de la densité de charge $p(x)$ qui lui est appliquée.

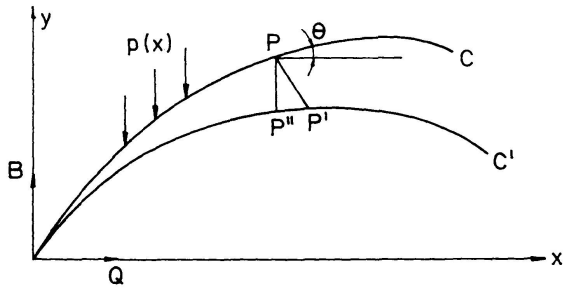


Fig. 4.

Désignons par Q et B les composantes horizontale et verticale de la réaction d'appui en O et par $-A$ le moment par rapport à 0 (compté positivement dans le sens trigonométrique) de cette réaction d'appui. En écrivant que le moment fléchissant au point P de coordonnées (x, y) de la fibre moyenne est nul, nous obtenons:

$$m(x) + A + Bx - Qy = 0 \tag{11}$$

expression dans laquelle $m(x)$ désigne la part du moment fléchissant due à la densité de charge $p(x)$:

$$m(x) = -\int_0^x p(\xi)(x-\xi)\,d\xi. \tag{12}$$

Dérivons l'équation (11) par rapport à x, nous obtenons:

$$-\int_0^x p(\xi)\,d\xi + B - Qy'(x) = 0. \tag{13}$$

Une nouvelle dérivation donne la relation classique:

$$Qy''(x) = -p(x). \tag{14}$$

Si l'on fait $x=0$ dans (13), on obtient la relation:

$$B = Qy'(0). \tag{15}$$

Donnons une déformation à l'arc; le point matériel P de coordonnées (x, y) vient au point P' de coordonnées $(x+u, y+v)$. Les quantités A, B, Q deviennent $A+\delta A$, $B+\delta B$, $Q+\delta Q$. Le moment fléchissant $M(x)$ au point P' de la fibre moyenne déformée a pour valeur, en désignant par $m(x)+\delta m(x)$ la part de ce moment due à la densité de charge $p(x)$:

$$M(x) = m(x) + \delta m(x) + A + \delta A + (B+\delta B)(x+u) - (Q+\delta Q)(y+v)$$

soit, en tenant compte de (11) et en négligeant les termes du second ordre:

$$M(x) = \delta m(x) + B u - Q v + \delta A + x \delta B - y \delta Q. \tag{16}$$

Calculons $\delta m(x)$; *puisque les charges sont appliquées aux points matériels de l'arc*, nous avons:

$$m(x) + \delta m(x) = -\int_0^x p(\xi)\,[x + u(x) - \xi - u(\xi)]\,d\xi$$

donc, en retranchant membre à membre l'équation (12) de l'équation précédente, nous obtenons:

$$\delta m(x) = -\int_0^x p(\xi)\,[u(x) - u(\xi)]\,d\xi$$

soit compte tenu de (14):

$$\delta m(x) = Q \int_0^x y''(\xi)\,[u(x) - u(\xi)]\,d\xi.$$

Une intégration par parties transforme l'équation précédente en:

$$\delta m(x) = -Q y'(0)\,u(x) + Q \int_0^x y'(\xi)\,u'(\xi)\,d\xi$$

soit en tenant compte des relations (2) et (15):

$$\delta m(x) = -B u(x) - Q \int_0^x y'^2(\xi)\,v'(\xi)\,d\xi.$$

Reportons cette valeur dans l'expression (16), nous obtenons:

$$M(x) = -Q\,[v + \int_0^x y'^2(\xi)\,v'(\xi)\,d\xi] + \delta A + x \delta B - y \delta Q.$$

Et, puisque $M = D v''$, la composante verticale du déplacement est une solution de *l'équation fondamentale:*

$$D v'' + Q\,[v + \psi_1] = \delta A + x \delta B - y \delta Q \tag{17}$$

dans laquelle ψ_1 est une fonction de x qui se déduit de la fonction $v(x)$ par *l'opérateur linéaire* L_1:

$$\psi_1 = L_1[v] = \int_0^x y'^2(\xi)\,v'(\xi)\,d\xi. \tag{18}$$

La solution générale de l'équation (17) dépend de façon linéaire et homogène de cinq constants: δA, δB, δQ et deux constantes d'intégration. En effet $v(x)$ est l'intégrale générale de l'équation différentielle linéaire du troisième ordre:

$$(D v'')' + Q\,(1 + y'^2)\,v' = \delta B - y' \delta Q$$

déduite de l'équation (18) par dérivation.

2. *Cas des charges liées à l'espace*

Conservons les hypothèses et les notations du paragraphe précédent mais calculons le moment fléchissant $M(x)$ au point $P''(x, y+z)$ de la fibre moyenne déformée qui a même abscisse que P. Puisque *les charges ont des lignes d'action fixes*, le moment des charges appliquées par rapport au point P'' est égal au moment $m(x)$ de ces mêmes charges par rapport au point P. Nous avons donc:

$$M(x) = m(x) + A + \delta A + (B + \delta B)\, x - (Q + \delta Q)(y + z)$$

soit en tenant compte de (11) et en négligeant l'infiniment petit du second ordre $z\,\delta Q$:

$$M(x) = \delta A + x\,\delta B - y\,\delta Q - z\,Q.$$

La relation $M = D\,v''$ nous donne donc l'équation:

$$D\,v'' + Q\,z = \delta A + x\,\delta B - y\,\delta Q.$$

En tenant compte des relations (2) et (5) que nous rappelons:

$$u' + v'\,y' = 0 \qquad z = v - u\,y'$$

nous voyons que les fonctions u et v sont des intégrales du système différentiel linéaire du troisième ordre:

$$D\,v'' + Q\,(v - u\,y') = \delta A + x\,\delta B - y\,\delta Q,$$
$$u' + v'\,y' = 0.$$

La fonction $v(x)$ dépend donc de façon linéaire et homogène de cinq constantes: δA, δB, δQ et deux constantes d'intégration.

Désignons par ψ_2 la fonction $-u\,y'$; nous voyons que la composante verticale du déplacement est une solution de *l'équation fondamentale:*

$$D\,v'' + Q\,[v + \psi_2] = \delta A + x\,\delta B - y\,\delta Q \tag{19}$$

dans laquelle la fonction φ_2 est une fonction de x qui se déduit de la fonction $v(x)$ par *l'opérateur linéaire* L_2:

$$\psi_2 = L_2[v] = y'(x) \int_0^x y'(\xi)\, v'(\xi)\, d\xi. \tag{20}$$

3. *Conséquences des résultats précédents*

Pour les deux modes d'application des charges envisagés, la composante verticale $v(x)$ est une solution de l'équation fondamentale:

$$D\,v'' + Q\,[v + \psi] = \delta A + x\,\delta B - y\,\delta Q \tag{21}$$

dans laquelle ψ se déduit de v par l'opérateur linéaire L_1 dans le cas des charges liées à l'arc, et par l'opérateur L_2 dans le cas des charges liées à l'espace.

Le terme ψ est un terme correctif d'autant plus faible que l'arc est plus surbaissé. Lorsqu'on néglige le terme ψ ce qui revient à négliger les déplace-

ments horizontaux de la fibre moyenne, on retrouve l'équation différentielle de la théorie élémentaire du flambement des arcs.

a) *Méthode théorique de calcul de la poussée critique:* Le calcul de la poussée critique est aisé lorsqu'on sait intégrer formellement l'équation fondamentale.

Examinons d'abord le cas d'un *arc encastré* ou d'un *arc a deux articulations* (fig. 2). La donction $v(x)$ dépend de façon linéaire et homogène de cinq constantes. Les cinq conditions aux limites (7) ou (8) fournissent donc cinq équations linéaires et homogènes entre ces cinq constantes; l'élimination des constantes entre ces équations donne une équation en Q dont la plus petite racine positive est la poussée critique.

Dans le cas d'un *arc à une seule articulation* ou d'un *arc à trois articulations* (fig. 3), nous devons écrire l'équation fondamentale pour chacun des arcs O_1A et O_2A. Le déplacement vertical dépend donc de façon linéaire et homogène de dix constantes:

$$\delta A_1, \delta A_2, \delta B_1, \delta B_2, \delta Q_1, \delta Q_2$$

et quatre constantes d'intégration. Mais ces dix constantes se réduisent à huit, car les équations d'équilibre de la statique exigent que:

$$\delta Q_1 = \delta Q_2 = \delta Q, \qquad \delta B_1 = -\delta B_2 = \delta B.$$

Les huit conditions aux limites (9) ou (10) donnent alors huit équations linéaires et homogènes entre les huit constantes; l'élimination des constantes entre ces équations donne une équation en Q dont la plus petite racine positive est la poussée critique.

b) *Cas d'un arc non funiculaire:* Dans ce cas le moment fléchissant $\mathfrak{M}(x)$ dans l'arc avant déformation n'est pas nul; l'équation (11) est remplacée par:

$$\mathfrak{M}(x) = m(x) + A + Bx - Qy.$$

En reprenant les calculs qui nous ont conduit à l'équation fondamentale, nous trouvons que $v(x)$ satisfait à l'équation:

$$Dv'' + Q[v+\psi] = \mathfrak{M}(x) + \delta A + x\delta B - y\delta Q.$$

La solution générale de cette équation s'obtient en ajoutant à la solution générale de l'équation fondamentale (21) une solution particulière de l'équation:

$$Dv'' + Q[v+\psi] = \mathfrak{M}(x).$$

Les constantes qui interviennent sont, dans chaque cas, déterminées par les conditions aux limites. On obtient ainsi autant d'équations linéaires que de constantes, mais ces équations ne sont plus homogènes. La poussée critique est la plus petite valeur de pour laquelle le déterminant principal du système d'équations précédentes s'annule. Le moment fléchissant $\mathfrak{M}(x)$ n'intervient

donc pas dans le calcul de la poussée critique. *La poussée critique est donc une caractéristique de l'arc qui ne dépend pas des charges appliquées, mais seulement de la façon dont ces charges sont appliquées* (charges liées à l'arc ou charges liées à l'espace).

III. Méthode des approximations successives

1. Calcul de la poussée critique par approximations successives

Nous allons d'abord définir un opérateur linéaire Ω permettant d'associer, à toute représentation approchée $v_0(x)$ de la déformation au moment du flambement, une représentation plus précise $v_1(x)$.

Examinons d'abord le cas d'un *arc encastré* ou d'un *arc à deux* articulations (fig. 2). Donnons nous une fonction de départ v_0 vérifiant les conditions aux limites (7) ou (8); il lui correspond une fonction ψ_0 par l'opérateur L_1 ou par l'opérateur L_2 selon que les charges sont liées à l'arc ou liées à l'espace. La fonction v_1 est la fonction qui vérifie les conditions aux limites (7) ou (8) et dont la dérivée seconde a pour expression:

$$v_1'' = \frac{-(v_0+\psi_0)+\delta A+x\,\delta B-y\,\delta Q}{D}.$$

Il suffit pour déterminer la fonction v_1 d'intégrer deux fois l'expression précédente et de déterminer δA, δB, δQ et les deux constantes d'intégration au moyen des conditions aux limites (7) ou (8).

Dans le cas d'un *arc à une seule articulation* ou d'un *arc à trois articulations* (fig. 3), nous nous donnons une fonction v_0 égale à $(v_1)_0$ sur O_1A et à $(v_2)_0$ sur O_2A, les fonctions $(v_1)_0$ et $(v_2)_0$ vérifiant les conditions aux limites (9) ou (10); l'opérateur linéaire L_1 (ou L_2) associe aux fonctions $(v_1)_0$ et $(v_2)_0$ les fonctions $(\psi_1)_0$ et $(\psi_2)_0$. La fonction v_1 est égale à $(v_1)_1$ sur O_1A et à $(v_2)_1$ sur O_2A; les fonctions $(v_1)_1$ et $(v_2)_1$ vérifient les conditions aux limites (9) ou (10) et ont pour dérivées secondes:

$$(v_1)_1'' = \frac{-[(v_1)_0+(\psi_1)_0]+\delta A_1+x\,\delta B-y\,\delta Q}{D},$$

$$(v_2)_1'' = \frac{-[(v_2)_0+(\psi_2)_0]+\delta A_2-x\,\delta B-y\,\delta Q}{D}.$$

Il suffit pour déterminer les fonctions $(v_1)_1$ et $(v_2)_1$ d'intégrer deux fois les expressions précédentes et de déterminer δA_1, δA_2, δB, δQ et les quatre constantes d'intégration au moyen des conditions aux limites (9) ou (10).

Nous avons ainsi défini dans tous les cas un opérateur linéaire Ω permettant de calculer v_1 connaissant v_0:

$$v_1 = \Omega[v_0]. \tag{23}$$

On peut donc définir une suite de fonctions $v_0, v_1, v_2 \ldots v_n$ telles que:

$$v_1 = \Omega[v_0], \quad v_2 = \Omega[v_1], \ldots, \quad v_n = \Omega[v_{n-1}], \ldots$$

Ceci posé, supposons que $v_0(x)$ soit, à un facteur près, la déformation qui se produit au moment du flambement. Si nous multiplions $v_0(x)$ par la valeur Q_c de la poussée critique, nous obtiendrons une fonction:

$$\Omega[Q_c v_0] = Q_c \Omega[v_0] = Q_c v_1(x)$$

qui doit être identique à $v_0(x)$. Nous aurions donc:

$$Q_c = \frac{v_0(x)}{v_1(x)}. \tag{24}$$

Mais, puisque $v_0(x)$ n'est qu'une approximation de la déformation au moment du flambement, le second membre de (24) n'est pas une constante. On obtiendra cependant une valeur approchée de la poussée critique en donnant à x dans la formule (24) une valeur particulière (celle qui correspond par exemple aux plus grandes valeurs de v_0 et de v_1.

Si l'approximation est jugée insuffisante parce que le second membre de (24) varie trop, on utilisera un des rapports de la suite:

$$\frac{v_1(x)}{v_2(x)}, \quad \frac{v_2(x)}{v_3(x)}, \quad \ldots, \quad \frac{v_{n-1}(x)}{v_n(x)}, \quad \ldots$$

qui tend vers la poussée critique.

Il résulte de ce qui précède que la poussée critique est la plus petite valeur propre de l'équation:

$$v(x) = Q\Omega[v(x)]. \tag{25}$$

Il est possible de montrer, dans chaque cas particulier, que l'équation (25) est une équation intégrale de FREDHOLM dont le noyau a généralement une forme assez complexe.

Des simplifications de calcul sont possibles dans le cas des arcs ayant un axe de symétrie. On peut dans ce cas distinguer le flambement symétrique et le flambement antisymétrique correspondant à des déformations au moment du flambement $v(x)$ paires ou impaires, les abscisses x étant comptées à partir de l'axe de symétrie.

En général, la poussée critique d'un arc encastré ou d'un arc à deux articulations symétriques correspond au flambement antisymétrique, tandis que la poussée critique d'un arc à une seule articulation ou d'un arc à trois articulations correspond au flambement symétrique.

2. Majoration des efforts dans un arc non funiculaire

On démontre que l'équation intégrale (25) a une infinité de solutions non identiquement nulles $V_1, V_2, \ldots, V_i, \ldots$ pour une infinité de valeurs croissantes de Q: $Q_1 < Q_2 < \ldots < Q_i < \ldots$ dont la plus petite est égale à la poussée

critique Q_c. Les solutions $V_1, V_2, \ldots, V_i, \ldots$ appelées fonctions fondamentales vérifient donc les identités:

$$V_1 = Q_1 \Omega [V_1], \quad V_2 = Q_2 \Omega [V_2], \ldots, \quad V_i = Q_i \Omega [V_i], \ldots$$

Ceci posé, reprenons l'équation (22) établie précédemment

$$D v'' + Q [v + \psi] = \mathfrak{M} (x) + \delta A + x \delta B - y \delta Q \tag{22}$$

et soit $v_0 (x)$ la déformation calculée par les théories classiques de la Résistance des Matériaux, en négligeant les déformations pour écrire les équations d'équilibre. Nous avons:

$$D v_0'' = \mathfrak{M} (x)$$

et nous pouvons remplacer l'équation (22) par l'équation intégrale linéaire:

$$v (x) = v_0 (x) + Q \Omega [v (x)]. \tag{26}$$

Développons $v_0 (x)$ en série de fonctions fondamentales:

$$v_0 (x) = a_1 V_1 (x) + a_2 V_2 (x) + \ldots + a_i V_i (x) + \ldots$$

et cherchons $v (x)$ sous forme d'une série de fonctions fondamentales:

$$v (x) = b_1 V_1 (x) + b_2 V_2 (x) + \ldots + b_i V_i (x) + \ldots$$

En reportant les expressions précédentes dans l'équation (26), on trouve sans peine que

$$b_i = \frac{a_i}{1 - \frac{Q}{Q_i}}$$

de sorte que:

$$v (x) = \frac{a_1}{1 - \frac{Q}{Q_1}} V_1 (x) + \frac{a_2}{1 - \frac{Q}{Q_2}} V_2 (x) + \cdots + \frac{a_i}{1 - \frac{Q}{Q_i}} V_i (x) + \cdots$$

Les coefficients a_i du développement de $v_0 (x)$ sont donc multipliés par des facteurs supérieurs à l'unité et tendant vers l'unité lorsque i augmente indéfiniment.

Le terme $a_1 V_1 (x)$ étant le terme prépondérant du développement de $v_0 (x)$, il en résulte, avec une bonne approximation que:

Dans un arc de poussée critique Q_c, les efforts et déformations calculés par les théories classiques de la Résistance des Matériaux doivent être multipliés par le facteur $\frac{1}{1 - \frac{Q}{Q_c}}$ *pour tenir compte de l'influence des déformations.*

IV. Méthode de l'énergie

Considérons l'arc funiculaire en équilibre sous les charges qui lui sont appliquées; cet équilibre sera stable si la fibre moyenne revient à sa position initiale d'équilibre après avoir subi une déformation, donc si le travail $\delta \mathfrak{T}$ des forces extérieures est inférieur à l'énergie δW emmagasinée dans l'arc au

cours de la déformation. La poussée critique s'obtiendra donc en écrivant que $\delta \mathfrak{T}$ est égal à δW.

1. Cas des charges liées à l'arc

Nous considérons un arc quelconque, et nous lui donnons une déformation compatible avec les liaisons imposées à l'arc. Dans chaque cas particulier étudié, la fonction $v(x)$ doit donc vérifier les conditions aux limites qui ont été indiquées précédemment.

Nous désignerons par $\mathfrak{F}$ l'ensemble des fonctions $v(x)$ vérifiant les conditions aux limites.

Calculons l'énergie δW emmagasinée dans l'arc au cours de la déformation; nous avons, les intégrales suivantes étant étendues d'une extrémité à l'autre de l'arc:

$$\delta W = \frac{1}{2}\int \frac{M^2\,ds}{EI} = \frac{1}{2}\int \frac{M^2\,dx}{EJ} = \frac{1}{2}\int \frac{M^2\,dx}{D}$$

et, puisque $M = D\,v''$:

$$\delta W = \tfrac{1}{2}\int D\,v''^2\,dx. \tag{27}$$

Calculons maintenant le travail $\delta \mathfrak{T}$ des forces extérieures. Supposons l'arc funiculaire des charges appliquées, ce qui, comme nous l'avons montré précédemment n'a pas d'influence sur la valeur de la poussée critique. En désignant par $p(x)$ la densité de charge appliquée à l'arc, nous avons, les intégrales qui figurent dans les formules qui suivent étant étendues d'une extrémité à l'autre de l'arc:

$$\delta \mathfrak{T} = -\int p\,v\,dx$$

et, puisque l'arc est funiculaire nous avons $Q\,y'' = -p$ donc:

$$\delta \mathfrak{T} = Q\int v\,y''\,dx.$$

Intégrons par parties, nous obtenons, v étant toujours nul aux extrémités de l'arc:

$$\delta \mathfrak{T} = -Q\int v'\,y'\,dx$$

soit, compte tenu de la formule (1):

$$\delta \mathfrak{T} = Q\int [u' + \tfrac{1}{2}(1+y'^2)\,v'^2]\,dx$$

et, puisque u est toujours nul aux extrémités de l'arc:

$$\delta \mathfrak{T} = \tfrac{1}{2}\,Q\int (1+y'^2)\,v'^2\,dx. \tag{28}$$

On remarquera qu'il est nécessaire de tenir compte des termes du second ordre pour calculer le travail des forces extérieures. Si l'on avait utilisé l'expression (2) au lieu de l'expression (1), on aurait trouvé une valeur nulle pour le travail des forces extérieures.

Le flambement a lieu dès que $\delta \mathfrak{T}$ dépasse δW; il en résulte immédiatement que la poussée critique Q_c a pour valeur:

$$Q_c = \underset{v \in \mathfrak{F}}{\text{Minimum}} \left[\frac{\int D v''^2 dx}{\int (1+y'^2) v'^2 dx} \right]. \tag{29}$$

Si la déformation $v(x)$, appartenant à l'ensemble $\mathfrak{F}$, n'est pas exactement celle qui se produit au moment du flambement, la formule (29) donne une valeur par excès de la poussée critique. On obtiendra une grande précision en choisissant pour $v(x)$ les fonctions $v_0(x), v_1(x), \ldots$ obenues par la méthode des approximations successives exposée précédemment; on utilise ainsi toutes les valeurs des fonctions calculées.

Le calcul des variations permet de montrer l'équivalence de la méthode des approximations successives et de la méthode de l'énergie.

2. Cas des charges liées à l'espace

Conservons les définitions du paragraphe précédent; le calcul de l'énergie δW emmagasinée dans l'arc est inchangé, et la formule (27) est encore exacte.

Par contre, le calcul du travail $\delta \mathfrak{T}$ des forces extérieures soulève des difficultés parce qu'il est difficile d'imaginer une liaison permettant d'appliquer à l'arc, durant la déformation, une densité de charge dont les lignes d'action sont liées à l'espace. Par exemple, on pourrait être tenté de prendre pour valeur de $\delta \mathfrak{T}$:

$$\delta \mathfrak{T} = -\int p z dx = Q \int y'' z dx.$$

Ce résultat est inexact, parce qu'il correspond à la liaison indiquée sur la fig. 5; cette liaison donne lieu à une densité de charge verticale p et à une densité de charge horizontale py'. Si l'on veut transmettre à l'arc une densité

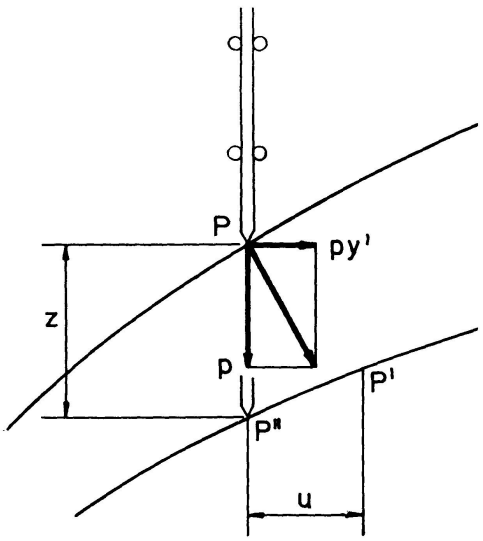


Fig. 5.

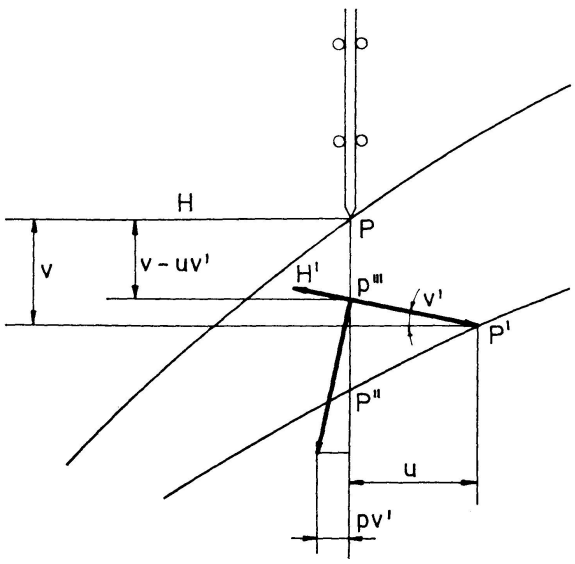


Fig. 6.

de charge verticale au moyen de la liaison indiquée sur la fig. 5, il faut que cette liaison soit une liaison avec frottement; il est alors nécessaire de tenir compte du travail négatif des forces de frottement dans l'évaluation de $\delta \mathfrak{T}$.

Pour appliquer au moyen d'un pointeau coulissant verticalement une densité de charge verticale à l'arc, on peut imaginer (fig. 6) qu'un élément indéformable horizontal PH a été soudé en P à la fibre moyenne. Après déformation cet élément vient en $P'H'$; P' est le même point matériel que P, et $P'H'$ n'est plus horizontal, mais a une pente $\varphi = v'$. Le pointeau s'abaissant de $PP''' = v - u\,v'$ le travail $\delta_1 \mathfrak{T}$ des forces exercées par le pointeau sur l'arc est

$$\delta_1 \mathfrak{T} = -\int p\,(v - u\,v')\,dx.$$

Mais, au cours de la déformation, si la densité de charge verticale appliquée à l'arc reste égale à p, la densité de charge horizontale appliquée à l'arc varie (linéairement si la déformation est petite) de 0 à $p\,v'$. Le travail $\delta_1 \mathfrak{T}$ est donc la somme du travail $\delta \mathfrak{T}$ de la composante verticale p (c'est le travail que nous cherchons), et du travail $\delta_2 \mathfrak{T}$ de la composante horizontale:

$$\delta_2 \mathfrak{T} = \tfrac{1}{2} \int p\,v'\,u\,dx.$$

Il en résulte que:

$$\delta \mathfrak{T} = \delta_1 \mathfrak{T} - \delta_2 \mathfrak{T} = -\int p\,(v - \tfrac{1}{2} u\,v')\,dx$$

ou, l'arc étant funiculaire de la densité de charge p:

$$\delta \mathfrak{T} = Q \int (v\,y'' - \tfrac{1}{2} u\,v'\,y'')\,dx.$$

Nous avons montré dans le paragraphe précédent que:

$$\int v\,y''\,dx = \tfrac{1}{2} \int v'^2 (1 + y'^2)\,dx$$

donc, nous obtenons finalement:

$$\delta \mathfrak{T} = \tfrac{1}{2}\, Q \int [v'^2 (1 + y'^2) - u\,v'\,y'']\,dx. \tag{30}$$

Compte tenu de la valeur (5) de z, l'expression (30) peut également s'écrire:

$$\delta \mathfrak{T} = \tfrac{1}{2} \int v'\,z'\,dx.$$

Dans toutes les formules, les intégrales sont étendues d'une extrémité à l'autre de l'arc.

Le flambement a lieu dès que $\delta \mathfrak{T}$ dépasse δW; il en résulte immédiatement que la poussée critique Q_c a pour valeur:

$$Q_c = \underset{v \in \mathfrak{F}}{\text{Minimum}} \left[\frac{\int D\,v''^2\,dx}{\int [(1 + y'^2)\,v'^2 - u\,v'\,y'']\,dx} \right]. \tag{31}$$

Le calcul des variations permet encore de montrer l'équivalence de la méthode des approximations successives et de la méthode de l'énergie.

Conclusion

Nous avons donné deux méthodes de calcul numérique de la poussée critique d'un arc, tant dans le cas pratique des charges liées à l'arc que dans le cas théorique des charges liées à l'espace. La méthode des approximations successives donne lieu à des calculs d'intégration numérique beaucoup plus longs que la méthode de l'énergie; elle paraît cependant indispensable pour trouver une déformation approchée $v(x)$ correcte, et non choisie au hasard, afin de pouvoir appliquer la méthode de l'énergie.

Dans le cas particulier d'un arc de fibre moyenne quelconque et de loi d'inertie quelconque, on obtiendra une valeur suffisamment précise de la poussée critique en opérant de la façon suivante:

a) En prenant pour fonction de départ $v_0(x)$ la déformation de la théorie élémentaire de l'arc parabolique d'inertie réduite constante, on déterminera, par intégration numérique, la première déformation $v_1(x)$ de la méthode des approximations successives.

b) On calculera la poussée critique par la méthode de l'énergie en prenant pour déformation $v_1(x)$.

Nous avons appliqué les méthodes précédentes aux arcs symétriques d'inertie réduite constante J à fibre moyenne parabolique. En désignant par $2a$ la portée de l'arc et par f sa flèche, la valeur approchée de la poussée critique peut se mettre dans tous les cas sous la forme:

$$Q_c = m\frac{\pi^2 E J}{a^2}\frac{1}{1+K\left(\frac{f}{2a}\right)^2}. \tag{32}$$

m et K étant des constantes données dans le tableau suivant:

Type d'Arc	m	K pour des charges liées		Observations
		à l'arc	à l'espace	
Arc encastré	2,0458	3,35	4,01	Flambement
Arc à 2 articulations	1	6,14	6,95	antisymétrique
Arc à 1 articulation	1,1132	1,15	1,36	Flambement
Arc à 3 articulations	0,7527	1,99	2,27	symétrique

Résumé

La théorie élémentaire du flambement des arcs néglige les déplacements horizontaux des points de la fibre moyenne de l'arc; cette théorie ne donne de résultats suffisamment précis que pour les arcs très surbaissés. Dès que la

flèche de l'arc est importante, elle conduit à surestimer beaucoup la poussée critique de l'arc et de ce fait est dangereuse.

Deux méthodes correctes de calcul numérique de la poussée critique sont données: la méthode des approximations successives et la méthode de l'énergie, tant dans le cas des charges liées à l'arc que dans le cas des charges liées à l'espace. Les différentes liaisons pouvant être imposées à l'arc ont été examinées: arc encastré, arc à deux articulations, arc à une seule articulation et arc à trois articulations.

Zusammenfassung

Die elementare Theorie der Knickung von Bogen vernachlässigt die waagrechten Verschiebungen der Nullachsen-Punkte des Bogens. Diese Theorie ergibt nur für sehr flache Bogen genügend genaue Ergebnisse. Sobald die Pfeilhöhe maßgebend wird, führt dies zu einer gefährlichen Überschätzung des kritischen Horizontalschubes.

Es werden zwei fehlerfreie Methoden der numerischen Berechnung des kritischen Schubes angegeben: Die fortgesetzte Annäherung sowie die Energiemethode. Sowohl für den Fall der in der Bogenebene liegenden Belastung als auch für räumliche Belastung. Verschiedene Bogenausbildungen wurden untersucht, nämlich den eingespannten, den Eingelenk-, Zweigelenk- und Dreigelenkbogen.

Summary

The elementary theory of the buckling of arches neglects the horizontal movements of the mean fibre of the arch; this theory gives sufficiently accurate results only for drop arches. As soon as the rise of the arch becomes considerable, it leads to a marked overestimation of the critical thrust of the arch and is therefore dangerous.

Two correct methods of numerical calculation of the critical thrust are given: the method of successive approximations and the energy method, both in the case of loads bound with the arch and in the case of loads bound with space. The different connections that can be imposed on the arch were examined: fixed arch, two-hinged arch, arch with a single hinge and three hinged arch.

Leere Seite
Blank page
Page vide

Ultimate Strength Tests of Reinforced Concrete Beams in Combined Torsion, Bending and Shear

Essais de rupture de poutres en béton armé soumises à l'action combinée de la torsion, de la flexion et du cisaillement

Bruchlasttests an Stahlbetonträgern unter kombinierter Beanspruchung aus Drillung, Biegung und Schub

HANS GESUND DONALD G. MILLS VICTOR M. MARTIN
University of Kentucky, Lexington, Kentucky

Introduction

The earliest major effort in the study of the behavior of reinforced concrete members in combined torion, bending and shear was made in Russia. More recently, important work has been done in the United States, Canada, Australia and India. The Russian work resulted in a series of publications by CHINENKOV [1], LIALIN [2], LESSIG [3, 4] and YUDIN [5, 6]. Some of it was experimental and some theoretical, with early emphasis placed on combined torsion and bending moment and combined torsion and shear. YUDIN later combined all three types of loading, but the experiments were conducted on rather small specimens (3.5 by 6.4 inches in cross section). He reported failure modes which were also observed in some of the specimens to be reported on here, namely that the failures were ". . . typical of tearing the center part of the beam from the end sections". A similar phenomenon may be observed in NYLANDER'S [7] report on tests of frames in which one member, reinforced both longitudinally and transversely, was subjected to torsion.

More recently, PANDIT and WARWARUK [8] tested sixteen specimens in combined torsion, bending and shear. These were larger than the Russian specimens (6 by 12 inches in cross section), but the sequence of loading was different. Whereas the Russians, and apparently all other investigators to date, have increased the torsional, bending and shear loads simultaneously in proportion, PANDIT and WARWARUK subjected their specimens first to some predetermined load level in transverse bending and shear alone, and then twisted them to failure.

Test results from several of their specimens will be checked against the torsional strength predicted by a rational equation to be developed in this paper.

A number of specimens were also tested under combined loading by WALSH, COLLINS, ARCHER and HALL [9], who then developed semi-empirical formulae [10] to predict the strengths of members subjected to the combined loading. The failures observed in these tests were similar to most of those to be described here, i.e. they occurred by rotation of sections of the specimens about hinges which formed near one face after inclined cracks had formed on the other faces. All reinforcement in this series consisted of round, undeformed, mild steel bars. The same type of reinforcement was used in tests conducted by RAMAKRISHNAN and VIJAYARANGAN [11, 12], whose results will also be checked against the theory to be developed here.

Almost all of the above mentioned work contained restrictions on specimen size, method of application or sequence of loading, type of reinforcement, and/or strength of concrete, which affected the results of the tests. Furthermore, reinforcement strains were measured only in some of the Russian tests and by PANDIT and WARWARUK. Other investigations into the effects of combined loading have concerned themselves with prestressed concrete beams and with reinforced concrete beams of cross section other than solid rectangular. Consequently it seemed advisable to extend the earlier work on rectangular reinforced concrete specimens conducted at the University of Kentucky [13, 14]. The results of this had indicated that a member subjected to combined torsion and bending, without shear, would fail by rotation about a hinge in the compression face of the member if the specimen were square in cross section and contained longitudinal reinforcement only or if it were square or rectangular and contained transverse reinforcement, but that it would fail by rotation about a hinge in one of the sides if it were rectangular and only reinforced longitudinally. Since most actual beams may be expected to be subjected to combined torsion, bending and shear, it was decided to study square specimens containing only longitudinal reinforcement and rectangular specimens containing both longitudinal and transverse reinforcement subjected to the triple loading.

Description of the Specimens

Ten beams were loaded in combined torsion, bending and shear. The first six were eight inches by eight inches in cross section and contained essentially only longitudinal reinforcement. The other four were six inches by twelve inches in cross section and contained both longitudinal and transverse reinforcement. An overall view of the test specimens and the loading scheme is given in figure 1. Various ratios of bending moment to torque could be obtained by changing the lengths of the arms. The ratio of shear to bending moment was kept constant by making the total lengths of all specimens equal. The loading

and support arms in all specimens were reinforced with three no. 4 bars on the tension side and two no. 4 bars on the compression side. The steel was detailed so that in all arms the two outside tension bars were bent around the beam reinforcement and back into the arm to provide compression reinforcement. The third tension bar was hooked around the bottom beam reinforcement for anchorage. Shear reinforcement in the form of no. 3 or no. 4 closed ties, spaced three inches center to center, was also provided in all arms.

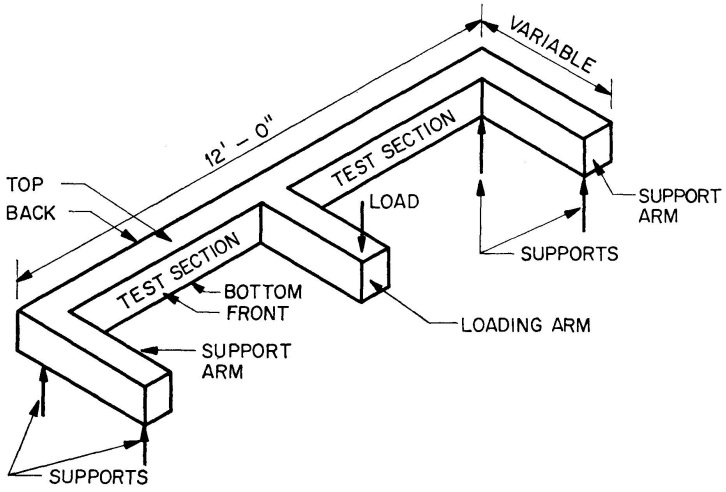


Fig. 1. Specimens and loading scheme.

The longitudinal reinforcement in the test sections of all specimens consisted of three no. 4 bars on the bottom and two no. 4 bars on the top. The test sections of specimens 1 through 6 were reinforced only with the longitudinal steel, except for two no. 3 closed ties placed three inches center to center from each other and from the arm reinforcement at each end of each test section to prevent local failure due to stress concentrations. The test sections of specimens 7 through 10 also contained transverse reinforcement. This consisted of no. 3 closed ties, spaced three inches center to center throughout the test sections except for the first three ties at each end, which were placed at two inches center to center, again in an attempt to prevent local failure. For further details see table I and figure 2.

All reinforcement consisted of intermediate grade deformed bars meeting the requirements of ASTM specifications A-15 and A-305. Yield stresses of the various bars used are given in table I. The concrete for all specimens was commercially obtained transit mix with the following composition: 5 bags cement, 1545 pounds sand, 1890 pounds stone (½ inch to ¾ inch chips), 1¼ pounds Pozzolith and, nominally, 37 gallons of water per cubic yard. Since it was considered desirable to have some variation in concrete strength, strict control was not exercised over the mix. The mixing water was added in the truck at the laboratory, but workability of the concrete rather than the precise quantity of water added was used as the controlling factor.

After being cast, the beams were cured at room temperature under wet burlap for seven days and the left to air dry in the laboratory. All specimens

Table I. Beam Properties

Specimen Number	Nominal[1]) M/T ratio	Cross Section (inches)	f_y Longitudinal Reinf. (psi)	Transverse Reinf. (psi)	f'_c[2]) (psi)
1	1	8× 8	43,000	—	6,025
2	2	8× 8	43,000	—	6,025
3	3	8× 8	43,000	—	4,350
4	4	8× 8	43,000	—	4,350
5	5	8× 8	46,250	—	5,100
6	6	8× 8	46,250	—	5,100
7	1	6×12	45,500	50,000	5,460
8	2	6×12	45,500	50,000	5,500
9	4	6×12	45,500	50,000	5,500
10	8	6×12	45,500	50,000	5,460

[1]) The ratios of the actual values varied slightly from this. See table II.
[2]) Average of three cylinders, obtained at time of test of associated specimen.

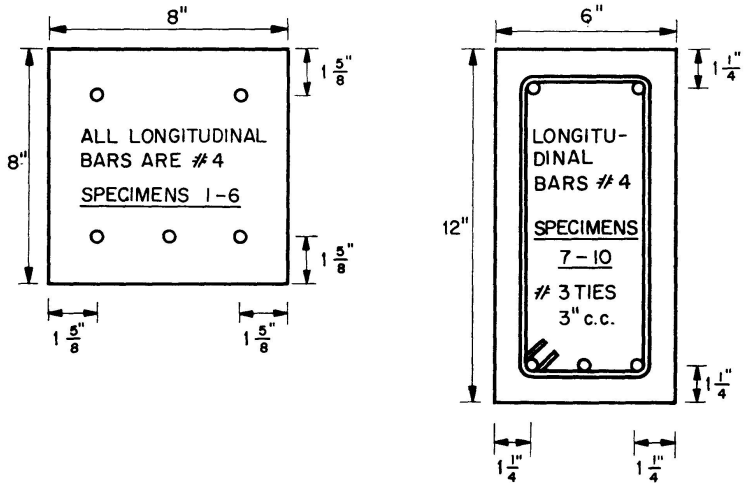


Fig. 2. Specimen cross sections.

were tested between thirty and sixty days after being cast. The accompanying cylinders were tested at the same time as the specimens. Strengths are recorded in table I.

SR-4 type A-7 strain gages were attached to the reinforcement at many points and type AR-1 rosettes were later attached to the concrete at locations where maximum tensile stresses were expected. It was thus possible to monitor the strains in the reinforcement and the concrete during the conduct of the tests and to deduce some information regarding the mode of failure later.

Conduct of Tests and Results

The general test setup is shown in figure 1. The load was applied to the center of each specimen in one to two thousand pound increments, the smaller increments being used near failure. After each increase, the load was held constant for a period of from five to twenty minutes while all strain gage readings and

loads were recorded and the crack patterns sketched and photographed. Except for the last one or two increments before failure, recheck of the strain gages showed that little creep occurred during the observation periods.

The behavior of the two sets of specimens was quite similar at relatively low loads, but differed markedly as the loading proceeded. Their final failure modes bore very little relationship to each other. Within each set, however, the response to the loading changed very little from specimen to specimen, though one could easily observe the differences caused by the changes in the moment/torque ratio. For example, in the set of six beams which contained only longitudinal reinforcement, it was possible to see the gradual changes in the crack patterns as the moment/torque ratio progressed from 1 to 6. In beam 1, the initial crack pattern consisted of cracks on all surfaces except the back (see figure 1 for the designations of the surfaces), inclined at between 37 and 45 degrees to the beam axis. This pattern had formed by the time a load equal to 80 percent of the failure load had been reached. Continued loading produced no remarkable deformations until, suddenly, a mechanism formed in one of the test sections, in which two segments of the beam rotated with respect to each other about an S-shaped hinge which formed on the back of the specimen, approximately at mid-height. At the same time, a piece of concrete was spalled off the bottom of the beam. Upon close examination it was found that this piece of concrete was a parallelopiped whose boundaries were: the bottom of the beam, the longitudinal bottom reinforcing bars, and parallel diagonal cracks approximately four inches apart, intersecting the front and back faces of the beam. Specimen 2 behaved very similarly. In this beam the first cracks were noticed when the load had reached approximately 38 percent of the failure load.

Specimen 3 showed considerable influence of bending. The cracks on the bottom made a larger angle with the axis of the beam and the early cracks on the front and back were almost vertical. Specimen 4 appeared to behave as though it were being loaded only in bending, with the classical bending crack pattern, until it suddenly collapsed with the formation of the S-shaped hinge on the back and the spalling of the parallelopiped from the bottom. The major failure crack pattern seemed to partially override the bending cracks and was almost identical with that formed in the previous three specimens. It is shown in figure 3. Specimens 5 and 6 behaved like specimen 4, but some crushing of the top surface and considerable widening of the bottom tension cracks was noticeable before the sudden torsional failure occurred. The strain gage readings indicated that all three bottom reinforcing bars of specimen 6 had yielded before the collapse.

Figure 4 shows a plot of bending moment versus strain for the longitudinal reinforcement in specimen 2. The strains were measured 12 inches from the face of the loading arm but the recorded moments are those at the face of the loading arm. The bending moments at the locations of the gages were approx-

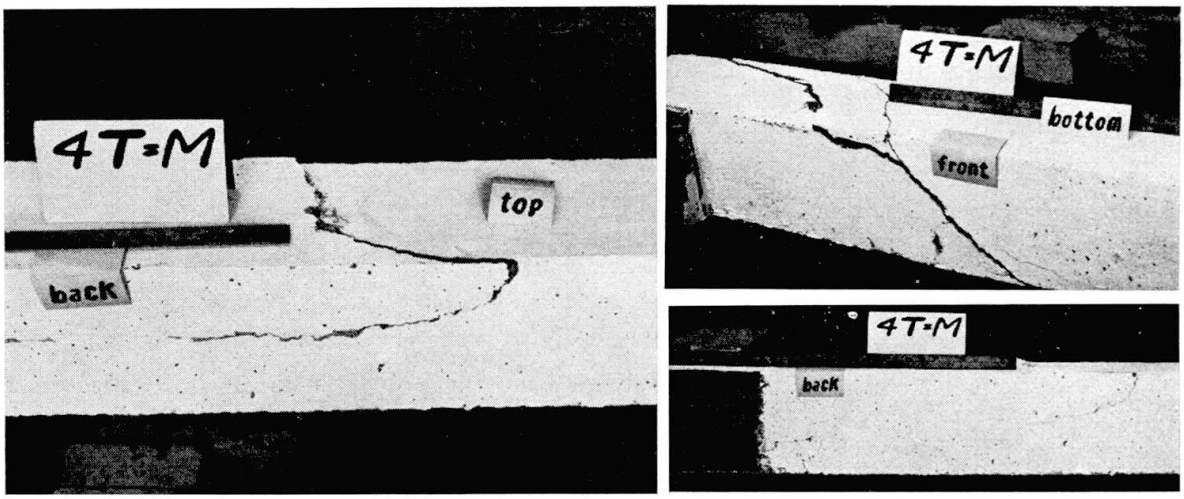


Fig. 3. Failure crack pattern of specimen 4.

imately 80% of those indicated. They are typical of the readings observed in specimens 1 through 6, and clearly indicate that the specimens were bent laterally, convex to the front, to such an extent that the front bars were subjected to an appreciable additional tensile strain. This additional strain caused the front bottom bar to yield long before the ordinary bending moment would have done so. The strain readings on specimens 7 through 10 also indicated more tension in the front than the rear bottom bars, but the differences were much smaller and the top bars were not consistent in this respect. The strain readings for specimen 5 appeared to indicate a reversal of this curvature, but

Table II. Test Results

Specimen Number	Bending Moment[1]) at Failure (in. kips)	Shear at Failure (kips)	Torque at Failure[2]) (inch-kips) about:		Theoretical Ultimate Moment (ACI Code)[4]) (inch-kips)		Theoretical Dowel Torque about Hinge in back (inch-kips) for Crack Spacing	
			Center Line	Hinge in back	Beam	Load Arm	Predicted	Actual
1	75.1	1.18	62.5	67.2	157	171	47.1	58.0
2	113.8	1.78	43.3	50.4	157	171	47.1	43.5
3	105.2	1.60	43.3	49.6	155	168	40.0	43.0
4	153.1	2.40	36.4	46.0	155	168	40.0	36.8
5	179.0	2.80	44.6	55.8	169	182	43.2	38.4
6	194.0	3.03	36.5	48.6	169	182	43.2	38.4
7	77.6	1.17	78.5	82.0	307	322	59.5	79.3
8	231	3.50	120.3	262[3])	307	322	—	—
9	281	4.26	73.2	172[3])	307	322	—	—
10	306	4.64	44.6	108[3])	307	322	—	—

[1]) Taken about the edge of the loading arm rather than about the center of the beam.
[2]) Calculated from the reactions of the test section which failed.
[3]) Calculated as load applied to specimen times length of loading arm to back of beam.
[4]) With ϕ set equal to 1.
— No values are reported here because it was not possible to predict the failure torque for the observed mode of failure.

there is a possibility that the gage wiring was transposed between the front and back bars in this specimen, and it is assumed that this happened.

Table II summarizes the test results. It should be noted that the bending moments at failure were calculated at the edge of the loading arm, i.e. at the ends of the test sections. Since the bending moment varied throughout each test section, it was decided to report only its maximum value. This does not mean, necessarily, that the failure always occurred adjacent to the loading arm. In fact, in specimens 2 and 3 it occurred nearer the supports, and in specimens 1, 4 and 5 the ties next to the loading arm apparently bounded the failure region. In specimen 6 the failed zone intruded on the tied region with some top surface crushing. The mode of failure of specimens 7 through 10 will be discussed later.

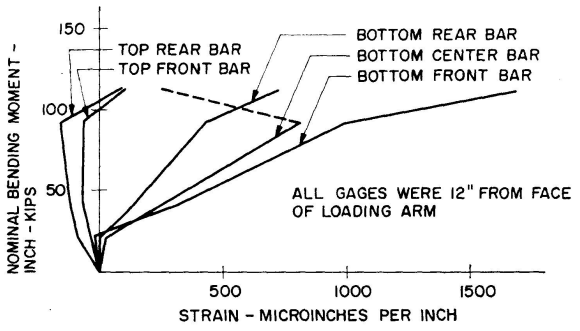


Fig. 4. Strain gage readings for specimen 2.

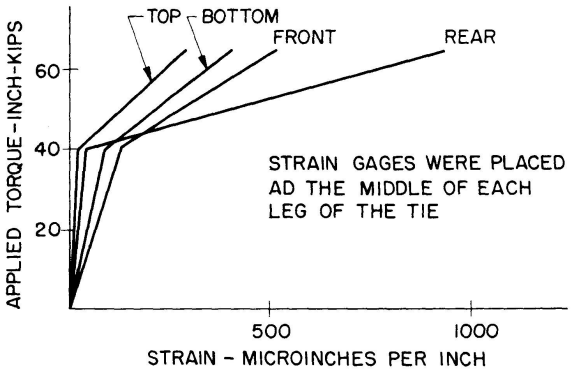


Fig. 5. Strains in one tie of specimen 7.

The shear was essentially constant throughout the test sections of all specimens, as was the torque. Two different torques are given in table II. The first one is the torque in each test section about the central axis of the beam, and the other is the torque in each test section about the hinge which formed in the back. Both were calculated from the support reactions, except in the case of specimens 7 through 10. It will be noticed that the torques about the hinge reported for these specimens were calculated as the product of the applied load and the length of the loading arm, measured to the back of the beam. This was done because this total applied torque is more relevant to the mode of failure observed in specimens 7 through 10. The theoretical ultimate bending strengths of both the beam sections and the loading arms are also given. These were calculated from equation 16–1 of the ACI Building Code with the capacity reduction factor, ϕ, set equal to 1. Equation 16–3 was not applicable since the compression reinforcement could not reach its yield stress. The last section of the table contains values of predicted torsional strength. These will be discussed later.

The behavior of specimen 7, the first of the rectangular, transversely reinforced beams, resembled that of specimens 1 and 2. The first cracks occurred at approximately 50 percent of the failure load. They were inclined at approx-

imately 45 degrees to the longitudinal axis of the beam and were initially observed on all faces except the top. The failure was of essentially the same form as in the earlier specimens, with a hinge forming on the back and a piece of concrete being forced out of the bottom. A small crack was also observed on the top face, at the junction of the loading arm and the main body of the specimen, as though the loading arm were suffering some bending distress at that point. The strain gages on the ties, some of which were attached on all sides, indicated that all the ties were in tension, but that none had reached the tensile yield strain prior to failure. The torque/strain graphs also showed a definite decrease in slope at the cracking load. See figure 5, which gives a rather typical plot of the strain readings.

Specimens 8, 9 and 10 behaved quite differently and their mode of failure is rather difficult to interpret. In all three, combined bending-torsional cracking, similar to that previously described for the square specimens, took place at lower loads. At failure, however, instead of large rotation in one test section, a failure surface formed on both sides of, and close to, the loading arms of specimens 8 and 9, with subsequent torsional rotation about hinges on the back, connecting the two failure surfaces in each member. At the same time the two surfaces were also connected by cracks across the top faces of the loading arms at their junctions with the beams. In fact, the total appearance of the failures was one in which the loading arms failed in tension at the top, simultaneously tearing out a piece of the adjacent beams. See figure 6, which shows specimen 9 after failure. In this case the hinge formed on the back just below the tops of the visible cracks.

These two specimens were also greatly influenced by the bending moments, since the strain readings showed that the tension reinforcement had yielded

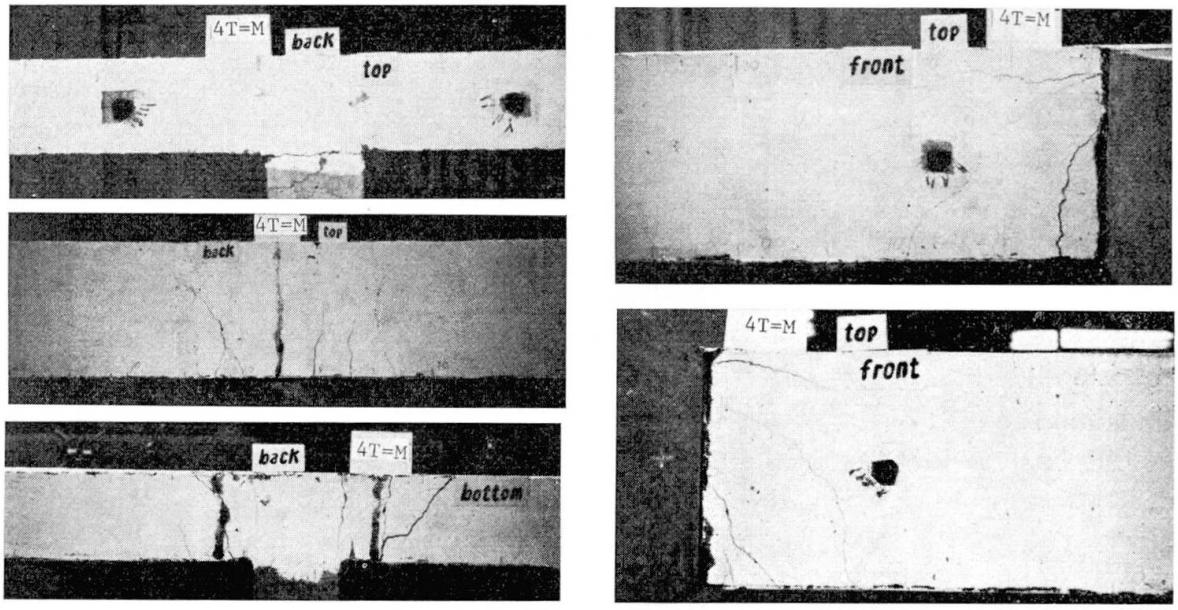


Fig. 6. Failure crack pattern of specimen 9.

prior to failure and, in the case of specimen 9, no torsional cracks appeared on the top surface. Specimen 10 was even more affected by the bending moment. Most cracks prior to failure seemed to be ordinary bending cracks which opened quite wide before the ultimate load was reached. No torsional type cracks appeared on the top surface. There was, however, a very marked crack again across the top of the loading arm and evidence, on the front of the specimen, that the arm had been torn out, taking with it a part of the beam. The tension reinforcement had again passed the yield point before collapse occurred. Strangely enough, the strain gages attached to the ties did not indicate that the ties yielded in any of these members.

Analysis

An analysis of the results observed in these tests requires consideration of three different phenomena. The first is the mode of failure of the square specimens containing only longitudinal reinforcement, the second is the mode of failure of the rectangular specimens containing both longitudinal and transverse reinforcement, and the third is the phenomenon of lateral bending, which may be a part of or may contribute to the other two effects.

Examining these in turn, one finds that the failure of the square specimens can be analysed in the light of a torsional dowel action theory of failure proposed in an earlier paper [13], for members failing by torsional rotation about a hinge in one side. In this, the equilibrium of a parallelopiped of concrete on the bottom of a member, similar to those tested here, was studied. The boundaries of this solid were assumed to be the bottom surface of the specimen, the plane containing the center lines of the longitudinal bottom reinforcement, and two parallel cracks on the bottom surface, spaced a distance, e, apart. The direction of these cracks was, at that time, assumed to be perpendicular to the axis of the member, in order to simplify the derivations and calculations. This agreed fairly well, also, with the test data then available. The forces acting on the top plane of the parallelopiped were then assumed to be the dowel forces from the longitudinal reinforcement, which has to resist most of the torque once the cross section is cracked, and vertical tensile stresses in the concrete which would tend to keep the parallelopiped from being spalled out of the beam. Since no other forces could act on it, the resultants of the vertical components of the dowel forces and the vertical tensile stresses in the concrete had to be in equilibrium. Therefore, analysing the parallelopiped as a biaxially eccentrically loaded tension member, the following equation was obtained for the maximum dowel resisting force the concrete could exert on the critical bar:

$$F_c = \frac{f_t e b}{[1+6(K_2-K_1)]\left(\sin\phi_c + \frac{1}{r_c}\sum_b r_i \sin\phi_i\right)}, \tag{1}$$

where F_c is the maximum bearing force the concrete can exert on a bar designated as the "critical" one; f_t is the modulus of rupture of the concrete; e is the distance between cracks measured parallel to the axis of the beam; b is the width of the beam; K_1 and K_2 are constants of proportionality such that $K_1 e$ is the perpendicular distance from a bending crack to the resultant of the vertical components of the dowel forcds and $K_2 b$ is the perpendicular distance from the side containing the hinge to the same resultant; r is the radial perpendicular distance from the hinge to the center of a longitudinal reinforcing bar, with the subscript c denoting distance to the bar designated as "critical" and the subscript i denoting the distances to the other bars; ϕ with the appropriate subscript is the angle any radius r makes with the vertical side of the beam containing the hinge; and $\sum_b$ indicates summation over the bottom bars only.

Once F_c was known, the total possible dowel resisting torque about the hinge could be expressed as

$$T_r = F_c\left(r_c + \frac{1}{r_c}\sum r_i^2\right), \tag{2}$$

where now the summation extended over all bars except the "critical" one and T_r consequently represented the total resisting torque which could be provided by all bars.

As was mentioned above, the cracks were assumed to be perpendicular to the beam axis in the original derivation. This was not found to be the case in all specimens in this investigation. Consequently, equation 1 was modified to the more general form for the biaxially eccentrically loaded tension member

$$F_c = \frac{f_t}{Q\left(\sin\phi_c + \frac{1}{r_c}\sum_b r_i \sin\phi_i\right)}, \tag{3}$$

where

$$Q = \frac{1}{A} + \frac{e_x}{I_{yy}} X + \frac{e_y}{I_{xx}} Y. \tag{4}$$

A is the cross sectional area of the top surface of the parallopiped; the coordinate system is based on the principal axes of inertia of the parallelogram formed by this surface; e_x and e_y are the coordinates of the resultant of the vertical components of the dowel forces and X and Y are the coordinates of the corner of the parallelogram expected to sustain the maximum tensile stress, all measured within this coordinate system. I_{xx} and I_{yy} are the principal moments of inertia about the indicated axes. e_x and e_y may be found by assuming, as before, that the dowel force exerted on the surrounding concrete by a bar will be proportional to its perpendicular distance from the hinge of rotation and that it will act a distance $K_1 e$ along the bar away from the bending crack. For calculation purposes, a value of $K_1 = \frac{1}{12}$ gave good results previously and was therefore used here again.

As a matter of interest, the value of F_c was calculated for specimens 1 through 6, once with the assumption that the cracks were perpendicular to the beam axis, i.e. using equation 1, and then again with the assumption that they made an angle of 60 degrees with the beam axis, which required use of equation 3. The results of the calculations differed by 3.2 percent, which is quite insignificant, given the physical assumptions on which these equations are based. This then indicates that it is not necessary to be able to predict the orientation of the cracks on the bottom surface accurately in order to apply the equations to a member.

Equations 2 and 3 were used to predict the dowel torional strengths of members 1 through 6 which contained no transverse reinforcement. They were also used to check the dowel strength of member 7 which failed in the same manner, even though transverse reinforcement was present. The results are presented in the last two colums of table II. (Here it should be noted that the torques are taken about the hinge on the back face of the specimen.) The theoretical torsional dowel strength is obviously directly proportional to the crack spacing. The work of BROMS and LUTZ [15, 16] indicated that the average crack spacing to be espected at high reinforcement stresses is approximately twice the effective cover. Based on this, the average crack spacing for members 1 through 6 should have been $3\frac{1}{4}$ inches. In the case of member 7 one would expect the spacing of the transverse reinforcement to be reflected in the crack spacing, which would cause it to be 3 inches. In this member, also, the dowel effect of the ties crossing the cracks had to be included. These figures were used to calculate the torques listed in the next-to-the-last column of table II. In the last column are the dowel torques predicted by the equations when the actual distances between the bending cracks bounding the failure parallelopipeds were used.

The moduli of rupture used in the calculations were taken to be $= 9\sqrt{f'_c}$. Some modulus of rupture specimens had been tested with the control cylinders, but the scatter of the data did not warrant identification of individual control beams with the torsional specimens. Despite the uncertainty of the tensile strength of the concrete and the other assumptions involved, it will be noted that the correlation between the theoretical dowel and the actual failure torques is quite good. The predicted strengths are, in every case, less than those obtained experimentally. This is to be expected, since the theory presented above does not take into account the resistance to rotation which will be provided by the uncracked concrete in the vicinity of the hinge. The dowel torsional strength should thus be a lower bound on the total torsional strength.

The method of analysis was also applied to specimens tested by others under similar loading conditions. The results are shown in table III. The crack spacing used for PANDIT and WARWARUK'S specimens was twice the cover, i.e. $3^1/_2$ inches, while that for RAMAKRISHNAN'S and VIJAYARANGAN'S specimens was $4^1/_2$ inches, which seemed to be approximately the average in the

Table III. Results of Tests by Others

Investigation	Specimen Number	Torque at Failure[1]) (inch-kips) about:		Predicted Dowel[2]) Torque about Hinge in back (inch-kips)
		Center Line	Hinge in back	
PANDIT and WARWARUK [8]	F-1	58	86	73
	F-2	83	102	73
	F-3	89	99	70
	G-1	73	104	70
	G-2	92	111	70
	G-3	103	113	72
	C_{1b}	23	37	23
RAMAKRISHNAN and VIJAYARANGAN [11]	C_3	22	37	23
	C_4	20	33	22
	C_5	23	38	23
	C_{6b}	22	34	22

[1]) Torque about the hinge was calculated by adding the product of the shear times half the width to the reported center line torque.

[2]) Using equations 1 and 2, with $f_t = 9\sqrt{f'_c}$ and, where necessary, with f'_c equal to 80% of the cube strength.

figures shown in that paper. BROMS' work would probably not be applicable to the latter specimens, since the reinforcement consisted of plain round bars. There were several factors which would cause inaccuracy. One of these, obviously, is the different sequence of loading used by PANDIT and WARWARUK. Another is the fact that their specimens did contain some transverse reinforcement, though relatively little in the examples chosen. (Specimens *F* contained no. 3 ties at 8 inches center to center and specimens *G* contained no. 2 ties spaced $3^1/_2$ inches center to center.) Nevertheless, one would expect that the ties would have some dowel effect, which was neglected in these calculations and would tend to increase the torsional strength above that predicted. RAMAKRISHNAN and VIJAYARANGAN used very low strength concrete and reported its cube strength. There is, therefore, some question regarding the accuracy of the calculation of the tensile strength.

Another factor which should be taken into account in these comparisons is the stress in the tensile reinforcement at the time of torsional failure. If the applied bending moment is small compared to the moment capacity of the beam, the tensile stresses in the reinforcement will be low. It must then be expected that, for monotonically increasing loading, the crack spacing will be considerably larger than that indicated by BROMS' and LUTZ' work for high reinforcement stresses [17]. This will then, obviously, have the effect of increasing the torque capacity of the specimens. Unfortunately, no valid expressions seem to have yet been devised to relate steel stress and crack spacing under this type of loading condition. However, it seems obvious that in an actual structure one must assume that eventually the crack spacing will reach the

minimum predicted by BROMS and LUTZ. If a correction factor for variation of crack spacing with steel stress could be applied to PANDIT'S and WARWARUK'S, and RAMAKRISHNAN'S and VIJAYARANGAN'S test results, the predicted dowel torques of the specimens with lower bending moments would be increased considerably, leading to higher lower bounds and to better correlations in table III.

It was not possible to analyse the mode of failure observed in specimens 8 through 10. As is evident from table II, the loading arms should have been sufficiently strong to prevent bending failure at their intersections with the beam portions of the specimens. Instead, the development of the tension cracks at the intersections clearly indicated that the arm reinforcement was yielding long before final collapse occurred. By dividing the bending moment in the loading arm at failure by the product of the cross sectional area of the arm reinforcement and the yield strength of that reinforcement, it was determined that the centroid of compression for each arm must have been located vertically between the hinge in the back and the usual location of this centroid.

Analyses of this phenomenon were also attempted by taking the moments of the dowel forces of all reinforcement crossing the failure surface about the hinge and also by summing the moments of the axial forces in all the transverse reinforcement crossing the failure surface, but both types of calculations gave predictions of torsional strengths quite different from those actually observed. The type of analysis used for specimens 1 through 7 could not validly be applied to these members since the mode of failure was obviously different. It is apparent, therefore, that the problem of the connections of a member in torsion to its supports must be studied further. In the mean time designers should be very careful and conservative in their detailing of such connections.

The last major phenomenon requiring discussion is the lateral bending which was observed in all specimens. As can be seen from figure 4, there were large differences in the strains observed in the various longitudinal bars. The result was that the front bottom bar yielded at a relatively low transverse bending moment. This behavior can be explained by reference to figure 7, which shows part of a specimen with everything past the failure surface removed. Also shown are the applied loads and reactions, and the horizontal and vertical components of the dowel forces. It is then evident that these

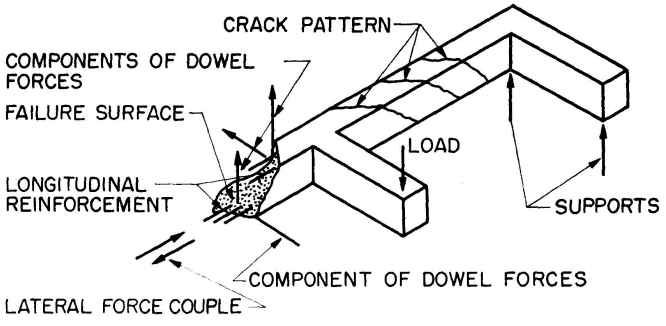


Fig. 7. Development of lateral Moment.

horizontal components will form a couple tending to rotate the free-body about a vertical axis. The resisting couple can only be supplied by the reinforcement, aided perhaps by shearing stresses in the uncracked concrete near the hinge. The magnitude of the applied lateral moment can be found, approximately, by calculating the horizontal components of the dowel forces applied to the concrete by the individual bars both on top and on the bottom, finding the resultant of each set of horinzontal components (note that they will not be equal, which means that some of the horizontal force must be taken in shear by the concrete at the hinge) multiplying each by half the horizontal distance between them and adding the two moments.

Using the same assumptions as those which were used to derive equations 1 through 3, one can find that the horinzontal component of dowel force in the "critical" bar at failure is

$$F_{cH} = F_c \cos \phi_c \tag{5a}$$

and the horizontal component of dowel force in any other bar at failure is

$$F_{iH} = F_i \cos \phi_i = F_c \left(\frac{r_i}{r_c}\right) \cos \phi_i . \tag{5b}$$

If the cracks on the top, bottom and front of each specimen were all inclined at 45 degrees to the beam axis and if the resultant horizontal force acted at the center of each bar group, the horizontal distance between the resultants would be equal to the width of the specimen plus the height, minus the top and bottom cover. Actually, it will be somewhat less than that since some of the cracks will make angles greater than 45 degrees with the axis and since the centroids of the horizontal forces will not be at the centers of the top and bottom surfaces. For calculation purposes it will be convenient to let the length of the lever arm be $K_3\,(b + h)$, where h is the overall height of the member.

It is now possible to write an approximate expression for the lateral bending moment:

$$M_{Lat.} = F_c \left(\cos \phi_c + \frac{1}{r_c} \sum r_i \cos \phi_i\right) \frac{K_3\,(b+h)}{2}, \tag{6}$$

where the summation extends over all bars except the "critical" one. Equation 6 can be rewritten by solving equation 2 for F_c and substituting this into equation 6:

$$M_{Lat.} = \frac{K_3 T_r\,(b+h)\left(\cos \phi_c + \frac{1}{r_c} \sum r_i \cos \phi_i\right)}{2\left(r_c + \frac{1}{r_c} \sum r_i^2\right)}. \tag{7}$$

If desired, this equation can be simplified somewhat before the numerical calculations are carried out. The value of K_3 was taken as 0.7 for specimens 1 through 6, which made $M_{Lat.} \doteq \frac{1}{2}\, T_r$ for these specimens.

It is then possible to check whether the longitudinal reinforcement is really resisting the lateral moments, by calculating the lateral moment couple set up in the top and bottom reinforcement by the differences in strain between the front and rear bars on the top and on the bottom. This was done for specimens 1 through 6, and the results are presented in table IV. The correspondence between the last two columns of the table is quite striking. Unfortunately it was not possible to make a comparison for specimen 7, since the strain gage on the bottom front bar failed at the beginning of the test. The rest of the specimens exhibited a different mode of failure and no comparison was attempted. As a matter of interest it might be noted that for specimens 7 through 10, $M_{Lat.} \doteq 0.9\, T_r$.

Table IV. Check of Lateral Bending Moments

Specimen Number	Strain difference[1]) (micro-inches/inch)		Lateral Bar Moment (inch-kips)	½ Predicted Theoretical Dowel Torque[3]) (inch-kips)
	Top bars	Bottom bars		
1	50	600	18.0	23.5
2	30	820	23.5	23.5
3	–200	820	17.1	20.0
4	40	650	19.0	20.0
5	650	200	23.4	21.6
6	–30	130[2])	9.5[2])	21.6

[1]) Just prior to failure.
[2]) All bottom reinforcement had yielded prior to collapse.
[3]) For the predicted crack spacing, from table II.
– The minus sign indicates that the front bar was subjected to a smaller tensile or larger compressive strain than the rear bar. This would tend to cause a lateral moment opposite to that of the other bars.

The vertical components of the dowel forces create an upward shear which, in the case of these specimens, was actually larger than the vertical shearing forces. This will simply have the effect of reversing the vertical shearing stresses in the uncracked concrete near the hinge.

In many of the specimens the top surface was crossed by cracks. It was further noticed that in most cases the compression reinforcement was either in tension or contained a very low compression strain at the time of failure, even though the bending moments were considerable. This would lead one to believe that the centroid of compression must have shifted. However, the lever arms of the tension reinforcement, as calculated from observed bending moments and average steel strains at or near failure, were of approximately the magnitude to be expected in pure bending. It is not possible, therefore, to draw any conclusions regarding the effect of torsion on the bending moment capacities of these specimens.

Conclusions

The following conclusions may be drawn from the foregoing:

1. Reinforced concrete beams subjected to combined torsion, bending and shear are likely to fail in torsion by rotation about a hinge on the vertical side on which the shearing stresses due to vertical shear and those due to the torque subtract from each other.

2. When the members contain only longitudinal reinforcement, they are able to resist torsion beyond the cracking load because of the dowel action of the reinforcement. Analysis of this dowel action provides a lower bound on the torsional strength of such members.

3. Interaction between shear and torque is based on the total torsion of the applied loading and the resisting dowel action about the hinge of rotation, for members containing only longitudinal reinforcement. The interaction between bending moment and torsional resistance for such members must be based on the variation in flexural crack spacing with stress in the tension reinforcement.

4. The dowel action will cause lateral bending moments which must be resisted by a rearrangement of the stresses in the reinforcement. The stresses involved are by no means negligible and can cause yielding in some bars at loads much lower than those which would cause yielding in ordinary bending.

5. When the members contain both longitudinal and transverse reinforcement, their connections to supporting or loading members appear to be much weaker than would have been suspected from conventional theory. It is therefore necessary to design such connections for much higher moments than those expected to be applied.

6. No conclusion could be drawn regarding the effect of torsion on the bending moment capacity of a member subjected to combined torsion, bending and shear, though there is some evidence that the lever arm of the tension reinforcement was not appreciably reduced by the torsional effects.

References

1. Chinenkov, Yu. V.: Study of the Behavior of Reinforced Concrete Elements in Combined Flexure and Torsion. Russian Concrete and Reinforced Concrete Institute (Moscow), V. 5, p. 29, 1959. Translated by Margaret Corbin as Foreign Literature Study No. 370, Portland Cement Association.
2. Lialin, I. M.: Experimental Investigation of Behavior of Rectangular Reinforced Concrete Beams Subjected to Combined Shear and Torsion. Russian Concrete and Reinforced Concrete Institute (Moscow), V. 5, 1959.
3. Lessig, N. N.: Theoretical and Experimental Investigation of Reinforced Concrete Beams Subjected to Combined Bending and Torsion. Design and Construction of Reinforced Concrete Structures, Moscow, 1958.
4. Lessig, N. N.: Determination of the Load Bearing Capacity of Reinforced Concrete Elements with Rectangular Cross Section Subjected to Flexure with Torsion. Russian

Concrete and Reinforced Institute (Moscow), V. 5, p. 5, 1959. Translated by Margaret Corbin as Foreign Literature Study No. 371, Portland Cement Association.

5. YUDIN, V. K.: Determination of the Load Bearing Capacity of Reinforced Concrete Elements of Rectangular Cross Section Under Combined Torsion and Bending. Beton i Zhelezobeton, No. 6, p. 265, 1962. Translated by Margaret Corbin as Foreign Literature Study No. 377, Portland Cement Association.
6. YUDIN, V. K.: Behavior of Reinforced Concrete Beams with Rectangular Cross Section Subjected to Combined Torsion and Flexure. Beton i Zhelezobeton, No. 1, p. 30, 1964. Translated by Margaret Corbin as Foreign Literature Study No. 431, Portland Cement Association.
7. NYLANDER, H.: Torsion and Torsional Restraint by Concrete Structures. Meddelanden Nr. 3, Staten Kommittee för Byggnadsforskning, Stockholm, Sweden, 1945.
8. PANDIT, G. S. and WARWARUK, J.: Torsional Strength and Behavior of Concrete Beams in Combined Loading. Preliminary Draft of a report, Department of Civil Engineering, University of Alberta, July 1965.
9. WALSH, P. F., COLLINS, M. P., ARCHER, F. E., and HALL, A. S.: Experiments on the Strength of Concrete Beams in Combined Flexure and Torsion. UNICIV Report No. R-15, University of New South Wales, Kensington, N.S.W., Australia, 1966.
10. COLLINS, M. P., WALSH, P. F., ARCHER, F. E. and HALL, A. S.: The Design of Rectangular Reinforced Concrete Beams Subjected to Combined Torsion, Bending and Shear. UNICIV Report No. R-16, University of New South Wales, Kensington, N.S.W., Australia, 1966.
11. RAMAKRISHNAN, V. and VIJAYARANGAN, B.: The Influence of Combined Bending and Torsion on Rectangular Beams Without Web Reinforcement. Indian Concrete Journal, V. 37, p. 412, 1963.
12. RAMAKRISHNAN, V. and VIJAYARANGAN, B.: Influence of Web Reinforcement on Reinforced Concrete Beams Subjected to Combined Bending and Torsion. Indian Concrete Journal, V. 39, No. 3, p. 89, 1965.
13. GESUND, H. and BOSTON, L. A.: Ultimate Strength in Combined Bending and Torsion of Concrete Beams Containing Only Longitudinal Reinforcement. Proc. ACI, V. 61, p. 1453, 1964.
14. GESUND, H., SCHUETTE, F. J., BUCHANAN, G. R. and GRAY, G. A.: Ultimate Strength in Combined Bending and Torsion of Concrete Beams Containing Both Longitudinal and Transverse Reinforcement. Proc. ACI, V. 61, p. 1509, 1964.
15. BROMS, B. B.: Crack Width and Crack Spacing in Reinforced Concrete Members. Proc. ACI, V. 62, p. 1237, 1965.
16. BROMS, B. B. and LUTZ, L. A.: Effects of Arrangement of Reinforcement on Crack Width and Spacing of Reinforced Concrete Members. Proc. ACI, v. 62, p. 1395, 1965.
17. KAAR, P. H. and MATTOCK, A. H.: High Strength Bars as Concrete Reinforcement, Part 4, Control of Cracking. Journal of the PCA Research and Development Laboratories, Vol. 5, No. 1, p. 15, 1963.

Summary

Ten reinforced concrete beams were tested in combined torsion, bending and shear. Six of the beams were eight inches by eight inches in cross section and contained only longitudinal reinforcement. The other four were six inches by twelve inches in cross section and contained both longitudinal and transverse reinforcement. The principal variable was the bending moment to torque ratio.

The strains in the members and their modes of failure were examined. Two different modes of failure were observed and a theoretical model for predicting a lower bound on the strengths of the members was developed for one of them. This model was also applied to a limited number of test results reported by others. The correlation was considered to be fairly good. It was discovered that the reinforcement, in resisting torsion, created lateral bending moments in the members. These changed the distribution of stress in the reinforcement, and led to the early yielding of some bars. A theoretical model was also developed to analyse this phenomenon. It agreed well with the test results.

Résumé

Dix poutres en béton armé ont été testées à la torsion, la flexion et le cisaillement combinés. Six de ces poutres avaient une section de 8×8 inches et n'étaient armées qu'en longueur. Les autres quatre avaient une section de 6×12 inches et étaient armées en longueur et en largeur. La principale variable était le rapport de la flexion à la torsion. On a examiné les tensions et le mode de rupture. Deux types de rupture ont été observés et pour l'un des deux, un modèle théorique a été développé, permettant de déterminer la limite inférieure des tensions de rupture. Ce modèle a été contrôlé avec un certain nombre de tests fait par d'autres, et l'on peut dire que la correspondance est assez bonne. On a découvert en outre que l'armature soumise à la torsion, produit des moments de flexion latéraux, ce qui mène à un changement de la répartition des tensions dans l'armature et à l'écoulement prématurée dans certaines barres. Pour analyser ce phénomène, on a développé un deuxième modèle, correspondant très bien avec les resultats des expériences.

Zusammenfassung

Es wurden zehn Stahlbetonträger untersucht, bei gleichzeitiger Torsions-, Biegungs- und Schubbeanspruchung. Darunter hatten sechs einen Querschnitt von 8×8 Zoll und waren nur längsarmiert. Die vier andern hatten einen Querschnitt von 6×12 Zoll und waren sowohl längs- als auch querarmiert. Die wichtigste Unabhängige dabei war das Verhältnis der Biegung zur Torsion. Beobachtet wurden die Spannungen und die Bruchart. Dabei stellte man zwei Bruchtypen fest. Für einen dieser Typen wurde ein Modell entwickelt, das die rechnerische Ermittlung der unteren Grenze der Bruchspannungen erlaubt. Dieses theoretische Modell wurde an verschiedenen fremden Tests geprüft und zeigte eine ziemlich gute Übereinstimmung mit den Meßresultaten. Man stellte fest, daß die torsionsbeanspruchte Stahlbewehrung Biegemomente in Querrichtung hervorruft. Dies änderte die Spannungsverteilung in der Bewehrung und führte bei einigen Bewehrungsstäben zum vorzeitigen Fließen. Um diese Erscheinung zu analysieren, wurde ein zweites Modell entwickelt, das gut mit den Meßwerten übereinstimmt.

The Finite Element Method in Application to Plane Stress

La méthode des éléments finis appliquée à des contraintes bi-dimensionnelles

Das Verfahren der Endlichen Elemente in der Anwendung auf ebene Spannungszustände

A. HRENNIKOFF
Sc. D., Research Professor of Civil Engineering, The University of British Columbia, Vancouver, B.C., Canada

General

The differential equations of the theory of elasticity governing the conditions of plane stress are based on statics, continuity of the material and its elasticity, in accordance with the constants E and μ. The assumption of continuity implies that the intermolecular spacing is an infinitesimal of a higher order compared to the dimensions dx and dy of the element analyzed.

With clear realization of these assumptions of the rigorous theory consider a model of a plate made of polygonal cells of repeating pattern, joined to each other at the nodes and possessing such properties as to make the nodes in the model and the plate move identically in conditions of any arbitrary uniform stress. If furthermore the size of mesh is visualized as an infinitesimal of a higher order than dx and dy, the equations of elasticity describing the action of the prototype should be equally applicable to the model which thus becomes in effect a simplified representation of the molecular structure of the plate. This reasoning is a demonstration of the proposition, sometimes questioned, that the finite element solution involving proper cells, would converge to the true values on infinite reduction of the size of mesh, provided of course that the rounding off errors of the computer solution are negligible.

Types of Finite Element Cells

Two kinds of cells are used in the finite element solution of plane stress problems: the framework cells, made of elastic bars[1] [2] and the no-bar cells[3] [4]. The former represent true elastic structures which may be actually constructed and sometimes even experimented with physically. The no-bar cells on the other hand are mathematical abstractions suitable for calculation but unsusceptible to physical reproduction.

The nature of the no-bar cells may be explained in the following manner. Imagine a plate of wide extent subjected to a simple stress condition such as uniform unidimensional strain ϵ_x or shearless bending in X direction. Isolate from this plate a polygonal area of the shape of the assumed finite element, holding it in equilibrium by the appropriate peripheral stresses. Assume now that the edge stresses are replaced by proper statically equivalent corner forces without affecting by this operation the corner displacements. This transforms the given piece of plate into the finite element proper which is in effect a body, whose corners move through the same distances as the same points in the plate when acted upon by corner forces statically equivalent to the edge stresses. The finite element must behave in such manner under several simple stress conditions. By combining these conditions in proper proportions it is possible to effect the separate x or y displacements of the corners of the cell and through that to find the stiffness matrix of the element relating its corner forces to the displacements.

There are certain ambiguities associated with the transformation of the edge stresses into the corner forces, for illustration of which it is necessary to consider in detail a specific example — a cell in the form of an equilateral trapezoid (Fig. 1).

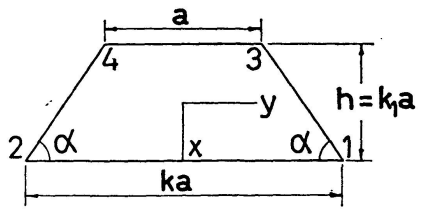


Fig. 1.

---

[1]) A. HRENNIKOFF: "Solution of Problems of Elasticity by the Framework Method". Journal of Applied Mechanics, ASME, New York, Vol. 63, December 1941.

[2]) A. HRENNIKOFF: "Framework Method and its Technique for Solving Plane Stress Problems". Publications of International Association for Bridge and Structural Engineering, Zurich, Switzerland, Vol. 9, 1949.

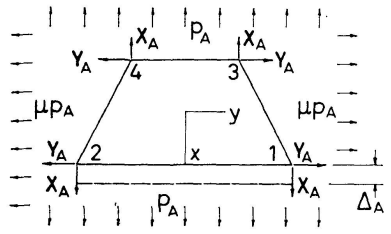
[3]) M. J. TURNER, R. W. CLOUGH, H. C. MARTIN and L. J. TOPP: "Stiffness and Deflection Analysis of Complex Structures". Journal of the Aeronautical Sciences, Vol. 23, No. 9, September 1956.

[4]) R. W. CLOUGH: "The Finite Element Method in Plane Stress Analysis". Proceedings of ASCE 2nd Conference on Electronic Computation, Pittsburgh, September, 1960.

Statics Type Stiffness Matrix of Equilateral Trapezoid

A quadrilateral cell has eight degrees of freedom with regard to u and v displacements of its four corners along the x and y axes. Single corner displacements may be effected by a combination of three rigid body movements in the plane of the cell and five basic stress conditions which may be assumed as follows:

A. Unilateral unit strain in x direction, ϵ_x (Fig. 2).



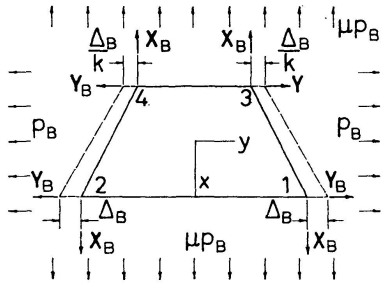
$$X_A = \frac{(1+k)\,t\,E\,\Delta_A}{4\,k_1\,(1-\mu^2)}$$

$$Y_A = \frac{\mu\,t\,E\,\Delta_A}{2\,(1-\mu^2)}$$

$$\Delta_A = \frac{p_A\,(1-\mu^2)\,k_1\,a}{t\,E}$$

Fig. 2.

B. Unilatera unit strain in y direction, ϵ_y (Fig. 3).



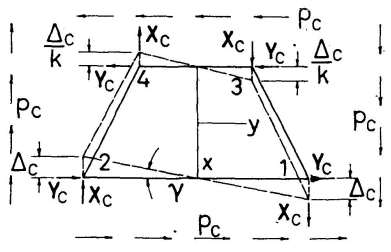
$$X_B = \frac{\mu\,(k+1)\,t\,E\,\Delta_B}{2\,k\,(1-\mu^2)}$$

$$Y_B = \frac{k_1\,t\,E\,\Delta_B}{k\,(1-\mu^2)}$$

$$\Delta_B = \frac{p_B\,(1-\mu^2)\,k\,a}{2\,t\,E}$$

Fig. 3.

C. Unit shear strain γ_{xy} (Fig. 4).



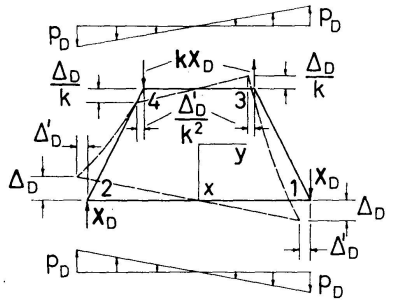
$$X_C = \frac{k_1\,t\,E\,\Delta_C}{2\,k\,(1+\mu)}$$

$$Y_C = \frac{(k+1)\,t\,E\,\Delta_C}{4\,k\,(1+\mu)}$$

$$\Delta_C = \frac{p_C\,(1+\mu)\,k\,a}{t\,E}$$

Fig. 4.

D. Shearless bending with stresses in x direction (Fig. 5).



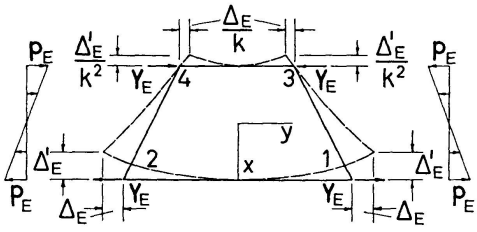
$$X_D = \frac{(k+1)\,t\,E\,\Delta_D}{6\,k\,k_1}$$

$$\Delta_D = \frac{p_D\,k_1\,a}{2\,t\,E}$$

$$\Delta'_D = \frac{\mu\,p_D\,k\,a}{4\,t\,E}$$

Fig. 5.

E. Shearless bending with stresses in y direction (Fig. 6).



$$Y_E = \frac{k_1\,t\,E\,\Delta_E}{3\,k}$$

$$\Delta_E = \frac{p_E\,k\,a}{2\,t\,E}$$

$$\Delta'_E = \frac{p_E\,k^2\,a}{4\,k_1\,t\,E}$$

Fig. 6.

Other suitable conditions may be used in place of D and E but the three uniform conditions A, B and C, or their equivalents, the uniform stresses, σ_x, σ_y and τ_{xy}, are compulsory.

The simplest way to determine the statically equivalent corner forces in the cell is to transfer its edge stresses to the adjacent corners by the law of the lever. This operation satisfies statics and at the same time carries the stresses only to the corners situated in the immediate vicinity of the edges in question. A weakness of this procedure will be pointed out later. The corner forces found by this method in all five stress conditions considered here are stated in Figs. 2—6.

The combination of the conditions A, C and D with $\Delta_A = 1/2\,u_1$, $\Delta_C = 1/4\,u_1$, and $\Delta_D = 1/4\,u_1$ results in a vertical displacement u_1 of the corner 1, with zero vertical displacements of the three other corners. However the condition D causes some unequal horizontal movements of the corners which must be cancelled by a horizontal rigid body movement and a horizontal displacement of the top edge to the left of the bottom edge by a shear condition C through a shear angle $\gamma = \frac{\mu\,(k^2-1)}{8\,k\,k_1^2\,a}\,u_1$. The corresponding corner forces are proportional to the ones shown in Fig. 4. The summation of the four sets of corner forces gives the stiffness matrix coefficients corresponding to the vertical movement u_1 of the corner 1.

The horizontal displacement v_1 of the same corner may be accomplished by the combination of the conditions B and E with $\Delta_A = \Delta_E = 1/4\,v_1$ and C,

involving a horizontal displacement $\Delta_C = 1/2\, v_1$ of the bottom edge to the right of the top edge, with the shear strain $\frac{v_1}{2\, k_1\, a_1}$. Since the condition E moves the corners of the top edge down towards the bottom edge this displacement must be corrected by addition of the condition A with $\Delta_A = \frac{(k^2-1)\, v_1}{8\, k\, k_1}$. The combination of these four conditions gives another set of stiffness matrix coefficients.

The corner forces produced by the displacements of the node 2 may be found by symmetry with the node 1, and the ones brought about by the movement of the top corners — by replacement of the parameters k and k_1 with $1/k$ and k_1/k respectively, in the corresponding expressions of forces caused by the bottom corner movements.

The force-displacement relation of the trapezoidal cell is given by Eq. (1)

$$\begin{bmatrix} P_1^x \\ P_1^y \\ P_2^x \\ P_2^y \\ P_3^x \\ P_3^y \\ P_4^x \\ P_4^y \end{bmatrix} = \begin{bmatrix} X_1^{u1} & X_1^{v1} & X_1^{u2} = X_2^{u1} & X_1^{v2} = -X_2^{v1} & X_1^{u3} & X_1^{v3} & X_1^{u4} = X_2^{u3} & X_1^{v4} = -X_2^{v3} \\ Y_1^{u1} & Y_1^{v1} & Y_1^{u2} = -Y_2^{u1} & Y_1^{v2} = Y_2^{v1} & Y_1^{u3} & Y_1^{v3} & Y_1^{u4} = -Y_2^{u3} & Y_1^{v4} = Y_2^{v3} \\ X_2^{u1} & X_2^{v1} & X_2^{u2} = X_1^{u1} & X_2^{v2} = -X_1^{v1} & X_2^{u3} & X_2^{v3} & X_2^{u4} = X_1^{u3} & X_2^{v4} = -X_1^{v3} \\ Y_2^{u1} & Y_2^{v1} & Y_2^{u2} = -Y_1^{u1} & Y_1^{v2} = Y_1^{v1} & Y_2^{u3} & Y_2^{v3} & Y_2^{u4} = -Y_1^{u3} & Y_2^{v4} = Y_1^{v3} \\ X_3^{u1} & X_3^{v1} & X_3^{u2} = X_4^{u1} & X_3^{v2} = -X_4^{v1} & X_3^{u3} & X_3^{v3} & X_3^{u4} = X_4^{u3} & X_3^{v4} = -X_4^{v3} \\ Y_3^{u1} & Y_3^{v1} & Y_3^{u2} = -Y_4^{u1} & Y_3^{v2} = Y_4^{v1} & Y_3^{u3} & Y_3^{v3} & Y_3^{u4} = -Y_4^{u3} & Y_3^{v4} = Y_4^{v3} \\ X_4^{u1} & X_4^{v1} & X_4^{u2} = X_3^{u1} & X_4^{v2} = -X_3^{v1} & X_4^{u3} & X_4^{v3} & X_4^{u4} = X_3^{u3} & X_4^{v4} = -X_3^{v3} \\ Y_4^{u1} & Y_4^{v1} & Y_4^{u2} = -Y_3^{u1} & Y_4^{v2} = Y_3^{v1} & Y_4^{u3} & Y_4^{v3} & Y_4^{u4} = -Y_3^{u3} & Y_4^{v4} = Y_3^{v3} \end{bmatrix} \cdot \begin{bmatrix} u_1 \\ v_1 \\ u_2 \\ v_2 \\ u_3 \\ v_3 \\ u_4 \\ v_4 \end{bmatrix}. \tag{1}$$

and the explicit expressions of the stiffness coefficients X and Y are presented in Table 1. The system adopted in their nomenclature involves one digit subscripts and two digit superscripts. The former indicate the node at which the force in question is applied, and the latter — the corner moved and the kind of the unit movement $u = 1$ or $v = 1$ creating the nodal force.

An important characteristic of this stiffness matrix is the absence of symmetry about the principal diagonal. Thus for example the coefficients Y_1^{u1} and X_1^{v1} are not equal. The asymmetry of the matrix leads to results violating the Betti's reciprocal theorem thus evincing a theoretical deficiency of the matrix.

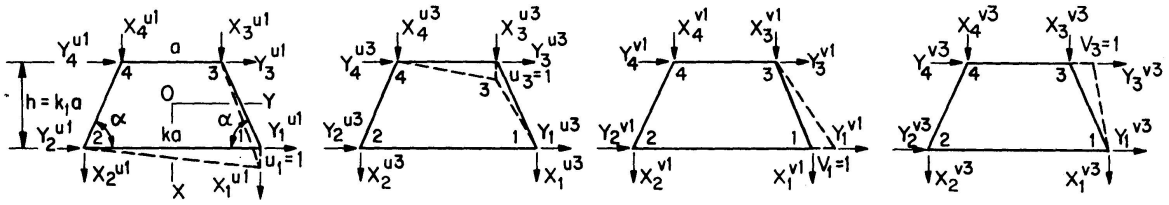
If the trapezoidal cell is transformed into a rectangle by making the parameter k equal to unity the matrix becomes symmetrical. Apparently its lack of symmetry reflects the asymmetry of the cell itself about the horizontal axis.

Energy Type Stiffness Matrix of Equilateral Trapezoid

Most of the authors employ a different stiffness matrix which is derived from the energy considerations[5]). Its commonly used implicit expression in

[5]) R. H. GALLACHER: "A Correlation Study of Methods of Matrix Structural Analysis". A Pergammon Press Book, the MacMillan Company, New York.

Table 1. No-bar Trapezoidal Cell Statics Type Stiffness Matrix (Unsymmetrical)



t = plate thickness $\qquad L = \dfrac{tE}{4(1-\mu^2)}$

$$X_1^{u1} = \left\{\frac{(1-\mu^2+3k)(k+1)}{6kk_1} + \frac{(1-\mu)[4k_1^2+\mu(k^2-1)]}{8kk_1}\right\}L, \qquad Y_1^{u1} = \left\{\frac{(k+1)+\mu(3k-1)}{4k} + \frac{\mu(1-\mu)(k^3+k^2-k-1)}{16kk_1^2}\right\}L.$$

$$X_2^{u1} = \left\{\frac{(-1+\mu^2+3k)(k+1)}{6kk_1} - \frac{(1-\mu)[4k_1^2+\mu(k^2-1)]}{8kk_1}\right\}L, \qquad Y_2^{u1} = \left\{\frac{(k+1)-\mu(5k+1)}{4k} + \frac{\mu(1-\mu)(k^3+k^2-k-1)}{16kk_1^2}\right\}L.$$

$$X_3^{u1} = \left\{-\frac{(4-\mu^2)(k+1)}{6k_1} + \frac{(1-\mu)[4k_1^2+\mu(k^2-1)]}{8kk_1}\right\}L, \qquad Y_3^{u1} = \left\{-\frac{(k+1)-\mu(5k+1)}{4k} - \frac{\mu(1-\mu)(k^3+k^2-k-1)}{16kk_1^2}\right\}L.$$

$$X_4^{u1} = \left\{-\frac{(2+\mu^2)(k+1)}{6k_1} - \frac{(1-\mu)[4k_1^2+\mu(k^2-1)]}{8kk_1}\right\}L, \qquad Y_4^{u1} = \left\{-\frac{(k+1)+\mu(3k+1)}{4k} - \frac{\mu(1-\mu)(k^3+k^2-k-1)}{16kk_1^2}\right\}L.$$

$$X_1^{u3} = \left\{-\frac{(4-\mu^2)(k+1)}{6k_1} + \frac{(1-\mu)[4k_1^2-\mu(k^2-1)]}{8k_1}\right\}L, \qquad Y_1^{u3} = \left\{\frac{(k+1)-\mu(k+5)}{4} - \frac{\mu(1-\mu)(k^3+k^2-k-1)}{16k_1^2}\right\}L.$$

$$X_2^{u3} = \left\{-\frac{(2+\mu^2)(k+1)}{6k_1} - \frac{(1-\mu)[4k_1^2-\mu(k^2-1)]}{8k_1}\right\}L, \qquad Y_2^{u3} = \left\{\frac{(k+1)+\mu(3-k)}{4} + \frac{\mu(1-\mu)(k^3+k^2-k-1)}{16k_1^2}\right\}L.$$

$$X_3^{u3} = \left\{\frac{[k(1-\mu^2)+3](k+1)}{6k_1} + \frac{(1-\mu)[4k_1^2-\mu(k^2-1)]}{8k_1}\right\}L, \qquad Y_3^{u3} = \left\{-\frac{(k+1)+\mu(3-k)}{4} + \frac{\mu(1-\mu)(k^3+k^2-k-1)}{16k_1^2}\right\}L.$$

$$X_4^{u3} = \left\{\frac{[-k(1-\mu^2)+3](k+1)}{6k_1} - \frac{(1-\mu)[4k_1^2-\mu(k^2-1)]}{8k_1}\right\} L, \qquad Y_4^{u3} = \left\{-\frac{(k+1)-\mu(k+5)}{4} + \frac{\mu(1-\mu)(k^3+k^2-k-1)}{16k_1^2}\right\} L.$$

$$X_1^{v1} = \frac{1}{2}\left\{\frac{k+\mu}{k} + \frac{k^3+k^2-k-1}{4kk_1^2}\right\} L, \qquad Y_1^{v1} = \left\{\frac{(4-\mu^2)k_1}{3k} + \frac{(k-\mu)(k+1)}{4kk_1}\right\} L.$$

$$X_2^{v1} = \frac{1}{2}\left\{\frac{-k+\mu(2k+1)}{k} + \frac{k^3+k^2-k-1}{4kk_1^2}\right\} L, \qquad Y_2^{v1} = \left\{-\frac{(4-\mu^2)k_1}{3k} + \frac{k(k+1)-\mu(2k^2+k-1)}{4kk_1}\right\} L.$$

$$X_3^{v1} = \frac{1}{2}\left\{\frac{k-\mu(2k+1)}{k} - \frac{k^3+k^2-k-1}{4kk_1^2}\right\} L, \qquad Y_3^{v1} = \left\{\frac{(2+\mu^2)k_1}{3k} - \frac{k(k+1)-\mu(2k^2+k-1)}{4kk_1}\right\} L.$$

$$X_4^{v1} = -\frac{1}{2}\left\{\frac{k+\mu}{k} + \frac{k^3+k^2-k-1}{4kk_1^2}\right\} L, \qquad Y_4^{v1} = -\left\{\frac{(2+\mu^2)k_1}{3k} + \frac{(k-\mu)(k+1)}{4kk_1}\right\} L.$$

$$X_1^{v3} = \frac{1}{2}\left\{-1+\mu(k+2) - \frac{k^3+k^2-k-1}{4k_1^2}\right\} L, \qquad Y_1^{v3} = \left\{\frac{(2+\mu^2)k_1}{3} - \frac{(k+1)+\mu(k^2-k-2)}{4k_1}\right\} L.$$

$$X_2^{v3} = \frac{1}{2}\left\{1+\mu k - \frac{k^3+k^2-k-1}{4k_1^2}\right\} L, \qquad Y_2^{v3} = \left\{-\frac{(2+\mu^2)k_1}{3} - \frac{(k+1)(1-\mu k)}{4k_1}\right\} L.$$

$$X_3^{v3} = \frac{1}{2}\left\{-1-\mu k + \frac{k^3+k^2-k-1}{4k_1^2}\right\} L, \qquad Y_3^{v3} = \left\{\frac{(4-\mu^2)k_1}{3} + \frac{(k+1)(1-\mu k)}{4k_1}\right\} L.$$

$$X_4^{v3} = \frac{1}{2}\left\{1-\mu(k+2) + \frac{k^3+k^2-k-1}{4k_1^2}\right\} L, \qquad Y_4^{v3} = \left\{-\frac{(4-\mu^2)k_1}{3} + \frac{(k+1)+\mu(k^2-k-2)}{4k_1}\right\} L.$$

the form of a product of several component matrices is convenient for computer work, but is apt to conceal some of its peculiarities and defects. This energy type matrix will be presented here explicitly, and it will be correlated with the matrix found by statics.

As explained above the stress condition of a cell corresponding to a unit displacement of one of its nodes may be described by combination of several stress conditions A to E. This makes it possible to express the stresses and displacements in the plate in terms of the particular node displacement. When all nodes are moved simultaneously, the stresses and displacements in the cell, including the values along the periphery, become linear functions of eight corner displacements u_1, v_1, u_2, etc.

Imagine eight nodal forces P_1^x, P_1^y, P_2^x, etc. statically equivalent to the edge stresses $\sigma_\perp$ (normal) and τ (tangential) and apply them in reversed directions, as the equilibrants of the edge stresses. The application of these corner forces does not affect the peripheral stresses $\sigma_\perp$ and τ. Give one of the corners, such as #1, a displacement du_1 and equate to zero the virtual work of the system corresponding to this displacement. As is well known, the work of deformation of a plate may be expressed either as an area integral or a line integral taken along the periphery, and the latter version will be used here. Of the eight corner forces only P_1^x does the virtual work.

Calling the virtual displacements developed on the edges of the cell $\lambda_\perp$-normal and λ_{11}-tangential, and the thickness of the plate t, the work equation may be stated in the following form:

$$P_1^x\,du_1 = t\int_{l\triangle} \sigma_\perp\,dl\,\frac{\partial\lambda_\perp}{\partial u_1}\,du_1 + t\int_{l\triangle} \tau\,dl\,\frac{\partial\lambda_{11}}{\partial u_1}\,du_1. \tag{2}$$

The increment du_1 may be cancelled and the partial derivatives may be viewed as the edge displacements produced by the unit movement of the corner $u_1 = 1$

$$\frac{\partial\lambda_\perp}{\partial u_1} = \lambda_\perp^{u_1=1} \quad \text{and} \quad \frac{\partial\lambda_{11}}{\partial u_1} = \lambda_{11}^{u1=1}.$$

Then

$$P_1^x = t\int_{l\triangle} \sigma_\perp\,\lambda_\perp^{u_1=1}\,dl + t\int_{l\triangle} \tau\,\lambda_{11}^{u1=1}\,dl. \tag{3}$$

This equation defines the terms in the first row of the stiffness matrix. Its individual terms are expressed thus:

$$X_1^{u1} = t\int_{l\triangle} (\sigma_\perp^{u1}\lambda_\perp^{u1} + \tau^{u1}\lambda_{11}^{u1})\,dl, \tag{4}$$

$$X_1^{v1} = t\int_{l\triangle} (\sigma_\perp^{v1}\lambda_\perp^{u1} + \tau^{v1}\lambda_{11}^{u1})\,dl \quad \text{etc.} \tag{5}$$

The terms in the other rows of the matrix are found in a similar manner, for example:

$$Y_1^{u1} = t\int_{l\triangle} (\sigma_\perp^{u1}\lambda_\perp^{v1} + \tau^{u1}{}_{11}^{v1})\,dl. \tag{6}$$

The significance of the subscript and the superscript symbols in X and Y was explained before. The edge stresses and displacements under the integral signs are produced by the unit displacements of one of the nodes. The stresses $\sigma_\perp$ and τ correspond to unit displacement of the corner indicated by the superscript in X or Y, while the displacements $\lambda_\perp$ and λ_{11} are produced by the unit displacements stated in their superscript, which matches the subscript of the term X or Y.

For simplicity of calculation the line integrals along the sloping sides of the cell 1—3 and 2—4 may be expressed through the X and Y components of the stresses and displacements rather than through the normal and tangential components, in accordance with the relation

$$\int (\sigma_\perp \lambda_\perp + \tau \lambda_{11})\, dl = \int \sigma_x \lambda_x\, dy + \int \sigma_y \lambda_y\, dx + \int \tau_{xy} \lambda_y\, dy + \int \tau_{xy} \lambda_x\, dx .$$

Care must be taken in using proper signs of stresses and displacements in these expressions.

Although the expressions X and Y (Eqs. 4, 5, 6) are extensively used (sometimes in a modified form) they are incorrect, because they imply that the virtual work of deformation of the material within the cell subjected to a simultaneous action of the edge stresses and the opposing corner forces is zero. This supposition is erroneous. Even though the corner forces and the edge stresses are balanced the internal stresses within the cell are still extant and there is no reason for their virtual work to be zero should the nodes be displaced.

The edge stresses brought about by any two single corner displacements, such as $u_1 = 1$ or $v_1 = 1$, are of course mutually balanced by themselves without the addition of the corner forces and so the magnitudes of the work done by the edge stresses of one of these conditions on the edge deformations of the other must be equal. The two sides of this work equation are the integral expressions of the matrix terms X_1^{v1} and Y_1^{u1} in Eqs. (5) and (6). This signifies the equality of these as well as of other symmetrically situated terms in the stiffness matrix. The symmetry of the energy type matrix is an advantage over the unsymmetrical matrix (Table 1) since it simplifies the computer work. The energy type matrix involves however some inconsistency to be pointed out presently.

Comparison of the Matrices

A comparison of the two types of stiffness matrix discussed here would clarify some of their peculiarities. In the stiffness matrix found by statics the edge stresses are assembled into the corner forces at the two adjacent corners by the law of the lever, while in the energy type matrix the same edge stresses are multiplied by the edge displacements produced by the movement of the corner and then added up. For a specific comparison take the term X_1^{v1} (Eq. (5)).

The edge stresses $\sigma_{\perp}^{v1}$ and τ^{v1} in its expression are produced by the displacement $v_1 = 1$, and the edge displacements $\lambda_{\perp}^{u1}$ and λ_{11}^{u1} — by the displacement $u_1 = 1$. The diagrams of $\lambda_{\perp}^{u1}$ and λ_{11}^{u1} may be viewed as the influence lines by whose ordinates the stresses $\sigma_{\perp}$ and τ created by any unit corner movement ($v_1 = 1$ in this case) must be multiplied and then summed up in order to form the force X_1 produced by the given movement ($u_1 = 1$ in this case). Of the eight corner displacements seven are equal to zero and only one, $u_1 = 1$, is distinct from zero.

Taking as an example a rectangular cell imagine as a possibility that the edge displacements corresponding to $u_1 = 1$ are all linear (Fig. 7). This means

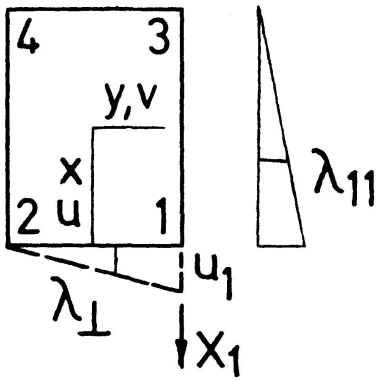


Fig. 7.

that of all edge displacements only $\lambda_{\perp}$ on the edge 1—2 and λ_{11} on the edge 1—3 are distinct from zero. Employment of the influence lines of the type of $\lambda_{\perp}$ and λ_{11} in Fig. 7 for calculation of X_1 is obviously equivalent to the application of the law of the lever. Under the stated conditions the terms X_1 found by the two methods should then be identical.

The linearity of the edge displacements was however used in this reasoning only as a tentative supposition, true for the uniform strain conditions A, B, and C but false for the flexural conditions D and E. Thus the condition D required for the displacement of $u_1 = 1$, results in parabolic normal displacements on the edges 1—3 and 2—4 directed inward on one edge and outward on the other. Parabolically distributed tangential displacements are present also on the edges 1—2 and 3—4. It so happens however that in all five basic stress conditions A to E the edge stresses on the opposite sides of the rectangle are equal, which results in mutual cancellation of the energy terms corresponding to the non-linear displacements. This makes the statics and the energy matrices for a rectangular cell identical, as well as symmetrical about the principal diagonal.

The situation is however different in the case of a trapezoidal cell. When such a cell is subjected to bending condition D its side edges become curved, and under the condition E its all four edges are curved. The diagrams of the edge displacements thus become non-linear, making the matrix terms, determined by the two methods, different. It is significant that a single corner displacement, such as $u_1 = 1$, produces displacements on the non-adjacent edges 2—4 and 4—3, as well as on the adjacent ones 1—2 and 1—3. This

means that the terms X_1 and Y_1 are contributed to partly by the stresses on the non-adjacent edges. The presence of such contributions appears logically unsound and must be viewed as a defect of the energy matrix.

Correlation of the Matrices

The two matrices may be correlated by finding the complementary terms whose addition to the terms of the statics type matrix transforms them into the terms of the energy matrix.

It was pointed out that integration of the edge stresses over the linear parts of the edge displacements, such as the ones in Fig. 7, produces the terms of the stiffness matrix found by statics. Then the complementary terms may be found by integration of the products of the edge stresses over the non-linear parts of the edge displacements with zero values at the corners. The nonlinear displacements are produced exclusively by the flexural conditions D and E, and their shape always conforms to the second order parabola with the ordinates measured from the chords passing through the ends. The ordinates of these parabolas are fully described by the midlength values.

Influence Lines of Complementary Terms X_1

The edge displacements considered here correspond to the corner movement $u_1 = 1$ (Fig. 8). Only the condition D is effective in producing the non-linear components of the edge displacements.

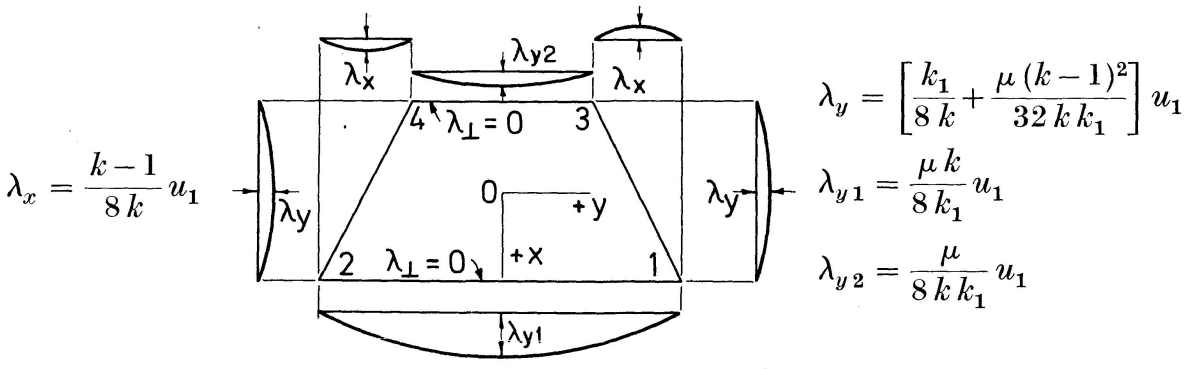


Fig. 8.

Edge 1—2. The normal displacements are linear. The nodes 1 and 2 move to the left (Fig. 5) the amount $\frac{\mu k}{2 k_1} \Delta_D = \frac{\mu k}{8 k_1} u_1$, while the mid-point remains at rest. The relative tangential displacement of the mid-point in relation to the ends is $\lambda_{y1} = +\frac{\mu k}{8 k_1} u_1$.

Edge 3—4. Similarly, the mid-point displacements are $\lambda_\perp = 0$, $\lambda_{y2} = +\frac{\mu}{8kk_1}u_1$.

Edge 1—3. The vertical displacements of the corners 1 and 3 are $+1/4\,u_1$ and $-\frac{u_1}{4k}$ respectively, and of the mid-point — zero. Then the displacement of the mid-point in relation to the ends is up $\lambda_x = \frac{k-1}{8k}u_1$.

The horizontal displacements are produced by two effects: the curvature and the μ effect.

By the elementary flexure formula, $\frac{1}{R} = \frac{M}{EI} = \frac{2\sigma}{Eh} = \frac{u_1}{4kk_1a^2}$ and the horizontal corner displacement to the left with reference to the mid-point is $\frac{(h/2)^2}{2R} = \frac{k_1}{8k}u_1$.

The horizontal displacements to the left of the corners 1 and 3 and of the mid-point produced by μ effect are respectively $\frac{\mu k u_1}{8k_1}$, $\frac{\mu u_1}{8kk_1}$ and $\frac{\mu(k+1)^2u_1}{8kk_1}$. This makes the relative displacement of the mid- point in relation to the straight line through the ends

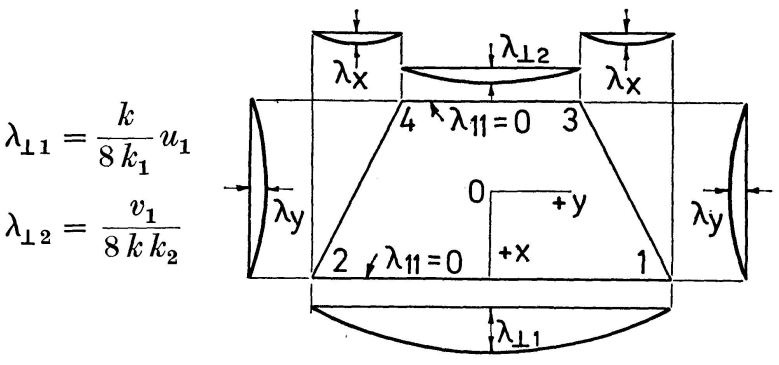
$$\frac{1}{2}\left(\frac{\mu k u_1}{8k_1} + \frac{\mu u_1}{8kk_1}\right) - \frac{\mu(k+1)^2u_1}{32kk_1} = \frac{\mu(k-1)^2}{32kk_1}.$$

The total horizontal displacement of the mid-point of the side 1—3 is

$$\lambda_y = +\frac{k_1}{8k}u_1 + \frac{\mu(k-1)^2}{32kk_1}u_1.$$

Edge 2—4. The displacements are equal in magnitude and opposite in sign compared to the ones on the edge 1—3.

The edge displacements determined here are shown in Fig. 8. If the quantity u_1 is made unity the curves become the influence lines of the complementary terms X_1 and X_2 of the energy stiffness matrices. They are valid for X_1 and X_2 produced by unit displacements u or v of any of the four corners. These influence lines are antisymmetrical about the vertical axis X.



$$\lambda_{\perp 1} = \frac{k}{8k_1}u_1 \qquad \lambda_{\perp 2} = \frac{v_1}{8kk_2}$$

$$\lambda_x = \left[\frac{\mu k_1}{8k} + \frac{(k-1)^2}{32kk_1}\right]v_1 \qquad \lambda_y = \frac{k-1}{8k}v_1$$

Fig. 9.

The influence lines of the terms Y_1 and $-Y_2$ corresponding to the displacement $v_1 = 1$ are shown in Fig. 9. They are brought about by the flexural condition E with $\Delta_E = 1/4\, v_1$. These lines are symmetrical about the vertical axis.

Complementary Term $X_1^{v_1}$. Energy Type Matrix Terms

The use of the influence lines of Figs. 8 and 9 is illustrated on the example of the complementary factor X_1^{v1} whose combination with the factor determined by statics produces the term X_1^{v1} of the energy stiffness matrix.

The displacement $v_1 = 1$ which creates the edge stresses used in calculation of X_1^{v1}, is made up of the stress conditions A, B, C and E of which only the stresses of the condition C are capable of making the products with the edge displacements of Fig. 8 distinct from zero, since the stresses of the condition C and the displacements are both antisymmetrical about the X axis. On the other hand the stresses of the condition A, B and E are symmetrical about the X axis, and the integral of their products with the ordinates of Fig. 8 is zero.

The edge stresses of the condition C are constant along all edges and they must be multiplied by the appropriate length of the edge and the mean displacement equal to 2/3 of the maximum ordinate of the parabolic influence line.

The unit shear force in condition C corresponding to $u_1 = 1$ is $\frac{tE}{4(1+\mu)\,k a_1}$. Then the values of the complementary terms of X_1^{v1} are as follows (Fig. 8).

Edge 1—2:
$$\frac{Et}{4(1+\mu)k_1 a}\,\frac{2}{3}\,\frac{\mu k}{8k_1}\,k a = \frac{\mu k^2 Et}{48(1+\mu)k_1^2}.$$

Edge 3—4:
$$-\frac{Et}{4(1+\mu)k_1 a}\,\frac{2}{3}\,\frac{\mu}{8kk_1}\,a = -\frac{\mu Et}{48(1+\mu)kk_1^2}.$$

Edges 1—3 and 2—4 are replaced with stepped lines made up of infinitesimal horizontal and vertical steps.

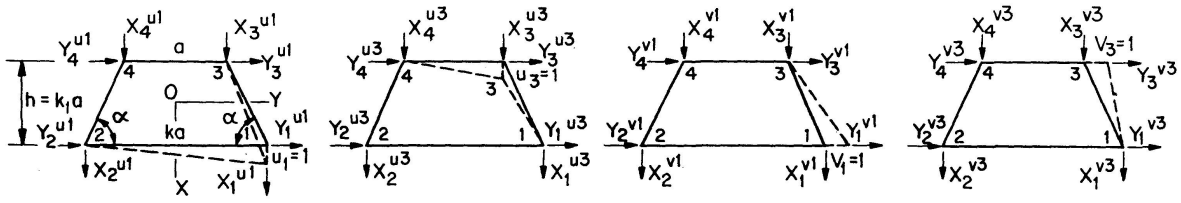
$$-\frac{2Et}{4(1+\mu)k_1 a}\left\{\frac{2}{3}\,\frac{(k-1)}{8k}\,k_1 a + \frac{2}{3}\left[\frac{k_1}{8k} + \frac{\mu(k-1)^2}{48kk_1}\right]\frac{(k-1)a}{2}\right\}.$$

Adding these up. The complement to

$$X_1^{v1} = \left[\frac{\mu(k+1)(k^2-1)}{64kk_1^2} - \frac{k-1}{16k}\right]\frac{Et}{(1+\mu)}.$$

The procedure described here allows determination of all complementary terms. Combination of the complementary terms with the statics type matrix terms (Table 1) results in the energy type stiffness matrix whose terms are presented in Table 2. As was pointed out earlier this matrix is symmetrical about its principal diagonal.

Table 2. No-bar Trapezoidal Cell Energy Type Stiffness Matrix (Symmetrical)



$$t = \text{plate thickness} \qquad L = \frac{tE}{4(1-\mu^2)}$$

$$X_1^{u1} = \left\{ \frac{k+1}{2k_1} + \frac{(1-\mu^2)(k+1)(k^2+1)}{12k^2k_1} + \frac{(1-\mu)(k+1)k_1}{4k^2} + \frac{\mu(1-\mu)(k^2-1)(k+1)[8k_1^2+\mu(k^2-1)]}{64k^2k_1^3} \right\} L,$$

$$Y_1^{u1} = \left\{ \frac{(\mu+1)(k+1)}{4k} + \frac{[2+\mu(1-\mu)](k^2-1)(k+1)}{16kk_1^2} \right\} L,$$

$$X_2^{u1} = \left\{ \frac{k+1}{2k_1} - \frac{(1-\mu)(k+1)k_1}{4k^2} - \frac{(1-\mu^2)(k+1)(k^2+1)}{12k^2k_1} - \frac{\mu(1-\mu)(k^2-1)(k+1)[8k_1^2+\mu(k^2-1)]}{64k^2k_1^3} \right\} L,$$

$$Y_2^{u1} = \left\{ \frac{(1-3\mu)(k+1)}{4k} - \frac{[2-\mu(1-\mu)](k^2-1)(k+1)}{16kk_1^2} \right\} L,$$

$$X_3^{u1} = \left\{ -\frac{k+1}{2k_1} + \frac{(1-\mu)(k+1)k_1}{4k} - \frac{(1-\mu^2)(k+1)(k^2+1)}{12kk_1} - \frac{\mu^2(1-\mu)(k^2-1)^2(k+1)}{64kk_1^3} \right\} L,$$

$$Y_3^{u1} = \left\{ -\frac{1-3\mu}{4} + \frac{\mu k}{2} - \frac{1-\mu}{4k} - \frac{[2k+\mu(1-\mu)](k^2-1)(k+1)}{16kk_1^2} \right\} L,$$

$$X_4^{u1} = \left\{ -\frac{k+1}{2k_1} - \frac{(1-\mu)(k+1)k_1}{4k} + \frac{(1-\mu^2)(k+1)(k^2+1)}{12kk_1} + \frac{\mu^2(1-\mu)(k^2-1)^2(k+1)}{64kk_1^3} \right\} L,$$

$$Y_4^{u1} = \left\{ -\frac{1+\mu}{4} - \frac{\mu k}{2} - \frac{1-\mu}{4k} + \frac{[2k-\mu(1-\mu)](k^2-1)(k+1)}{16kk_1^2} \right\} L,$$

$$Y_1^{v1} = \left\{ \frac{3(2-\mu^2)kk_1+(2+\mu^2)k_1}{6k^2} + \frac{(k^2-\mu)(k+1)}{4k^2k_1} + \frac{(k^2-1)^2(k+1)}{32k^2k_1^3} \right\} L,$$

$$X_2^{v1} = -Y_2^{u1},$$

$$Y_2^{v1} = \left\{ -\frac{3(2-\mu^2)kk_1+(2+\mu^2)k_1}{6k^2} + \frac{[(1-2\mu)k^2+\mu](k+1)}{4k^2k_1} - \frac{(k^2-1)^2(k+1)}{32k^2k_1^3} \right\} L,$$

$$X_3^{v1} = \left\{ \frac{k+1}{4} - \frac{\mu(3+k)}{4} - \frac{\mu}{2k} - \frac{[2+\mu(1-\mu)k](k^2-1)(k+1)}{16kk_1^2} \right\} L,$$

$$Y_3^{v1} = \left\{ \frac{(2+\mu^2)(k+1)k_1}{6k} - \frac{(1-\mu)(k+1)}{4k_1} - \frac{(k^2-1)^2(k+1)}{32kk_1^3} \right\} L,$$

$$X_4^{v1} = \left\{ \frac{\mu(k-1)}{4} - \frac{\mu}{2k} - \frac{k+1}{4} - \frac{[2-\mu(1-\mu)k](k^2-1)(k+1)}{16kk_1^2} \right\} L,$$

$$Y_4^{v1} = \left\{ -\frac{(2+\mu^2)(k+1)k_1}{6k} - \frac{(1-\mu)(k+1)}{4k_1} + \frac{(k^2-1)^2(k+1)}{32kk_1^3} \right\} L,$$

$$X_2^{u2} = X_2^{u1}, \qquad Y_2^{u2} = -Y_1^{u1}, \qquad X_3^{u2} = X_4^{u1}, \qquad X_4^{u2} = X_3^{u1}, \qquad Y_4^{u2} = -Y_3^{u1},$$

$$Y_3^{u2} = \left\{ \frac{k+1}{4k} + \frac{\mu k}{2} + \frac{\mu(k-1)}{4k} - \frac{[2k-\mu(1-\mu)](k^2-1)(k+)}{16kk_1^2} \right\} L,$$

$$Y_2^{v2} = Y_1^{v1}, \qquad X_3^{v2} = -X_4^{v1}, \qquad Y_3^{v2} = Y_4^{v1},$$

$$X_4^{v2} = \left\{ -\frac{1-3\mu}{4} + \frac{\mu}{2k} - \frac{(1-\mu)k}{4} + \frac{[2+\mu(1-\mu)k](k^2-1)(k+1)}{16kk_1^2} \right\} L,$$

$$Y_4^{v2} = \left\{ \frac{(2+\mu^2)(k+1)k_1}{6k} - \frac{(1-\mu)(k+1)}{4k_1} - \frac{(k^2-1)^2(k+1)}{32kk_1^3} \right\} L,$$

$$X_3^{u3} = \left\{ \frac{k+1}{2k_1} + \frac{(1-\mu^2)(k+1)(k^2+1)}{12k_1} + \frac{(1-\mu)(k+1)k_1}{4} - \frac{\mu(1-\mu)(k^2-1)(k+1)[8k_1^2-\mu(k^2-1)]}{64k_1^3} \right\} L,$$

$$Y_3^{u3} = \left\{ \frac{[2+\mu(1-\mu)](k^2-1)(k+1)}{16k_1^2} - \frac{(1+\mu)(k+1)}{4} \right\} L,$$

$$X_4^{u3} = \left\{ \frac{k+1}{2k_1} - \frac{(1-\mu)(k+1)k_1}{4} - \frac{(1-\mu^2)(k+1)(k^2+1)}{12k_1} + \frac{\mu(1-\mu)(k^2-1)(k+1)[8k_1^2-\mu(k^2-1)]}{64k_1^3} \right\} L,$$

$$Y_4^{u3} = \left\{ -\frac{(1-3\mu)(k+1)}{4} - \frac{[2-\mu(1-\mu)](k^2-1)(k+1)}{16k_1^2} \right\} L,$$

$$Y_3^{v3} = \left\{ \frac{3(2-\mu^2)k_1+(2+\mu^2)kk_1}{6} + \frac{(1-\mu k^2)(k+1)}{4k_1} + \frac{(k^2-1)^2(k+1)}{32k_1^3} \right\} L,$$

$$Y_4^{v3} = \left\{ -\frac{3(2-\mu^2)k_1+(2+\mu^2)kk_1}{6} + \frac{(k+1)(1-2\mu+\mu k^2)}{4k_1} - \frac{(k^2-1)^2(k+1)}{32k_1^3} \right\} L,$$

$$X_4^{v3} = -Y_4^{u3}, \qquad X_4^{u4} = X_3^{u3}, \qquad Y_4^{u4} = -Y_3^{u3}, \qquad Y_4^{v4} = Y_3^{v3}.$$

Intercell Continuity

The continuity of displacements of the neighbouring cells in the finite element model is preserved at the nodes, but not necessarily along the intercell boundaris and there is a difference of opinion with regard to the significance of this discontinuity. Some authors maintain firmly that the displacements must be continuous across the boundaries if the solution of the model is to converge to the true solution of the structure. This view has apparently been prompted by the use of the Rayleigh-Ritz principle for the derivation of the energy stiffness matrix.

For this purpose a grid of reference points is established over the plate under investigation with the interspaces between the nodes having the shape of the finite elements. The values of the displacements of these points, converging to the exact values on reduction of mesh, may be determined by the Rayleigh-Ritz principle, whose application results in the same energy type matrix as the one found above. The necessary condition for the applicability of the principle is continuity of the displacements along the internodal lines.

It follows from this discussion that the displacement continuity along the intercell boundaries is a *sufficient* condition for the validity of the finite element method, but not the *necessary* condition. Irrespective of the edge continuity the finite element method is valid because of the identity of the differential equations of elasticity in application, on the one hand, to the solid plate and on the other — to the finite element model of proper deformability with infinitesimal mesh size.

It may be pointed out that the edge continuity has no meaning in application to the bar cells, which by their very nature are joined only at the nodes.

Triangular no-bar cells preserve edge continuity under all conditions, while the rectangular do not. Yet the precision of the results obtained with the rectangular cells has been found invariably much better than with the triangular ones of comparable size.

Appraisal of Imperfections of Stiffness Matrices

The existence of two different stiffness matrices of unsymmetrical no-bar finite elements calls for their comparison. No fault can be detected in the derivation of the statics type matrix, yet its asymmetry violates the basic structural principle of reciprocity. The inconsistency must be charged against the inexact nature of the method of no-bar finite element.

The energy type matrix may appear more attractive in view of its symmetry, but the error committed in its derivation in neglecting a part of the virtual work speaks against it. Furthermore the inclusion of certain edge stresses into the corner forces on the opposite side of the cell is contrary to common sense.

The defects discussed here do not apply to a rectangular no-bar cell or to a cell in the form of a triangle of any kind. It may be observed that the matrix of a quadrilateral framework cell is free from the faults of its no-bar counterpart because unlike the latter it is an actual structure and as such it is subject to the law of reciprocity.

The practical significance of the defects of the unsymmetrical no-bar cells should not, however, be exaggerated. On reduction of the size of cells the state of stress in the neighbourhood of the individual units approaches uniformity, diminishing by that the effect of the flexure conditions D and E, responsible for the inconsistencies of both types of the no-bar matrix. This means that the errors induced by the defects of the matrices tend to disappear on reduction of the size of mesh.

Comparison of the models made of bar and no-bar cells is worthy of comment. The stiffness matrix of the former is based on the uniform stress conditions, and of the latter — on the uniform conditions assisted by shearless bending. At first glance one might expect better results with the no-bar cells in view of their seemingly better conformity to the actual state of stress in the prototype. The present author himself at one time held this view[6]). However, the actual results have not confirmed the expectation, apart from some cases (like that of an end loaded wide cantilever beam), favouring the no-bar cells. It appears that the non-uniform components of the actual stresses in the prototype are normally not of the nature of shearless bending of conditions D and E, and for this reason they are not described any better by the matrix of the no-bar cell than by the one of the framework cell.

Conclusions

1. On infinite reduction of the size of the mesh the finite element solution of a plane stress problem converges to the true solution, provided the rounding off errors of the computer are negligible. This is true with regard to both the bar cells and the no-bar cells of a proper pattern.

2. Two types of stiffness matrix are available for the unsymmetrical no-bar cells, the statics type and the energy type. They are mutually related by the "complementary" terms which may be found by the use of influence lines.

3. Both types of the no-bar stiffness matrix contain some theoretical defects reflecting the inexact nature of the method utilizing cells of finite size. The framework cells are free from comparable defects.

4. The stiffness matrix of the framework cell and the energy type matrix of the no-bar cell are symmetrical about their principal diagonals, and so they

---

[6]) A. Hrennikoff and S. Tezcan: "Analysis of Cylindrical Shells by the Finite Element Method". International Conference on Shell Structures, Leningrad, U.S.S.R., 1966.

have an advantage in the computer work over the statics matrix of the no-bar cell, which does not possess the symmetry.

5. The continuity of the displacements on the intercell boundaries is not compulsory for the validity of the method.

6. The precision of the results obtained with the three matrices is not greatly different for the same shape and size of cells.

Appendix. Notation

a	small base of a trapezoidal cell
E	modulus of elasticity
h	height of a trapezoidal cell
k	ratio of bases of a trapezoid
k_1	ratio of height to base of a trapezoid
l	distance along boundary of cell
t	plate thickness
u, v	displacements along x and y axes, nodal displacements
x, y	coordinates, coordinate axes
X, Y	nodal forces, terms of stiffness matrix
α	base angle in a trapezoidal cell
ϵ	normal strain
γ	shearing strain
$\sigma, \sigma_\perp$	normal stress, normal stress on cell boundary
τ	shearing stress, shearing stress on cell boundary
$\lambda_\perp, \lambda_{11}$	displacements on cell boundary perpendicular and parallel to it
λ_x, λ_y	displacements on cell boundary parallel to x and y axes
μ	Poisson's ratio
Δ	nodal displacement

Summary

The purpose of this paper is clarification of some aspects of the Finite Element method which so far have not been studied sufficiently closely.

Two kinds of cells used in the analysis of plane stress by the Finite Element method, framework cells and the no-bar cells, are examined in detail. Two distinct types of stiffness matrix associated with the latter are presented in explicit form for a cell having the shape of an equilateral trapezoid. Some inconsistencies inherent in these matrices are pointed out and their effect on the results is discussed.

Résumé

Ce papier a pour but de mettre plus de clarté dans quelques aspects de la méthode des éléments finis, qui n'ont pas encore été étudiés à fond jusqu'à ce jour.

Deux éléments utilisés par la méthode des éléments finis dans l'analyse de contraintes bi-dimensionnelles, sont examinés en détail: l'élément de barre et l'élément de plaque. Deux types distincts de matrice associée avec ces éléments sont présentés explicitement pour un élément ayant la forme d'un trapèze équilatéral. L'attention est tirée sur quelques irrégularités inhérentes à ces matrices, et leur effet sur le résultat est discuté.

Zusammenfassung

Zweck dieser Schrift ist, verschiedene Auffassungen des Endlichen-Elementen-Verfahrens zu klären, derart wie es bis jetzt in seinem Umfange noch nicht geschehen ist.

Zwei Zellenarten, die in der Analyse der ebenen Spannungen vom Endlichen-Elementen-Verfahren angewandt werden, nämlich Stabwerkszelle und Scheibenelement, werden genau untersucht. Zwei verschiedene Steifigkeitsmatrizen, mit letzteren verbunden, werden explizit für ein Trapezelement aufgeführt. Auf einige innewohnenden Unstetigkeiten dieser Matrizen wird hingewiesen und der Einfluß auf das Ergebnis untersucht.

Leere Seite
Blank page
Page vide

The Response of Beam and Slab Bridges to Moving Forces

Comportement de ponts-dalles sous charges mobiles

Verhalten von Platten- und Balkenbrücken unter beweglichen Lasten

K. T. SUNDARA RAJA IYENGAR
Professor of Civil Engineering

K. S. JAGADISH
Lecturer in Civil Engineering

Indian Institute of Science, Bangalore – 12, India

Introduction

The dynamic response of a Highway bridge under moving loads is usually studied by treating the bridge as a beam. Such a treatment would be satisfactory if the span/width ratio of the bridge is large. It is known that a good majority of the highway bridges may have spans comparable to the widths. For such bridges, the beam theory is not adequate and a suitable two-dimensional theory will have to be adopted to consider the influence of the transverse flexibility of the bridge on its response.

There have been a few publications in the literature, which take the transverse flexibility of the bridge into account while studying its response. ALFARO and VELETSOS [1] have conducted some experimental studies on the response of an aluminium bridge model subjected to a moving sprung load. Later, ORAN and VELETSOS [2] developed an analytical solution to predict the response of the bridge under moving sprung loads, taking the two-dimensional behaviour of the bridge into consideration. In their analysis, the beam and slab highway bridge has been considered as a plate continuous over the beams. Lagrange's equations of motion have been derived and they have been solved numerically using the Newmark-β procedure.

In this paper the beam and slab Highway bridge is analysed as an orthotropic plate simply supported at two opposite edges. The orthotropic plate approximation is often used while studying the static load distribution effects in beam and slab bridges. It is believed that the extension of the orthotropic plate theory to the dynamic bridge problem would be instructive. This approach

is felt to be more convenient for numerical studies than the plate-over-beams analysis used by ORAN and VELETSOS.

The response of a Highway bridge to moving vehicles is usually studied by treating the vehicle as a sprung load. Sometimes the vehicle is also represented by a moving force ignoring its dynamic characteristics. Although the sprung load analysis is more realistic, this paper confines itself to the problem of the bridge under moving force for several reasons. The study of the bridge response under moving force yields useful information on two aspects. Firstly, the study isolates the influence of the speed parameter and secondly it reveals the degree of participation of the various modes in the response.

Analysis

An orthotropic plate bridge simply supported at the edges $x = 0$ and a, and free at the edges $y = \pm b/2$, will now be considered (Fig. 1). A force P is considered to move with uniform velocity "v" in the X-direction along the line $y = c$. P is assumed to be distributed over a square of side $2e$.

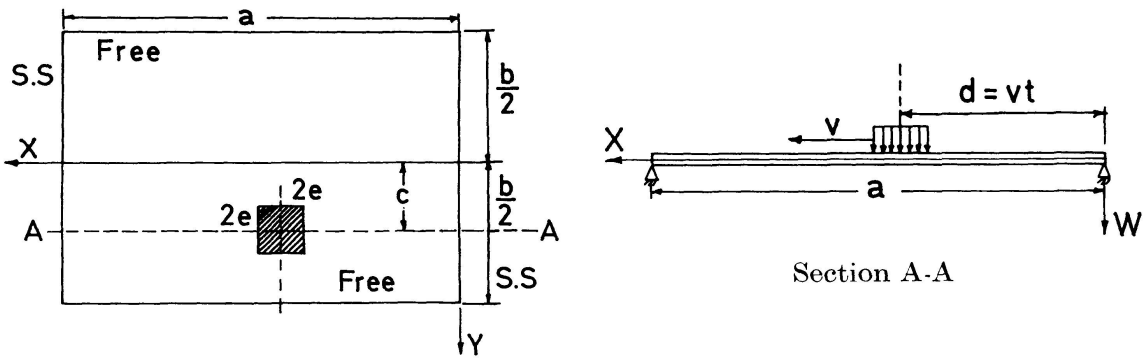


Fig. 1. The orthotropic plate under moving force.

The bridge will be assumed to possess no damping in the following analysis. FOSTER and OEHLER [3] and OEHLER [4] have reported some typical values of damping in actual bridges. Their measurements have shown that the damping values are of the order of 1 per cent of the critical. The neglect of damping appears to be quite reasonable because of the low damping capacity of Highway bridges. The equation of motion of the bridge under the moving force may now be written as

$$D_x \frac{\partial^4 W}{\partial x^4} + 2 H_{xy} \frac{\partial^4 W}{\partial x^2 \partial y^2} + D_y \frac{\partial^4 W}{\partial y^4} + \rho \frac{\partial^2 W}{\partial t^2} = F(x, y, t). \tag{1}$$

D_x, H_{xy} and D_y are the orthotropic plate rigidities and $W(x, y, t)$ is the dynamic deflection of the bridges. $F(x, y, t)$ represents the moving force-distribution function. ρ is the mass per unit area of the bridge. The deflection W will now be separated into two parts:

$$W(x,y,t) = \overline{W}(x,y,t) + U(x,y,t), \tag{2}$$

where $\overline{W}$ satisfies the equation

$$D_x \frac{\partial^4 \overline{W}}{\partial x^4} + 2H_{xy} \frac{\partial^4 \overline{W}}{\partial x^2 \partial y^2} + D_y \frac{\partial^4 \overline{W}}{\partial y^4} = F(x,y,t). \tag{3}$$

$\overline{W}$ represents the deflection of an orthotropic plate whose mass is neglected, under the action of a moving force P. This deflection can be obtained by static analysis and is dependent only on the position of the moving force on the bridge and not on its speed. $\overline{W}$ will be referred to as the "crawl solution".

Combining Eqs. (1), (2) and (3),

$$D_x \frac{\partial^4 U}{\partial x^4} + 2H_{xy} \frac{\partial^4 U}{\partial x^2 \partial y^2} + D_y \frac{\partial^4 U}{\partial y^4} + \rho \frac{\partial^2 U}{\partial t^2} = -\rho \frac{\partial^2 \overline{W}}{\partial t^2}. \tag{4}$$

It may be observed that it is easier to solve Eqs. (3) and (4) separately, than the composite Eq. (1). The difficulty in solving (1) arises due to the concentration in the force P. Eq. (4) is free from this difficulty since the inertia force $\rho \frac{\partial^2 \overline{W}}{\partial t^2}$ is well distributed over the bridge surface. The problem of the concentration of the force still persists in Eq. (3) but it is handled with far greater convenience since the time dependence of $\overline{W}$ is known beforehand from the time dependence of $F(x,y,t)$. The solution of Eq. (4) does not present any problem. $U(x,y,t)$ will be referred to as the "inertia force solution".

The solutions of Eqs. (3) and (4) will now be obtained by using the characteristic functions of the orthotropic plate. These functions have been studied in detail by SUNDARA RAJA IYENGAR and NARAYANA IYENGAR [5, 6]. The various characteristic functions are presented in Appendix. Let $Y_{mn}(y) \operatorname{Sin} \frac{m\pi x}{a}$ represent the deflection shape of the orthotropic plate in one of its modes. Let p_{mn} be the circular frequency of vibration for the same mode. The orthogonal property of the characteristic functions $Y_{mn} \operatorname{Sin} \frac{m\pi x}{a}$ can be made use of in expanding arbitrary functions by a series of these functions.

The function $F(x,y,t)$ may be defined as

$$F(x,y,t) = \frac{P}{4e^2} \quad \text{if, } d-e<x<d+e \text{ and } c-e<y<c+e,$$

$$= 0 \quad \text{if, } x<d-e \text{ or } >d+e \text{ and } y<c-e \text{ or } >c+e,$$

where $d = vt$.

This function may now be expanded by a double series. The series assumes the form:

$$F(x,y,t) = \sum_{m=1,\ldots}^{\infty} \sum_{n=1,\ldots}^{\infty} b_{mn}(t)\, Y_{mn}(y) \operatorname{Sin} \frac{m\pi x}{a}. \tag{6}$$

Hence,
$$b_{mn}(t) \int_0^a \int_{-b/2}^{+b/2} Y_{mn}^2 \operatorname{Sin}^2 \frac{m\pi x}{a}\, dx\, dy = P \operatorname{Sin} \frac{m\pi v t}{a} f_{mn},$$

where $$f_{mn} = \frac{\operatorname{Sin}\frac{m\pi e}{a}}{\frac{m\pi e}{a}} \frac{1}{2e} \int_{c-e}^{c+e} Y_{mn}\, dy.$$

Putting $$K_{mn}\, a\, b = \int_0^a \int_{-b/2}^{+b/2} Y_{mn}^2 \operatorname{Sin}^2 \frac{m\pi x}{a}\, dx\, dy;$$

$$b_{mn}(t) = \frac{P f_{mn}}{K_{mn}\, a\, b} \operatorname{Sin} \frac{m\pi v t}{a}. \tag{7}$$

Now $\overline{W}(x, y, t)$ may also be expanded by a series in terms of $Y_{mn} \operatorname{Sin}\frac{m\pi x}{a}$.

$$\overline{W}(x, y, t) = \sum_{m=1,\ldots}^{\infty} \sum_{n=1,\ldots}^{\infty} a_{mn}(t)\, Y_{mn} \operatorname{Sin} \frac{m\pi x}{a}. \tag{8}$$

Combining (3), (6) and (8)

$$a_{mn}(t) = \frac{P a^2}{D_x} \frac{a}{b} \frac{f_{mn}}{K_{mn} \lambda_{mn}} \operatorname{Sin} \frac{m\pi v t}{a}, \tag{9}$$

where $$\lambda_{mn} = \frac{\rho\, p_{mn}^2\, a^4}{D_x}.$$

This equation is a consequence of the fact that $Y_{mn} \operatorname{Sin}\frac{m\pi x}{a}$ is a characteristic function of the orthotropic plate. Hence

$$\overline{W} = \frac{P a^2}{D_x} \frac{a}{b} \sum_{m=1,\ldots}^{\infty} \sum_{n=1,\ldots}^{\infty} \frac{f_{mn}}{\lambda_{mn} K_{mn}} \operatorname{Sin} \frac{m\pi v t}{a} Y_{mn} \operatorname{Sin} \frac{m\pi x}{a}. \tag{10}$$

The solution of Eq. (4) may now be taken in the form

$$U(x, y, t) = \sum_{m=1,\ldots}^{\infty} \sum_{n=1,\ldots}^{\infty} q_{mn}(t)\, Y_{mn} \operatorname{Sin} \frac{m\pi x}{a}. \tag{11}$$

Combining Eqs. (4), (10) and (11),

$$\ddot{q}_{mn} + p_{mn}^2 q_{mn} = \frac{P a^2}{D_x} \frac{a}{b} \frac{f_{mn}}{\lambda_{mn} K_{mn}} \frac{m^2 \pi^2 v^2}{a^2} \operatorname{Sin} \frac{m\pi v t}{a}, \tag{12}$$

$$m = 1, 2 \ldots, \qquad n = 1, 2 \ldots$$

The solution of this set of equations is quite straightforward and can be completed if the initial conditions are known. In this paper, the bridge will be considered to be at rest initially. Accordingly,

$$W(x, y, 0) = 0 \tag{13a}$$

and $$\frac{\partial W}{\partial t}(x, y, 0) = 0. \tag{13b}$$

These equations lead to the relations,

$$U(x,y,0) = -\overline{W}(x,y,0)$$

and
$$\frac{\partial U}{\partial t}(x,y,0) = -\frac{\partial \overline{W}}{\partial t}(x,y,0)$$

or,
$$q_{mn}(0) = 0 \quad \text{and} \quad \dot{q}_{mn}(0) = -\frac{Pa^2}{D_x}\frac{a}{b}\frac{f_{mn}}{\lambda_{mn}K_{mn}}\alpha_m,$$

where
$$\alpha_m = \frac{m\pi v}{a}.$$

The solution of (12) can now be finally expressed as,

$$q_{mn}(t) = \frac{Pa^2}{D_x}\frac{a}{b}\frac{f_{mn}}{\lambda_{mn}K_{mn}}\frac{\alpha_m^2}{(p_{mn}^2-\alpha_m^2)}\left\{\operatorname{Sin}\alpha_m t - \frac{p_{mn}}{\alpha_m}\operatorname{Sin}p_{mn}t\right\} \tag{14}$$

Computation of Amplification Factors

From (2), it follows that

$$W = \frac{Pa^2}{D_x}\left[\delta_D + \frac{a}{b}\sum_{m=1,\ldots}^{\infty}\sum_{n=1,\ldots}^{\infty}\frac{f_{mn}}{\lambda_{mn}K_{mn}}Y_{mn}\operatorname{Sin}\frac{m\pi x}{a}\frac{\alpha_m^2}{(p_{mn}^2-\alpha_m^2)}\right.$$
$$\left.\cdot\left\{\operatorname{Sin}\alpha_m t - \frac{p_{mn}}{\alpha_m}\operatorname{Sin}p_{mn}t\right\}\right], \tag{15}$$

where
$$\delta_D = \frac{a}{b}\sum_{m=1,\ldots}^{\infty}\sum_{n=1,\ldots}^{\infty}\frac{f_{mn}}{\lambda_{mn}K_{mn}}\operatorname{Sin}\alpha_m t\, Y_{mn}\operatorname{Sin}\frac{m\pi x}{a}. \tag{16}$$

δ_D can be computed by summing the series in (16). Since the speed does not influence the values of δ_D directly, the values can be obtained for closely spaced load positions after setting $vt = d$. The resulting influence line can be used to compute the values of δ_D for any load position by interpolation, irrespective of the speed of the moving force. The dynamic amplification factor for deflection may now be defined as

$$AFD = \frac{W D_x}{Pa^2(\delta_D)_{max}}. \tag{17}$$

The expression for the moment amplification factor may be deduced in a similar manner.

Now,
$$M_x = -D_x\frac{\partial^2 W}{\partial x^2}$$

neglecting the Poisson's ratio effect.

Hence,
$$M_x = P\left[\delta_M + \frac{a}{b}\sum_{m=1,\ldots}^{\infty}\sum_{n=1,\ldots}^{\infty}\frac{f_{mn}}{\lambda_{mn}K_{mn}}\frac{\alpha_m^2 m^2\pi^2}{(p_{mn}^2-\alpha_m^2)}\right.$$
$$\left.\cdot\left\{\operatorname{Sin}\alpha_m t - \frac{p_{mn}}{\alpha_m}\operatorname{Sin}p_{mn}t\right\}Y_{mn}\operatorname{Sin}\frac{m\pi x}{a}\right], \tag{18}$$

where $$\delta_M = \frac{a}{b} \sum_{m=1,\ldots}^{\infty} \sum_{n=1,\ldots}^{\infty} \frac{f_{mn}}{\lambda_{mn} K_{mn}} \operatorname{Sin} \alpha_m t \, m^2 \pi^2 Y_{mn} \operatorname{Sin} \frac{m \pi x}{a}. \tag{19}$$

The computation of δ_M can be carried out for various load positions irrespective of the speed of the moving force. The amplification factor for M_x now takes the form,

$$AFM = \frac{M_x}{P(\delta_M)_{max}}. \tag{20}$$

The computation of the maximum amplification factors for deflection and moment requires the values of W_{max} and $M_{x\,max}$. These are to be obtained from the expressions (15) and (18) respectively. To this end, the deflection and moment are calculated at closely spaced values of "t" and the maximum values are picked out from the history curves so obtained.

Numerical Studies

The values of the amplification factors for deflection and moment can be computed by considering a suitable number of terms in the series (15) and (18). The results of the numerical studies are presented in two forms — (a) The amplification spectra and (b) The history curves. The amplification spectra are the plots of maximum amplifications of deflection and moment against the speed parameter. The speed parameter may be defined as $\alpha = \frac{vT}{2a}$ where "v" is the speed of the force and T is the fundamental period of the bridge. The history curves reveal the time variation of the bridge deflection and moment at a particular point as the force crosses the bridge with a definite speed.

The most important variable besides the speed parameter, is the transverse position of the moving force. In this study, two values of the transverse position are considered by taking $c = 0.45\,b$ and $c = 0.0$. The former corresponds to the eccentrically loaded case and the latter to the concentrically loaded case. It is not feasible to consider $c = 0.5\,b$ for the eccentric loading since the force is considered to be distributed over a finite area. In all the computations e/b is taken to be 0.05.

The values of δ_D and δ_M are first computed for fixed locations of the moving force. The values of these coefficients for any position of the moving force may then be found by interpolation. The determination of the dynamic deflection and the moment now requires the summation of series in (15) and (18). This may be carried out by considering a finite number of terms depending on the rapidity of convergence of the series. The time variation of the deflection and moment at any point in the bridge has to be studied by selecting a definite time interval. This interval naturally depends on the highest frequency appearing in the series. In what follows, the computation has been carried out

by selecting the time interval to be one-tenth the period of the highest mode considered. The maximum values of the deflection and the moment can also be picked out while studying the time variation of these quantities. These values may then be used to compute the maximum amplification factors.

The results of the various numerical studies are presented in the following sections. The entire procedure has been programmed in Fortran to work on the CDC-3600 computer at the Tata Institute of Fundamental Research, Bombay. The dynamic deflection and moment have been computed only for points at midspan. Five points at midspan have been considered: $y = \pm 0.45\,b$; $y = \pm 0.225\,b$ and $y = 0.0$. All the dynamic quantities are presented as ratios of the maximum static effects at the point under study.

Two typical Highway bridges are considered for detailed numerical investigation. The dimensions and the properties of the two bridges are presented in Table A.

Table A. Details of bridges considered

No.	Bridge Type	Span	a/b	D_x/D_y	$H/\sqrt{D_x D_y}$	$\sqrt{D_x}$ (kg·m)$^{1/2}$	ρ kg·sec^2/m^3
1	Slab	5 m	1.0	1.0	1.0	2500.0	60.0
2	Beam and Slab	20 m	2.0	100.0	0.4	25000.0	90.0

It is believed that the two bridges are representative of a good majority of Highway bridges where two-dimensional effects are prominent.

Convergence of the Solution

The convergence of the series in (15) and (18) are studied by considering different number of terms. The time histories for AFD and AFM for various number of terms considered are presented in Figs. 2 to 5. In all these figures a maximum of three modes are considered and the highest mode corresponds to $m = 1$ and $n = 3$. The solutions by considering lesser number of terms are also plotted to study the convergence.

Fig. 2 shows the behaviour of AFD for the beam and slab bridge under eccentric loading, the speed parameter being 0.193. The figure shows that the difference between the 2-mode solution and the 3-mode solution is small. The solutions for four modes and five modes were also computed and the resulting AFD's were found to coincide with the 3-mode solution on the graph. The figure also shows that the substantial component of the response consists of the first three modes of vibration of the bridge.

Fig. 3 shows the variation of AFM for the beam and slab bridge under eccentric loading. The speed parameter is again equal to 0.193. The con-

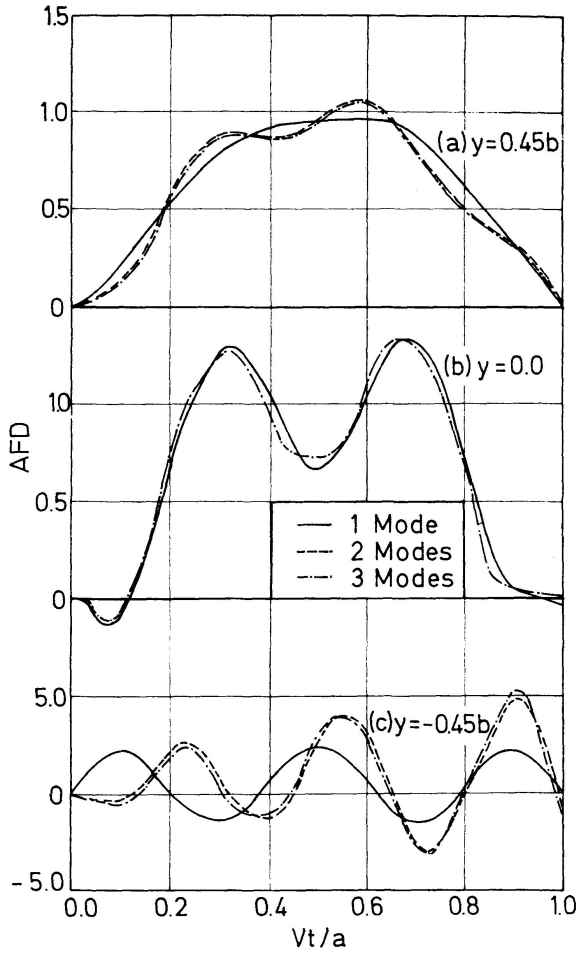


Fig. 2. Influence of various modes on the midspan deflection in the beam and slab bridge.
Force along $y = 0.45\ b$; $\alpha = 0.193$.

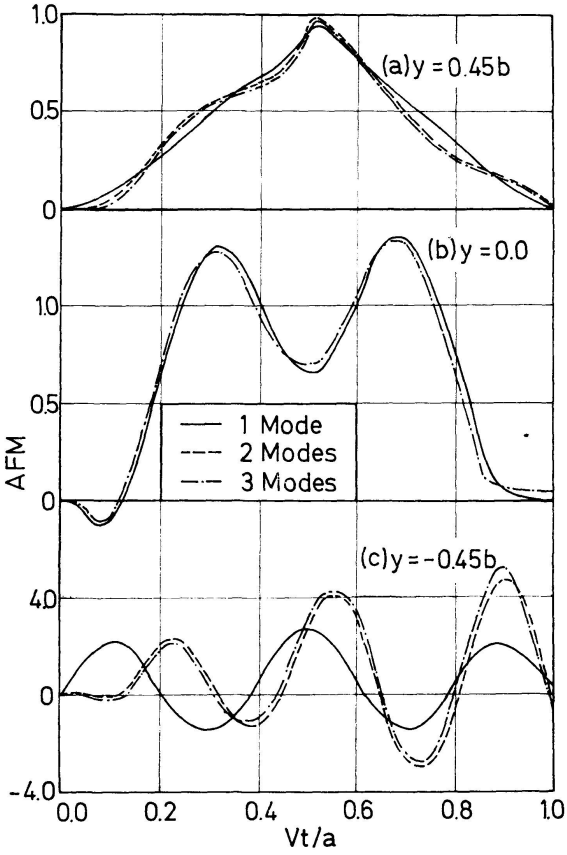


Fig. 3. Influence of various modes on the midspan moment (M_x) in the beam and slab bridge.
Force along $y = 0.45$; $\alpha = 0.193$.

vergence of the dynamic moment is seen to be quite satisfactory. Consideration of higher modes did not cause any appreciable change in the values of AFM and the first three modes may be considered to dominate the response. Fig. 4 shows the AFM variation for the beam and slab bridge under concentric loading. Because of the concentric loading, the second mode does not participate in the response and only the first mode and the third mode affect the moment and deflection values. The convergence of the values is again seen to be satisfactory with the first three modes. Consideration of more terms did not lead to any change in the graphs presented in Fig. 4.

Fig. 5 shows the behaviour of AFM for the slab bridge under eccentric loading, the speed parameter being 0.197. The consideration of modes more than three again did not introduce any noticeable changes in the history curves. Although the Figs. 4 and 5 consider the convergence of AFM, the convergence for AFD for the same cases was also found to be quite satisfactory. Comparison of the two series in (15) and (18) shows that the terms

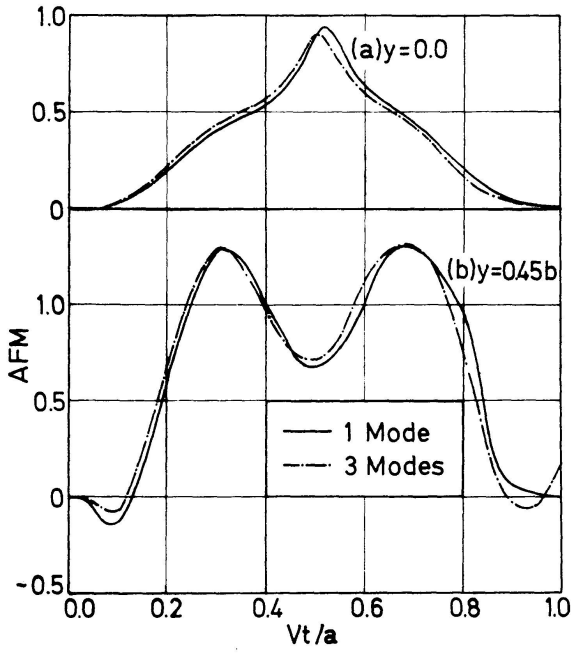


Fig. 4. Influence of various modes on the midspan moment (M_x) in the beam and slab bridge.
Force along $y = 0.0$; $\alpha = 0.193$.

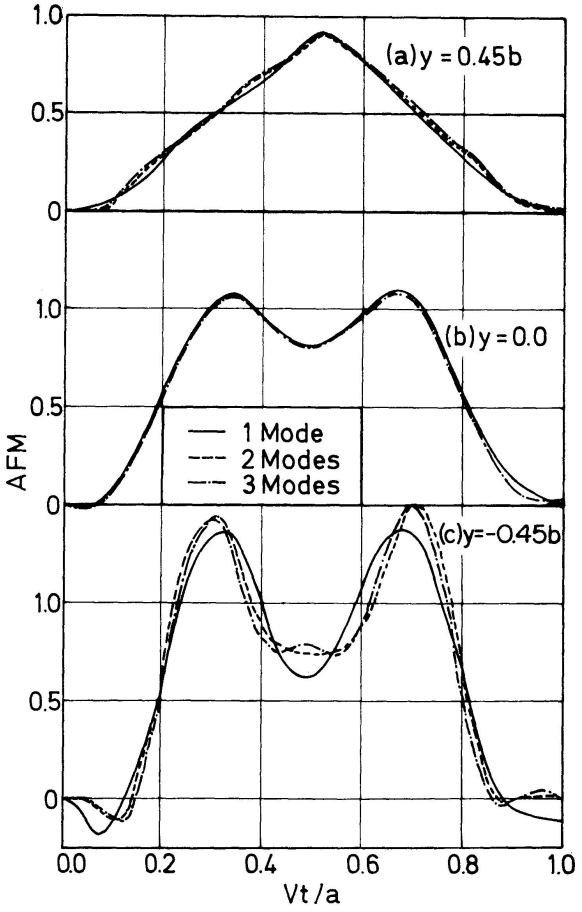


Fig. 5. Influence of various modes on the midspan moment (M_x) in the slab bridge.
Force along $y = 0.45\ b$; $\alpha = 0.197$.

are practically identical and the same rapidity of convergence may be expected for both AFM and AFD.

The convergence studies made in the above considered only terms with $m = 1$. Some sample calculations were made including the term corresponding to $m = 3$ and $n = 1$. It was found that the addition of this term did not alter any of the history curves presented. The influence of modes with m greater than unity may therefore be safely neglected for the midspan response. Modes with $m = 2$ need not be considered for midspan response as such modes will have a nodal line at the midspan. These modes would be of importance while considering the response of points away from the midspan.

The Amplification Spectra

The maximum dynamic amplification of any response quantity of the bridge under a moving force may be conveniently studied by drawing spectral curves. In this study the maximum amplification factors for deflection and

moment (M_x) at midspan are plotted against the speed parameter α. Three points at midspan are considered: $y = \pm 0.45b$ and $y = 0.0$. The spectra are drawn for (a) the eccentrically loaded case ($c = 0.45b$) and (b) the concentrically loaded case ($c = 0.0$). The slab bridge and the beam and slab bridge considered earlier are analysed for the spectral curves. All the computations are made taking 5 modes ($m = 1$ for all modes) into consideration.

The spectra are presented in Figs. 6 to 9. Figs. 6 and 7 refer to the concentric loading of the slab bridge and the beam and slab bridge respectively. In each figure, the spectral curves by the simple beam theory are also inserted for comparison. The two figures show that the amplification factors for $y = 0$ and $x = a/2$ in concentrically loaded bridges follow much the same pattern found in the midspan of a beam. The amplifications of $y = 0$ and $x = a/2$ in the two bridges are somewhat lesser in magnitude than the amplifications at the midspan of a beam. The amplification factors are larger at the edges than at $y = 0$ and $x = a/2$. The $(AFM)_{max}$ and $(AFD)_{max}$ values at the edges are practically identical in both the bridges. The amplifications at the edges of the beam and slab bridge are quite large and reach values of the order of 1.5 for the higher speeds.

Figs. 8 and 9 show the $(AFM)_{max}$ and $(AFD)_{max}$ values in the slab bridge and the beam and slab bridge respectively, due to eccentric loading. The amplification factors at the loaded edge ($y = 0.45b$) do not closely follow the

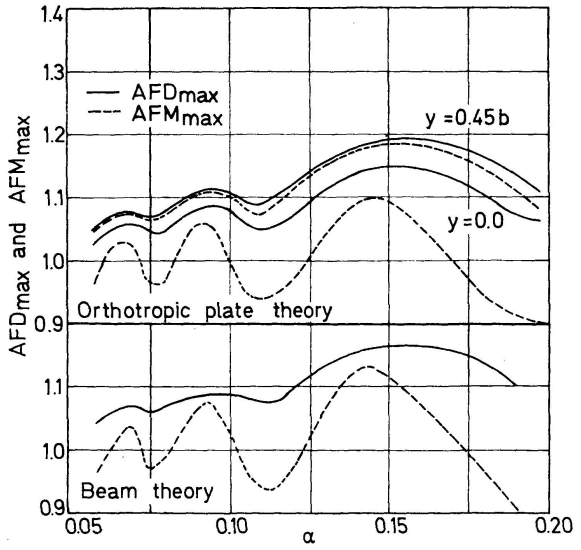


Fig. 6. Amplification spectra for the slab bridge with concentric moving force. Force along $y = 0.0$.

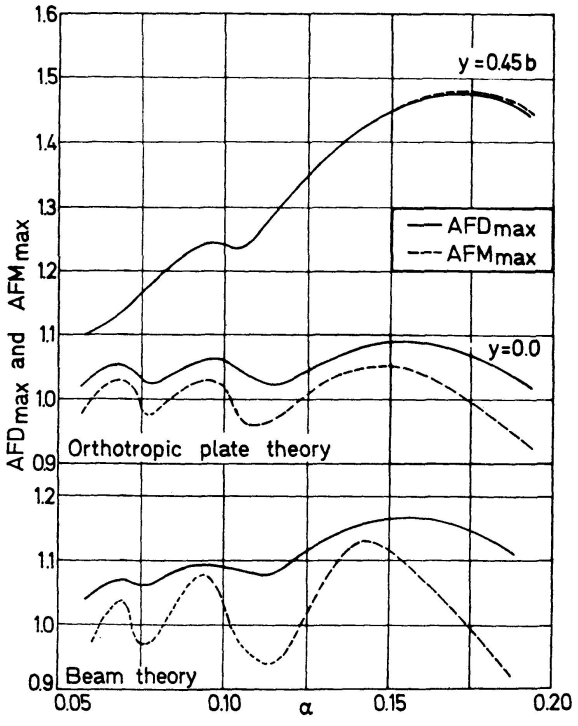


Fig. 7. Amplification spectra for the beam and slab bridge with concentric moving force. Force along $y = 0.0$.

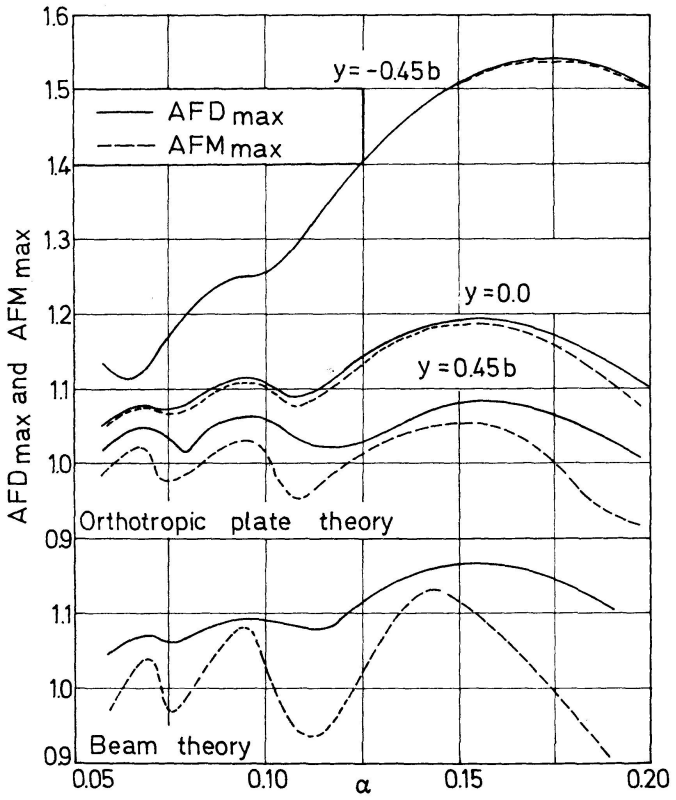


Fig. 8. Amplification spectra for the slab bridge with eccentric moving force.
Force along $y = 0.45\ b$.

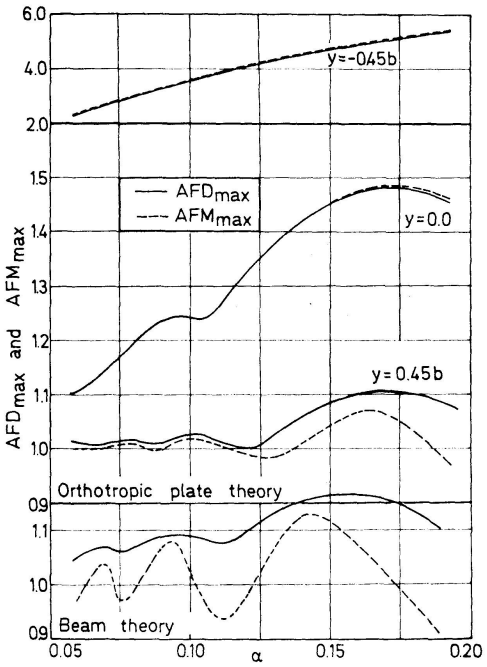


Fig. 9. Amplification spectra for the beam and slab bridge with eccentric moving force.
Force along $y = 0.45\ b$.

pattern found in beams. The disparity between the beam theory and the two-dimensional theory is greater for the beam and slab bridge. The unloaded edge ($y = -0.45b$) experiences quite large amplifications. There are considerable differences between the behaviour of the slab bridge and the beam and slab bridge with reference to the response of the unloaded edge. The beam and slab bridge shows pronounced oscillations at the unloaded edge in contrast to the slab bridge.

When the beam and slab bridge is subjected to eccentric loading, the unloaded edge experiences amplifications of the order of 5.0 for the higher speeds of the moving force.

The Transverse Distribution of Dynamic Effects

Fig. 10 shows the profile variation of the midspan deflection and moment in the beam and slab bridge as the force moves along, the speed parameter being 0.193. The figure refers to concentric loading ($c = 0.0$). The dynamic profiles are plotted in bold lines for various positions of the force along the

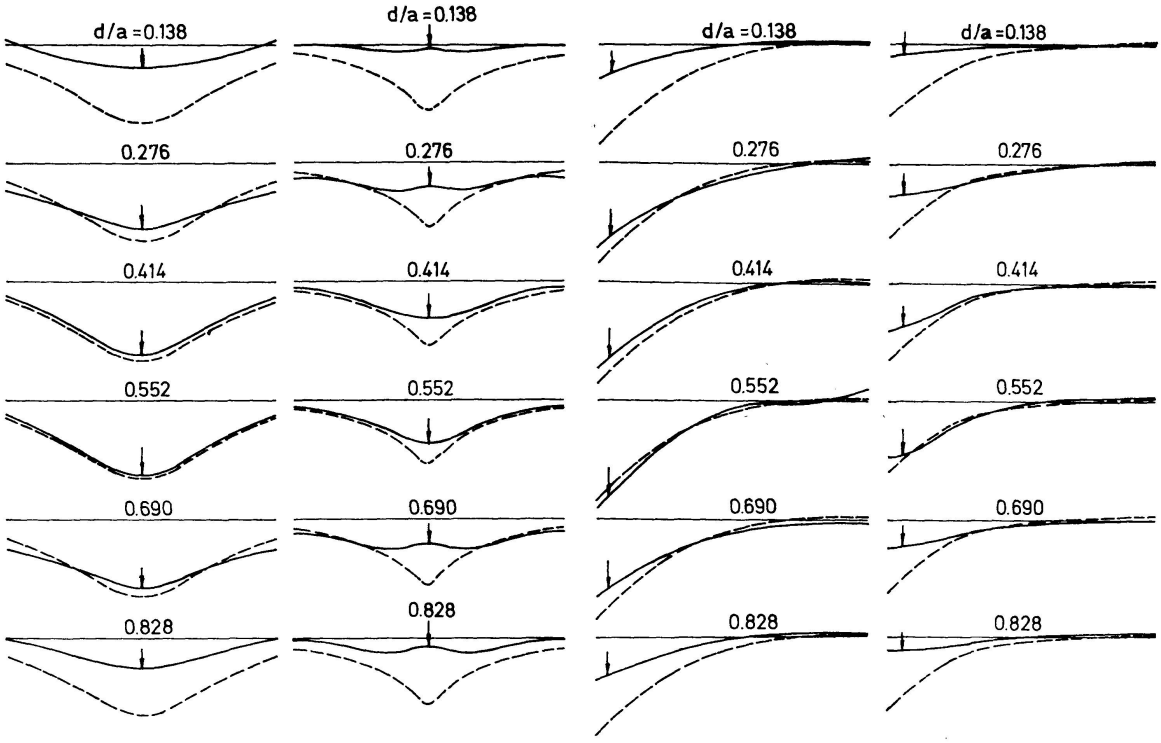


Fig. 10. Transverse distribution of dynamic deflection and moment at midspan of the beam and slab bridge.
Force along $y = 0.0$; $\alpha = 0.193$.

Fig. 11. Transverse distribution of dynamic deflection and moment at midspan of the beam and slab bridge.
Force along $y = 0.45\,b$; $\alpha = 0.193$.

bridge. The static deflection profile at midspan, when the force is also at midspan, is shown in dotted lines along with each profile sketch.

The dynamic deflection profile is seen to be dominated by the contribution of the fundamental and the second symmetric modes. The change in the profile as the force moves from $d = 0.552\,a$ to $d = 0.69\,a$ clearly indicates the participation of the second symmetric mode. Fig. 10b) shows the dynamic moment variation (M_x) at midspan. Unlike the maximum static moment at midspan, the dynamic moment is more uniformly distributed across the width of the bridge. This may be attributed to the distributing effect of the inertia forces of the bridge.

Fig. 11a) shows the midspan deflection profile of the beam and slab bridge as the force moves eccentrically along $y = +0.45\,b$. The speed parameter is again 0.193. The participation of the various modes is more complex in eccentric loading than what is found in concentric loading. Fig. 11b) shows the midspan moment (M_x) variation across the width for eccentric loading of the beam and slab bridge. The dynamic distribution of the deflection and the moment M_x are both seen to be more uniform than the maximum static profiles.

History Curves

The history curve for any response quantity shows the quantity as a function of time as the force crosses the bridge. Some typical history curves for the deflection and moment at midspan of the two bridges are presented here.

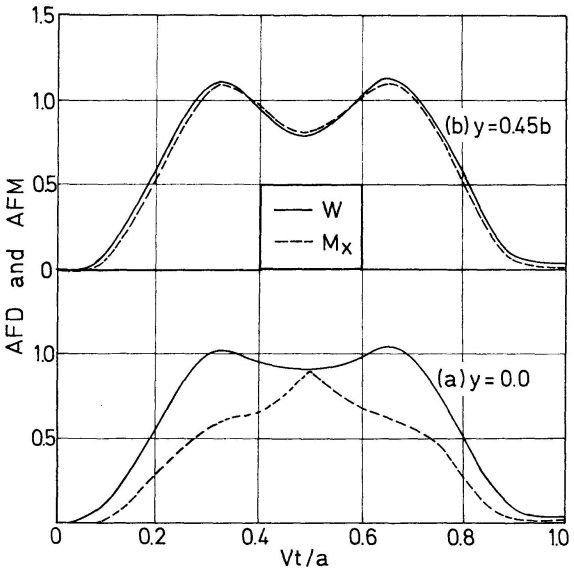


Fig. 12. History curves for the midspan deflection and moment amplifications in the slab bridge.
Force along $y = 0.0$; $\alpha = 0.197$.

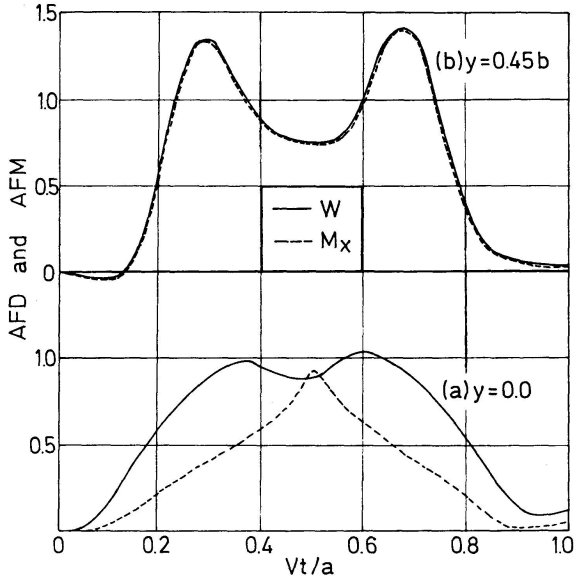


Fig. 13. History curves for the midspan deflection and moment amplifications in the beam and slab bridge.
Force along $y = 0.0$; $\alpha = 0.193$.

Figs. 12 and 13 show the history curves for the slab bridge and the beam and slab bridge respectively, when the moving force is concentric. The speed parameter is 0.197 for the slab bridge and 0.193 for the beam and slab bridge. There are considerable differences between the moment (M_x) and deflection curves for $y = 0.0$. This may be attributed to the differences between the static influence lines for the two quantities. The influence line for M_x at $y = 0$ and $x = 0.5\,a$ has a very sharp peak at the centre. The deflection influence line for the same point happens to be a much smoother curve. Even after adding the inertia effects, the differences between the time variation of the two quantities show up in the history curves. It is also seen that the maximum dynamic moment for $y = 0.0$ occurs when the force is very close to midspan if not at the midspan. The maximum dynamic deflection at $y = 0.0$ may occur even when the force is well removed from midspan. The situation is somewhat different for midspan points at $y = \pm 0.45\,b$, wherein the moment and deflection amplifications follow each other very closely. In contrast to the point $y = 0.0$, the inertia effects are comparable to the static effects at the points $y = \pm 0.45\,b$.

Figs. 14 to 16 show the history curves for eccentrically loaded bridges. Fig. 14 refers to the slab bridge subjected to an eccentric moving force, the

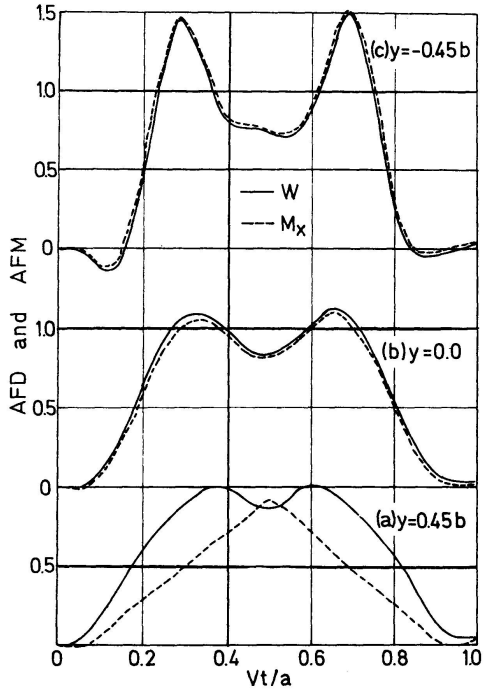


Fig. 14. History curves for the midspan deflection and moment amplifications in the slab bridge. Force along $y = 0.45\,b$; $\alpha = 0.197$.

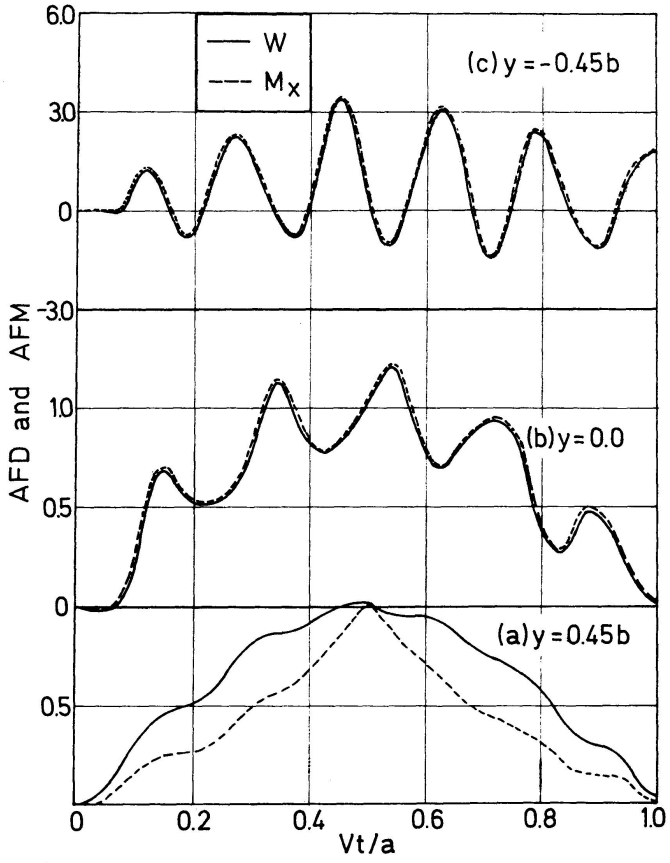


Fig. 15. History curves for midspan deflection and moment amplifications in the beam and slab bridge. Force along $y = 0.45b$; $\alpha = 0.097$.

speed parameter being 0.197. Figs. 15 and 16 refer to the beam and slab bridge under eccentric moving force, the speed parameter values being 0.097 and 0.193 respectively. The history curves for $y = +0.45\,b$ and $x = 0.5\,a$ follow much the same trend followed by the curves for the midspan point at $y = 0.0$ in the case of concentric loading. The inertia effects dominate the response as points farther away from the line of loading are considered. This is especially true for the beam and slab bridge, where the edge $y = -0.45\,b$ reveals an interesting feature. The point at midspan of this bridge corresponding to $y = -0.45\,b$, executes a beating type motion as the force moves along the edge $y = +0.45\,b$. The dynamic effects in this case are far in excess of the static response values. Large amplifications are obtained and the maximum amplification may occur when the force is nearing the support $x = a$ (Fig. 16). This beat phenomenon is observed for both the values of the speed parameter ($\alpha = 0.097$ and 0.193) considered in Figs. 15 and 16. This behaviour may be directly attributed to the frequency distribution existing in the beam and slab bridge. In Table B the frequencies of the two bridges described in Table A, are tabulated. The Table shows that the first two frequencies of the beam and slab bridge are quite close. This closeness of the frequencies causes the

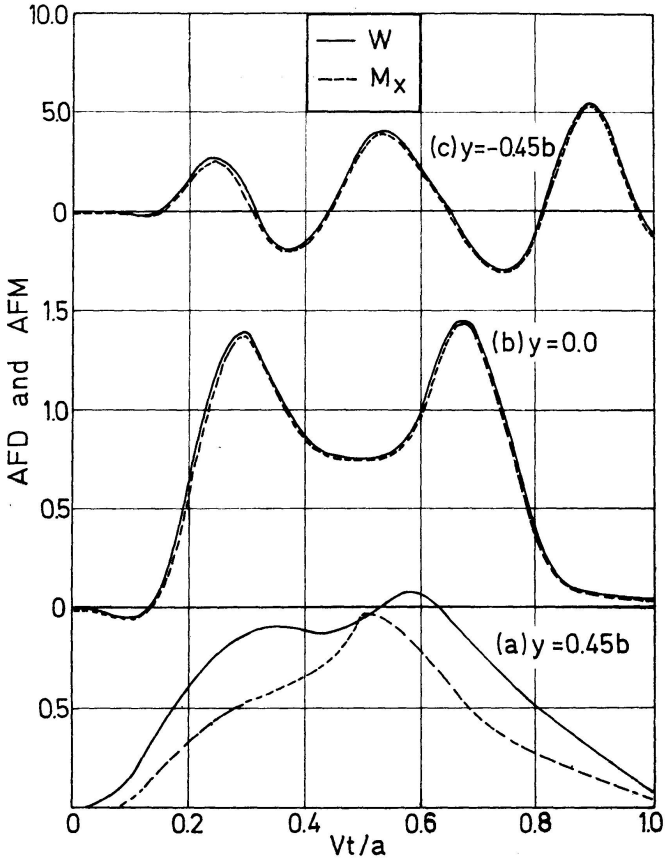


Fig. 16. History curves for midspan deflection and moment amplifications in the beam and slab bridge. Force along $y = 0.45b$; $\alpha = 0.193$.

beat type phenomenon at the unloaded edge. The frequencies of the slab bridge are quite sparsely distributed and the unloaded edge of this bridge does not show the beating motion for eccentric loading.

Table B. Frequencies of the bridges

Type	Frequencies in c/s ($m = 1$ for all modes)			
	Fundamental	I Asymmetric	II Symmetric	II Asymmetric
Slab	20.27	36.73	80.57	159.3
Beam and Slab	10.34	12.09	18.98	33.88

Conclusions

Some general conclusions may be drawn from the results obtained for the two typical bridges. The conclusions may be summarised as follows:

a) The midspan response of the Highway bridge is influenced mostly by the first three modes of vibration. Although this conclusion has been drawn with

reference to two bridges, it may be extended to other bridges where the frequencies of the first three modes are clustered together. It has been shown by SUNDARA RAJA IYENGAR, JAGADISH and NARAYANA IYENGAR [7] that the frequencies of most of the Highway bridges follow this pattern.

b) When a bridge is subjected to a concentric moving force, the amplification factors for points below the moving force follow the trend found in beams. The values of the amplifications found by the orthotropic plate theory are smaller than the values found by the beam theory. When the bridge is under eccentric moving force, the amplifications for points below the moving force do not closely follow the trend found in beams.

c) For a point underneath the moving force the maximum moment occurs when the force is at the point or very close to it. The maximum deflection at the point can occur even when the force has moved away from the point.

d) The maximum amplification increases as points away from the line of loading are considered. The largest amplifications are realised at the unloaded edge of a bridge under eccentric loading. This effect is more pronounced in the beam and slab bridge than in the slab bridge. If the first two frequencies of a bridge are very close, the unloaded edge executes a beating type motion, when the bridge is under eccentric moving force.

Notations

AFD	Amplification factor for deflection
AFM	Amplification factor for moment
a	Span of the bridge
b	Width of the bridge
c	y-co-ordinate of the moving force
$d = v\,t$	x-co-ordinate of the moving force at any instant
D_x, D_y, H_{xy}	Orthotropic plate constants
e	Half the side of the square distributing the force over the bridge surface
p_{mn}	Circular frequency of the orthotropic plate
U	Inertia force solution
v	Speed of the force
W	Dynamic deflection of the plate
$\overline{W}$	Crawl solution
α_{mn}, β_{mn}	Parameters in the plate characteristic function
$\alpha_m = \frac{m\pi v}{a}$	Crossing frequency
$\alpha = \frac{vT}{2a}$	Speed parameter
δ_D, δ_M	Influence coefficients for static deflection and moment
λ_{mn}	Frequency parameter
ρ	Mass per unit area of the orthotropic plate

Appendix

The expressions for $Y_{mn}(y)$ are presented in this appendix. The functions $Y_{mn}\,\mathrm{Sin}\frac{m\pi x}{a}$ happen to be the shape functions of an orthotropic plate with two opposite edges simply-supported and the other two free. The expressions for the functions may be easily obtained by a free-vibration analysis of the plate.

Modes symmetric in $y-n$ is odd

(I) $D_1 \neq 0$,

$$Y_{mn}(y) = \frac{\mathrm{Cosh}\frac{\alpha_{mn}y}{b}}{\mathrm{Cosh}\frac{\alpha_{mn}}{2}} + \frac{\alpha_{mn}^2 - \frac{D_1}{D_y}\frac{m^2\pi^2b^2}{a^2}}{\beta_{mn}^2 + \frac{D_1}{D_y}\frac{m^2\pi^2b^2}{a^2}} \frac{\mathrm{Cos}\frac{\beta_{mn}y}{b}}{\mathrm{Cos}\frac{\beta_{mn}}{2}}.$$

where α_{mn} and β_{mn} satisfy the equations,

$$\tan\frac{\beta_{mn}}{2} = -\frac{\alpha_{mn}}{\beta_{mn}}\left[\frac{\beta_{mn}^2 + \frac{D_1}{D_y}\frac{m^2\pi^2b^2}{a^2}}{\alpha_{mn}^2 - \frac{D_1}{D_y}\frac{m^2\pi^2b^2}{a^2}}\right]^2 \tanh\frac{\alpha_{mn}}{2}$$

and

$$\alpha_{mn}^2 = \frac{2H_{xy}}{D_y}\frac{m^2\pi^2b^2}{a^2} + \beta_{mn}^2.$$

(II) $D_1 = 0$,

$$Y_{m1}(y) = 1$$

and

$$\beta_{m1} = 0.$$

For values of n greater than unity, expressions of (I) may be used.

Modes antisymmetric in $y-n$ is even

$$Y_{mn}(y) = \frac{\mathrm{Sinh}\frac{\alpha_{mn}y}{b}}{\mathrm{Sinh}\frac{\alpha_{mn}}{2}} + \left[\frac{\alpha_{mn}^2 - \frac{D_1}{D_y}\frac{m^2\pi^2b^2}{a^2}}{\beta_{mn}^2 + \frac{D_1}{D_y}\frac{m^2\pi^2b^2}{a^2}}\right]\frac{\mathrm{Sin}\frac{\beta_{mn}y}{b}}{\mathrm{Sin}\frac{\beta_{mn}}{2}},$$

where α_{mn} and β_{mn} satisfy the equations,

$$\tan\frac{\beta_{mn}}{2} = \frac{\beta_{mn}}{\alpha_{mn}}\left[\frac{\alpha_{mn}^2 - \frac{D_1}{D_y}\frac{m^2\pi^2b^2}{a^2}}{\beta_{mn}^2 + \frac{D_1}{D_y}\frac{m^2\pi^2b^2}{a^2}}\right]^2 \tanh\frac{\alpha_{mn}}{2}$$

and

$$\alpha_{mn}^2 = \frac{2H_{xy}}{D_y}\frac{m^2\pi^2b^2}{a^2} + \beta_{mn}^2.$$

References

1. J. P. Alfaro and A. S. Veletsos: "Dynamic behaviour of an I-Beam Bridge Model Under a Smoothly Rolling Load". Civil Engineering Studies, Structural Research Series No. 167, University of Illinois, 1958.
2. C. Oran and A. S. Veletsos: "Analysis of Static and Dynamic Response of Simple-Span, Multigirder Highway Bridges". Civil Engineering Studies, Structural Research Series No. 221, University of Illinois, 1961.
3. G. M. Foster and L. T. Oehler: "Vibrations and deflections of Rolled-beam and Plate-Girder Bridges". Highway Research Board Bulletin 124, National Academy of Science, Washington D.C., 1956.
4. L. T. Oehler: "Vibration Susceptibilities of various Highway Bridge Types". Proceedings of the American Society of Civil Engineers, Paper No. 1318, Vol. 83, ST 4, July 1957.
5. K. T. Sundara Raja Iyengar and R. Narayana Iyengar: "Free Vibration of Beam and Slab Bridges". Publ. IABSE, Vol. 27, 1967.
6. R. Narayana Iyengar: "Studies in the Free Vibration of Beam and Slab and Interconnected Girder Bridges". Thesis submitted for the degree of the Master of Science in Engineering, Indian Institute of Science, Bangalore, 1966.
7. K. T. Sundara Raja Iyengar, K. S. Jagadish and R. Narayana Iyengar: "Free Vibration of Beam and Slab Bridges". The Journal of the Institute of Engineers (India), Vol. XLVIII, No. 1, Pt CI 1, September 1967 (Special).

Summary

The dynamic response of simple-span beam and slab Highway bridges subjected to a moving concentrated force is studied. The Highway bridge is treated as an orthotropic plate, and the normal mode method is used in the response analysis. Numerical results are presented for typical cases in the form of amplification spectra and history curves.

Résumé

L'auteur étudie le comportement dynamique de ponts d'autoroute en dalle, à une seule ouverture, sous une force mobile concentrée. La méthode normale est employée pour l'analyse du comportement, le pont étant assimilé à une dalle orthotrope. Pour les cas-types, des valeurs numériques sont données sous forme de spectres amplificateurs et de courbes d'hystérésie.

Zusammenfassung

Der Autor behandelt das dynamische Verhalten von einfachen Platten- und Balkenbrücken für Autobahnen unter einer konzentrierten, beweglichen Kraft. Die Brücke wird als orthotrope Platte behandelt und die Rechenwerte mit der normalen Methode ermittelt. Für typische Fälle sind numerische Werte angegeben in der Form von Vergrößerungsspektren und Hysteresiskurven.

Die Verschiebungsmethode in der Theorie der dünnwandigen Stäbe und ein neues Berechnungsmodell des Stabes mit in seinen Ebenen deformierbaren Querschnitten

Displacement-Method in the Theory of Thin-Walled Members, and a New Calculation-Model for the Thin-Walled Bars with Deformable Contours

La méthode des déplacements dans la théorie des membres à parois minces et un nouveau modèle de calcul pour des membres à parois minces avec contour déformable

CURT F. KOLLBRUNNER
Dr. sc. techn., Dr. h. c., Zollikon, Zürich

NIKOLA HAJDIN
Dr. sc. techn., Professor an der Universität Beograd

1. Einleitung

Vor über fünf Jahren begannen wir die Theorie der dünnwandigen Stäbe systematisch zu bearbeiten.

Bisher hat sich unsere Arbeit auf die Probleme der linearen Theorie beschränkt und ist in den Publikationen [1] bis [6] erschienen. In der Folge beabsichtigen wir, mit unserer Arbeit weitere wesentliche Bereiche, welche mit dem Gebiet der dünnwandigen Stäbe und ihrer Anwendung im Bauwesen zusammenhängen, zu erfassen[1]).

In den letzten Jahren wurde die lineare Theorie durch eine ganze Anzahl von Verfassern eingehend behandelt. Der Hauptzweck unserer bisherigen Arbeit war eine Zusammenfassung und Vereinheitlichung der auf diesem Gebiete gewonnenen Erkenntnisse unter besonderer Berücksichtigung ihrer praktischen Anwendung zu schaffen.

Einige Ergebnisse dieser in den erwähnten Monographien behandelten Arbeit stellen unseres Erachtens nach einen Beitrag zur Theorie dieser Konstruktionen dar:

In der Arbeit [3] ist die Statik der Systeme dünnwandiger Stäbe mit offenem Profil als eine Erweiterung der Lehren der klassischen Statik gebracht. Der

---

[1]) Ein Teil dieser Probleme wurde im Artikel [7] erwähnt.

Aufbau der Theorie erfolgt in erster Linie durch die konsequente Anwendung des Prinzips der virtuellen Arbeit bei der Variation der Spannungen sowie durch die Entwicklung der verallgemeinerten Kraftgrößenmethode.

Eine sehr ausführliche Übersicht und Darlegungen der einzelnen Methoden für die praktische Berechnung dünnwandiger Stäbe mit geschlossenem Profil wurde in der Publikation [4] gebracht.

In dieser Veröffentlichung wurde ein besonderes Gewicht auf die Erläuterung der Verfahren von BENSCOTER [7], UMANSKI [8] und HEILIG [9], sowie auf den Vergleich derselben mit der genaueren Theorie von WLASSOW [10] gelegt.

Die Ergebnisse dieser Vergleiche sind vom praktischen Standpunkt aus interessant, doch können wir an dieser Stelle nicht näher auf sie eingehen.

Eine ausführliche kritische Darlegung des Berechnungsverfahrens von KUBITZKI, welches auf dem sog. Schubfeldschema beruht, wurde im letzten Kapitel der Publikation [4] gebracht.

Die Theorie des langen prismatischen Faltwerks bzw. des dünnwandigen Stabes mit in seinen Ebenen deformierbaren Querschnitten unter Anwendung der Verschiebungsmethode wurde eingehend in der Arbeit [5] behandelt. Die in dieser Publikation dargelegte Theorie konnte in einer genügend allgemeinen Form entwickelt werden, so daß in ihr als Sonderfälle die sogenannten Theorien des steifknotigen und des gelenkigen Faltwerks sowie die klassische Theorie der Wölbkrafttorsion enthalten sind.

Abgesehen von diesen Sonderfällen ist es, unabhängig von der für die Analyse angewendeten Methode, außerdem noch möglich zwei Berechnungsmodelle aus dem allgemeinen Berechnungsmodell zu gewinnen.

Das erste kann als eine Erweiterung der klassischen Theorie der Wölbkrafttorsion auf Querschnitte, deren Wandstärke nicht ausgesprochen klein im Vergleich zu seinen übrigen linearen Abmessungen ist, angesehen werden[2]).

In diesem Beitrag wird das zweite Berechnungsmodell behandelt, welches eine Theorie des Faltwerkes unter Berücksichtigung auch der Torsionsmomente ermöglicht.

2. Verformung des Stabes

Wir betrachten einen geraden dünnwandigen Stab mit offenem Querschnitt. Die beliebig geformte Profilmittellinie ersetzen wir durch einen Polygonzug. Die Wandstärke t zwischen zwei Knoten sei konstant.

Die Lage eines beliebigen Punktes auf der Mittelfläche ist durch die Koordinaten s und z bestimmt. Die Koordinate s ist die längs der Profilmittellinie gemessene Entfernung des Punktes von einer vorher bestimmten Erzeugenden

[2]) Siehe die Arbeit [5], Kapitel 10.

und z dessen Abstand von einem beliebigen Querschnitt, gemessen längs der Stabachse (Fig. 1).

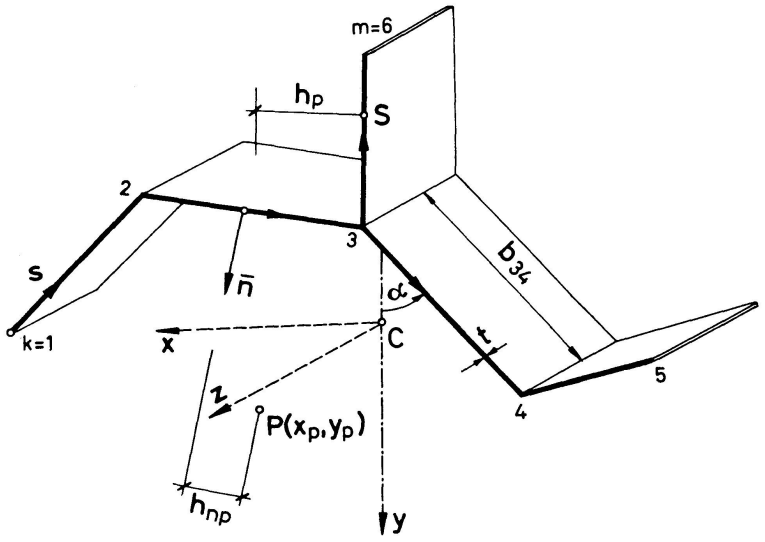


Fig. 1.

Den Abstand eines beliebigen, nicht auf der Mittelfläche gelegenen Punktes von derselben gemessen in Richtung der inneren Normalen bezeichnen wir mit e.

Außer dem Koordinatensystem s, z und e führen wir das Kartesische Koordinatensystem x, y und z ein, wobei wir, der Einfachheit halber, für die Achsen x und y die Hauptträgheitsachsen des Querschnitts wählen.

Die Verschiebungen der Punkte der Mittelfläche in den Richtungen s und z bezeichnen wir mit v und w und die Verschiebungskomponenten in den Richtungen x und y mit ξ und η.

In bezug auf die Verformung der Mittelfläche des Stabes treffen wir die folgenden Voraussetzungen:

1. Die den Stab bildenden Platten erleiden in der Querrichtung keine Dehnungen, d.h. $\epsilon_s = 0$.
2. Die Gleitverzerrung γ_{zs} in der Mittelfläche des Stabes wird vernachlässigt.

Die erste Voraussetzung besagt, daß die Verschiebungen der Knoten der Profilmittellinie in der Ebene des Querschnittes gleich sind den entsprechenden Verschiebungen von Knoten einer kinematischen Kette, deren einzelne Glieder aus in diesen Knoten gelenkig miteinander verbundenen Stäben bestehen, deren Achsen mit den Seiten der polygonalen Profilmittellinie zusammenfallen.

Die Zahl der voneinander unabhängigen Verschiebungen $V_i = V_i(z)$ $(i = 1, 2 \ldots n)$ ist gleich dem Freiheitsgrad der kinematischen Kette.

Wir wählen für die ersten drei unabhängigen Parameter die Verschiebungen des Querschnitts in den Richtungen x und y und dessen Verdrehung um den beliebigen Punkt P (Fig. 1):

$$V_1 = \xi_0, \qquad V_2 = \eta_0, \qquad V_3 = \varphi_P. \tag{1}$$

Die übrigen $n-3$-Verschiebungen beschreiben die Formänderung des Querschnittes in seiner Ebene (siehe z. B. das Verschiebungsdiagramm in der Fig. 2a) für den Fall, daß wir die vollkommene Starrheit der Platten in der Querschnittsebene und ihre gelenkige Verbindung in den Knoten voraussetzen.

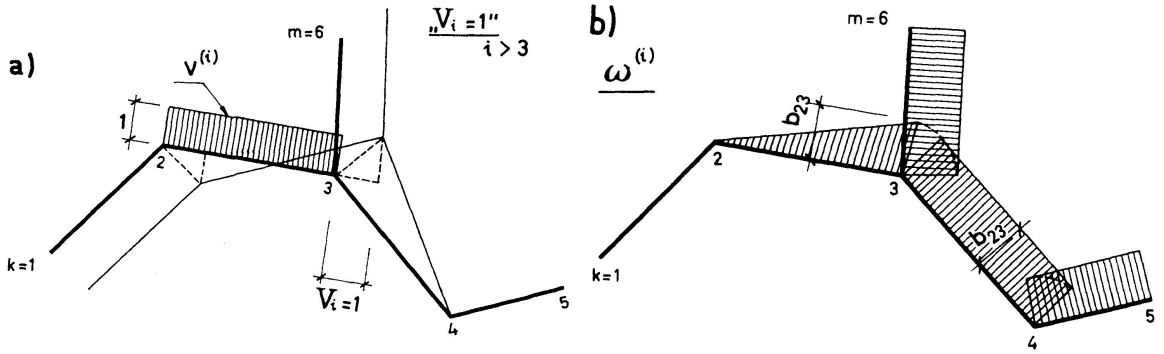


Fig. 2.

Die Verschiebung des beliebigen Punktes in Richtung der Tangente an die Profilmittellinie können wir in der folgenden Form ausdrücken:

$$v(z,s) = \sum_{i=1}^{n} V_i(z)\, v^{(i)}(s). \tag{2}$$

Die Funktion $v^{(i)}$ stellt die Verschiebungen v für $V_i = 1$ dar (Fig. 2a).

Insbesondere ist:

$$v^{(1)} = -\sin\alpha, \qquad v^{(2)} = \cos\alpha, \qquad v^{(3)} = h_P, \tag{3}$$

wo α der Winkel ist, welchen die positive y-Achse mit der Profilmittellinie einschließt und h_p der Abstand der Tangente an die Profilmittellinie von P ist.

Aus der zweiten Voraussetzung folgt:

$$\frac{\partial w}{\partial s} = -\frac{\partial v}{\partial z} \quad \text{bzw.} \quad w(z,s) = -\int_0^s \frac{\partial v}{\partial s} ds + W_0(z).$$

Durch Einsetzen des Ausdrucks (2) für v erhalten wir:

$$w(z,s) = -\sum_{i=0}^{n} V_i'(z)\, \omega^{(i)}(s) \tag{4}$$

wo: $$\omega^{(0)} = 1, \qquad \omega^{(i)} = \int_0^s v^{(i)} ds \quad \text{und} \quad V_0' = -W_0(z) \tag{5a,b,c}$$

sind. Insbesondere ist:

$$\omega^{(1)} = x, \qquad \omega^{(2)} = y, \qquad \omega^{(3)} = \int_0^s h_P ds = \omega_P. \tag{6}$$

Wir wählen ein System orthogonaler Funktionen $\omega_\Theta^{(i)}(s)$, $i = 0, 1, 2 \ldots n$:

$$\omega_\Theta^{(0)} = 1, \qquad \omega_\Theta^{(1)} = x, \qquad \omega_\Theta^{(2)} = y \tag{7}$$

und

$$\omega_\Theta^{(i)} = \omega^{(i)} + \sum_{j=0}^{i-1} \beta_{ij}\, \omega_\Theta^{(j)}, \qquad i = 3, 4 \ldots n. \tag{8}$$

Aus der Orthogonalitätsbedingung erhalten wir:

$$\beta_{ij} = \frac{\int_s t\,\omega^{(i)}\,\omega_\Theta^{(j)}\,ds}{\int_s t\,[\omega_\Theta^{(j)}]^2\,ds}, \tag{9}$$

wobei sich die bestimmten Integrale im Zähler und Nenner über die gesamte Länge der Profilmittellinie erstrecken.

Statt $v^{(i)}$ erhalten wir:

$$\begin{aligned} v_\Theta^{(i)} &= v^{(i)}, && \text{für} \quad i = 1,2 \\ \text{und} \qquad v_\Theta^{(i)} &= v^{(i)} + \sum_{j=0}^{i-1} \beta_{ij}\, v_\Theta^{(j)}, && \text{für} \quad i = 3,4\ldots n. \end{aligned} \tag{10}$$

Den neu eingeführten Funktionen entsprechen die neuen, verallgemeinerten Parameter $\Theta_i(z)$:

$$\begin{aligned} \Theta_i &= V_i, && \text{für} \quad i = 1,2 \\ \text{und} \qquad \Theta_i &= V_i + \sum_{j=1}^{i-1} \beta_{ij}\,\Theta_j, && \text{für} \quad i = 3,4\ldots n. \end{aligned} \tag{11}$$

Man kann leicht ersehen, daß $\omega_\Theta^{(3)} = \Omega$ sie sog. normierte sektorielle Koordinate und $v^{(3)} = h$ der Abstand der Tangente an die Profilmittellinie vom Schubmittelpunkt D ist.

Mit den neu eingeführten Funktionen erhalten wir statt der Ausdrücke (2) und (4) für v und w:

$$v(z,s) = \sum_{i=0}^{n} \Theta_i(z)\, v_\Theta^{(i)}(s), \tag{12}$$

$$w(z,s) = -\sum_{i=0}^{n} \Theta_i'(z)\, \omega_\Theta^{(i)}(s), \tag{13}$$

wobei $$v_\Theta^0 = 0 \quad \text{ist.} \tag{14}$$

Die Parameter Θ_i bestimmen vollständig die Verschiebungen der Knoten $k\,(k = 1,2\ldots n)$ in der Ebene des Querschnittes, wobei wir auch die Enden der Profilmittellinie zu den Knoten zählen (siehe Fig. 1).

Für die Verschiebung u in Richtung der inneren Normalen zur Mittelfläche führen wir eine Näherungslösung von der Form ein:

$$u(z,s) = \sum_{i=0}^{n} \Theta_i(z)\, u_\Theta^{(i)}(s) + \sum_{k=1}^{m} \Phi_k(z)\, u_\Phi^{(k)}(s) + u_p(z,s). \tag{15}$$

In diesem Ausdruck bedeuten Φ_k die unbekannten, durch die Formänderung des Querschnittes hervorgerufenen Knotenverdrehungen und $u_\Theta^{(i)}$ sowie $u_\Phi^{(k)}$ bekannte, durch die folgenden Ausdrücke bestimmte Funktionen:

$$\begin{aligned} u_\Theta^{(0)} &= 0, \quad u_\Theta^{(1)} = \cos\alpha, \quad u_\Theta^{(2)} = \sin\alpha, \quad u_\Theta^{(3)} = h_n, \\ u_\Theta^{(i)} &= \sum_{k=1}^{m} \sum_{r=1}^{R} \alpha_{kr}^{(i)}\, u_\Theta^{(kr)}, \qquad i = 4,5\ldots n, \end{aligned} \tag{16}$$

$$u_{\Phi}^{(kr)} = \sum_{r=1}^{R} u_{\Phi}^{(kr)} \tag{17}$$

und

$$u_p = \sum_{r=1}^{R} u_{kr,p}\,. \tag{18}$$

Die in den Ausdrücken (15) bis (17) neu eingeführten Bezeichnungen haben die folgende Bedeutung:

h_n: Abstand der Normalen zur Mittelfläche vom Schubmittelpunkt D;

$\alpha_{kr}^{(i)}$: Projektion der Verschiebung des Knotens k in Richtung der Normalen auf die Platte kr, welche die Knoten k und r verbindet, für den Zustand $\Theta_i = 1$, $(i = 4, 5 \ldots n)$;

$u_{\Theta}^{(kr)}$: definiert die elastische Fläche des unendlich langen, an den Rändern k und r (Fig. 3) eingespannten Plattenstreifens für den Fall, daß die Kante k die Einheitssenkung erleidet.

$$u_{\Theta}^{(kr)} = \frac{s_{rk}}{b_{kr}}\left[1 - \frac{s_{kr}(s_{kr} - s_{rk})}{b_{kr}^2}\right], \tag{19}$$

R: Gesamtzahl, $r = 1, 2 \ldots R$ der an den Knoten k angeschlossenen Platten.

Die im Ausdruck (17) angeführte Funktion

$u_{\Phi}^{(kr)}$: definiert die elastische Fläche des unendlich langen, an den Rändern k und r eingespannten Plattenstreifens für den Fall, daß die Kante k (Fig. 4) die Einheitsverdrehung erfährt.

$$u_{\Phi}^{(kr)} = -\frac{s_{kr}\, s_{rk}^2}{b_{kr}^2}. \tag{20}$$

Die Funktion

$u_{kr,p}$ definiert die elastische Fläche des erwähnten Plattenstreifens zufolge der in der Richtung der Normalen zur Mittelfläche wirkenden, gegebenen Belastung $\overline{p}_n$.

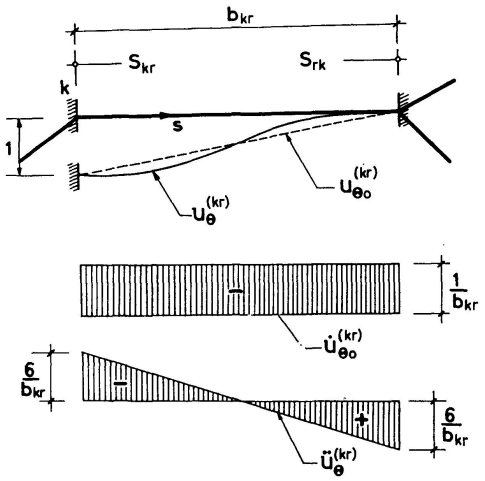


Fig. 3.

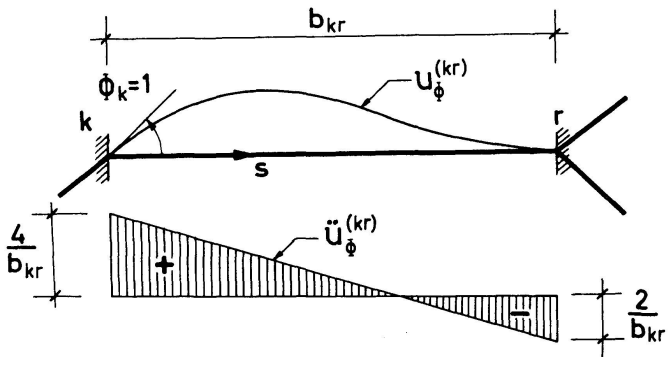


Fig. 4.

3. Schnittkräfte. Gleichgewichtsbedingungen. Grundlegende Differentialgleichungen des Problems und Randbedingungen

Hinsichtlich der Schnittkräfte wollen wir folgende Vereinfachungen annehmen:

a) Die Biegungsmomente m_z in der Längsrichtung werden vernachlässigt, ebenso wie der Einfluß der Krümmung u'' in der Längsrichtung auf die Biegungsmomente m_s in der Querrichtung.

b) Die Torsionsmomente m_{zs} zwischen je zwei Knoten mögen konstant und proportional der spezifischen Verdrehung der diese Knoten verbindenden Sehne sein.

Für die Schnittkräfte n_z, m_{zs} und m_s erhalten wir, unter Berücksichtigung dieser Vereinfachungen sowie der Voraussetzungen über die Verformung des Stabes und des *Hooke*schen Gesetzes:

$$n_z = E' t w', \qquad m_{zs} = E' \frac{t^3}{12}(1-\nu)\,\dot{u}_0', \qquad m_s = -E' \frac{t^3}{12}\ddot{u}, \tag{21}$$

wo $\dot{u}_0$ die Verdrehung der Sehne zwischen zwei benachbarten Knoten und

$$E' = \frac{E}{1-\nu^2} \qquad \text{ist.}$$

Durch Einsetzen der Ausdrücke (15) und (13) für u und w in die Gleichung (21) erhalten wir:

$$\begin{aligned} n_z &= -E' t \sum_{i=0}^{n} \Theta_i'' \,\omega_\Theta^{(i)}, \\ m_{zs} &= -\frac{E' t^3}{12}(1-\nu) \sum_{i=0}^{n} \Theta_i' \,\dot{u}_{\Theta 0}^{(i)}, \\ m_s &= -\frac{E' t^3}{12}\left(\sum_{i=0}^{n} \Theta_i \,\ddot{u}^{(i)} + \sum_{k=1}^{m} \Phi_k \,\ddot{u}_\Phi^{(k)} \right) + m_{s,p}, \end{aligned} \tag{22}$$

wo
$$\dot{u}_{\Theta 0}^{(0)} = \dot{u}_{\Theta 0}^{(1)} = \dot{u}_{\Theta 0}^{(2)} = 0, \qquad \dot{u}_{\Theta 0}^{(3)} = 1, \qquad \dot{u}_{\Theta 0}^{(i)} = \sum_{k=1}^{m} \sum_{r=1}^{R} \alpha_{kr}^{(i)} \,\dot{u}_{\Theta 0}^{(kr)} \tag{23}$$

und
$$m_{s,p} = -E' \frac{t^3}{12} \dot{u}_p' \tag{24}$$

bedeuten. Für $\dot{u}_{\Theta 0}^{(kr)}$ (Fig. 3) erhalten wir:

$$\dot{u}_{\Theta 0}^{(kr)} = -\frac{1}{b_{kr}}. \tag{25}$$

Wir schneiden aus dem Stabe ein durch die Querschnitte z_0 und $z_0 + dz$ begrenztes Element heraus und lassen auf dasselbe die entsprechenden Kräfte wirken (Fig. 5). Die beliebige Belastung mit den Komponenten $\overline{p}_z$, $\overline{p}_s$ und $\overline{p}_n$ greift in den Punkten der Mittelfläche an.

Die Gleichgewichtsbedingungen stellen wir unter Anwendung des Prinzips der virtuellen Verschiebungen auf:

$$\overline{W} + \overline{U} = 0, \tag{26}$$

wo $\overline{W}$ die Arbeit der äußeren und $\overline{U}$ die Arbeit der inneren Kräfte bei den gegebenen virtuellen Verschiebungen der Punkte des Elementes sind.

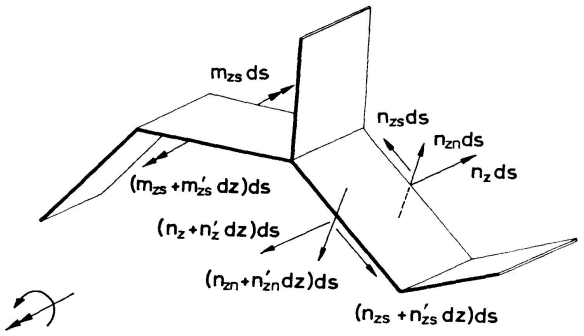


Fig. 5.

Die Punkte der Profilmittellinie des Querschnittes $z=z_0$ erfahren die virtuellen Verschiebungen $\overline{u}$, $\overline{v}$ und $\overline{w}$. Für den Querschnitt $z=z_0+dz$ betragen diese Verschiebungen $\overline{u}+\overline{u}'\,dz$, $\overline{v}+\overline{v}'\,dz$ und $\overline{w}=\overline{w}'\,dz$.

Für die Arbeiten $\overline{W}$ und $\overline{U}$, bezogen auf die Einheit der Stablänge, erhalten wir:

$$\overline{W} = \int_s (n_{zn}\,\overline{u} + n_{zs}\,\overline{v} + n_z\,\overline{w} - m_{zs}\,\dot{\overline{u}})'\,ds + \int_s (\overline{p}_n\,\overline{u} + \overline{p}_s\,\overline{v} + \overline{p}_z\,\overline{w})\,ds,$$

$$\overline{U} = -\int_s (n_z\,\overline{w}' - 2\,m_{zs}\,\dot{\overline{u}}' + m_s\,\ddot{\overline{u}})\,ds.$$

Durch Einsetzen dieser Ausdrücke in die Gleichung (26) erhalten wir:

$$\begin{aligned}&\int_s (n'_{zn}\,\overline{u} + n'_{zs}\,\overline{v} + n'_z\,\overline{w} - m'_{zs}\,\dot{\overline{u}} + n_{zn}\,\overline{u}' + n_{zs}\,\overline{v}' + m_{zs}\,\dot{\overline{u}}' + m_s\,\ddot{\overline{u}})\,ds \\ &\quad + \int_s (\overline{p}_n\,\overline{u} + \overline{p}_s\,\overline{v} + \overline{p}_z\,\overline{w})\,ds = 0.\end{aligned} \tag{27}$$

Für die virtuellen Verschiebungen $\overline{u}$, $\overline{v}$ und $\overline{w}$ wählen wir Ausdrücke von der gleichen Form wie die Ausdrücke (12), (13) und (15) für $u_p \equiv 0$, jedoch führen wir statt Θ_i und Φ_k die Parameter $\overline{\Theta}_i$ und $\overline{\Phi}_k$ als beliebige Funktionen der Koordinate z ein. Diese sind, allgemein genommen, unabhängig von der wirklichen Belastung des Stabes.

Auf diese Weise erhalten wir:

$$\begin{aligned}&\sum_{i=0}^{n} \overline{\Theta}_i \Big[\int_s (n'_{zn}\,u^{(i)}_{\Theta} + n'_{zs}\,v^{(i)}_{\Theta} - m'_{zs}\,\dot{u}^{(i)}_{\Theta} + m_s\,\ddot{u}^{(i)}_{\Theta})\,ds + \int_s (\overline{p}_s\,v^{(i)}_{\Theta} + \overline{p}_n\,u^{(i)}_{\Theta})\,ds\Big] \\ &+ \sum_{i=0}^{n} \overline{\Theta}'_i \Big[\int_s (-n'_z\,\omega^{(i)}_{\Theta} + n_{zn}\,u^{(i)}_{\Theta} + n_{zs}\,v^{(i)}_{\Theta} + m_{zs}\,\dot{u}^{(i)}_{\Theta})\,ds - \int_s \overline{p}_z\,\omega^{(i)}_{\Theta}\,ds\Big] \\ &+ \sum_{k=1}^{m} \overline{\Phi}_k \Big[\int_s (n'_{zn}\,u^{(k)}_{\Phi} - m'_{zs}\,\dot{u}^{(k)}_{\Phi} + m_s\,\ddot{u}^{(k)}_{\Phi})\,ds + \int_s \overline{p}_n\,u^{(k)}_{\Phi}\,ds\Big] \\ &+ \sum_{k=1}^{m} \overline{\Phi}'_k \Big[\int_s m_{zs}\,\dot{u}^{(k)}_{\Phi} + n_{zn}\,u^{(k)}_{\Phi}\Big]\,ds = 0.\end{aligned} \tag{28}$$

Die Befriedigung dieser Gleichung erfordert, daß die vier Ausdrücke in den eckigen Klammern für jedes $i\,(i=0,1,2\ldots n)$ und für jedes $k\,(k=1,2\ldots m)$ Null sein müssen.

Die Nullsetzung dieser Ausdrücke ergibt, nach dem Einsetzen der Gleichungen (22) für die Größen n_z, m_{zs} und m_s, das folgende System von Gleichungen:

$$\begin{aligned}
\int_s (n'_{zn}\,u^{(i)}_{\Theta}+n'_{zs}\,v^{(i)}_{\Theta})\,ds &= E'\,[\sum_{j=0}^{n}(\ddot{b}_{ij}\Theta_j-2\,\kappa\dot{b}^0_{ij}\Theta''_j)+\sum_{l=1}^{m}\ddot{c}_{il}\Phi_l]\\
&\quad-\int_s(\bar{p}_s\,v^{(i)}_{\Theta}+\bar{p}_n\,u^{(i)}_{\Theta}+m_{s,p}\,\ddot{u}^{(i)}_{\Theta})\,ds,\\
\int_s (n_{zn}\,u^{(i)}_{\Theta}+n_{zs}\,v^{(i)}_{\Theta})\,ds &= E'\,[-a_{ii}\Theta'''_i+2\,\kappa\sum_{j=0}^{n}\dot{b}^0_{ij}\Theta'_j]+\int_s\bar{p}_z\,\omega^{(i)}_{\Theta}\,ds,\\
&\qquad i=0,1,2\ldots n, \qquad\qquad (29\,\text{a—d})\\
\int_s n'_{zn}\,u^{(k)}_{\Phi}\,ds &= E'\,[\sum_{j=0}^{n}\ddot{c}_{kj}\Theta_j+\sum_{l=1}^{m}\ddot{d}_{kl}\Phi_l]-\int_s(m_{s,p}\,\ddot{u}^{(k)}_{\Phi}+\bar{p}_n\,u^{(k)}_{\Phi})\,ds,\\
\int_s n_{zn}\,u^{(k)}_{\Phi}\,ds &= 0,\\
&\qquad k=1,2\ldots m.
\end{aligned}$$

In diesen Gleichungen bedeuten:

$$\kappa=\frac{G}{E'},\quad a_{ii}=\int_s t\,[\omega^{(i)}_{\Theta}]^2\,ds,\quad \dot{b}^0_{ij}=\frac{1}{12}\int_s t^3\,\dot{u}^{(i)}_{\Theta}\,\dot{u}^{(j)}_{\Theta 0}=\frac{1}{12}\int_s t^3\,\dot{u}^{(i)}_{\Theta 0}\,\dot{u}^{(j)}_{\Theta 0}\,ds, \quad (30\,\text{a—c})$$

$$\ddot{b}_{ij}=\frac{1}{12}\int_s t^3\,\ddot{u}^{(i)}_{\Theta}\,\ddot{u}^{(j)}_{\Theta}\,ds,\qquad \ddot{c}_{il}=\frac{1}{12}\int_s t^3\,\ddot{u}^{(i)}_{\Theta}\,\ddot{u}^{(l)}_{\Theta}\,ds, \quad (30\,\text{d, e})$$

$$\ddot{c}_{kj}=\frac{1}{12}\int_s t^3\,\ddot{u}^{(k)}_{\Phi}\,\ddot{u}^{(j)}_{\Theta}\,ds,\qquad \ddot{d}_{kl}=\frac{1}{12}\int_s t^3\,\ddot{u}^{(k)}_{\Phi}\,\ddot{u}^{(l)}_{\Phi}\,ds. \quad (30\,\text{f, g})$$

Die bestimmten Integrale der Ausdrücke (30 b–g) erhalten wir, unter Berücksichtigung der Gleichungen (16), (23) für $i=4,5\ldots n$ sowie (17) als lineare Kombinationen von Größen (Fig. 3 und 4):

$$\begin{aligned}
\int \dot{u}^{(kr)}_{\Theta 0}\,\dot{u}^{(kr)}_{\Theta 0}\,ds &= -\int \dot{u}^{(kr)}_{\Theta 0}\,u^{(rk)}_{\Theta 0}\,ds = \frac{1}{b_{kr}},\\
\int \ddot{u}^{(kr)}_{\Theta}\,u^{(kr)}_{\Theta}\,ds &= -\int \ddot{u}^{(kr)}_{\Theta 0}\,u^{(rk)}_{\Theta 0}\,ds = \frac{12}{b_{kr}},\\
\int \ddot{u}^{(kr)}_{\Theta}\,\ddot{u}^{(kr)}_{\Phi}\,ds &= -\int \ddot{u}^{(kr)}_{\Theta}\,\ddot{u}^{(rk)}_{\Phi}\,ds = -\int \ddot{u}^{(kr)}_{\Phi}\,\ddot{u}^{(rk)}_{\Theta}\,ds = -\frac{6}{b_{kr}},\\
\int \ddot{u}^{(kr)}_{\Phi}\,u^{(kr)}_{\Phi}\,ds &= \frac{4}{b_{kr}},\qquad \int \ddot{u}^{(kr)}_{\Phi}\,\ddot{u}^{(rk)}_{\Phi}\,ds = -\frac{2}{b_{kr}},
\end{aligned}\qquad (31)$$

wobei die bestimmte Integration in den Grenzen $s_{kr}=0$ und $s_{kr}=b_{kr}$ ausgeführt wurde.

Durch Elimination erhalten wir aus dem Gleichungssystem (29):

$$a_{ii}\Theta_i'''' = \frac{1}{E'}A_{i0}, \qquad \text{für } i = 0, 1, 2 \tag{32}$$

und

$$a_{ii}\Theta_i'''' + \sum_{j=3}^{n}(-4\kappa \dot{b}_{ij}^{0}\Theta_j'' + \ddot{b}_{ij}\Theta_j) + \sum_{l=1}^{m}\ddot{c}_{il}\Phi_l = \frac{1}{E'}A_{i0},$$
$$\sum_{j=3}^{n}\ddot{c}_{kj}\Theta_j + \sum_{l=1}^{m}\ddot{d}_{kl}\Phi_l = \frac{1}{E'}B_{k0}, \tag{33}$$
$$i = 3, 4 \ldots n, \qquad k = 1, 2 \ldots m,$$

wo:

$$A_{i0} = \int_s m_{s,p}\ddot{u}_{\Theta}^{(i)}\,ds + \int_s (\bar{p}_n u_{\Theta}^{(i)} + \bar{p}_s v_{\Theta}^{(i)} + \bar{p}_z' w_{\Theta}^{(i)})\,ds \tag{34}$$

und

$$B_{k0} = \int_s m_{s,p}\ddot{u}_{\Phi}^{(k)}\,ds + \int_s \bar{p}_n u_{\Phi}^{(k)}\,ds$$

sind.

Es kann gezeigt werden, daß sich diese Glieder auch in der folgenden Form ausdrücken lassen[3]):

$$A_{i0} = \sum_{k=1}^{m}\sum_{r=1}^{R} p_{kr}\alpha_{kr}^{(i)} + \int_s (\bar{p}_s v_{\Theta}^{(i)} + \bar{p}_z' \omega_{\Theta}^{(i)})\,ds, \tag{35}$$
$$B_{k0} = \sum_{r=1}^{R} m_k,$$

wo (Fig. 6) p_{kr} die Knotenlast im Knoten k und m_{kr} das Einspannmoment des Plattenstreifens kr in diesem Knoten zufolge der gegebenen Belastung $\bar{p}_n$ sind.

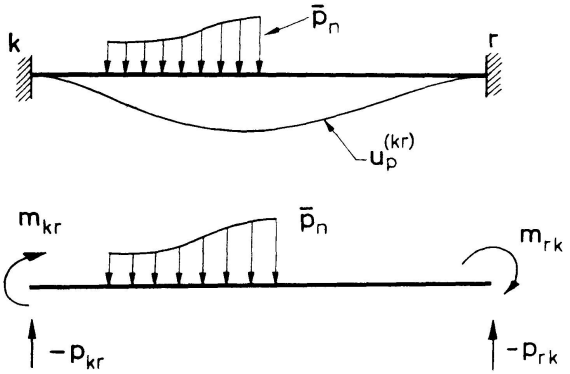


Fig. 6.

In Hinblick auf die Bedeutung der Parameter $V_i = \Theta_i$ für $i = 0, 1$ und 2 [Gleichungen (1)] sowie unter Berücksichtigung der Werte $\omega^{(0)}$, $\omega^{(1)}$ und $\omega^{(2)}$ [Gleichungen (5a) und (6)], ferner, weil zufolge Gleichung (5c) $V_0' = -W_0(z)$ ist, können wir die Gleichungen (32) in der folgenden Form anschreiben:

$$E'\,F\,W_0'' = -p_z, \qquad E'\,I_{xx}\xi_0'''' = p_x + m_x', \qquad E'\,I_{yy}\eta_0'''' = p_y + m_y', \tag{36}$$

wo:

$$p_z = \int_s \bar{p}_z\,ds, \quad p_x = \int_s (-\bar{p}_n\sin\alpha + \bar{p}_s\cos\alpha)\,ds, \quad m_x = \int_s \bar{p}_z x\,ds,$$
$$p_y = \int_s (\bar{p}_n\cos\alpha - \bar{p}_s\sin\alpha)\,ds, \qquad m_y = \int_s \bar{p}_z y\,ds \tag{37}$$

sind.

Die Gleichungen (36) sind offenbar die Differentialgleichungen für die Axial-

[3]) Siehe [5], Kapitel 4.

und Biegungsbeanspruchung des dünnwandigen Stabes mit in ihren Ebenen nichtdeformierbaren Querschnitten.

Die Randbedingungen für das Gleichungssystem (34) können durch Verschiebungen, durch Kräfte oder durch beide Arten von Einwirkungen gegeben sein.

Die Verschiebungen der Stabenden müssen in der gleichen Form gegeben sein wie die Verschiebungen u, v und w der Punkte der Mittelfläche. Die Randbedingungen können auf die Ausdrücke:

$$\Theta_i = \Theta_i^*, \qquad \Theta_i' = \Theta_i^{*\prime} \tag{38}$$

zurückgeführt werden, wobei Θ_i^* und $\Theta_i^{*\prime}$ Parameter sind, welche durch die gegebenen Verschiebungen der Punkte des Endquerschnitts bestimmt werden.

Die Randbedingungen durch die Kräfte stellen wir unter Anwendung des Prinzips der virtuellen Verschiebungen auf:

$$\int_s [(n_{zn} - n_{zn}^*)\,\bar{u} + (n_{zs} - n_{zs}^*)\,\bar{v} + (n_z - n_z^*)\,\bar{w} - (m_{zs} - m_{zs}^*)\,\dot{\bar{u}}]\,ds = 0.$$

Die Größen n_{zn}^*, n_{zs}^* und n_z^* sind die äußeren, am Endquerschnitt angreifenden Kräfte und m_{zs}^* ist das äußere, verteilte Torsionsmoment.

Durch Einsetzen der Ausdrücke (22) für n_z und m_{zs} und Verwendung derselben Ausdrücke für die virtuellen Verschiebungen wie vorher, erhalten wir, nach der Elimination der Kräfte n_{zn} und n_{zs}:

$$a_{ii}\Theta_i''' - 4\kappa \sum_{j=3}^{n} \dot{b}_{ij}^0 \Theta_j' = -\frac{1}{E'} Q_i^*, \qquad a_{ii}\Theta_i'' = -\frac{1}{E'} M_i^*, \tag{39}$$

wo:

$$\begin{aligned} Q_i^* &= -\int_s \bar{p}_z \omega_\Theta^{(i)}\,ds + \int_s (n_{zn}^* u_{\Theta 0}^{(i)} + n_{zs}^* v_\Theta^{(i)} - m_{zs}^* \dot{u}_{\Theta 0})\,ds, \\ M_i^* &= \int_s n_z^* \omega_\Theta^{(i)}\,ds \qquad \text{sind.} \end{aligned} \tag{40}$$

Die Lösung des Problems wird auf die Integration des Systems der Differentialgleichungen (34) zurückgeführt.

Die unbekannten Größen Θ_i und Φ_k werden als Komponenten der Spaltenvektoren $\boldsymbol{\Theta}$ und $\boldsymbol{\Phi}$ aufgefaßt:

$$\boldsymbol{\Theta} = \begin{Vmatrix} \Theta_3 \\ \Theta_4 \\ \vdots \\ \Theta_r \end{Vmatrix}, \qquad \boldsymbol{\Phi} = \begin{Vmatrix} \Phi_1 \\ \Phi_2 \\ \vdots \\ \Phi_m \end{Vmatrix}. \tag{41}$$

Aus den Koeffizienten a_{ii} bilden wir die Diagonalmatrix $\boldsymbol{A}$ und aus den Koeffizienten $\dot{b}_{ij}^0$ und $\ddot{b}_{ij}$ die quadratischen Matrizen $\dot{\boldsymbol{B}}^0$ und $\ddot{\boldsymbol{B}}$ von der Ordnung $n-2$. Ferner bilden wir aus den Koeffizienten $\ddot{c}_{il}$ die Rechtecksmatrix $\ddot{\boldsymbol{C}}$ mit $n-2$ Zeilen und m Spalten und aus den Koeffizienten $\ddot{d}_{kl}$ die quadratische Matrix $\ddot{\boldsymbol{D}}$ von der Ordnung m.

Das Gleichungssystem können wir nun in der folgenden Form schreiben:

$$\boldsymbol{A}\,\boldsymbol{\Theta}'''' - 4\kappa \dot{\boldsymbol{B}}^0\,\boldsymbol{\Theta}'' + \ddot{\boldsymbol{B}}\,\boldsymbol{\Theta} + \ddot{\boldsymbol{C}}\,\boldsymbol{\Phi} = \frac{1}{E'}\boldsymbol{A}_0, \qquad \tilde{\ddot{\boldsymbol{C}}}\,\boldsymbol{\Theta} + \ddot{\boldsymbol{D}}\,\boldsymbol{\Phi} = \frac{1}{E'}\boldsymbol{B}_0, \tag{42}$$

wo $\tilde{\ddot{C}}$ die transponierte Matrix von $\ddot{C}$ ist und

$$\boldsymbol{A}_0 = \left\| \begin{matrix} A_{30} \\ A_{40} \\ \vdots \\ A_{n0} \end{matrix} \right\|, \qquad \boldsymbol{B}_0 = \left\| \begin{matrix} B_{10} \\ B_{20} \\ \vdots \\ B_{m0} \end{matrix} \right\| \tag{43}$$

sind.

Durch Elimination aus dem System (42) erhalten wir[4]):

$$\boldsymbol{A}\,\boldsymbol{\Theta}'''' - 4\kappa \dot{\boldsymbol{B}}^0\,\boldsymbol{\Theta}'' + \boldsymbol{H}\,\boldsymbol{\Theta} = \frac{1}{E'}\boldsymbol{H}_0, \tag{44}$$

wo $$\boldsymbol{H} = \ddot{\boldsymbol{B}} - \ddot{\boldsymbol{C}}\,\ddot{\boldsymbol{D}}^{-1}\,\tilde{\ddot{\boldsymbol{C}}} \quad \text{und} \quad \boldsymbol{H}_0 = \boldsymbol{A}_0 - \ddot{\boldsymbol{C}}\,\ddot{\boldsymbol{D}}^{-1}\,\boldsymbol{B}_0 \tag{45}$$

sind.

Die Randbedingungen (38) und (39) lauten in Matrizenform:

$$\boldsymbol{\Theta} = \boldsymbol{\Theta}^*, \qquad \boldsymbol{\Theta}' = \boldsymbol{\Theta}^{*\prime} \tag{46}$$

und $$\boldsymbol{A}\,\boldsymbol{\Theta}''' - 4\kappa \dot{\boldsymbol{B}}^0\,\boldsymbol{\Theta}' = \frac{1}{E'}\boldsymbol{Q}^*, \qquad \boldsymbol{A}\,\boldsymbol{\Theta}'' = -\frac{1}{E'}\boldsymbol{M}^*, \tag{47}$$

wo $\boldsymbol{Q}^*$ und $\boldsymbol{M}^*$ Vektoren mit den Komponenten Q_i^* und M_i^* sind.

Liste der Bezeichnungen

b	Breite der einzelnen Platte
e	Abstand von der Mittelfläche in Richtung der Normalen
h	Abstand der Tangente zur Profilmittellinie von der Drehachse
h_n	Abstand der Normalen zur Profilmittellinie von der Drehachse
m_s, m_z	Biegemomente der einzelnen Platte
m_{sz}	Torsionsmoment der einzelnen Platte
m_x, m_y	Äußere verteilte Biegemomente
n_s, n_z	Normalkräfte der einzelnen Platte
n_{zs}	Schubkraft der einzelnen Platte
n_{sn}, n_{zn}	Querkräfte der einzelnen Platte
$\overline{p}_n$, $\overline{p}_s$, $\overline{p}_z$	Flächenbelastungen in den Richtungen n, s, z
p_x, p_y, p_z	Linienbelastungen in den Richtungen x, y, z
s	Koordinate der Profilmittellinie
t	Wandstärke
u	Verschiebung der Punkte der Mittelfläche in Richtung zu ihrer Normalen
v	Verschiebung der Punkte der Mittelfläche in Richtung der Tangente zur Profilmittellinie

[4]) Die allgemeine Lösung dieser Gleichung wird in der Publikation [5], Kapitel 5, gezeigt.

w	Verschiebung in Richtung der Stabachse
x, y, z	Kartesische Koordinaten der Punkte der Mittelfläche
C	Schwerpunkt
D	Schubmittelpunkt
E	Elastizitätsmodul
F	Querschnittsfläche
G	Schubmodul
$I_{xx} = \int_F x^2 t\, ds$	Flächenträgheitsmoment
$I_{yy} = \int_F y^2 t\, ds$	Flächenträgheitsmoment
U, V, W, Θ	Verschiebungsparameter
$\overline{U}$	Arbeit der virtuellen inneren Kräfte
$\overline{W}$	Arbeit der virtuellen äußeren Kräfte
α	Winkel
γ_{zs}	Gleitung im Punkte der Mittelfläche
$\epsilon_n, \epsilon_s, \epsilon_z$	Dehnungen der Mittelfläche
ν	*Poisson*sche Zahl
ξ, η	Verschiebungskomponenten in den Richtungen x und y
φ	Verdrehung des Stabes
ω	Sektorielle Koordinate, Einheitsverwölbung
Ω	Normierte sektorielle Koordinate
Φ	Verdrehung des Knotens

Literatur

A. Mitteilungen der Technischen Kommission der Schweizer Stahlbau-Vereinigung, Verlag Schweizer Stahlbau Vereinigung, Zürich

[1] C. F. Kollbrunner und N. Hajdin: Die St.-Venantsche Torsion, Heft 26 (Sept. 1963).

[2] C. F. Kollbrunner und N. Hajdin: Wölbkrafttorsion dünnwandiger Stäbe mit offenem Profil, Teil I, Heft 29 (Okt. 1964).

[3] C. F. Kollbrunner und N. Hajdin: Wölbkrafttorsion dünnwandiger Stäbe mit offenem Profil, Teil II, Heft 30 (März 1965).

[4] C. F. Kollbrunner und N. Hajdin: Wölbkrafttorsion dünnwandiger Stäbe mit geschlossenem Profil, Heft 32 (Juni 1966).

B. Andere Publikationen

[5] C. F. Kollbrunner und N. Hajdin: Dünnwandige Stäbe mit in ihren Ebenen deformierbaren Querschnitten. Theorie der Faltwerke nach der Verschiebungsmethode. Institut für bauwissenschaftliche Forschung, Heft 1, Januar 1968. Verlag Leemann, Zürich.

[6] C. F. Kollbrunner und N. Hajdin: Betrachtungen zur Theorie der dünnwandigen Stäbe und ihre Anwendung im Bauwesen. Schweiz. Bauzeitung Nr. 41 (84. Jg.), 1966, S. 715—719.

[7] S. U. Benscoter: A Theory of Torsion Bending for Multicell Beams. Journ. of Appl. Mechanics, Bd. 21, 1954, H. 1, S. 25—34.

[8] A. A. Umanski: Torsion und Biegung dünnwandiger Luftfahrtkonstruktionen (Aviakonstrukcij). Oborongis, 1939, Moskau (russisch).
[9] R. Heilig: Beitrag zur Theorie der Kastenträger beliebiger Querschnittsform. Stahlbau 1961, H. 11, S. 333—349.
[10] W. Z. Wlassow: Dünnwandige elastische Stäbe. Fismatgis, Moskau, 1959 (russisch). Deutsche Fassung von E. Duda, VEB Verlag für Bauwesen, Berlin 1964.

Zusammenfassung

Der Artikel bezieht sich auf die Theorie des Faltwerks, in welcher außer den Biegemomenten in der Querrichtung zum Unterschied der klassischen Faltwerkstheorie auch die Torsionsmomente berücksichtigt werden.

Dank des Umstandes, daß für die grundlegenden Unbekannten die Verschiebungsparameter eingeführt werden, ermöglicht diese Theorie eine relativ einfache Berechnung.

Im Unterschied zum in der Faltwerkstheorie üblichen Verfahren der Zerlegung des Systems in die einzelnen Platten, wird in der gebrachten Theorie die Deformation der Stab-Schale einheitlich für das ganze Tragwerk beschrieben. Man erhält schließlich ein System von Differentialgleichungen, welches ebenso wie die Randbedingungen in Matrizenform dargestellt wird.

Summary

The article treats the theory of folded structures which, contrary to the classical theory, takes into account also the torsional moments, besides the transversal bending moments.

This theory permits a relatively easy calculation in introducing for the basic unknowns the deflection parameters.

Contrary to the ordinary procedure of decomposing the system into individual plates, the present theory explains the deformation of the beam-shell uniformly for the whole structure. Thus, we receive finally a system of differential equations which can be written in form of matrices in the same way as the boundary conditions.

Résumé

L'article traite de la théorie des voûtes polygonales qui, contrairement à la théorie classique, tient également compte du moment de torsion en plus du moment de flexion transversal.

Cette théorie permet un calcul relativement facile, en introduisant pour les inconnues de base les paramètres de déplacement.

Contrairement au procédé habituel de décomposition des voûtes polygonales en plaques isolées, la présente théorie décrit la déformation de la poutre-coque uniformément pour toute la construction. On obtient ainsi finalement un système d'équations différentielles, qui peut être mis sous la forme de matrice, tout comme les conditions de bord.

The Approximation of Stability Effects on Frames

Une approximation des facteurs influant sur la stabilité de portiques

Näherungen für Stabilitätseinflüsse an Rahmen

ALFRED KORN
Assistant Professor of Civil Engineering, University of Kentucky, Lexington, Ky., U.S.A.

Introduction

The inelastic behavior of multi-story frameworks can be appreciably influenced by stability effects. An approximate method for computing the maximum load carrying capacity of inelastic frames has been proposed by MERCHANT [1]. In this method the maximum capacity as influenced by stability effects, P_m, is related to the rigid-plastic collapse load, P_p, and the elastic critical load, P_c.

$$\frac{1}{P_m} = \frac{1}{P_p} + \frac{1}{P_c}. \tag{1}$$

Horne has shown that the empirical relationship has some theoretical justification for frames bent into a double curvature configuration that is similar to the mode shape for sidesway buckling [2]. Therefore, the prediction is generally valid for frames subjected to appreciable horizontal loads. The available experimental results indicate that the Merchant formula reasonably describes the maximum load carrying capacity of one and two story frames [3].

For the usually encountered framework, the elastic critical load is very much larger than the rigid-plastic collapse load. Consequently, HORNE has noted that the accuracy of Eq. (1) can be maintained without the necessity of having "exact" elastic critical loads [4]. By using approximate buckling loads, the computational work required to use the MERCHANT formula is considerably reduced and the method becomes more practical to employ.

The object of this paper is to compare the results obtained from the Merchant prediction with the collapse loads obtained by the more accurate method of computerized elastic-plastic analysis. The elastic and collape load behavior

of eight multi-story frames, with and without stability effects, has already been described by this author [5]. The previously reported research is used to compute crude estimates of the elastic critical loads. In addition, the exact critical loads are computed and used to demonstrate that the Merchant prediction remains virtually unaltered by the use of approximate buckling loads.

Computation of Critical Loads

The determination of "exact" elastic critical loads requires considerable computational effort. Critical loads have been obtained by several methods: moment distribution, stiffness matrix techniques and eigenvalue computations. The latter two methods are suitable for the computerized investigations of large frameworks, but require the performance of repeated analyses. STEVENS and SCHMIDT have presented additional techniques based on the amplification of artificially introduced components of the buckled shape [6]. Their methods utilize the Southwell plot in order to obtain initial estimates of the critical load. Improvements of the estimated critical load are obtained by iterative techniques. The process can be terminated prematurely if approximate critical loads are all that is needed.

A few researchers have reported methods for computing approximate critical loads to be specifically used in the Merchant formula. HORNE has used rigid-plastic-rigid analysis to derive approximate elastic critical loads [4]. STEVENS has used energy techniques for the same purpose [7]. The approach used by Stevens results in the definition of the maximum allowable horizontal structure sway as a function of the elastic critical load. In either case, the approximation requires the performance of some sort of analysis, although the work is considerably reduced from that required for an exact computation of critical load.

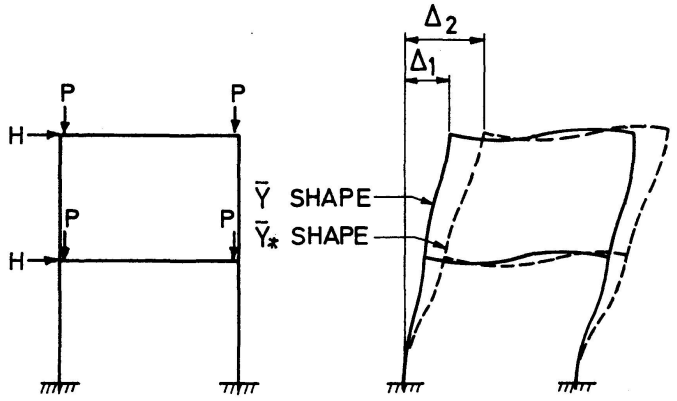
Approximate Critical Loads by Elastic Analyses

The results of elastic analyses can be used to approximate critical loads by the following procedure.

Assume that the deformations obtained from the usual first order, linear-elastic frame analysis are denoted by the vector $\bar{y}$ (see Fig. 1). Let the vector be described in terms of all of the i mode shapes of the frame, $\bar{y}_i$, associated with all of the i critical loads, P_i.

$$\bar{y} = a_1\bar{y}_1 + a_2\bar{y}_2 + a_3\bar{y}_3 + \ldots a_i\bar{y}_i, \tag{2}$$

where, a_i represents the participation of the ith mode in the description of the deflected shape. Furthermore, assume that the deformations given by a second order analysis (stability effects included) are $\bar{y}_*$. Then the relationship between



Frame and loading

——— First order analysis
——— Second order analysis
Deformed shapes

Fig. 1. Elastic frame deformations.

the amplified $\bar{y}_*$ deformations and the first order deformations is given by

$$\bar{y}_* = \frac{a_1 \bar{y}_1}{1-\frac{P}{P_1}} + \frac{a_2 \bar{y}_2}{1-\frac{P}{P_2}} + \frac{a_3 \bar{y}_3}{1-\frac{P}{P_3}} + \cdots \frac{a_i \bar{y}_i}{1-\frac{P}{P_i}}, \tag{3}$$

where, P represents the vertical load set imposed on the structure.

If the loads are such that the first order deformations an *entirely* those of the first mode, then the ratio of the second and first order deflections would be a constant value throughout the frame. Denoting the ratio of $\bar{y}_*$ to $a_1 \bar{y}_1$ by α, and using λ_c to represent the proportional multiplier of the loads P needed to cause the first critical load set, P_1,

$$\alpha = \frac{1}{1-\frac{1}{\lambda_c}}. \tag{4a}$$

Solving for λ_c,

$$\lambda_c = \frac{\alpha}{\alpha - 1}. \tag{4b}$$

Although Eqs. (4) are true only for a very special case, the behavior of a frame subjected to appreciable horizontal loads is such that the structure primarily deforms into the double curvature configuration similar to that of the most critical sidesway buckling mode. Since only approximate critical loads are needed for use in the Merchant prediction, Formula (4b) can be utilized. Furthermore, α can be approximated by the ratio of second order to first order horizontal sway at the top of the frame. With reference to Fig. 1, this ratio is given by Δ_2/Δ_1. Therefore, the approximate critical load can be directly obtained from first and second order elastic frame analyses. It is to be noted that this method is essentially the starting point for the more accurate iterative computation of critical loads presented by STEVENS and SCHMIDT [6]. They have also suggested that the ratio α be taken as the average of the deformation

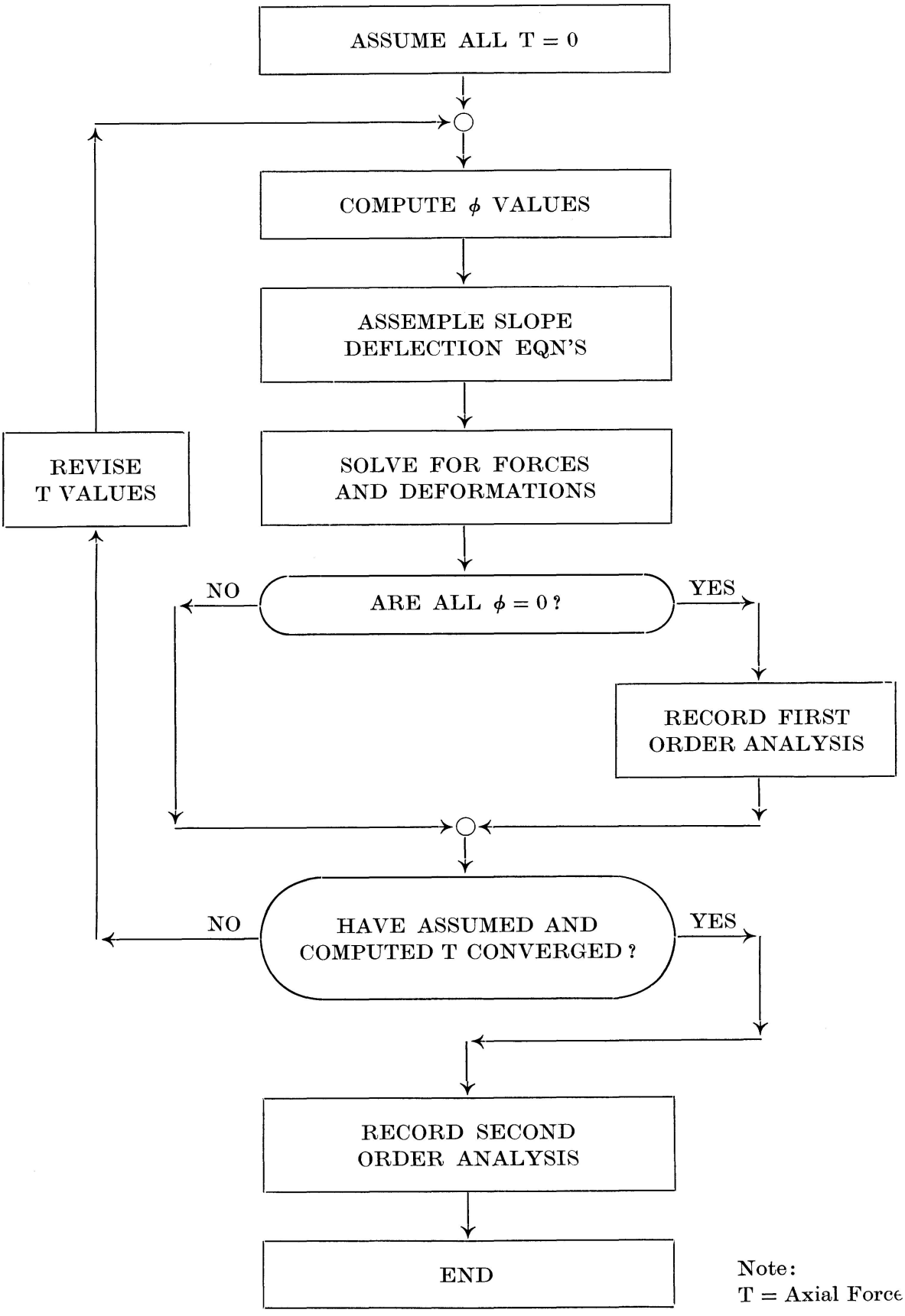


Fig. 2. Flow chart; unified elastic analysis.

ratios at all of the stories of the frame. For the particular application considered here, the refinement will be shown to be unnecessary.

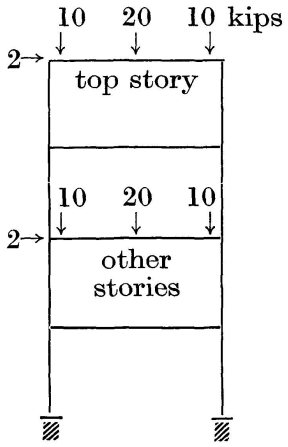
Second order elastic analysis has been programmed by HARRISON [8] and has been used by several other researchers as an integral part of elastic-plastic computer programs. For the computation of approximate critical loads, it is advantageous to unify first and second order analysis in a single program. One convenient method can be based on the slope deflection equations with stability functions that have been presented by BLEICH [9]. In this method, the slope deflection equations have coefficients dependent on the axial loads acting on the members. For a member subjected to axial load, T, and having stiffness and length of EI and L respectively, the stability factor, Φ, determines the slope deflection coefficients. The factor Φ is given by,

$$\Phi = L\left[\sqrt{\frac{T}{EI}}\right]. \tag{5}$$

When Φ is set equal to zero, the coefficients for the usual linear analyses are obtained. Thus, it is possible to obtain both first and second order analyses by formulating a second order analysis by an iterative procedure starting from the assumption that all Φ values are zero. The first computation describes the linear-elastic behavior of the frame. As the values of Φ are continually refined to account for more precise axial loads, the iteration quickly converges to yield second order deformations. The process is described by the flow chart shown in Fig. 2.

Frames and Loadings

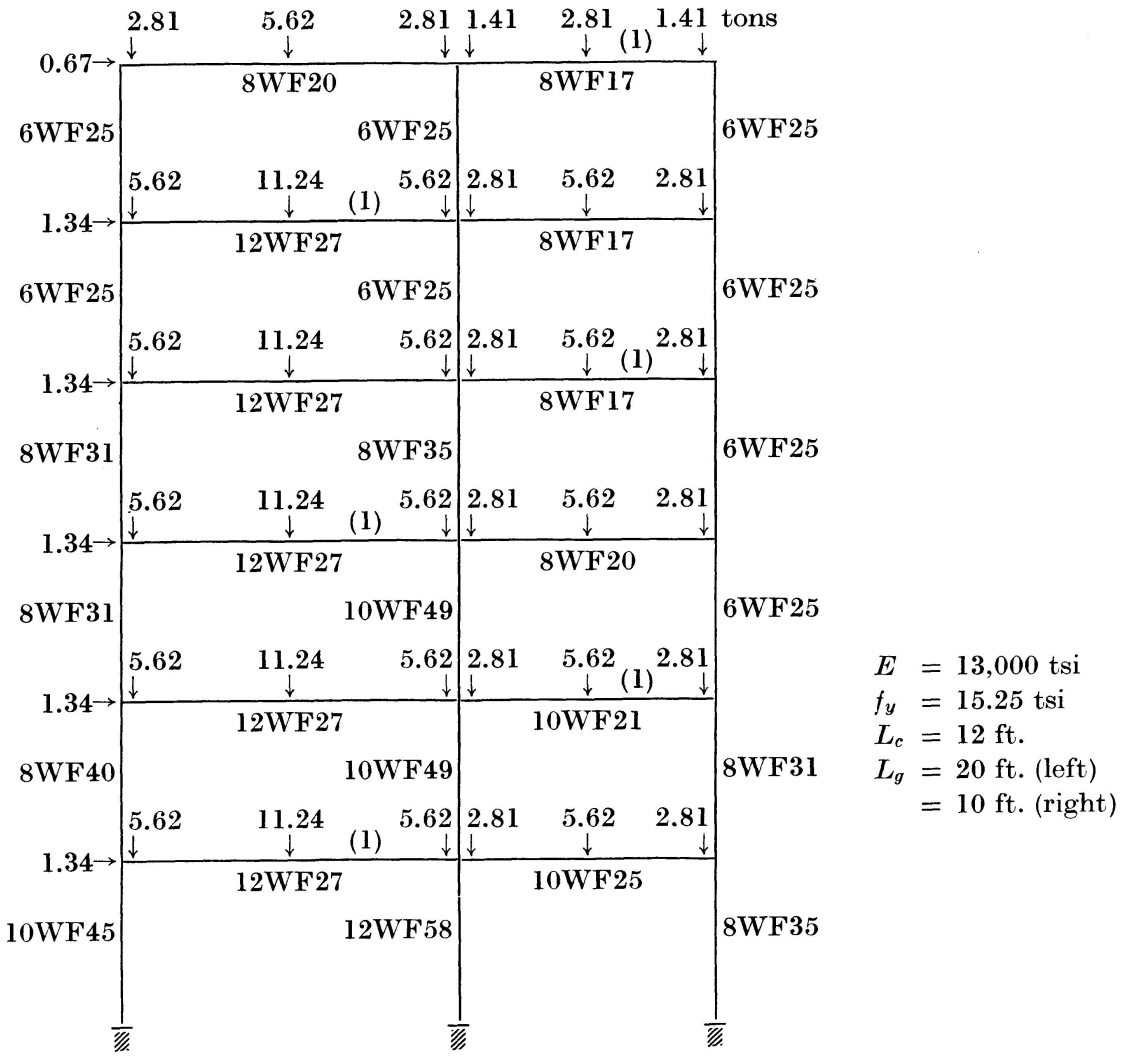
The dimensions, properties and loadings for the eight frames that have been analyzed are shown in Figs. 3 through 6. Modulus of elasticity, yield stress, column length and girder length (E, f_y, L_c and L_g respectively) are shown for each frame. The wide flange sections that have been used are also



All members are fictitious

I	= 144 in.^{4}	f_y	= 36 ksi
M_p	= 160 ft.k.	L_c	= 25 ft.
A	= 11.75 in.^{2}	L_g	= 20 ft.
E	= 30,000 ksi		

Fig. 3. Frame 4—1.



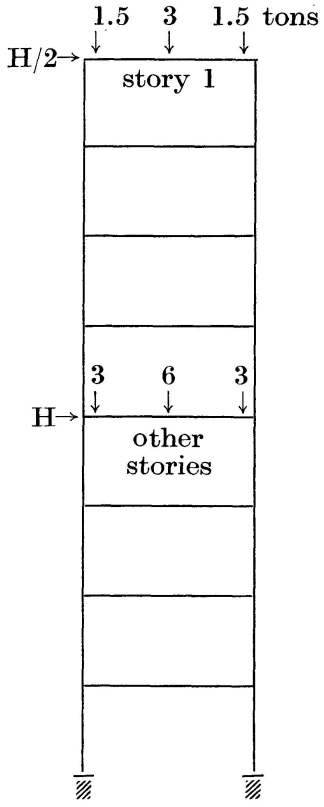
Note: Frame 6—1 shown. Frame 6—2 is identical except for half vertical loads in girder spans marked [1].

Fig. 4. Six story frames.

indicated on the figures. Where fictitious or approximate members have been used, the fully plastic moment, M_p, the moment of inertia, I, and the area, A, are also indicated. Frame designation is given by a numeral indicating the number of stories, followed by an identification number after a dash. Thus $8-2$ indicates the second of the eight story frames to be considered.

The working loads are indicated on the figures. Horizontal forces are applied at each story and a three point concentrated load system has been applied on each girder. The three point system (1/4 of the total load at each girder end and 1/2 at the center of the girder) is used to simulate uniform loads. In several cases, the loadings are given in ton units (1 ton = 2.24 kips) for frames obtained from the British literature.

Frame $4-1$ has been chosen to illustrate a frame particularly susceptible to stability effects. The six-story, two-bay frames are identical with respect to members, configuration and horizontal loadings. Frame $6-1$ is subjected



Columns

Story	Frame 8—1	Frame 8—2	Frames 8—3 and 8—4
1	6 WF 15.5	6 WF 15.5	6 WF 15.5
2	8 WF 31	8 WF 24	8 WF 24
3	do	do	8 WF 28
4	8 WF 35	8 WF 28	8 WF 40
5	10 WF 49	10 WF 39	10 WF 45
6	12 WF 79	12 WF 58	10 WF 60
7	14 WF 87	14 WF 68	10 WF 66
8	14 WF 95	14 WF 74	14 WF 68

Girders

Story	Frame 8—1	Frame 8—2	Frames 8—3 and 8—4
1	8 WF 17	8 WF 20	8 WF 17
2	8 WF 20	10 WF 21	10 WF 21
3	10 WF 21	10 WF 25	10 WF 29
4	12 WF 27	12 WF 31	12 WF 31
5	14 WF 30	14 WF 34	14 WF 34
6	14 WF 34	14 WF 38	14 WF 43[1])
7	do	14 WF 43	14 WF 53
8	14 WF 38	14 WF 48	14 WF 61

E = 13,000 tsi
f_y = 15.25 tsi
$L_c = L_g$ = 10 ft.
H = 2.2 t (Frames 8—1, 2 and 3)
1.1 t (Frame 8—4)

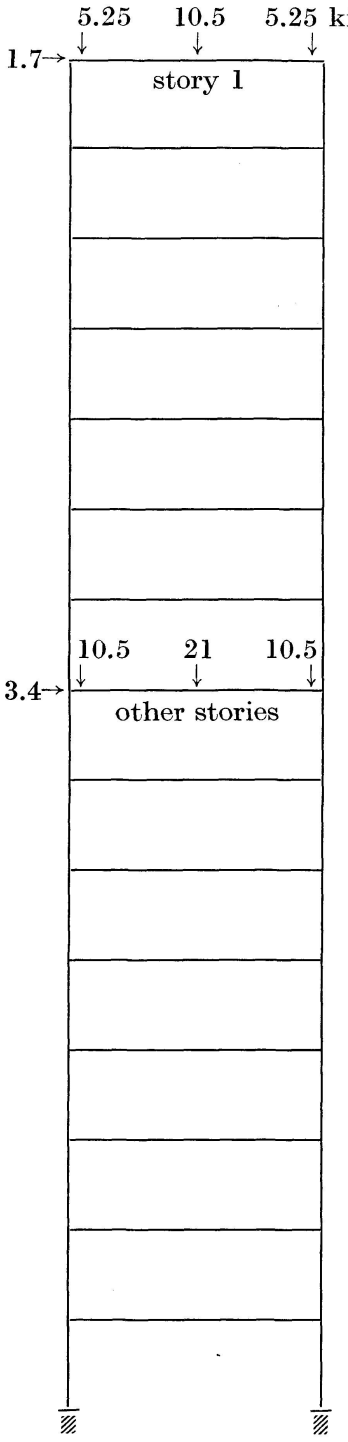
[1]) Fictitious M_p used (99.7 ft.tons).

Fig. 5. Eight story frames.

to full vertical loads, wheras the companion, $6-2$, has vertical loads applied in a "checkerboard pattern" of full and half loading. All of the eight story frames are identical in dimensions and vertical loading. Frames $8-1$, $8-2$, and $8-3$ also have identical horizontal loadings, their only difference being in the proportions of the members. Frame $8-4$ is identical to $8-3$, except that only half of the horizontal forces are applied. Frame $15-1$ is the most slender of the structures considered, having a height-to-width ratio of 10.5 to 1. For a more complete description of the source of the frames, the reader is referred to Reference [5].

Results of the Analyses

The results of all the exact and approximate calculations are summarized in Table 1. Previously performed elastic-plastic analyses have been used to furnish values of the amplification factors at working loads and the first and second order collapse load factors (α, λ_p and λ_2 respectively). The elastic-



Story	Columns	Girders
1	8 WF 17	8 WF 20
2	8 WF 28	10 WF 25
3	10 WF 39	12 WF 27
4	do	12 WF 36
5	12 WF 40	do
6	12 WF 50	12 WF 45
7	12 WF 58	14 WF 53
8	14 WF 61	14 WF 61
9	14 WF 74	do
10	14 WF 84	14 WF 74
11	14 WF 111	14 WF 78
12	do	14 WF 84
13	do	16 WF 88
14	14 WF 127	16 WF 96
15	14 WF 136	18 WF 96

E = 30,000 ksi
f_y = 36 ksi
L_c = 14 ft.
L_g = 20 ft.

Fig. 6. Frame 15—1.

plastic analyses include the effects of bending deformations only, since axial deformations had negligible effects on the maximum frame capacity [5]. In all cases, monotonically increasing proportional loads were applied up to the maximum frame capacity. The plastic moment capacity of each member was continually for existing axial load in accordance with the bi-linear formula of the A.I.S.C. [10].

Table 1. Critical loads and collapse loads

Frame	From Elastic-Plastic Analysis, Reference 5			Elastic Critical Loads, λ_c			Merchant Loads, λ_m, Formula 1 [5]			Exact $\frac{\lambda_m}{\lambda_2}$
	α [1]	λ_p [2]	λ_2 [3]	Exact	Approx. [4]	Approx. ÷ Exact	Exact	Approx.	Approx. ÷ Exact	
4—1	1.2961	2.067	1.286	4.00	4.38	1.10	1.36	1.40	1.03	1.06
6—1	1.1021	1.571	1.367	9.89	10.8	1.09	1.36	1.37	1.01	0.99
6—2	1.0750	1.719	1.524	13.2	14.3	1.08	1.52	1.53	1.01	1.00
8—1	1.0267	1.649	1.414	33.5	38.5	1.15	1.57	1.58	1.01	1.10
8—2	1.0273	1.511	1.424	30.6	37.6	1.23	1.44	1.45	1.01	1.01
8—3	1.0244	1.814	1.646	37.1	42.0	1.13	1.73	1.74	1.01	1.05
8—4	1.0243	2.905	2.836	37.1	42.2	1.14	2.69	2.76	1.03	0.95
15—1	1.0779	1.632	1.403	12.2	13.8	1.13	1.44	1.46	1.01	1.03

[1] $\alpha = \Delta_2/\Delta_1$ = Amplification of top sway at working loads.
[2] λ_p = Load factor for rigid-plastic collapse.
[3] λ_2 = Load factor at collapse, second-order elastic-plastic analysis.
[4] Approximate critical loads computed from Formula 4b.
[5] Exact and approximate λm values are based on exact and approximate critical loads respectively.

$$\begin{aligned} M_{pc} &= M_p && (P/P_y \leqq 0.15), \\ M_{pc} &= 1.18\, M_p\,[1 - P/P_y] && (P/P_y > 0.15). \end{aligned} \tag{6}$$

Here, the reduced and fully plastic moments are given by M_{pc} and M_p respectively. The existing axial load in the member is P, and the fully yielded capacity of the section is denoted by P_y. It is to be noted that information for calculating α was automatically obtained by the performance of first and second order elastic-plastic analysis.

The critical loads, λ_c, were computed by two methods. Exact values were calculated by formulating the slope deflection equations with stability functions and equating the determinant of the resulting stiffness matrix to zero [9]. For this purpose, each in-span girder load was replaced by two equal loads acting over the adjacent columns. Trial values of load factor were chosen and the determinant of the stiffness matrix was calculated. By means of interpolation, accurate values of the critical loads were obtained. Approximate critical loads were obtained by substituting the previously determined values of α into Eq. (4b). Exact and approximate Merchant loads were obtained by using the values of λ_p in conjunction with the exact and approximate critical loads.

The approximately calculated critical loads were anywhere from 8 to 23 percent higher than the true critical loads. Thus, the approximations are considered to be crude. Improved estimates of λ_c could have been obtained by averaging the values of α obtained at each story level of the frame. In the case of Frame 4 – 1, the values of α from the top to the bottom story were 1.2961, 1.3161, 1.3398 and 1.3375 respectively. By using any one of the stories

to describe α, the greatest variation in λ_c would have been from 3.94 to 4.38. The value of λ_c would have been 4.10 if averaging were employed. However, the crude value of λ_c is seen to be entirely adequate when employed in the already empirical Merchant formula. The approximate Merchant load is at worst 3% higher than the exact Merchant load.

For the frames in question, the Merchant formula gave reasonable estimates of the maximum frame capacity. At worst, the empirical prediction was 5% low or 10% high. The predictions for Frames 6 – 1, 6 – 2 and 8 – 2 were almost identical to the values obtained by second order elastic-plastic analysis. However, the virtue of the Merchant formula is seen to be its ability to describe the correct trends of frame behavior. Frame 4 – 1 lost 38 percent of its potential load carrying capacity due to stability effects — Formula 1 predicted a 37 percent loss. All of the other frames were relatively insensitive to stability effects, losing at most 14 percent of their rigid-plastic capacity. Here, the Merchant prediction tended to considerably underestimate stability effects. Yet, when Eq. (1) denoted insignificant frame stability effects, the effects were indeed insignificant. In no case did the Merchant prediction describe an incorrect trend of frame behavior. It is to be noted that the Merchant formula has been used here in conjunction with reduced plastic moments. The validity of using reduced plastic moments is justified solely by the correctness of the empirical results.

Acknowledgements

The elastic-plastic analyses utilized in this paper were performed in the Department of Civil and Environmental Engineering, Washington University, St. Louis, Missouri. The research was supported by funds granted by the American Iron and Steel Institute. Computing services were made available by the National Science Foundation.

The remainder of the research has been performed in the Department of Civil Engineering of the University of Kentucky.

References

1. MERCHANT, W.: "The Failure Load of Rigid Jointed Frameworks as Influenced by Stability". The Structural Engineer, Vol. 32, July, 1954, p. 185—190.
2. HORNE, M. R.: "Instability and the Plastic Theory of Structures". Transactions of the Engineering Institute of Canada, Vol. 4, No. 2, 1960, p. 31—43.
3. HORNE, M. R. and MERCHANT, W.: "The Stability of Frames". Pergamon Press, 1965, p. 146—151.
4. HORNE, M. R.: "Generalised Approximate Method of Assessing the Effect of Deformation on Failure Loads". Publication, International Association of Bridge and Structural Engineers, Zurich, Vol. 23, 1963, p. 205—218.

5. KORN, A. and GALAMBOS, T. V.: "The Behavior of Elastic-Plastic Frames". Accepted for Publication, Journal of the Structural Division, ASCE.
6. STEVENS, L. K. and SCHMIDT, L. C.: "Determination of Elastic Critical Loads". Journal of the Structural Division, ASCE, Vol. 89, No. ST 6, Proc. Paper 3723, December, 1963, p. 137—158.
7. STEVENS, L. K.: "Elastic Stability of Practical Multi-Story Frames". Proceedings, Institution of Civil Engineers, London, Vol. 36, Paper 6955, January, 1967, p. 99—117.
8. HARRISON, H. B.: "The Second-Order Elastic Analysis of Plane Rigid Frames". Fritz Engineering Laboratory Report No. 297.17, Lehigh University, November, 1965.
9. BLEICH, F.: "Buckling Strength of Metal Structures". McGraw-Hill Book Company, Inc., 1952, Chapters 6 and 7.
10. "Specification for the Design, Fabrication and Erection of Structural Steel for Buildings". American Institute of Steel Construction, April, 1963, Section 2.3, Formula 21.

Summary

A method for computing crude estimates of elastic critical loads has been utilized in the empirical predictions of maximum frame capacity. The crude estimates have been shown to be more than adequate when used solely for the Merchant prediction. Furthermore, the empirical Merchant prediction described the correct general trends of carrying capacity that were obtained by second order elastic-plastic analysis.

Résumé

Pour obtenir une prévision empirique des capacités de charges maximales de huit portiques plans, à plusieurs étages, rectangulaires et non entretoisés, on s'est servi d'une méthode permettant une estimation grossière des charges élastiques critiques. Or pour la «prévision Merchant», cette estimation grossière se montre plus que suffisante. Un des avantages de la méthode proposée est qu'elle permet de contrôler le comportement élastique des portiques.

Les capacités maximales des portiques, trouvées avec la «prévision Merchant» ont été comparées aux résultats obtenus par un calcul élasto-plastique du second ordre. Dans tous les cas, la relation empirique donne l'allure générale correcte de la capacité de charge. Ainsi, on a tout intérêt à se servir de la formule de Merchant, avec des charges critiques approximées et des charges de rupture rigide-plastique estimées, pour détecter d'éventuels portiques particulièrement sensibles à des instabilités.

Zusammenfassung

Ein Verfahren zur groben, schätzenden Berechnung elastischer, kritischer Lasten ist für die empirische Voraussage maximaler Tragfähigkeit von acht mehrstöckigen, unversteiften, rechteckigen und ebenen Stockwerkrahmen angewandt worden. Die grobe Schätzung ist durch die Merchant-Voraussage (Merchant prediction) mehr als genügend. Ein Vorteil der vorgeschlagenen Methode besteht darin, daß das elastische Rahmenverhalten für Prüfungen verwendbar ist. Die maximale Tragfähigkeit der Merchant-Voraussage ist mit den Ergebnissen der elasto-plastischen Analyse zweiter Ordnung verglichen worden. In allen Fällen beschreibt die empirische Beziehung die genaue Richtung der Tragfähigkeit. Demgemäß möge der Gebrauch der genäherten, kritischen Lasten und die geschätzten Traglasten in den Merchant-Formeln für Rahmen verwendet werden, die möglicherweise empfindlich auf große Stabilitätseinflüsse sind.

Inelastic Stability of Tapered Wide-Flange Columns

Stabilité de colonnes émincées à larges ailes dans le domaine plastique

Stabilität von zugespitzten Breitflanschstützen im plastischen Bereich

K. H. LIN
Ph. D., Associate Senior Research Engineer, General Motors Research Laboratories, Warren, Michigan, U.S.A.

E. C. ROSSOW
Ph. D., Associate Professor of Civil Engineering

S. L. LEE
Ph. D., Professor of Civil Engineering

Northwestern University, Evanston, Illinois, U.S.A.

1. Introduction

The behavior of symmetrically and linearly tapered wide-flange columns made of elastic-plastic materials and subjected to arbitrary end loading which causes bending in addition to axial compression is investigated. The interaction curves for tapered cantilever columns are obtained numerically neglecting any torsional-flexural behavior. Approximate equations for these curves are presented to facilitate the determination of the load carrying capacity of simply supported columns.

Numerous analytical studies have been made of the elastic buckling of axially loaded tapered columns [1–6]. The elastic stability of tapered columns subjected to combined bending and thrust has been treated by several investigators [7–11]. While the inelastic buckling of axially loaded tapered columns has been studied [12–14], little work has been done on the inelastic stability of tapered columns subjected to eccentric loading although columns of uniform cross section under such loading have been analyzed [15–18].

2. Assumptions

The present analysis is based on the following assumptions; the material is elastic-perfectly plastic as shown in Fig. 1; the material is homogeneous and

isotropic in both the elastic and plastic states; plane sections remain plane during bending; deflections, slopes, and curvatures are small and are confined to the plane of the web; the effect of the shear stresses on yielding and curvature is neglected; residual stresses and strain reversal are not considered; instability of snap through type occurs in the plane of web which coincides with the plane of loading; and the idealized section is characterized by an H-shape, where the flange thickness is very small but finite.

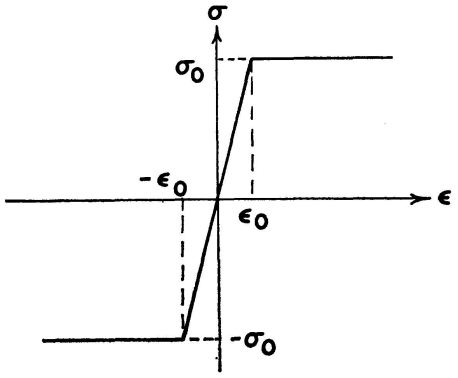


Fig. 1. Idealized stress-strain relationship.

3. Tapered Columns

The column considered herein is symmetrically and linearly tapered along its length by varying the depth of the web but keeping the flange width and thickness constant. The taper slope, denoted by a and defined as the change of the half-depth per unit length of the column, may assume positive or negative values depending on whether the larger or the smaller section is chosen as the reference section. To facilitate the analysis that follows, a rectangular coordinate system is introduced as shown in Fig. 2.

For the reference section where the origin is located, designate the radius of gyration about the strong axis by r_0, the half-depth by b_0, the web area by A_{w0}, and the flange-web area ratio, A_f/A_{w0} by R_0. The nondimensional distance from the origin and the deflection of the centroidal axis are defined respectively, as

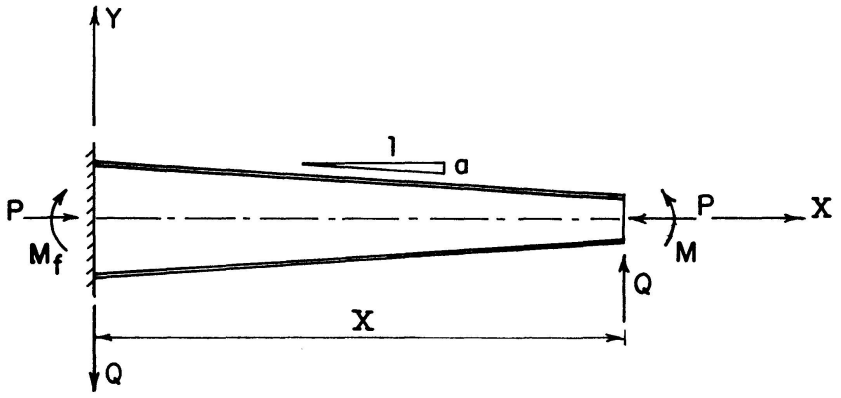


Fig. 2. Tapered wide-flange cantilever column under arbitrary end loads.

$$x = \frac{X}{r_0} \tag{1}$$

and

$$y = \frac{Y}{r_0}. \tag{2}$$

By introducing a parameter

$$\lambda = a\frac{r_0}{b_0}. \tag{3}$$

The following expressions are readily derived for any section.

$$b = b(x) = b_0(1-\lambda x), \tag{4}$$

$$A_w = A_w(x) = A_{w0}(1-\lambda x), \tag{5}$$

$$A = A(x) = A_{w0}(R_0+1-\lambda x), \tag{6}$$

$$R = R(x) = \frac{R_0}{1-\lambda x}, \tag{7}$$

$$I = I(x) = A_{w0}b_0^2(1-\lambda x)^2[R_0+\tfrac{1}{3}(1-\lambda x)], \tag{8}$$

$$S = S(x) = A_{w0}b_0(1-\lambda x)[R_0+\tfrac{1}{3}(1-\lambda x)], \tag{9}$$

$$Z = Z(x) = A_{w0}b_0(1-\lambda x)[R_0+\tfrac{1}{2}(1-\lambda x)], \tag{10}$$

$$r = r(x) = b_0(1-\lambda x)\sqrt{\frac{R_0+\frac{1}{3}(1-\lambda x)}{R_0+1-\lambda x}}, \tag{11}$$

where b, A_w, A, R, I, S, Z and r are respectively, the half-depth, the web area, the total area, the flange-web area ratio, the moment of inertia, the elastic section modulus, the plastic section modulus, and the radius of gyration. Setting $x=0$ in Eq. 11 and substituting into Eq. 3 leads to

$$\lambda = a\sqrt{\frac{R_0+\frac{1}{3}}{R_0+1}}. \tag{12}$$

4. Stress Zones

When a wide-flange section shown in Fig. 3 (a) is subjected to a compressive axial force P and a bending moment M, one of the three stress distributions, referred to as elastic, primary plastic, and secondary plastic, as shown in Figs. 3 (b), (c), and (d) will result.

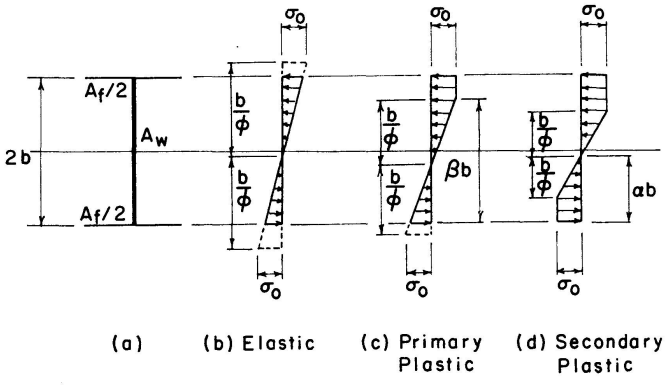


Fig. 3. Cross section and stress distribution due to bending and compression.

The nondimensional axial force and moment are defined, respectively, as

$$p = p(x) = \frac{P}{P_0(x)} \tag{13}$$

and

$$m = m(x) = \frac{M(x)}{M_0(x)}, \tag{14}$$

in which

$$P_0(x) = \sigma_0 A(x) \tag{15}$$

and

$$M_0(x) = \sigma_0 Z(x), \tag{16}$$

where σ_0 denotes the yield stress of the material.

Referring to Fig. 3 (d), the condition $1/\phi = 0$, where ϕ denotes the nondimensional curvature, defines the limit of statical admissibility. The plastic moment is given by

$$m_{pl}(x) = \frac{R_0 + 1 - \lambda x}{R_0 + \frac{1}{2}(1 - \lambda x)}[1 - p(x)] \quad \text{for} \quad \frac{1 - \lambda x}{R_0 + 1 - \lambda x} \leqq p(x) \leqq 1, \tag{17a}$$

$$m_{pl}(x) = 1 - \frac{[(R_0 + 1 - \lambda x)\, p(x)]^2}{(2R_0 + 1 - \lambda x)(1 - \lambda x)} \quad \text{for} \quad 0 \leqq p(x) \leqq \frac{1 - \lambda x}{R_0 + 1 - \lambda x}. \tag{17b}$$

Referring to Fig. 3 (b), the condition of initial yield, which defines the boundary between the elastic and the primary plastic zones, gives

$$m_e(x) = \frac{R_0 + \frac{1}{3}(1 - \lambda x)}{R_0 + \frac{1}{2}(1 - \lambda x)}[1 - p(x)]. \tag{18}$$

The boundary between the primary and the secondary plastic zones is given by the condition $\beta = 2/\phi$ in Fig. 3 (c) and is expressed by

$$m_p = \frac{1}{R_0 + \frac{1}{2}(1 - \lambda x)} \left\{ R_0 + \tfrac{1}{3}(1 - \lambda x) \left[1 + \frac{R_0 + 1 - \lambda x}{1 - \lambda x} p(x) - 2 \left(\frac{R_0 + 1 - \lambda x}{1 - \lambda x} p(x) \right)^2 \right] \right\}. \tag{19}$$

The admissible domain and the boundaries for each stress zone are described by Eqs. 17, 18, and 19 in a p-m plane shown in Fig. 4.

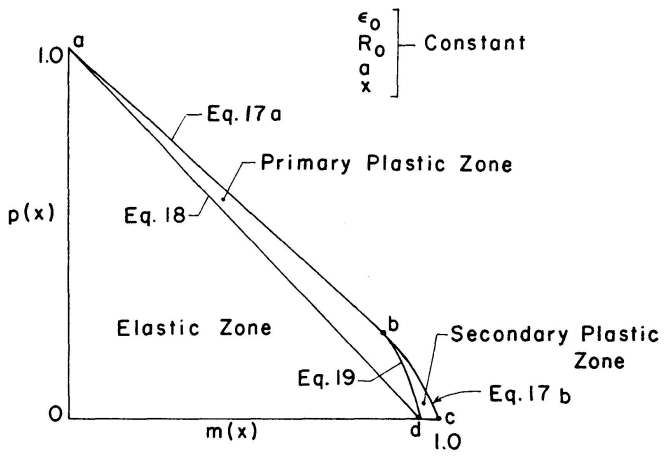


Fig. 4. Stress zones.

5. Curvature Functions

The nondimensional curvature at any section is defined as

$$\phi = \frac{\Phi}{\Phi_0}, \tag{20}$$

where Φ is the actual curvature, $\Phi_0 = \epsilon_0/b$ is the curvature at initial yield due to pure bending, and ϵ_0 is the strain at yield point. The function $\phi(m, p)$ for each stress zone can be readily expressed as follows.

In the elastic zone,

$$\phi = \frac{R_0 + \frac{1}{2}(1-\lambda x)}{R_0 + \frac{1}{3}(1-\lambda x)} m(x), \tag{21}$$

in the primary plastic zone,

$$\phi = \frac{8}{9} \frac{(R_0 + 1 - \lambda x)[1 - p(x)]}{(1-\lambda x)\left\{U\left(U + \frac{2R_0}{1-\lambda x}\right) + \left[U + \frac{2R_0}{3(1-\lambda x)}\right]\sqrt{U\left[U + \frac{8R_0}{3(1-\lambda x)}\right]}\right\}}, \tag{22a}$$

in which

$$U = 1 - \frac{R_0 + \frac{1}{2}(1-\lambda x)}{R_0 + 1 - \lambda x} \frac{m(x)}{1 - p(x)}, \tag{22b}$$

while in the secondary plastic zone,

$$\phi = \frac{1}{\sqrt{3\left\{\frac{2R_0 + 1 - \lambda x}{1-\lambda x}[1 - m(x)] - \left[\frac{R_0 + 1 - \lambda x}{1-\lambda x} p(x)\right]^2\right\}}}. \tag{23}$$

Eqs. (21), (22), and (23) are derived for positive moment, hence the absolute value of m must be used and ϕ replaced by $(-\phi)$ in cases where the moment is negative.

6. Equilibrium Equations

When the tapered cantilever column is subjected to an axial force P, a shear force Q, and a bending moment M at the free end as shown in Fig. 2, the conditions of equilibrium require that

$$m(x) = \frac{1}{[R_0 + \frac{1}{2}(1-\lambda x)](1-\lambda x)}\left[(R_0 + \tfrac{1}{2}) m_f - \sqrt{(R_0+1)(R_0+\tfrac{1}{3})}(p_f y + q_f x)\right], \tag{24}$$

in which $p_f = P/P_0(0)$, $q_f = Q/P_0(0)$, $m_f = M_f/M_0(0)$, and M_f = the fixed end moment. The relation between $p(x)$ and p_f is given by

$$p(x) = \frac{1-\lambda x}{R_0 + 1 - \lambda x} p_f. \tag{25}$$

7. Differential Equation

From the small deflection theory and Eqs. 2 and 20, it follows that

$$\frac{d^2Y}{dX^2} = \frac{1}{r_0}y'' = \frac{\epsilon_0}{b}\phi, \tag{26}$$

in which prime denotes differentiation with respect to x. Introducing Eqs. (3), (4) and (12) in Eq. (26) leads to

$$y'' = \sqrt{\frac{R_0+\frac{1}{3}}{R_0+1}}\,\frac{\epsilon_0}{1-\lambda x}\phi. \tag{27}$$

Substitution of Eqs. (24) and (25) into the appropriate curvature function, i.e., Eq. (21), (22), or (23), and the results into Eq. (27) yields the differential equation for each stress zone.

The boundary conditions

$$y(0) = y'(0) = 0 \tag{28}$$

being both specified at one end of the column make this an initial-value problem.

8. Numerical Integration

The numerical solution of the initial value problem defined by Eqs. (27) and (28) is obtained by a step-by-step integration procedure. Let the subscript i denote the discrete stations evenly spaced along the x-axis such that $x_i = (i-1)\Delta x$, $i = 1, 2, 3\ldots$ Approximating the second derivative in Eq. (27) by a three-term central difference formula, upon application of the boundary conditions, Eq. (28), leads to

$$y_2 = \tfrac{1}{2}\epsilon_0(\Delta x)^2\sqrt{\frac{R_0+\frac{1}{3}}{R_0+1}}\,\phi_1 \tag{29}$$

and in general

$$y_{i+1} = \frac{\epsilon_0(\Delta x)^2}{1-\lambda x_i}\sqrt{\frac{R_0+\frac{1}{3}}{R_0+1}}\,\phi_i + 2y_i - y_{i-1} \quad \text{for } i \geqq 2. \tag{30}$$

For given values of p_f, q_f, and m_f, the values of m_i and p_i can be obtained from Eqs. (24) and (25), respectively. Having determined the stress zone from Eqs. (17), (18), and (19), the appropriate curvature function ϕ_i, Eqs. (21), (22) or (23), is chosen. The value of y_{i+1} can then be computed by means of Eq. (30).

9. Equilibrium Curves

By means of the marching procedure described above, the values of m can be plotted against x for various values of m_f as shown in Fig. 5 (a), provided

the values of ϵ_0, R_0, a, p_f, and q_f are specified. The m-x curves are referred to as equilibrium curves of the tapered cantilever column.

If $|m|$ nowhere exceeds m_e, the column is entirely elastic. In some of the equilibrium curves, $m_e < |m| < m_{pl}$ in a portion of the column. For some values of m_f, the equilibrium curves intersect the curves $m = \pm m_{pl}$ at some point x. Beyond this point, the equilibrium curve is statically inadmissible and need not be considered.

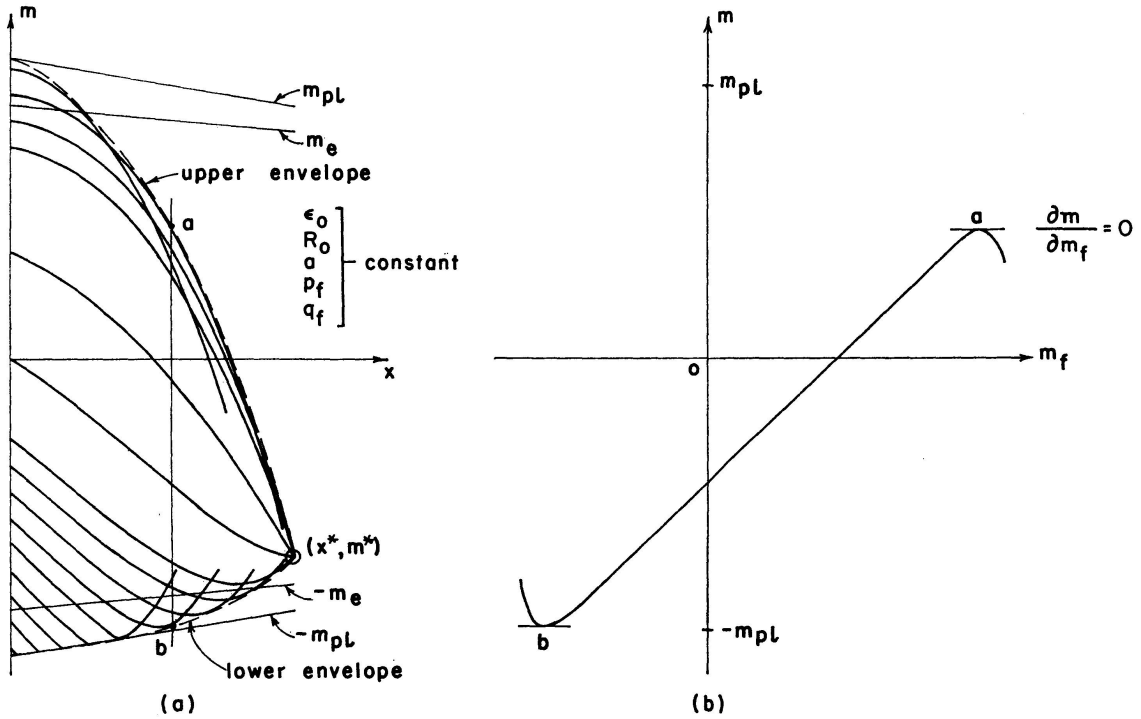


Fig. 5. Moment equilibrium curves and envelopes.

It is of interest to observe that all the elastic equilibrium curves pass through a common point (x^*, m^*). For the inelastic equilibrium curves, the value of x corresponding to m^* are always smaller than x^*. The existence of the common point (x^*, m^*), of the elastic equilibrium curves implies that x^* and m^* are both independent of m_f. If q_f vanishes, all the elastic equilibrium curves meet at $(x^*, 0)$. Thus, x^* is the nondimensional elastic buckling length or Euler length.

10. Elastic Tapered Columns

Elasting Buckling Length x^*. Consider an elastic cantilever column subjected to an axial force P at the free end. The differential equation for the centroidal axis of the slightly bent column is

$$(C_1 x^3 + C_2 x^2 + C_3 x + C_4) y'' + C_5 y = C_5 \delta, \tag{31}$$

in which $C_1=\lambda^3$, $C_2=-3\lambda^2(R_0+1)$, $C_3=3\lambda(2R_0+1)$, $C_4=-(3R_0+1)$, $C_5=-(3R_0+1)$, $\epsilon_0 p_f$ and δ is the arbitrary deflection at the free end. The boundary conditions are

$$y(0) = 0, \tag{32a}$$

$$y'(0) = 0, \tag{32b}$$

$$y(x^*) = \delta. \tag{32c}$$

Examining the coefficient function of Eq. (31) indicates that $x=0$ is an ordinary point and $x=(3R_0+1)/\lambda$ and $x=1/\lambda$ are both regular singular points. The complementary function takes the form of an infinite power series which converges uniformly for $0 \leqq x < |1/\lambda|$.

Taking the solution of the boundary value problem defined by Eqs. (31) and (32) in the form $y=\delta+\sum_{k=0}^{\infty} a_k x^k$ and demanding the nontrivial solution lead to the elastic buckling criterion

$$\sum_{k=0}^{\infty} a_k (x^*)^k = 0, \tag{33}$$

in which

$$a_0 = -\delta, \tag{34a}$$

$$a_1 = 0, \tag{34b}$$

$$a_2 = -\frac{C_5}{2C_4}, \tag{34c}$$

$$a_k = -\frac{1}{k(k-1)C_4}\{a_{k-1}(k-1)(k-2)C_3 + a_{k-2}[(k-2)(k-3)C_2 + C_5] + a_{k-3}(k-3)(k-4)C_1\}, \qquad k = 3, 4, 5, \ldots \tag{34d}$$

For a given value of p_f, the smallest positive real root x^* of Eq. (33) is the elastic buckling length of the cantilever column.

The Euler length x^* can also be obtained with excellent accuracy by intersecting any elastic equilibrium curve for $q_f=0$ with the x-axis by means of the numerical integration procedure. It must be pointed out that if $a<0$, the Euler length is obtainable from Eq. (33) for $x^*<|1/\lambda|$, whereas the numerical solution is always valid. The x^*-p_f curves for various taper slopes are presented in solid lines in Fig. 6.

Determination of m^*. Consider the cantilever column subjected to general loading at the free end as shown in Fig. 2. Assuming that the column is entirely elastic, the differential equation may be obtained by combining Eqs. (21), (24), and (27) as

$$(C_1 x^3 + C_2 x^2 + C_3 x + C_4) y'' + C_5 y = C_5 \left[\frac{2R_0+1}{2\sqrt{(R_0+1)(R_0+\frac{1}{3})}}\left(\frac{m_f}{p_f}\right) - \left(\frac{q_f}{p_f}\right)x\right]. \tag{35}$$

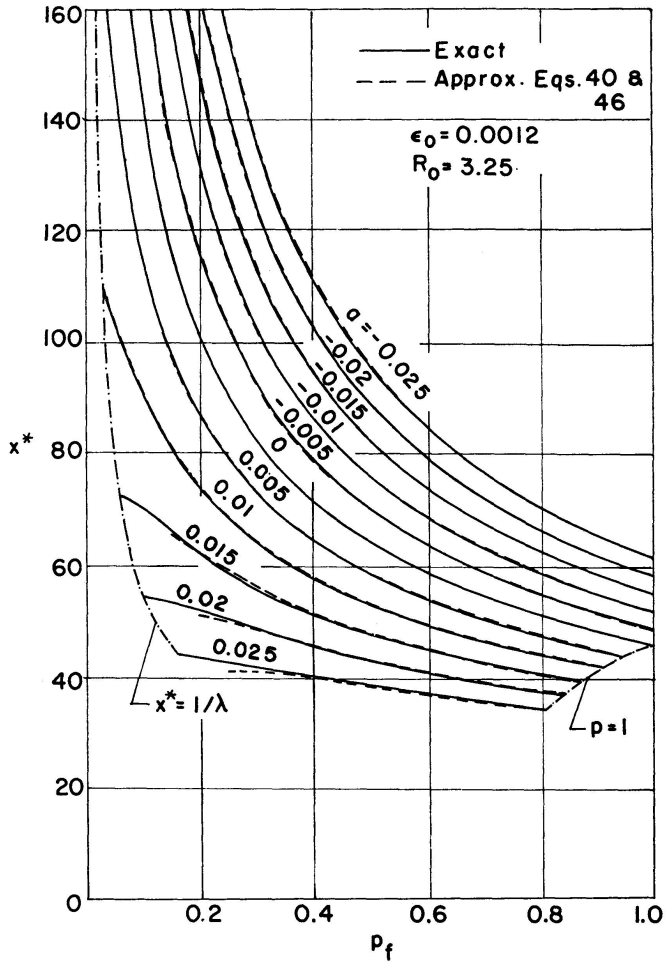


Fig. 6. Euler lengths of tapered cantilever columns.

The boundary conditions are

$$y(0) = 0, \tag{36a}$$

$$y'(0) = 0. \tag{36b}$$

The homogeneous equation corresponding to Eq. (35) is identical to that corresponding to Eq. (31).

Solving the initial value problem defined by Eqs. (35) and (36) and substituting the solution into Eq. (24) leads to the equation of the elastic equilibrium curve

$$m(x) = \frac{1}{[R_0 + \frac{1}{2}(1-\lambda x)](1-\lambda x)} \{(R_0+\tfrac{1}{2})\, m_f - \sqrt{(R_0+1)(R_0+\tfrac{1}{3})}\, p_f \sum_{k=1}^{\infty} c_k x^k\}, \tag{37}$$

in which

$$c_0 = -\frac{2R_0+1}{2\sqrt{(R_0+1)(R_0+\frac{1}{3})}} \left(\frac{m_f}{p_f}\right), \tag{38a}$$

$$c_1 = \frac{q_f}{p_f}, \tag{38b}$$

$$c_2 = \frac{(2R_0+1)\epsilon_0}{4\sqrt{(R_0+1)(R_0+\frac{1}{3})}} m_f, \tag{38c}$$

$$c_k = -\frac{1}{k(k-1)C_4}\{c_{k-1}(k-1)(k-2)C_3 + c_{k-2}[(k-2)(k-3)C_2 + C_5] + c_{k-3}(k-3)(k-4)C_1\}, \qquad k = 3, 4, 5, \ldots \tag{38d}$$

Since the common point (x^*, m^*) of elastic equilibrium curves is independent of m_f, it is appropriate to set $m_f = 0$ in Eqs. (37) and (38) to obtain the expression for m^* in the form

$$m^* = m(x^*) = -\frac{\sqrt{(R_0+1)(R_0+\frac{1}{3})}}{[R_0+\frac{1}{2}(1-\lambda x^*)](1-\lambda x^*)} p_f \sum_{k=1}^{\infty} c_k (x^*)^k. \tag{39}$$

It is important to observe that the coefficients, $c_k, k = 1, 2, 3, \ldots$, hence m^* are linear functions of q_f.

The expression for m^* given by Eq. (39) is valid only when $x^* < |1/\lambda|$. However, the value of m^* can always be obtained numerically as the value of m for any elastic curves at $x = x^*$. The $m^* - p_f$ curves for various taper slopes are presented in solid lines for a particular value of q_f as shown in Fig. 7. The values of m^* for other values of q_f can be obtained by linear proportioning.

Insensitivity of x^* and m^* to R_0. It is observed that the values of x^* and m^* are insensitive to the variation of the parameter R_0. The following approximate expressions for x^* and m^* are derived on the basis of $R_0 = 3.25$.

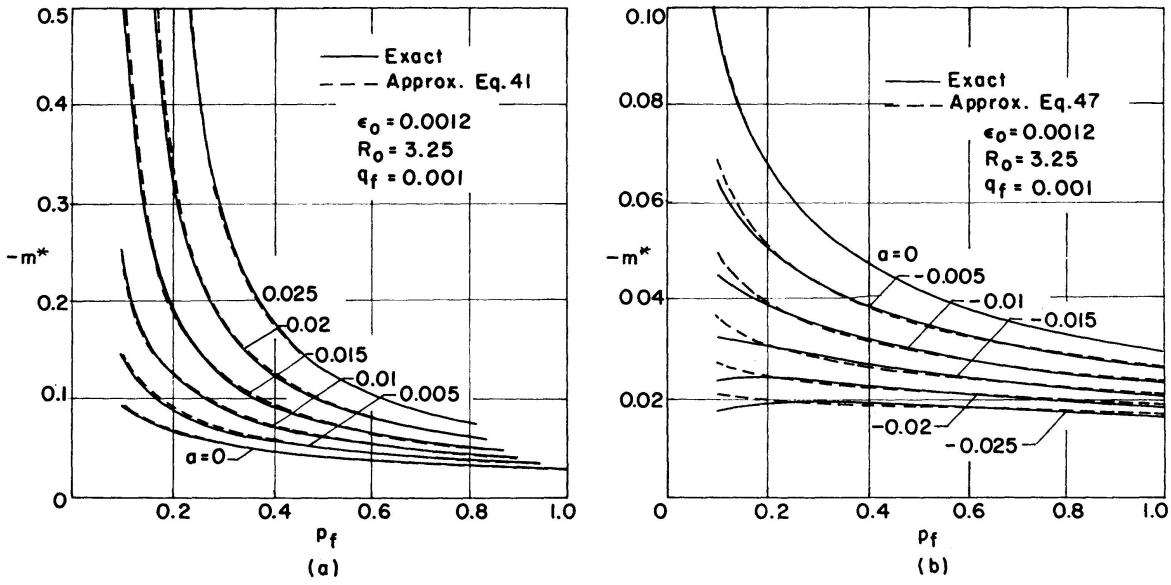


Fig. 7. Variation of m^* with p_f and a.

11. Approximate Expressions for x^* and m^*

The values of x^* and m^* for $R_0 = 3.25$ and $\epsilon_0 = 0.0012$, corresponding to A 36 steel, for taper slopes in the range $-0.025 \leqq a \leqq 0.025$ may be approximated by the following expressions.

For $0 \leqq a \leqq 0.025$,

$$x^* = \frac{\pi}{\sqrt{0.0048\, p_f}} - \frac{481.1\, a^{0.9647}}{p_f^{[0.9953/(10^{1.14\, a})]}}, \tag{40}$$

$$m^* = -q_f \{10^{[\alpha_m/(p_f^{\beta_m})-6]} + \Delta_m H(p_{fc} - p_f)\}, \tag{41}$$

in which

$$\left.\begin{aligned} \alpha_m &= 7.480 + 9.20\, a \\ \beta_m &= 0.02816 + 1.495\, a \end{aligned}\right\} \text{ for } 0 \leqq a \leqq 0.0125 \tag{42a, 42b}$$

$$\left.\begin{aligned} \alpha_m &= 7.414 + 14.50\, a \\ \beta_m &= 0.03229 + 1.165\, a \end{aligned}\right\} \text{ for } 0.0125 \leqq a \leqq 0.025 \tag{43a, 43b}$$

$$\Delta_m = \frac{(a/0.015)^{7.85}}{(p_f/0.30)^{5.32}}, \tag{44}$$

$$p_{fc} = -0.2625 + 32.5\, a \tag{45}$$

and H denotes the Heaviside unit function, i.e., $H(\eta) = 0$ for $\eta < 0$ and $H(\eta) = 1$ for $\eta > 0$.

For $-0.025 \leqq a \leqq 0$

$$x^* = \frac{\pi}{\sqrt{0.0048\, p_f}} + \frac{688.1\, (-a)^{1.027}}{p_f^{[1.007/(10^{0.587\, a})]}}, \tag{46}$$

$$m^* = -q_f \times 10^{[\alpha_m/(p_f^{\beta_m})-6]}, \tag{47}$$

in which

$$\left.\begin{aligned} \alpha_m &= 7.469 + 9.20\, a \\ \beta_m &= 0.02695 + 0.867\, a \end{aligned}\right\} \text{ for } -0.025 \leqq a \leqq -0.0125 \tag{48a, 48b}$$

$$\left.\begin{aligned} \alpha_m &= 7.480 + 10.10\, a \\ \beta_m &= 0.02816 + 0.964\, a \end{aligned}\right\} \text{ for } -0.0125 \leqq a \leqq 0 \tag{49a, 49b}$$

The approximate Euler lengths obtained from Eqs. (40) and (46) are plotted as dashed lines in Fig. 6. The approximate values of m^* obtained from Eqs. (41) and (47) are plotted as dashed lines in Fig. 7. It is seen that, in both cases, the approximation is satisfactory for practical purposes.

12. Interaction Curves

For a given set of ϵ_0, R_0, a, p_f, and q_f, a family of equilibrium curves, as shown in Fig. 5 (a), can be constructed. From this family of curves, an $m - m_f$ curve can be plotted for a given value of x such as shown in Fig. 5 (b). At point a or b where the slope of the $m - m_f$ curve vanishes, i.e.,

$$\frac{\partial m}{\partial m_f} = 0 \tag{50}$$

the column is in the state of neutral equilibrium. Thus, Eq. (50) defines the limit of stability and is used as the inelastic stability criterion. The loci of all maximum points such as a and minimum points such as b corresponding to different values of x represent, respectively, the upper and lower envelopes

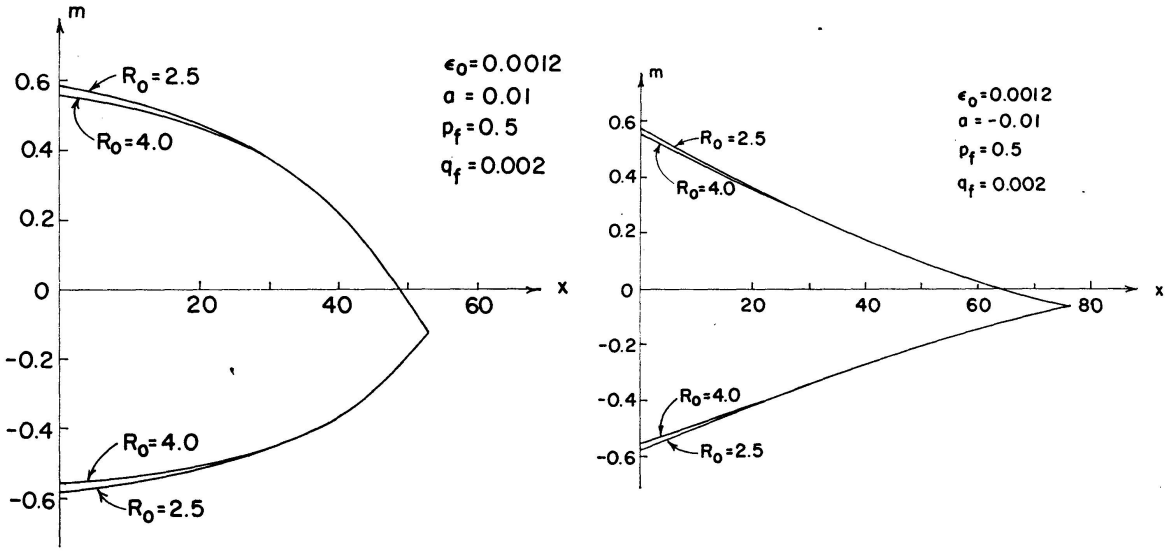


Fig. 8. Influence of R_0 on interaction curves.

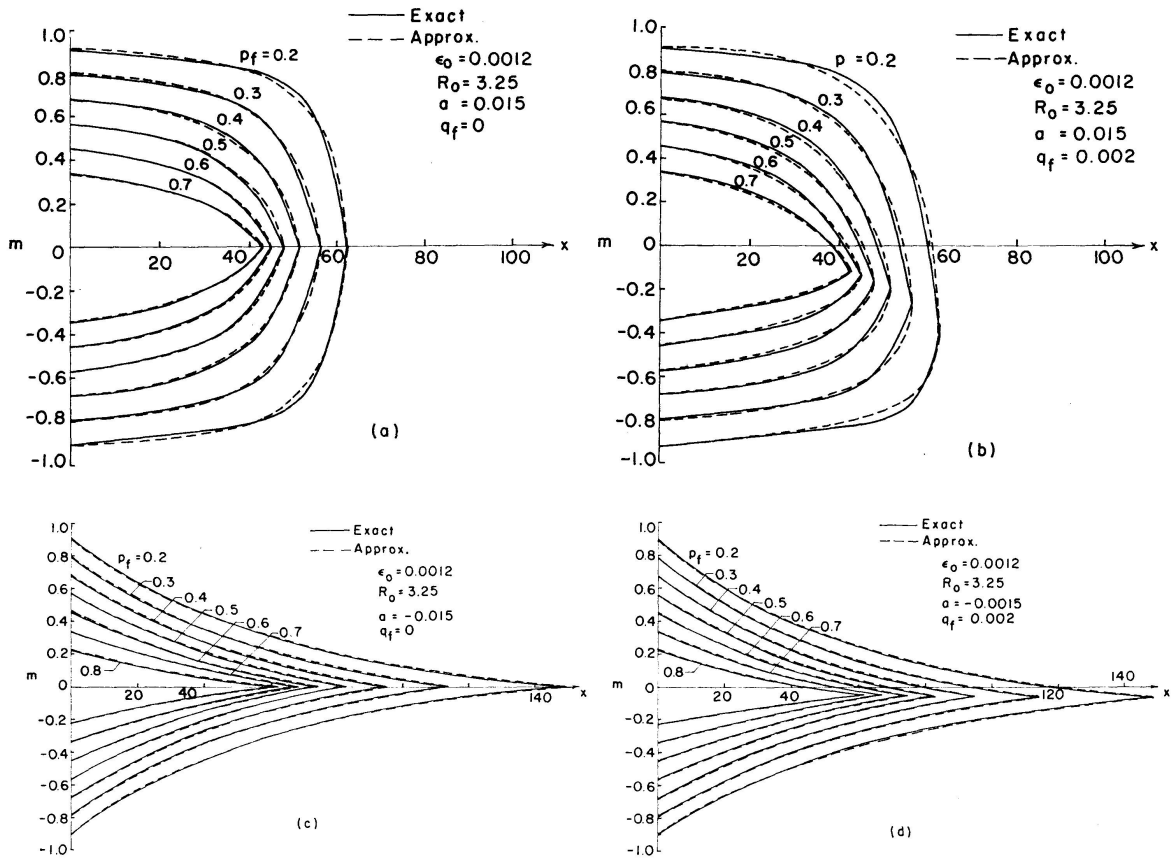


Fig. 9. Interaction curves.

of the family of equilibrium curves as shown in Fig. 5 (a). The envelopes are referred to as interaction curves and define the ultimate strength of the tapered cantilever column under various end loading conditions.

It is found that the interaction curve is insensitive to the parameter R_0 as shown in Fig. 8. Typical interaction curves are presented in Fig. 9.

Let q_f^* and q_f^{**} be the values of q_f which satisfy, respectively,

$$m^* = -m_e^*, \tag{51}$$

$$m^* = -m_{pl}^*, \tag{52}$$

where m_e^* and m_{pl}^* are, respectively, the values of m_e and m_{pl} at $x=x^*$. The $q_f^*-p_f$ and $q_f^{**}-p_f$ curves for various taper slopes are shown in Fig. 10.

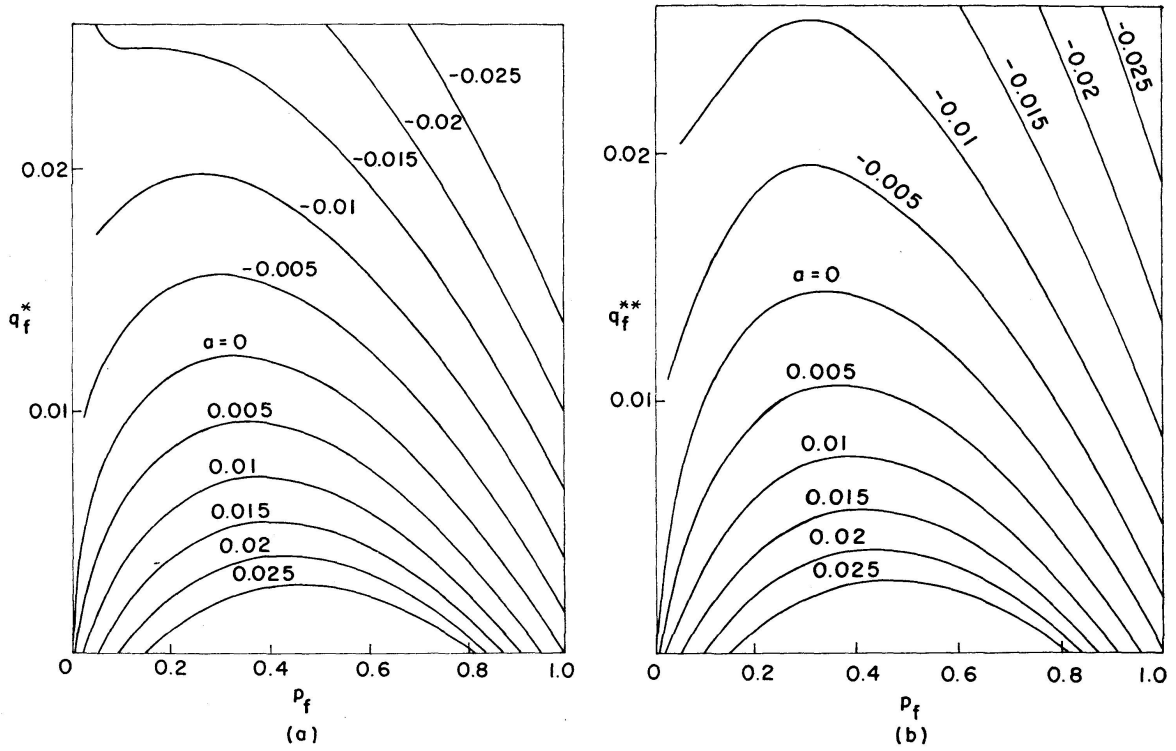


Fig. 10. q_f^* and q_f^{**}—p_f curves.

The intersection of the upper and lower envelopes is the same as the common point (x^*, m^*) of the elastic equilibrium curves as long as $q_f \leqq q_f^*$. When q_f exceeds q^*, neither the elastic equilibrium curve nor the common point exists. However, the numerical value of m^* can still be computed as if the column were infinitely elastic. For $q_f^* < q_f \leqq q_f^{**}$, it can be shown that the point (x^*, m^*) still defines the intersection of the envelopes.

For $q_f \geqq q_f^*$, the $-m_{pl}(x)$ curve, which is independent of q_f, completely governs the lower envelope and the intersection, denoted by (x^{**}, m^{**}), shifts along the lower envelope toward the negative x-direction as q_f increases. Therefore, the maximum admissible length x^{**} is smaller than the Euler length x^*. The computed (x^*, m^*), which lies outside of the admissible domain,

will be used in the next section as a fictitious end point of the upper envelope for obtaining approximate interaction equations. The point (x^{**}, m^{**}) can be located numerically by intersecting the upper and lower envelopes.

13. Approximate Interaction Equation

The actual interaction curves constructed for $R_0 = 3.25$ and $\epsilon_0 = 0.0012$ for taper slopes in the ranges $0.005 \leqq |a| \leqq 0.025$ may be approximated by the following expressions.

The upper envelope is approximated by

$$m = \overline{m} + (m^* - \overline{m})\,\xi + \mu\,[10 - 10\,(a - 0.01)\,H\,(a - 0.01)] \tag{53}$$

and the lower envelope by

$$m = -\overline{m} + (m^* + \overline{m})\,\xi + \mu\,[10 - 10\,(a - 0.01)\,H\,(a - 0.01)] \quad \text{for } 0 \leqq q_f \leqq q_f^{**}, \tag{54a}$$

$$m = -\overline{m} + (m_{pl}^* + \overline{m}) \quad \text{for } q_f \geqq q_f^{**}, \tag{54b}$$

in which $\overline{m} = m_{pl}(0)$, $m_{pl}^* = m_{pl}(x^*)$, $\xi = x/x^*$, x^* is obtained from Eq. (40) or Eq. (46), m^* from Eq. (41) or Eq. (47) and

$$\left.\begin{aligned} \mu &= C\,\bar{\xi}\,(1 - \bar{\xi}^2)^n && (55a)\\ n &= \frac{(1 - \bar{\xi}^2)}{2\,\bar{\xi}^2} && (55b)\\ C &= \frac{\bar{\mu}}{\bar{\xi}\,(1 - \bar{\xi}^2)^n} && (55c) \end{aligned}\right\} \quad \text{for } \bar{\xi} \geqq 0.5,$$

$$\left.\begin{aligned} \mu &= C\,(1 - \xi)\,(2\,\xi - \xi^2)^n && (56a)\\ n &= \frac{2\,\bar{\xi} - \bar{\xi}^2}{2\,(1 - \bar{\xi})^2} && (56b)\\ C &= \frac{\bar{\mu}}{(1 - \bar{\xi})\,(2\,\bar{\xi} - \bar{\xi}^2)^n} && (56c) \end{aligned}\right\} \quad \text{for } \bar{\xi} \leqq 0.5.$$

The new variables $\bar{\xi}$ and $\bar{\mu}$ in Eqs. (55) and (56) are functions of a, p_f, and q_f and defined as follows:

For $0.005 \leqq a \leqq 0.025$,

$$\bar{\xi} = 0.5254 \times 10^{[8.31\,a + (p_f - 0.4)\,\psi_1]} - (23\,p_f + 7)\,q_f, \tag{57}$$

$$\bar{\mu} = 3.743\,a^{0.6057} - (p_f - 0.4)\,\psi_2 + 1641000\,a^{2.685}\,(2\,p_f)^{-\sqrt{3}}\,q_f \tag{58}$$

for the upper envelope, and

$$\bar{\xi} = 0.5254 \times 10^{[8.31\,a + (p_f - 0.4)\,\psi_1]} + [22 - 38.44 \times 10^{-35.43\,a} + (p_f - 0.4)\,\psi_3]\,q_f, \tag{59}$$

$$\bar{\mu} = -3.743\,a^{0.6057} - (p_f - 0.4)\,\psi_2 + 8.464 \times 10^{48.74\,a}\,(2.5\,p_f)^{\psi_4}\,q_f \tag{60}$$

for the lower envelope, in which

$$\psi_1 = 0.4354\,a^{-0.1401} - 1 \qquad \text{for } p_f \leqq 0.4, \tag{61a}$$

$$\psi_1 = -4.242\,a^{0.9247} \qquad \text{for } p_f \geqq 0.4, \tag{61b}$$

$$\psi_2 = -21.47\,a^{0.6888} \qquad \text{for } p_f \leqq 0.4 \text{ and } a \leqq 0.02, \tag{62a}$$

$$\psi_2 = -1.45 \qquad \text{for } p_f \leqq 0.4 \text{ and } a \geqq 0.02, \tag{62b}$$

$$\psi_2 = -17.48\,a^{0.785} \qquad \text{for } p_f \geqq 0.4, \tag{62c}$$

$$\psi_3 = -35 \qquad \text{for } p_f \leqq 0.4, \tag{63a}$$

$$\psi_3 = -15 \qquad \text{for } p_f \geqq 0.4, \tag{63b}$$

$$\psi_4 = -0.931 \times 10^{15.49\,a} \qquad \text{for } p_f \geqq 0.4, \tag{64a}$$

$$\psi_4 = -0.2644 \times 10^{27.67\,a} \qquad \text{for } p_f \geqq 0.4. \tag{64b}$$

For $-0.025 \leqq a \leqq -0.005$

$$\bar{\xi} = 0.1012\,(-a)^{-0.3544} \times 10^{(p_f - 0.4)\psi_5} + (1.4 - 15\,p_f)\,q_f, \tag{65}$$

$$\bar{\mu} = \psi_6 - 6.705\,p_f^{-0.4949}\,q_f \tag{66}$$

for the upper envelope, and

$$\bar{\xi} = 0.1012\,(-a)^{-0.3544} \times 10^{(p_f - 0.4)\psi_5} + [0.0153\,(-a)^{-1.75\,b}\,p_f^{1.337} - 1]\,q_f, \tag{67}$$

$$\bar{\mu} = \psi_6 - 6.705\,p_f^{-0.4949}\,q_f \tag{68}$$

for the lower envelope, in which

$$\psi_5 = 0.2 - 5\,a \qquad \text{for } p_f \leqq 0.4, \tag{69}$$

$$\psi_5 = 0.1875 \qquad \text{for } p_f \geqq 0.4, \tag{70}$$

$$\psi_6 = 11.52\,(-a)^{0.7619} \times 10^{-0.3745\,(-a)^{-0.331}\,p_f} \qquad \text{for } p_f \leqq 0.6, \tag{71a}$$

$$\psi_6 = 11.52\,(-a)^{0.7619} \times 10^{-[0.2247(-a)^{-0.331} + 2\,p_f - 1.2]} \qquad \text{for } p_f \geqq 0.6. \tag{71b}$$

The curves defined by Eqs. (53) and (54) are plotted in dashed lines alongside the actual interaction curves in Fig. 9 and show reasonably close approximation. Being insensitive to the parameter R_0, the interaction curves in Fig. 9 or the approximate expressions given by Eqs. (53) and (54) may be applied for practical purposes to tapered wide-flange cantilever columns made of A 36 steel for $2.5 \leqq R_0 \leqq 4.0$.

In the case where q_f exceeds q_f^{**}, the intersection of the upper and lower envelopes, i.e., (x^{**}, m^{**}), is readily located by solving Eqs. (53) and (54b) simultaneously.

It should be pointed out that the interaction equations presented above do not apply for the range $-0.005 < a < 0.005$. In practice, tapered columns in this range are hardly used.

14. Simply Supported Columns

The approximate interaction equations, Eqs. (53) and (54), derived for cantilever columns can be extended to the treatment of the simply supported tapered column shown in Fig. 11 (a). The column is subjected to axial force P

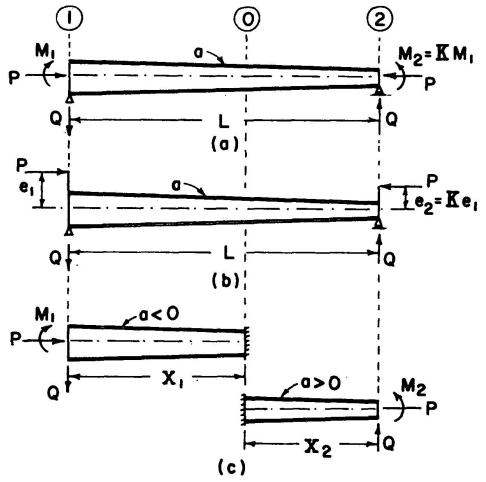


Fig. 11. Simply supported tapered columns.

and unequal end moments M_1 and M_2 where $M_2 = K M_1$, for $-1 \leqq K \leqq 1$. The simply supported column of length L may be considered as two cantilever columns of lengths X_1 and X_2 with the fixed end located at section 0 as shown in Fig. 11 (c). The taper slopes of the two cantilever columns are of the same magnitude but of opposite sign and the fixed end is taken as the reference section.

Referring to Fig. 11 (c), the right segment X_2 is subjected to the same type of loading as the cantilever column of Fig. 2. However, the shear force Q acting on the left segment X_1 is opposite in sense to that shown in Fig. 2. Therefore, the corresponding interaction curves for the left segment must be turned upside down as shown in Fig. 12 where the x_1-axis is directed toward the left for convenience in the combined $m - x_1$ and $m - x_2$ planes.

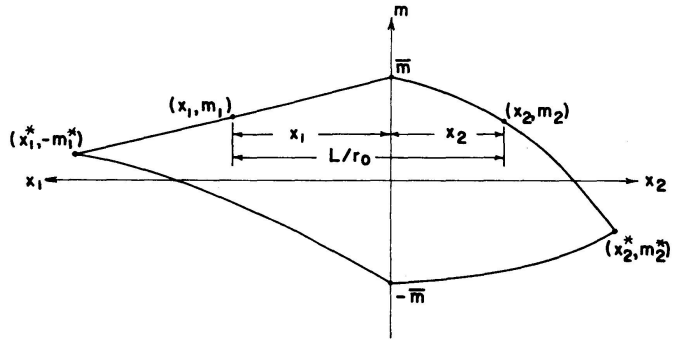


Fig. 12. Interaction curves for a simply supported tapered column.

The values of x_1 and x_2 at the point where the column becomes unstable are not known *a priori*. However, the relation

$$x_1 + x_2 = \frac{L}{r_0} \tag{72}$$

must hold true and the points (x_1, m_1) and (x_2, m_2) must both lie on the interaction curves. In other words, the solution of the stability problem is reduced to solving three simultaneous algebraic equations by a trial-and-error procedure outlined in the following.

Suppose p_1 and K are specified for a given column, and the critical value of m_1 is to be determined. Referring to Fig. 11, let R_1 and r_1 be the flange-web area ratio and the radius of gyration, respectively, of section 1 and $\lambda_1 = a\sqrt{(R_1+1/3)/(R_1+1)}$ in which a assumes a positive value. A trial reference section 0 is located by assuming a value of X_1/r_1. The relation

$$\left(\frac{r_1}{r_0}\right) = \frac{\sqrt{\frac{R_1+\frac{1}{3}}{R_1+1}}}{\frac{R_1+\frac{1}{3}\left[1-\lambda_1\left(\frac{X_1}{r_1}\right)\right]}{\sqrt{R_1+1-\lambda_1\left(\frac{X_1}{r_1}\right)}}\left[1-\lambda_1\left(\frac{X_1}{r_1}\right)\right]} \tag{73}$$

is readily established in view of Eq. (11), and x_1 and x_2 are then obtained, respectively, from

$$x_1 = \left(\frac{X_1}{r_1}\right)\left(\frac{r_1}{r_0}\right), \tag{74a}$$

$$x_2 = \left(\frac{L}{r_1} - \frac{X_1}{r_1}\right)\left(\frac{r_1}{r_0}\right). \tag{74b}$$

The nondimensional axial force with reference to section 0 is given by

$$p_f = \frac{R_1+1}{R_1+1-\lambda_1\left(\frac{X_1}{r_1}\right)} p_1. \tag{75}$$

Knowing p_f, the corresponding x^* for the right and left segments are computed, respectively, from Eqs. (40) and (46). The value of m^*_{pl} for each segment are obtained from Eq. (41) or (47).

Next assume a trial value of m_1, corresponding to which

$$m_2 = \kappa m_1 \tag{76a}$$

where

$$\kappa = \frac{(R_1+\frac{1}{2})}{\left\{R_1+\frac{1}{2}\left[1-\lambda_1\left(\frac{L}{r_1}\right)\right]\right\}\left[1-\lambda_1\left(\frac{L}{r_1}\right)\right]} K, \tag{76b}$$

the nondimensional shear force is given by

$$q_f = \frac{m_1}{\left(\frac{L}{r_1}\right)} \frac{(R_1+\frac{1}{2})(1-K)}{\sqrt{\frac{R_1+\frac{1}{3}}{R_1+1}}\left[R_1+1-\lambda_1\left(\frac{X_1}{r_1}\right)\right]}. \tag{77}$$

The value of m^*, which is a function of q_f, for the right segment is obtained from Eq. (41). In the case where $m^* < -m^*_{pl}$, the intersection of the upper and lower envelopes, (x^{**}, m^{**}), must be computed by the method described in Section 13. For the left segment, m^* corresponding to Q acting in the direction opposite to that shown in Fig. 11 (c) is obtained from Eq. (47).

Table 1. Classification of Interaction Equations

Case	Left Segment, $a<0$, $x=x_1$			Right Segment, $a>0$, $x=x_2$	
1a 1b 1c 1d	$0 \leqq q_f \leqq q_f^{**}$ i. e., $0 \geqq m^* \geqq -m_{pl}^*$	$m_1 \geqq -m^*$ $m_1 \leqq -m^*$	Eqs. 54a, 67, 68 Eqs. 53, 65, 66	$0 \leqq q_f \leqq q_f^{**}$ i. e., $0 \geqq m^* \geqq -m_{pl}^*$	$m_2 \geqq m^*$ Eqs. 53, 57, 58 $m_2 \leqq m^*$ Eqs. 54a, 59, 60 $m_2 \geqq m^*$ Eqs. 53, 57, 58 $m_2 \leqq m^*$ Eqs. 54a, 59, 60
2a 2b 2c 2d	$0 \leqq q_f \leqq q_f^{**}$ i. e., $0 \geqq m^* \geqq -m_{pl}^*$	$m_1 \geqq -m^*$ $m_1 \leqq m^* \leqq m_{pl}^*$	Eqs. 54a, 67, 68 Eqs. 53, 65, 66	$q_f \geqq q_f^{**}$ i. e., $m^* \leqq -m_{pl}^*$	$m_2 \geqq m^{**}$ Eqs. 53, 57, 58 $m_2 \leqq m^{**}$ Eqs. 54b $m_2 \geqq m^{**}$ Eqs. 53, 57, 58 $m_2 \leqq m^{**}$ Eqs. 54b

Note: m is replaced by $-m$ when Eqs. 53 and 54 are applied to the left segment.

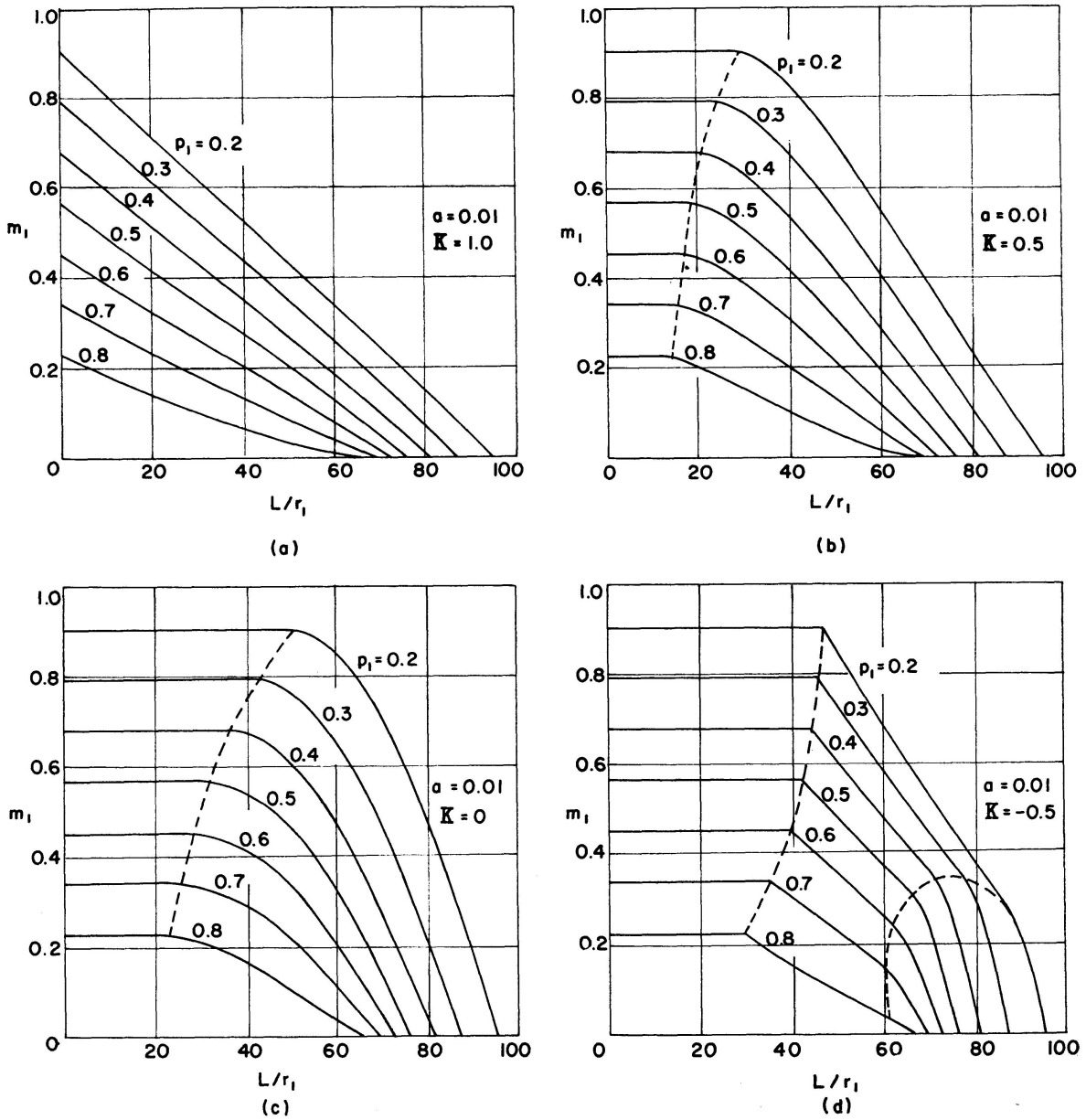


Fig. 13. Column curves (A 36 steel).

The value of q_f determines which set of the approximate interaction curves is to be used for the solution of a given problem. Two cases, each contains four subcases, thus arise and are listed in Table 1.

Once the appropriate set of interaction equations is chosen for the particular case listed in Table 1, the values of the interaction curves at x_1 and x_2 can be computed and compared with the trial values of m_1 and m_2, respec-

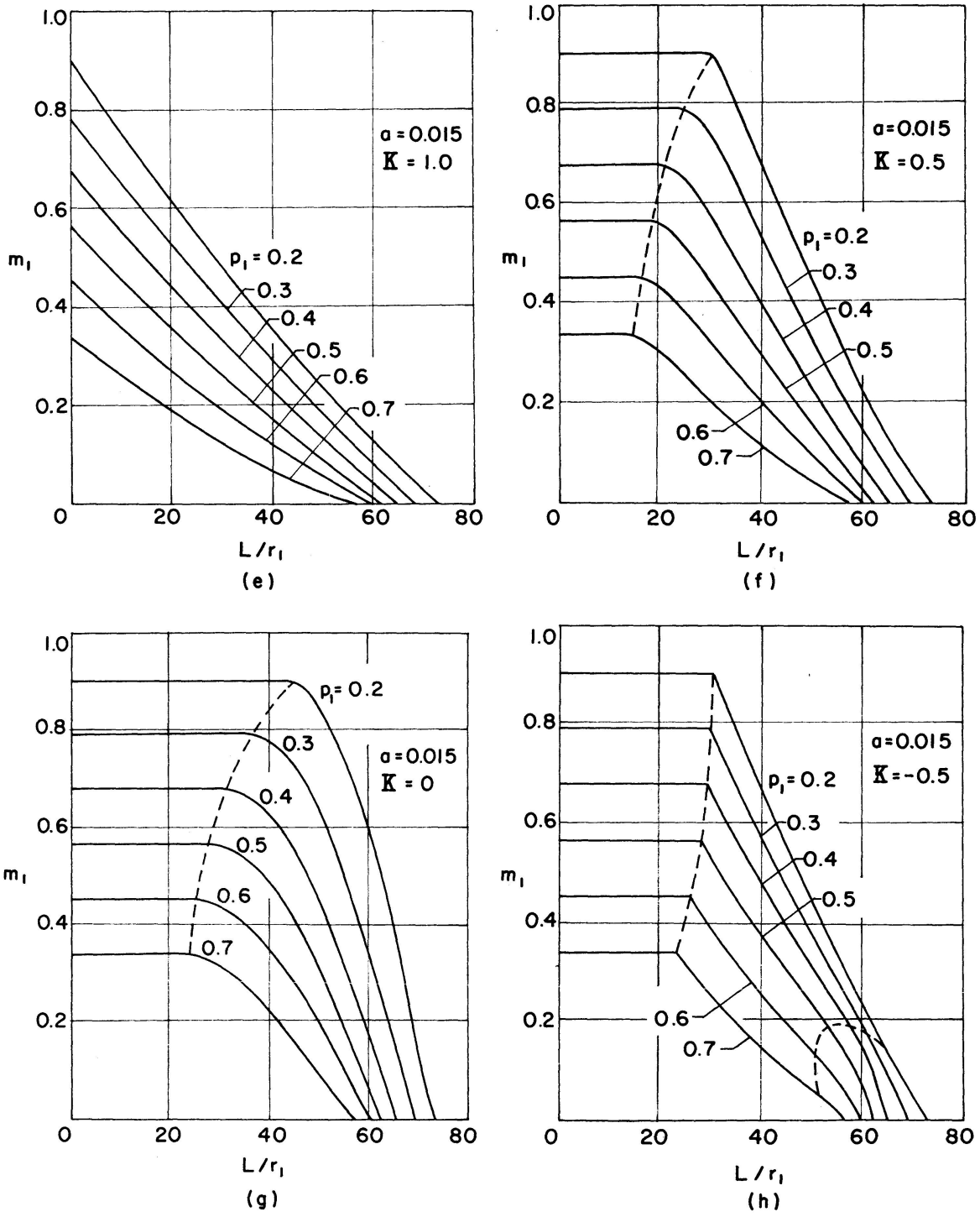


Fig. 13. Column curves (A 36 steel).

tively. The trial value of m_1 is varied until the interaction equation for each segment is satisfied. However, the two interaction equations may not be satisfied for the same trial value of m_1. It is necessary to vary the trial value of X_1/r_1 and to repeat the above-mentioned process until both interaction equations are satisfied simultaneously. The corresponding value of m_1 gives the critical end moment.

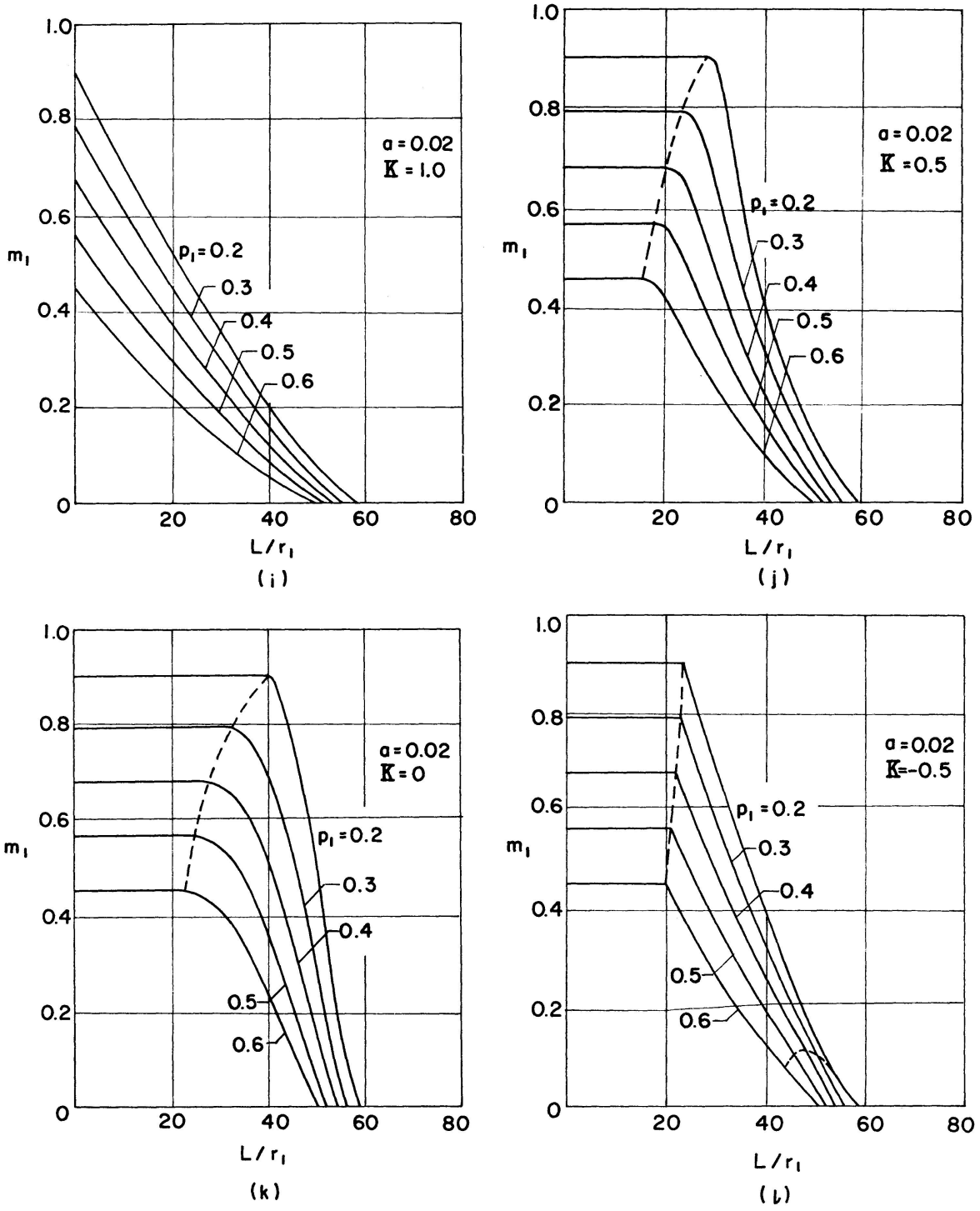


Fig. 13. Column curves (A 36 steel).

The trial-and-error procedure described above, taking into account all the cases shown in Table 1, is built into a computer program.

15. Column Curves

Column curves, i.e., $m_1 - L/r_1$ curves, are prepared for A 36 steel in Fig. 12 for various combinations of the parameters a, p_1, and K. These curves can be used to solve for ultimate loads of A 36 steel wide-flange columns subjected to various end loading conditions.

It is of interest to observe that for the case where $K = 1$, i.e., Figs. 13 (a), (e), and (i), the carrying capacity of the columns is governed entirely by instability. For $0 \leqq K < 1$, the ultimate load carrying capacity is governed either by yielding of the large end section for short columns or by instability for longer columns, and the demarcation line between these two regions is shown by the dashed line in Figs. 13 (b), (c), (f), (g), (j) and (k). When $K < 0$, there are three different regions, separated by the dashed lines shown in Fig. 13 (d), (h), and (l), representing, from left to right, yielding of the large end section, yielding of the small end section, and instability.

16. Illustrative Examples

A few examples illustrating the use of the approximate interaction equations as well as the column curves are given in the following.

Example 1. A tapered wide-flange cantilever column made of A 36 steel is loaded as shown in Fig. 2. Find the critical values of the applied end moment m if $L/r_0 = 35$, $R_0 = 3.25$, $a = 0.015$, $p_f = 0.5$, and $q_f = 0.002$.

Eqs. (40) and (41) give, respectively, $x^* = 47.88$ and $m^* = -0.1586$. Setting $x = 0$ in Eq. (17a) yields $\overline{m} = 0.5667$ and, referring to Fig. 10, it is found that $0 < q_f < q_f^{**}$ in this case.

Upper limit: Substituting a, p_f, and q_f into Eqs. (57) and (58) give $\bar{\xi} = 0.6491$ and $\bar{\mu} = 0.2710$ for which $n = 0.6866$ is obtained from Eq. (55b) and $C = 0.6079$ from Eq. (55c). Substituting $\xi = 35/47.88$ into Eq. (55a) gives $\mu = 0.2629$. Finally Eq. (53) yields $m = 0.2863$ which is the upper limit of m.

Lower limit: Substituting a, p_f, and q_f into Eqs. (59) and (60) give $\bar{\xi} = 0.7045$ and $\bar{\mu} = -0.1513$, respectively, for which $n = 0.5073$ is obtained from Eq. (55b) and $C = -0.3041$ from Eq. (55c). Substituting $\xi = 35/47.88$ into Eq. (55a) yields $\mu = -0.1508$. Finally, Eq. (54a) yields $m = -0.4117$, which is the lower limit of m.

As long as $-0.4117 < m < 0.2863$, the column is stable. The values obtained from the actual interaction curves, Fig. 9 (b), are $-0.422 < m < 0.304$.

Example 2. A tapered wide-flange column made of A 36 steel is simply supported and eccentrically loaded as shown in Fig. 11 (b). Find the critical

value of p_1 at which the column passes from stable to unstable equilibrium if $L/r_1 = 40$, $R_1 = 2.5$, $a = 0.015$, $e_2/e_1 = 0.5$. and $e_1' = e_1 A_1/Z_1 = m_1/p_1 = 0.8$.

From Fig. 13 (f), an $m_1 - p_1$ curve for $L/r_1 = 40$ is constructed as shown in Fig. 14. The solution is obtained by intersecting this curve with the straight line $m_1 = 0.8\, p_1$. This gives $p_1 = 0.442$ as the critical value for which $m_1 = p_1 e_1' = 0.3536$.

Using $p_1 = 0.442$ in solving the approximate interaction equations for m_1, by means of the trial-and-error procedure described in Section 14, yields $m_1 = 0.3547$ which verifies the graphical solution.

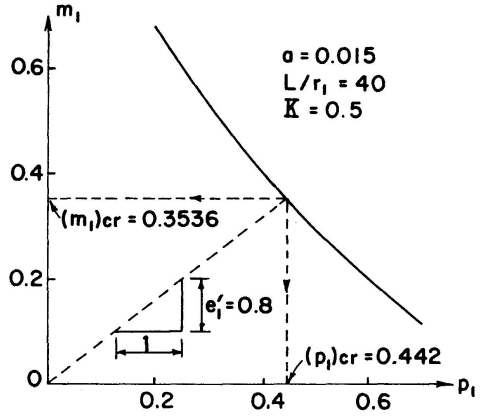


Fig. 14. Graphical solution of example 2.

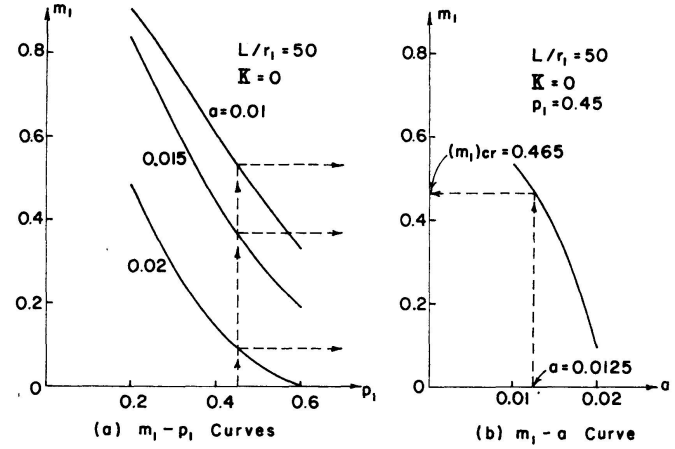


Fig. 15. Graphical solution of example 3.

Example 3. A simply supported tapered wide-flange column made of A 36 steel, as shown in Fig. 11 (a), is subjected to the end moment at the left end in addition to the axial force, i. e., $K = 0$. Find the maximum value of the end moment for which the column remains stable if $L/r_1 = 50$, $R_1 = 2.5$, $a = 0.0125$, and $p_1 = 0.45$.

From Figs. 13 (c), (g), and (k), the $m_1 - p_1$ curves for $L/r_1 = 50$ are plotted for three different values of a as shown in Fig. 15 (a). From these curves, read off the values of m_1 at $p_1 = 0.45$ and plot them against a as shown in Fig. 15 (b) from which $m_1 = 0.465$ is obtained for $a = 0.0125$. The value obtained from the approximate interaction equations is $m_1 = 0.472$.

17. Conclusions

The method presented above leads to a more realistic evaluation of the strength of tapered columns than is possible either from a consideration of elastic behavior only, or from the elementary treatment of columns concentrically loaded into the plastic range.

The curvature functions, expressed in closed form, are also valid for box sections provided the stress-strain relationship and cross sections are idealized the same way.

The excellent agreement between the exact solution and the numerical solution for x^* and m^* assures the applicability of the latter which is straightforward and less time-consuming. It is observed that the interaction curves are insensitive to the parameter R_0. For practical purposes, $R_0 = 3.25$ is used to derive the approximate interaction equations. It schould be pointed out that for materials other than A 36 steel, the approximate expressions must be rederived.

The carrying capacity of simply supported columns is governed by inelastic instability, yielding at the large end, or yielding at the small end depending on the combination of the parameters a, K and p_1.

With appropriate modifications in the formulations, the present method can be extended to investigate the inelastic stability of columns of nonlinear taper, or elastic-strain hardening materials.

18. References

1. Dinnik, A. N.: Design of Columns of Varying Cross Section. Transactions, ASME, Vol. 51, APM-51-11, 1929, p. 105—114, and Vol. 54, APM-54-16, 1932, p. 165—171.
2. Timoshenko, S. P., and Gere, J. M.: Theory of Elastic Stability. 2nd ed., McGraw-Hill Book Co., Inc., New York, 1961, p. 125—132.
3. Nakagawa, H.: Buckling of Columns with Tapered Part. Transactions, Japan Society of Mechanical Engineers, Vol. 3, No. 11, May, 1937, p. 111—119.
4. Miesse, C. C.: Determination of the Buckling Load for Columns of Variable Stiffness. Transactions, ASME, Vol. 71, 1949, p. 406—410.
5. Bleich, F.: Buckling Strength of Metal Structures. McGraw-Hill Book Co., Inc., New York, 1952, p. 186—192.
6. Gere, J. M. and Carter, W. O.: Critical Buckling Loads for Tapered Columns. Journal of the Structural Division, ASCE, Vol. 88, No. ST 1, Proc. Paper 3045, February, 1962, p. 1—11.
7. Gatewood, B. E.: Buckling Loads for Beams of Variable Cross Section under Combined Loads. Journal of the Aeronautical Sciences, Vol. 22, No. 4, April, 1955, p. 281—282.
8. Fogel, C. M. and Ketter, R. L.: Elastic Strength of Tapered Columns. Journal of the Structural Division, ASCE, Vol. 88, No. ST 5, Proc. Paper 3301, October 1962, p. 67—106.
9. Bulter, D. J. and Anderson, G. B.: The Elastic Buckling of Tapered Beam-Columns. Welding Journal, Vol. 42, 1963, p. 29-S—36-S.
10. Lee, G. C. and Kawai, T.: Elastic Stability of Tapered Members. Civil Engineering Project Report No. 44, Department of Civil Engineering, State University of New York at Buffalo, Buffalo, N. Y., April, 1967.
11. Culver, C. G. and Preg, S. M., Jr.: Elastic Stability of Tapered Beam-Columns. Journal of the Structural Division, ASCE, Vol. 94, No. ST 2, Proc. Paper 5796, February, 1968, p. 455—470.
12. Young, D. H.: Inelastic Buckling of Variable Section Columns. Transactions, ASME, Vol. 67, 1945, p. A-166-169.
13. Goldberg, J. E., Bogandoff, J. L. and Lo, H.: Inelastic Buckling of Nonuniform Columns. Transactions, ASCE, Vol. 122, 1957, p. 722—730.

14. Appl, F. J. and Smith, J. O.: Buckling of Inelastic, Tapered, Pin-Ended Columns. Journal of the Engineering Mechanics Division, ASCE, Vol. 94, No. EM 2, Proc. Paper 5897, April, 1968, p. 549—558.
15. Horne, M. R.: The Elastic-Plastic Theory of Compression Members. Journal of the Mechanics and Physics of Solids, Vol. 4, 1956, p. 104—120.
16. Hauck, G. F. and Lee, S. L.: Stability of Elasto-Plastic Wide-Flange Columns. Journal of the Structural Division, ASCE, Vol. 89, No. St 6, Proc. Paper 3738, December, 1963, p. 297—324.
17. Lee, S. L. and Hauck, G. F.: Buckling of Steel Columns under Arbitrary End Loads. Journal of the Structural Division, ASCE, Vol. 90, No. ST 2, Proc. Paper 3872, April, 1964, p. 179—200.
18. Lee, S. L. and Anand, S. C.: Buckling of Eccentrically Loaded Steel Columns. Journal of the Structural Division, ASCE, Vol. 93, No. ST 2, Proc. Paper 4796, April, 1967, p. 351—370.

Summary

The stability of symmetrically and linearly tapered wide-flange columns made of elastic-plastic materials and subjected to combined bending and axial loads is investigated. Torsional-flexural behavior is not considered. Approximate interaction equations are derived for cantilever columns. These interaction equations are used to determine the load carrying capacity of simply supported columns subjected to arbitrary end loading conditions. Column curves for A 36 steel are prepared. Numerical examples are given to illustrate the use of the approximate interaction equations as well as the column curves.

Résumé

Des études de stabilité sous sollicitation combinée flexion-compression ont été faites sur des colonnes émincées symétriquement et linéairement, à larges ailes et en un matériau élastoplastique. Les effets de torsion de flexion ont été négligés. Pour les colonnes encastrées, on a développé des équations d'interaction approximées, qui servent à déterminer la charge de rupture de colonnes simples, soumises à des conditions de charge arbitraires. Des courbes pour colonnes en acier A 36 sont en préparation. Des valeurs numériques sont données pour illustrer l'emploi des équations et des courbes.

Zusammenfassung

Symmetrisch und linear verjüngte Breitflanschstützen aus elastoplastischem Material wurden unter einer gleichzeitigen Biege- und Druckbeanspruchung auf ihre Stabilität untersucht. Das Biegedrillverhalten wurde dabei nicht berücksichtigt. Für eingespannte Stützen wurden Näherungsgleichungen entwickelt, mit deren Hilfe man die Bruchlast von einfachen Stützen für beliebige Lastfälle bestimmen kann. Diagramme für Stützen aus Stahl A 36 sind in Vorbereitung. Es wurden numerische Werte gegeben, um den Gebrauch der Gleichungen und der Diagramme zu veranschaulichen.

Comportement postcritique des plaques cisaillées raidies
Deuxième partie: Répartition des contraintes et analyse de l'état limite

Verhalten von ausgesteiften Platten bei Schub im überkritischen Bereich
2. Teil: Spannungsverteilung und Analyse des Grenzzustandes

Postbuckling Behaviour of Stiffened Plates Subjected to Pure Shear
2nd Part: Distribution of Stress and Analysis of the Limit State

CH. MASSONNET
Professeur Ordinaire à l'Université de Liège

M. ŠKALOUD
Doc. Ing. Csc. à l'Institut de Mécanique Théorique et Appliquée de l'Académie des Sciences de Prague

J. DONEA
Ingénieur Physicien. Ancien Aspirant F.N.R.S. Université de Liège

Introduction

Le présent rapport constitue la seconde partie d'une étude consacrée au comportement postcritique des plaques raidies cisaillées uniformément.

Dans une première partie publiée dans les mémoires de l'A.I.P.C. [1], nous avons exposé la mise en équation du problème et présenté les valeurs de la charge critique de voilement ainsi que de la déformée dans le cas particulier d'une plaque carrée renforcée par un raidisseur vertical médian de rigidité relative comprise entre zéro et trois.

L'objet de la présente note consiste en l'étude de la répartition des contraintes et l'analyse de l'état limite dans le même cas particulier d'une plaque carrée raidie cisaillée uniformément.

Par souci de clarté, il nous a paru intéressant de résumer très brièvement dans un premier paragraphe les hypothèses de base de notre analyse. Le lecteur désireux de trouver un exposé détaillé de la question consultera la référence [1].

1. Bref rappel des hypothèses de travail

L'étude linéaire du voilement des plaques raidies cisaillées uniformément nous a conduit à représenter la déformée W de l'âme par l'expression à 6 paramètres:

$$W = f_1 \sin\frac{\pi x}{2a}\sin\frac{3\pi y}{b} + f_2 \sin\frac{3\pi x}{2a}\sin\frac{\pi y}{b} + f_3 \sin\frac{2\pi x}{a}\sin\frac{2\pi y}{b}$$
$$+ f_4 \sin\frac{\pi x}{2a}\sin\frac{\pi y}{b} + f_5 \sin\frac{\pi x}{a}\sin\frac{2\pi y}{b} + f_6 \sin\frac{3\pi x}{2a}\sin\frac{3\pi y}{b}. \tag{1.1}$$

Les axes coordonnés sont disposés comme l'indique la fig. 1; b est la hauteur de la plaque, sa largeur est $2a$.

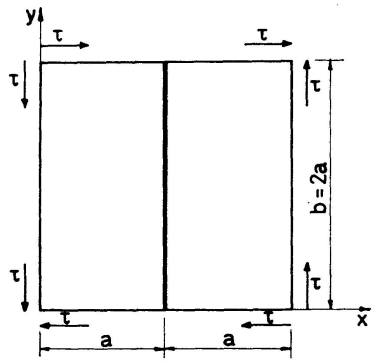


Fig. 1.

L'expression (1.1.) satisfait visiblement les conditions aux limites relatives à la déformée d'une plaque simplement appuyée sur son contour.

La fonction d'Airy génératrice des contraintes membranaires a été obtenue comme solution de l'équation de VON KARMAN:

$$\frac{\partial^4\phi}{\partial x^4} + 2\frac{\partial^4\phi}{\partial x^2\partial y^2} + \frac{\partial^4\phi}{\partial y^4} = E\left[\left(\frac{\partial^2 w}{\partial x\,\partial y}\right)^2 - \frac{\partial^2 w}{\partial x^2}\frac{\partial^2 w}{\partial y^2}\right]. \tag{1.2}$$

Nous avons admis qu'au cours du voilement les bords opposés de la plaque restent rectilignes et se rapprochent librement. Nous avons supposé, en outre, que la plaque peut se déplacer librement sur les éléments qui la limitent dans la direction du bord correspondant.

Les paramètres f_i caractérisant la déformée de la plaque sont les inconnues du problème. Ils ont été déterminés par la méthode énergétique de Rayleigh-Ritz en fonction de la rigidité relative du raidisseur et de la sollicitation de cisaillement.

2. Contraintes membranaires

2.1. Les expressions analytiques

Les contraintes membranaires sont fournies par les doubles dérivations de la fonction d'Airy:

$$\sigma_{xm} = \frac{\partial^2\phi}{\partial y^2}, \qquad \sigma_{ym} = \frac{\partial^2\phi}{\partial x^2}, \qquad \tau_m = \frac{-\partial^2\phi}{\partial x\,\partial y}. \tag{2.1}$$

Nous désignerons par α le rapport a/b de la demi-longueur et de la hauteur

de la plaque et par τ_{cr}^* la contrainte critique de cisaillement de la plaque non raidie de référence, à savoir:

$$\tau_{cr}^* = 0{,}8625 \frac{\pi^2 E}{\lambda^2}.$$

E est le module de Young et λ l'élancement b/e.

Avec ces notations et en divisant les paramètres f_i de la déformée par l'épaisseur e de la plaque, les expressions analytiques des contraintes membranaires s'écrivent:

$$\begin{aligned}
\frac{\sigma_{xm}}{\tau_{cr}^*} = -1{,}159 \Bigg[& \frac{1}{32\alpha^2} f_1^2 \cos\frac{6\pi y}{b} + \frac{9}{32\alpha^2} f_2^2 \cos\frac{2\pi y}{b} + \frac{1}{2\alpha^2} f_3^2 \cos\frac{4\pi y}{b} \\
& + \frac{1}{32\alpha^2} f_4^2 \cos\frac{2\pi y}{b} + \frac{1}{8\alpha^2} f_5^2 \cos\frac{4\pi y}{b} + \frac{9}{32\alpha^2} f_6^2 \cos\frac{6\pi y}{b} \\
& + f_1 f_2 \left(\frac{-4\alpha^2}{1+8\alpha^2+16\alpha^4} \cos\frac{2\pi x}{a} \cos\frac{4\pi y}{b} + \frac{25\alpha^2}{16(1+2\alpha^2+\alpha^4)} \cos\frac{2\pi x}{a} \cos\frac{2\pi y}{b} \right. \\
& \quad \left. + \frac{100\alpha^2}{1+32\alpha^2+256\alpha^2} \cos\frac{\pi x}{a} \cos\frac{4\pi y}{b} - \frac{16\alpha^2}{1+8\alpha^2+16\alpha^4} \cos\frac{\pi x}{a} \cos\frac{2\pi y}{b} \right) \\
& + f_1 f_3 \left(\frac{-4\alpha^2}{1+8\alpha^2+16\alpha^4} \cos\frac{5\pi x}{2a} \cos\frac{5\pi y}{b} + \frac{196\alpha^2}{625+200\alpha^2+16\alpha^4} \cos\frac{5\pi x}{2a} \cos\frac{\pi y}{b} \right. \\
& \quad + \frac{4900\alpha^2}{81+1800\alpha^2+10000\alpha^4} \cos\frac{3\pi x}{2a} \cos\frac{5\pi y}{b} \\
& \quad \left. - \frac{100\alpha^2}{81+72\alpha^2+16\alpha^4} \cos\frac{3\pi x}{2a} \cos\frac{\pi y}{b} \right) \\
& + f_1 f_4 \left(\frac{-4\alpha^2}{1+32\alpha^2+256\alpha^4} \cos\frac{\pi x}{a} \cos\frac{4\pi y}{b} + \frac{4\alpha^2}{1+8\alpha^2+16\alpha^4} \cos\frac{\pi x}{a} \cos\frac{2\pi y}{b} \right. \\
& \quad \left. + \frac{1}{16\alpha^2} \cos\frac{4\pi y}{b} - \frac{1}{16\alpha^2} \cos\frac{2\pi y}{b} \right) \\
& + f_1 f_5 \left(\frac{-400\alpha^2}{81+1800\alpha^2+10000\alpha^4} \cos\frac{3\pi x}{2a} \cos\frac{5\pi y}{b} \right. \\
& \quad + \frac{64\alpha^2}{81+72\alpha^2+16\alpha^4} \cos\frac{3\pi x}{2a} \cos\frac{\pi y}{b} \\
& \quad \left. + \frac{1600\alpha^2}{1+200\alpha^2+10000\alpha^4} \cos\frac{\pi x}{2a} \cos\frac{5\pi y}{b} - \frac{16\alpha^2}{1+8\alpha^2+16\alpha^4} \cos\frac{\pi x}{2a} \cos\frac{\pi y}{b} \right) \\
& + f_1 f_6 \left(\frac{324\alpha^2}{1+72\alpha^2+1296\alpha^4} \cos\frac{\pi x}{a} \cos\frac{6\pi y}{b} \right. \\
& \quad \left. - \frac{81\alpha^2}{16+288\alpha^2+1296\alpha^4} \cos\frac{2\pi x}{a} \cos\frac{6\pi y}{b} \right) \\
& + f_2 f_3 \left(\frac{900\alpha^2}{1+72\alpha^2+1296\alpha^4} \cos\frac{\pi x}{2a} \cos\frac{3\pi y}{b} - \frac{4\alpha^2}{1+8\alpha^2+16\alpha^4} \cos\frac{\pi x}{2a} \cos\frac{\pi y}{b} \right.
\end{aligned}$$

$$
\begin{aligned}
&- \frac{36\,\alpha^2}{2401 + 3528\,\alpha^2 + 1296\,\alpha^4} \cos\frac{7\pi x}{2a} \cos\frac{3\pi y}{b} \\
&+ \frac{100\,\alpha^2}{2401 + 392\,\alpha^2 + 16\,\alpha^4} \cos\frac{7\pi x}{2a} \cos\frac{\pi y}{b}\Bigg) \\
&+ f_2 f_4 \Bigg(\frac{-\alpha^2}{16\,(1 + 2\,\alpha^2 + \alpha^4)} \cos\frac{2\pi x}{a} \cos\frac{2\pi y}{b} + \frac{4\,\alpha^2}{1 + 8\,\alpha^2 + 16\,\alpha^4} \cos\frac{\pi x}{a} \cos\frac{2\pi y}{b}\Bigg) \\
&+ f_2 f_5 \Bigg(\frac{-16\,\alpha^2}{1 + 8\,\alpha^2 + 16\,\alpha^4} \cos\frac{\pi x}{2a} \cos\frac{\pi y}{b} + \frac{576\,\alpha^2}{1 + 72\,\alpha^2 + 1296\,\alpha^4} \cos\frac{\pi x}{2a} \cos\frac{3\pi y}{b} \\
&- \frac{144\,\alpha^2}{625 + 1800\,\alpha^2 + 1296\,\alpha^4} \cos\frac{5\pi x}{2a} \cos\frac{3\pi y}{b} \\
&+ \frac{64\,\alpha^2}{625 + 200\,\alpha^2 + 16\,\alpha^4} \cos\frac{5\pi x}{2a} \cos\frac{\pi y}{b}\Bigg) \\
&+ f_2 f_6 \Bigg(\frac{36\,\alpha^2}{81 + 72\,\alpha^2 + 16\,\alpha^4} \cos\frac{3\pi x}{a} \cos\frac{2\pi y}{b} \\
&- \frac{36\,\alpha^2}{81 + 288\,\alpha^2 + 256\,\alpha^4} \cos\frac{3\pi x}{a} \cos\frac{4\pi y}{b} \\
&- \frac{9}{16\,\alpha^2} \cos\frac{2\pi y}{b} + \frac{9}{16\,\alpha^2} \cos\frac{4\pi y}{b}\Bigg) \\
&+ f_3 f_4 \Bigg(\frac{-4\,\alpha^2}{81 + 72\,\alpha^2 + 16\,\alpha^4} \cos\frac{3\pi x}{2a} \cos\frac{\pi y}{b} + \frac{4\,\alpha^2}{1 + 8\,\alpha^2 + 16\,\alpha^4} \cos\frac{3\pi x}{2a} \cos\frac{3\pi y}{b} \\
&+ \frac{36\,\alpha^2}{625 + 200\,\alpha^2 + 16\,\alpha^4} \cos\frac{5\pi x}{2a} \cos\frac{\pi y}{b} \\
&- \frac{36\,\alpha^2}{625 + 1800\,\alpha^2 + 1296\,\alpha^4} \cos\frac{5\pi x}{2a} \cos\frac{3\pi y}{b}\Bigg) \\
&+ f_3 f_5 \Bigg(\frac{144\,\alpha^2}{1 + 32\,\alpha^2 + 256\,\alpha^4} \cos\frac{\pi x}{2a} \cos\frac{4\pi y}{b} \\
&- \frac{16\,\alpha^2}{81 + 288\,\alpha^2 + 256\,\alpha^4} \cos\frac{3\pi x}{a} \cos\frac{4\pi y}{b}\Bigg) \\
&+ f_3 f_6 \Bigg(\frac{-36\,\alpha^2}{1 + 8\,\alpha^2 + 16\,\alpha^4} \cos\frac{\pi x}{2a} \cos\frac{\pi y}{b} + \frac{8100\,\alpha^2}{1 + 200\,\alpha^2 + 10000\,\alpha^4} \cos\frac{\pi x}{2a} \cos\frac{5\pi y}{b} \\
&+ \frac{324\,\alpha^2}{2401 + 392\,\alpha^2 + 16\,\alpha^4} \cos\frac{7\pi x}{2a} \cos\frac{\pi y}{b} \\
&- \frac{900\,\alpha^2}{2401 + 9800\,\alpha^2 + 10000\,\alpha^4} \cos\frac{7\pi x}{2a} \cos\frac{5\pi y}{b}\Bigg) \\
&+ f_4 f_5 \Bigg(\frac{144\,\alpha^2}{1 + 72\,\alpha^2 + 1296\,\alpha^4} \cos\frac{\pi x}{2a} \cos\frac{3\pi y}{b} \\
&+ \frac{16\,\alpha^2}{81 + 72\,\alpha^2 + 16\,\alpha^4} \cos\frac{3\pi x}{2a} \cos\frac{\pi y}{b}\Bigg)
\end{aligned}
$$

$$+f_4 f_6\left(\frac{36\,\alpha^2}{1+32\,\alpha^2+256\,\alpha^4}\cos\frac{\pi x}{a}\cos\frac{4\pi y}{b}\right.$$
$$\left.+\frac{9\alpha^2}{16+32\,\alpha^2+16\,\alpha^4}\cos\frac{2\pi x}{a}\cos\frac{2\pi y}{b}\right)$$
$$+f_5 f_6\left(\frac{3600\,\alpha^2}{1+200\,\alpha^2+10000\,\alpha^4}\cos\frac{\pi x}{2a}\cos\frac{5\pi y}{b}\right.$$
$$\left.\left.+\frac{144\,\alpha^2}{625+200\,\alpha^2+16\,\alpha^4}\cos\frac{5\pi x}{2a}\cos\frac{\pi y}{b}\right)\right]-\frac{p_x}{\tau^*_{cr}}. \qquad (2.2a)$$

$$\frac{\sigma_{ym}}{\tau^*_{cr}}=-4{,}636\left[\frac{9\,\alpha^2}{8}f_1^2\cos\frac{\pi x}{a}+\frac{\alpha^2}{8}f_2^2\cos\frac{3\pi x}{a}+\frac{\alpha^2}{2}f_3^2\cos\frac{4\pi x}{a}\right.$$
$$+\frac{\alpha^2}{8}f_4^2\cos\frac{\pi x}{a}+\frac{\alpha^2}{2}f_5^2\cos\frac{2\pi x}{a}+\frac{9\,\alpha^2}{8}f_6^2\cos\frac{3\pi x}{a}$$
$$+f_1 f_2\left(\frac{-\alpha^2}{1+8\,\alpha^2+16\,\alpha^4}\cos\frac{2\pi x}{a}\cos\frac{4\pi y}{b}+\frac{25\,\alpha^2}{16\,(1+2\,\alpha^2+\alpha^4)}\cos\frac{2\pi x}{a}\cos\frac{2\pi y}{b}\right.$$
$$\left.+\frac{25\,\alpha^2}{4\,(1+32\,\alpha^2+256\,\alpha^4)}\cos\frac{\pi x}{a}\cos\frac{4\pi y}{b}-\frac{4\,\alpha^2}{1+8\,\alpha^2+16\,\alpha^4}\cos\frac{\pi x}{a}\cos\frac{2\pi y}{b}\right)$$
$$+f_1 f_3\left(\frac{-\alpha^2}{1+8\,\alpha^2+16\,\alpha^4}\cos\frac{5\pi x}{2a}\cos\frac{5\pi y}{b}+\frac{1225\,\alpha^2}{625+200\,\alpha^2+16\,\alpha^4}\cos\frac{5\pi x}{2a}\cos\frac{\pi y}{b}\right.$$
$$+\frac{441\,\alpha^2}{81+1800\,\alpha^2+10000\,\alpha^4}\cos\frac{3\pi x}{2a}\cos\frac{5\pi y}{b}$$
$$\left.-\frac{225\,\alpha^2}{81+72\,\alpha^2+16\,\alpha^4}\cos\frac{3\pi x}{2a}\cos\frac{\pi y}{b}\right)$$
$$+f_1 f_4\left(\frac{-\alpha^2}{4\,(1+32\,\alpha^2+266\,\alpha^4)}\cos\frac{\pi x}{a}\cos\frac{4\pi y}{b}+\frac{\alpha^2}{1+8\,\alpha^2+16\,\alpha^4}\cos\frac{\pi x}{a}\cos\frac{2\pi y}{b}\right)$$
$$+f_1 f_5\left(\frac{-36\,\alpha^2}{81+1800\,\alpha^2+10000\,\alpha^4}\cos\frac{3\pi x}{2a}\cos\frac{5\pi y}{b}\right.$$
$$+\frac{144\,\alpha^2}{81+72\,\alpha^2+16\,\alpha^4}\cos\frac{3\pi x}{2a}\cos\frac{\pi y}{b}$$
$$\left.+\frac{16\,\alpha^2}{1+200\,\alpha^2+10000\,\alpha^4}\cos\frac{\pi x}{2a}\cos\frac{5\pi y}{b}-\frac{4\,\alpha^2}{1+8\,\alpha^2+16\,\alpha^4}\cos\frac{\pi x}{2a}\cos\frac{\pi y}{b}\right)$$
$$+f_1 f_6\left(-\frac{9\,\alpha^2}{4}\cos\frac{\pi x}{a}+\frac{9\,\alpha^2}{4}\cos\frac{2\pi x}{a}+\frac{9\,\alpha^2}{1+72\,\alpha^2+1296\,\alpha^4}\cos\frac{\pi x}{a}\cos\frac{6\pi y}{b}\right.$$
$$\left.-\frac{9\,\alpha^2}{16\,(1+18\,\alpha^2+81\,\alpha^4)}\cos\frac{2\pi x}{a}\cos\frac{6\pi y}{b}\right)$$
$$+f_2 f_3\left(\frac{25\,\alpha^2}{1+72\,\alpha^2+1296\,\alpha^4}\cos\frac{\pi x}{2a}\cos\frac{3\pi y}{b}-\frac{\alpha^2}{1+8\,\alpha^2+16\,\alpha^4}\cos\frac{\pi x}{2a}\cos\frac{\pi y}{b}\right.$$
$$\left.-\frac{49\,\alpha^2}{2401+3528\,\alpha^2+1296\,\alpha^4}\cos\frac{7\pi x}{2a}\cos\frac{3\pi y}{b}\right.$$

$$+\frac{1225\alpha^2}{2401+392\alpha^2+16\alpha^4}\cos\frac{7\pi x}{2a}\cos\frac{\pi y}{b}\Big)$$

$$+f_2f_4\Big(-\frac{\alpha^2}{4}\cos\frac{\pi x}{a}+\frac{\alpha^2}{4}\cos\frac{2\pi x}{a}-\frac{\alpha^2}{16\,(1+2\alpha^2+\alpha^4)}\cos\frac{2\pi x}{a}\cos\frac{2\pi y}{b}$$

$$+\frac{\alpha^2}{1+8\alpha^2+16\alpha^4}\cos\frac{\pi x}{a}\cos\frac{2\pi y}{b}\Big)$$

$$+f_2f_5\Big(\frac{-4\alpha^2}{1+8\alpha^2+16\alpha^4}\cos\frac{\pi x}{2a}\cos\frac{\pi y}{b}+\frac{16\alpha^2}{1+72\alpha^2+1296\alpha^4}\cos\frac{\pi x}{2a}\cos\frac{3\pi y}{b}$$

$$-\frac{100\alpha^2}{625+1800\alpha^2+1296\alpha^4}\cos\frac{5\pi x}{2a}\cos\frac{3\pi y}{b}$$

$$+\frac{400\alpha^2}{625+200\alpha^2+16\alpha^4}\cos\frac{5\pi x}{2a}\cos\frac{\pi y}{b}\Big)$$

$$+f_2f_6\Big(\frac{81\alpha^2}{81+72\alpha^2+16\alpha^4}\cos\frac{3\pi x}{a}\cos\frac{2\pi y}{b}$$

$$-\frac{81\alpha^2}{4\,(81+288\alpha^2+256\alpha^4)}\cos\frac{3\pi x}{a}\cos\frac{4\pi y}{b}\Big)$$

$$+f_3f_4\frac{-9\alpha^2}{81+72\alpha^2+16\alpha^4}\cos\frac{3\pi x}{2a}\cos\frac{\pi y}{b}+\frac{\alpha^2}{1+8\alpha^2+16\alpha^4}\cos\frac{3\pi x}{2a}\cos\frac{3\pi y}{b}$$

$$+\frac{225\alpha^2}{625+200\alpha^2+16\alpha^4}\cos\frac{5\pi x}{2a}\cos\frac{\pi y}{b}$$

$$-\frac{25\alpha^2}{625+1800\alpha^2+1296\alpha^4}\cos\frac{5\pi x}{2a}\cos\frac{3\pi y}{b}\Big)$$

$$+f_3f_5\Big(-\alpha^2\cos\frac{\pi x}{a}+\alpha^2\cos\frac{3\pi x}{a}+\frac{9\alpha^2}{1+32\alpha^2+256\alpha^4}\cos\frac{\pi x}{a}\cos\frac{4\pi y}{b}$$

$$-\frac{9\alpha^2}{81+288\alpha^2+256\alpha^4}\cos\frac{3\pi x}{a}\cos\frac{4\pi y}{b}\Big)$$

$$+f_3f_6\Big(\frac{-9\alpha^2}{1+8\alpha^2+16\alpha^4}\cos\frac{\pi x}{2a}\cos\frac{\pi y}{b}+\frac{81\alpha^2}{1+200\alpha^2+10000\alpha^4}\cos\frac{\pi x}{2a}\cos\frac{5\pi y}{b}$$

$$+\frac{3969\alpha^2}{2401+392\alpha^2+16\alpha^4}\cos\frac{7\pi x}{2a}\cos\frac{\pi y}{b}$$

$$-\frac{441\alpha^2}{2401+9800\alpha^2+10000\alpha^4}\cos\frac{7\pi x}{2a}\cos\frac{5\pi y}{b}\Big)$$

$$+f_4f_5\Big(\frac{4\alpha^2}{1+72\alpha^2+1296\alpha^4}\cos\frac{\pi x}{2a}\cos\frac{3\pi y}{b}$$

$$+\frac{36\alpha^2}{81+72\alpha^2+16\alpha^4}\cos\frac{3\pi x}{2a}\cos\frac{\pi y}{b}\Big)$$

$$+f_4f_6\Big(\frac{9\alpha^2}{4\,(1+32\alpha^2+256\alpha^4)}\cos\frac{\pi x}{a}\cos\frac{4\pi y}{b}$$

$$+\frac{9\alpha^2}{16(1+2\alpha^2+\alpha^4)}\cos\frac{2\pi x}{a}\cos\frac{2\pi y}{b}\Bigg)$$
$$+f_5 f_6\Bigg(\frac{36\alpha^2}{1+200\alpha^2+10000\alpha^4}\cos\frac{\pi x}{2a}\cos\frac{5\pi y}{b}$$
$$+\frac{900\alpha^2}{625+200\alpha^2+16\alpha^4}\cos\frac{5\pi x}{2a}\cos\frac{\pi y}{b}\Bigg)\Bigg]-\frac{p_y}{\tau_{cr}^*}. \tag{2.2b}$$

$$\frac{\tau_m}{\tau_{cr}^*}=-2{,}318\Bigg[f_1 f_2\Bigg(\frac{-2\alpha^2}{1+8\alpha^2+16\alpha^4}\sin\frac{2\pi x}{a}\sin\frac{4\pi y}{b}$$
$$+\frac{25\alpha^2}{16(1+2\alpha^2+\alpha^4)}\sin\frac{2\pi x}{a}\sin\frac{2\pi y}{b}+\frac{25\alpha^2}{1+32\alpha^2+256\alpha^4}\sin\frac{\pi x}{a}\sin\frac{4\pi y}{b}$$
$$-\frac{8\alpha^2}{1+8\alpha^2+16\alpha^4}\sin\frac{\pi x}{a}\sin\frac{2\pi y}{b}\Bigg)$$
$$+f_1 f_3\Bigg(\frac{-2\alpha^2}{1+8\alpha^2+16\alpha^4}\sin\frac{5\pi x}{2a}\sin\frac{5\pi y}{b}$$
$$+\frac{490\alpha^2}{625+200\alpha^2+16\alpha^4}\sin\frac{5\pi x}{2a}\sin\frac{\pi y}{b}$$
$$+\frac{1470\alpha^2}{81+1800\alpha^2+10000\alpha^4}\sin\frac{3\pi x}{2a}\sin\frac{5\pi y}{b}$$
$$-\frac{150\alpha^2}{81+72\alpha^2+16\alpha^4}\sin\frac{3\pi x}{2a}\sin\frac{\pi y}{b}\Bigg)$$
$$+f_1 f_4\Bigg(\frac{-\alpha^2}{1+32\alpha^2+256\alpha^4}\sin\frac{\pi x}{a}\sin\frac{4\pi y}{b}+\frac{2\alpha^2}{1+8\alpha^2+16\alpha^4}\sin\frac{\pi x}{a}\sin\frac{2\pi y}{b}\Bigg)$$
$$+f_1 f_5\Bigg(\frac{-120\alpha^2}{81+1800\alpha^2+10000\alpha^4}\sin\frac{3\pi x}{2a}\sin\frac{5\pi y}{b}$$
$$+\frac{96\alpha^2}{81+72\alpha^2+16\alpha^4}\sin\frac{3\pi x}{2a}\sin\frac{\pi y}{b}$$
$$+\frac{160\alpha^2}{1+200\alpha^2+10000\alpha^4}\sin\frac{\pi x}{2a}\sin\frac{5\pi y}{b}-\frac{8\alpha^2}{1+8\alpha^2+16\alpha^4}\sin\frac{\pi x}{2a}\sin\frac{\pi y}{b}\Bigg)$$
$$+f_1 f_6\Bigg(\frac{54\alpha^2}{1+72\alpha^2+1296\alpha^4}\sin\frac{\pi x}{a}\sin\frac{6\pi y}{b}$$
$$-\frac{27\alpha^2}{16(1+18\alpha^2+81\alpha^4)}\sin\frac{2\pi x}{a}\sin\frac{6\pi y}{b}\Bigg)$$
$$+f_2 f_3\Bigg(\frac{150\alpha^2}{1+72\alpha^2+1296\alpha^4}\sin\frac{\pi x}{2a}\sin\frac{3\pi y}{b}-\frac{2\alpha^2}{1+8\alpha^2+16\alpha^4}\sin\frac{\pi x}{2a}\sin\frac{\pi y}{b}$$
$$-\frac{42\alpha^2}{2401+3528\alpha^2+1296\alpha^4}\sin\frac{7\pi x}{2a}\sin\frac{3\pi y}{b}$$
$$+\frac{350\alpha^2}{2401+392\alpha^2+16\alpha^4}\sin\frac{7\pi x}{2a}\sin\frac{\pi y}{b}\Bigg)$$

$$+f_2 f_4\left(\frac{-\alpha^2}{16\,(1+2\,\alpha^2+\alpha^4)}\sin\frac{2\pi x}{a}\sin\frac{2\pi y}{b}+\frac{2\,\alpha^2}{1+8\,\alpha^2+16\,\alpha^4}\sin\frac{\pi x}{a}\sin\frac{2\pi y}{b}\right)$$

$$+f_2 f_5\left(\frac{-8\,\alpha^2}{1+8\,\alpha^2+16\,\alpha^4}\sin\frac{\pi x}{2a}\sin\frac{\pi y}{b}+\frac{96\,\alpha^2}{1+72\,\alpha^2+1296\,\alpha^4}\sin\frac{\pi x}{2a}\sin\frac{3\pi y}{b}\right.$$
$$-\frac{120\,\alpha^2}{625+1800\,\alpha^2+1296\,\alpha^4}\sin\frac{5\pi x}{2a}\sin\frac{3\pi y}{b}$$
$$\left.+\frac{160\,\alpha^2}{625+200\,\alpha^2+16\,\alpha^4}\sin\frac{5\pi x}{2a}\sin\frac{\pi y}{b}\right)$$

$$+f_2 f_6\left(\frac{54\,\alpha^2}{81+72\,\alpha^2+16\,\alpha^4}\sin\frac{3\pi x}{a}\sin\frac{2\pi y}{b}\right.$$
$$\left.-\frac{27\,\alpha^2}{81+288\,\alpha^2+256\,\alpha^4}\sin\frac{3\pi x}{a}\sin\frac{4\pi y}{b}\right)$$

$$+f_3 f_4\left(\frac{-6\,\alpha^2}{81+72\,\alpha^2+16\,\alpha^4}\sin\frac{3\pi x}{2a}\sin\frac{\pi y}{b}+\frac{2\,\alpha^2}{1+8\,\alpha^2+16\,\alpha^4}\sin\frac{3\pi x}{2a}\sin\frac{3\pi y}{b}\right.$$
$$+\frac{90\,\alpha^2}{625+200\,\alpha^2+16\,\alpha^4}\sin\frac{5\pi x}{2a}\sin\frac{\pi y}{b}$$
$$\left.-\frac{30\,\alpha^2}{625+1800\,\alpha^2+1296\,\alpha^4}\sin\frac{5\pi x}{2a}\sin\frac{3\pi y}{b}\right)$$

$$+f_3 f_5\left(\frac{36\,\alpha^2}{1+32\,\alpha^2+256\,\alpha^4}\sin\frac{\pi x}{a}\sin\frac{4\pi y}{b}\right.$$
$$\left.-\frac{12\,\alpha^2}{81+288\,\alpha^2+256\,\alpha^4}\sin\frac{3\pi x}{a}\sin\frac{4\pi y}{b}\right)$$

$$+f_3 f_6\left(\frac{-18\,\alpha^2}{1+8\,\alpha^2+16\,\alpha^4}\sin\frac{\pi x}{2a}\sin\frac{\pi y}{b}+\frac{810\,\alpha^2}{1+200\,\alpha^2+10000\,\alpha^4}\sin\frac{\pi x}{2a}\sin\frac{5\pi y}{b}\right.$$
$$+\frac{1134\,\alpha^2}{2401+392\,\alpha^2+16\,\alpha^4}\sin\frac{7\pi x}{2a}\sin\frac{\pi y}{b}$$
$$\left.-\frac{630\,\alpha^2}{2401+9800\,\alpha^2+10000\,\alpha^4}\sin\frac{7\pi x}{2a}\sin\frac{5\pi y}{b}\right)$$

$$+f_4 f_5\left(\frac{24\,\alpha^2}{1+72\,\alpha^2+1296\,\alpha^4}\sin\frac{\pi x}{2a}\sin\frac{3\pi y}{b}+\frac{24\,\alpha^2}{81+72\,\alpha^2+16\,\alpha^4}\sin\frac{3\pi x}{2a}\sin\frac{\pi y}{b}\right)$$

$$+f_4 f_6\left(\frac{9\,\alpha^2}{1+32\,\alpha^2+256\,\alpha^4}\sin\frac{\pi x}{a}\sin\frac{4\pi y}{b}+\frac{9\,\alpha^2}{16+32\,\alpha^2+16\,\alpha^4}\sin\frac{2\pi x}{a}\sin\frac{2\pi y}{b}\right)$$

$$+f_5 f_6\left(\frac{360\,\alpha^2}{1+200\,\alpha^2+10000\,\alpha^4}\sin\frac{\pi x}{2a}\sin\frac{5\pi y}{b}\right.$$
$$\left.\left.+\frac{360\,\alpha^2}{625+200\,\alpha^2+16\,\alpha^4}\sin\frac{5\pi x}{2a}\sin\frac{\pi y}{b}\right)\right]-\frac{\tau}{\tau_{cr}^*}. \qquad (2.2\,\mathrm{c})$$

Dans les expressions (2.2.a) et (2.2.b), p_x et p_y représentent les valeurs moyennes des sollicitations normales aux bords de la plaque.

Dans l'hypothèse admise du rapprochement libre des bords opposés au cours du voilement, ces quantités sont nulles.

2.2. Valeurs numériques des contraintes membranaires

Les valeurs numériques des contraintes membranaires σ_{xm}, σ_{ym}, τ_m ont été calculées pour une plaque carrée de côté $2\,a$, cisaillée uniformément et renforcée par un raidisseur vertical médian de rigidité relative γ/γ^* comprise entre zéro et trois.

Les valeurs de la sollicitation extérieure de cisaillement τ ainsi que celles des contraintes sont exprimées par leur rapport à la charge critique τ_{cr}^* de la plaque non raidie de référence.

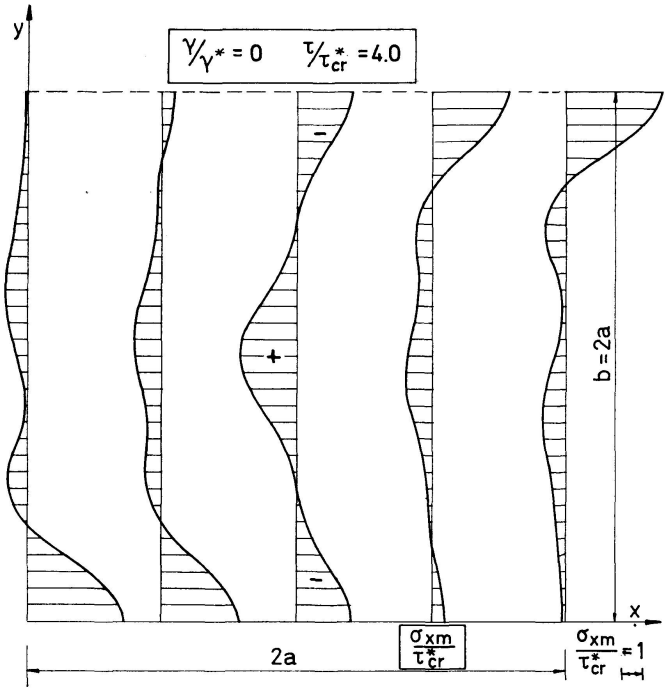


Fig. 2.

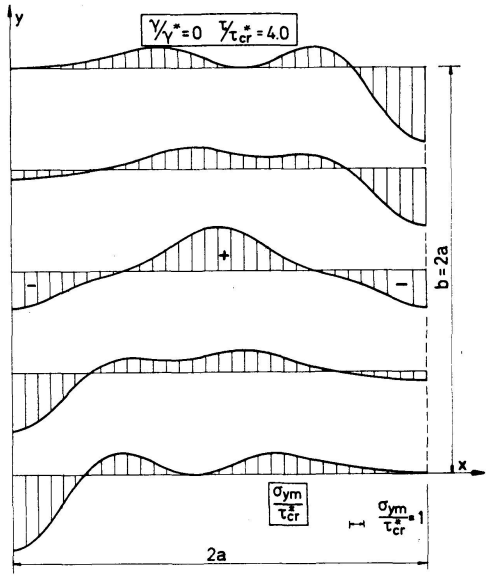


Fig. 3.

Les figures 2 et 3 montrent respectivement les allures de σ_{xm} et σ_{ym} pour $\gamma/\gamma^* = 0$ et $\tau/\tau_{cr}^* = 4$. Il apparaît clairement sur ces figures que les contraintes ont des valeurs égales en deux points symétriques par rapport au centre de la plaque. De plus, ces contraintes sont auto-équilibrées puisque les sollicitations normales moyennes au bord de la plaque sont nulles.

On constate par les calculs détaillés que, si le passage de $\gamma/\gamma^* = 0$ à $\gamma/\gamma^* = 1$ réduit très sensiblement les valeurs des contraintes membranaires, le passage de $\gamma/\gamma^* = 1$ à $\gamma/\gamma^* = 3$ provoque une réduction nettement moins forte.

Que γ/γ^* soit égal à 1, 2 ou 3, la contrainte σ_{xm} a son maximum positif au

point ($x=0$, $y=a$) et son maximum négatif au point ($x=0{,}75\,a$, $y=0$). La contrainte σ_{ym} a son maximum positif au point ($x=0{,}75\,a$, $y=0{,}25\,a$) et son maximum négatif au point ($x=0$, $y=0{,}25\,a$).

Les figures 4, 6 et 8 montrent l'allure de σ_{xm} pour $\tau/\tau^*_{cr}=4$ et $\gamma/\gamma^*=1, 2, 3$. Les diagrammes des contraintes sont limités à la demi-plaque ($p\leqq x\leqq a$; $0\leqq y\leqq 2\,a$) pour les raisons de symétrie déjà mentionnées.

Les figures 5 et 7 donnent l'allure de σ_{ym} pour $\tau/\tau^*_{cr}=4$ et $\gamma/\gamma^*=1$ et 2. Les diagrammes sont limités à la portion ($0\leqq x\leqq 2\,a$; $0\leqq y\leqq a$) de la plaque. On constatera sur toutes ces figures que les contraintes membranaires sont auto-équilibrées.

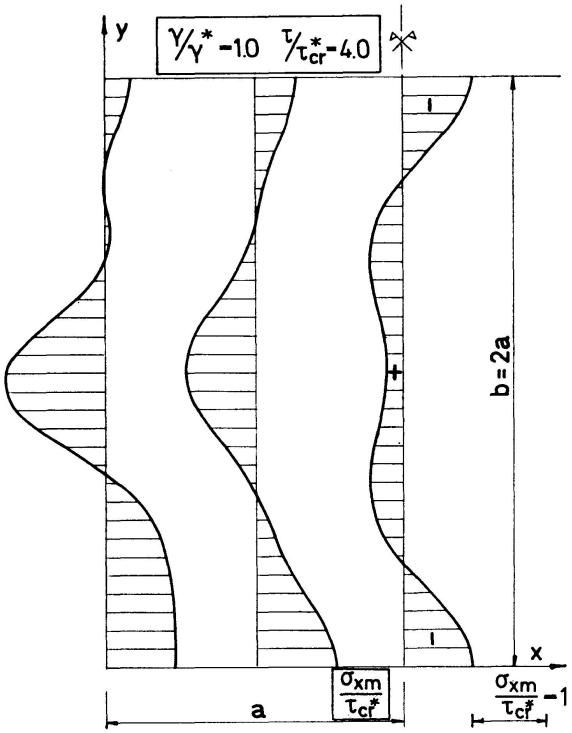


Fig. 4.

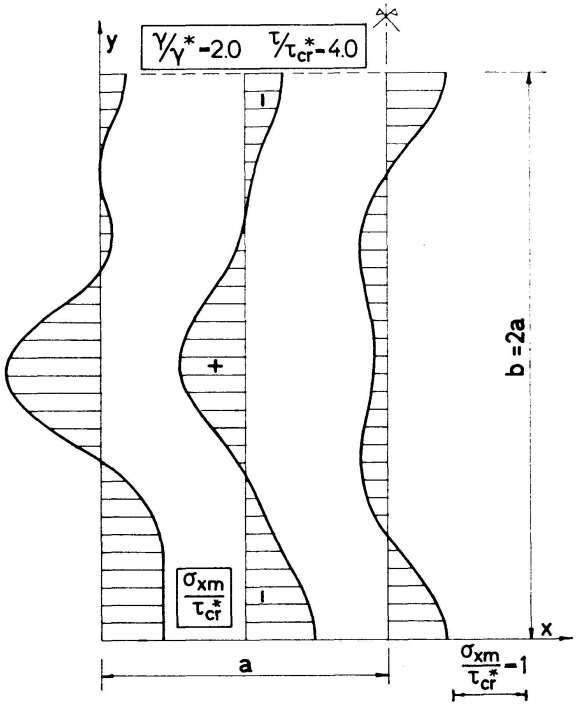


Fig. 6.

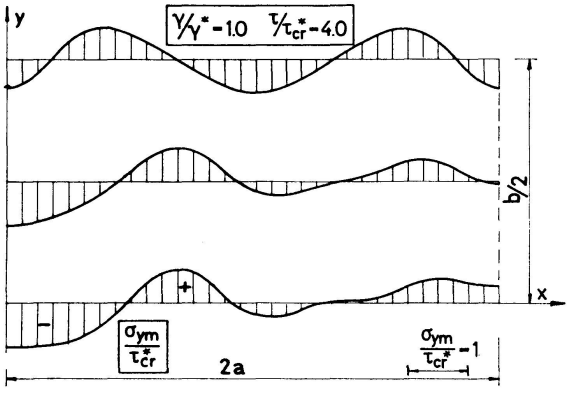


Fig. 5.

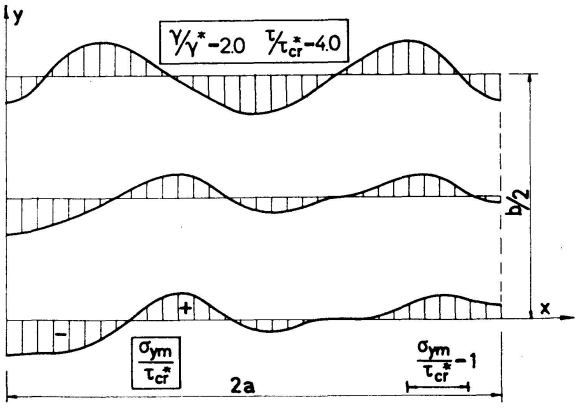


Fig. 7.

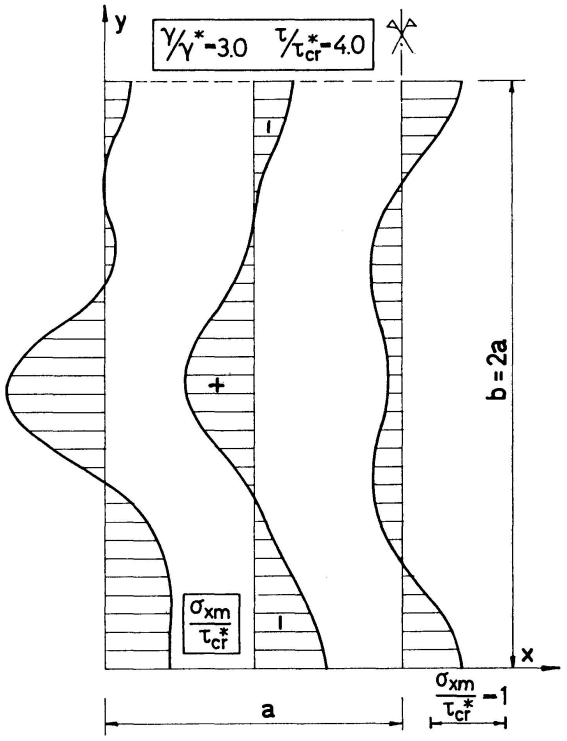


Fig. 8.

3. Contraintes de flexion

3.1. Expressions analytiques

Les contraintes de flexion varient linéairement sur l'épaisseur e de la plaque. Leurs valeurs maxima ont pour expression:

$$\sigma_{xf} = \mp \frac{E\,e}{2\,(1-\nu^2)} \left(\frac{\partial^2 w}{\partial x^2} + \nu \frac{\partial^2 w}{\partial y^2} \right),$$

$$\sigma_{yf} = \mp \frac{E\,e}{2\,(1-\nu^2)} \left(\frac{\partial^2 w}{\partial y^2} + \nu \frac{\partial^2 w}{\partial x^2} \right), \tag{3.1}$$

$$\tau_f = \mp G\,e \frac{\partial^2 w}{\partial x\,\partial y} = \mp \frac{E\,e}{2\,(1+\nu)} \frac{\partial^2 w}{\partial x\,\partial y}.$$

Il est avantageux d'exprimer ces contraintes par leur rapport à la contrainte critique de la plaque non raidie de référence.

Compte tenu de l'expression (1.1.) de la déformée w, on obtient pour une plaque carrée de côté $2a$:

$$\frac{\sigma_{xf}}{\tau_{cr}^*} = \mp\left(2{,}357\, f_1 \sin\frac{\pi x}{2a}\sin\frac{3\pi y}{2a} + 5{,}924\, f_2 \sin\frac{3\pi x}{2a}\sin\frac{\pi y}{2a}\right.$$
$$+ 10{,}957\, f_3 \sin\frac{2\pi x}{a}\sin\frac{\pi y}{a} + 0{,}8281\, f_4 \sin\frac{\pi x}{2a}\sin\frac{\pi y}{2a}$$
$$\left. + 3{,}312\, f_5 \sin\frac{\pi x}{a}\sin\frac{\pi y}{a} + 7{,}453\, f_6 \sin\frac{3\pi x}{2a}\sin\frac{3\pi y}{2a}\right),$$

$$\frac{\sigma_{yf}}{\tau_{cr}^*} = \mp\left(5{,}924\, f_1 \sin\frac{\pi x}{2a}\sin\frac{3\pi y}{2a} + 2{,}357\, f_2 \sin\frac{3\pi x}{2a}\sin\frac{\pi y}{2a}\right.$$
$$+ 5{,}606\, f_3 \sin\frac{2\pi x}{a}\sin\frac{\pi y}{a} + 0{,}8281\, f_4 \sin\frac{\pi x}{2a}\sin\frac{\pi y}{2a} \qquad (3.2)$$
$$\left. + 3{,}312\, f_5 \sin\frac{\pi x}{a}\sin\frac{\pi y}{a} + 7{,}453\, f_6 \sin\frac{3\pi x}{2a}\sin\frac{3\pi y}{2a}\right),$$

$$\frac{\tau_f}{\tau_{cr}^*} = \mp 2\left(1{,}338\, f_1 \cos\frac{\pi x}{2a}\cos\frac{3\pi y}{2a} + 1{,}338\, f_2 \cos\frac{3\pi x}{2a}\cos\frac{\pi y}{2a}\right.$$
$$+ 3{,}567\, f_3 \cos\frac{2\pi x}{a}\cos\frac{\pi y}{a} + 0{,}446\, f_4 \cos\frac{\pi x}{2a}\cos\frac{\pi y}{2a}$$
$$\left. + 1{,}784\, f_5 \cos\frac{\pi x}{a}\cos\frac{\pi y}{a} + 4{,}013\, f_6 \cos\frac{3\pi x}{2a}\cos\frac{3\pi y}{2a}\right).$$

3.2. Valeurs numériques des contraintes de flexion

Le manque de place ne nous permet pas de reproduire les valeurs numériques des contraintes de flexion pour les valeurs 0, 1, 2 et 3 de γ/γ^* et une sollicitation extérieure $\tau/\tau_{cr}^* = 3{,}5$, 4, 6 et 8.

On remarque par l'étude de ces valeurs que, pour la plaque non raidie, les contraintes σ_{xf} et σ_{yf} sont maximum au centre, ce qui est évident puisque les contraintes de flexion ont la même allure que la déformée.

L'allure des contraintes σ_{xf} et σ_{yf} pour $\tau/\tau_{cr}^* = 4$ est donnée aux figures 9 et 10 pour une moitié de la plaque.

Comme pour les contraintes membranaires, le passage de $\gamma/\gamma^* = 0$ à $\gamma/\gamma^* = 1$ réduit très sensiblement les contraintes, tandis que le passage de $\gamma/\gamma^* = 1$ à $\gamma/\gamma^* = 3$ provoque une réduction nettement moins forte.

Que γ/γ^* soit égal à 1, 2 ou 3, le maximum positif de σ_{xf} a lieu au point $(x = 0{,}75\,a,\ y = 0{,}5\,a)$, le maximum négatif au point $(x = 0{,}25\,a,\ y = 0{,}75\,a)$. Quant à σ_{yf}, le maximum positif a lieu au point $(x = 0{,}75\,a,\ y = 0{,}5\,a)$, le maximum négatif au point $(x = 0{,}25\,a,\ y = a)$.

Les figures 11 et 12 montrent l'allure de σ_{xf} et σ_{yf} pour $\gamma/\gamma^* = 2$ et $\tau/\tau_{cr}^* = 4$.

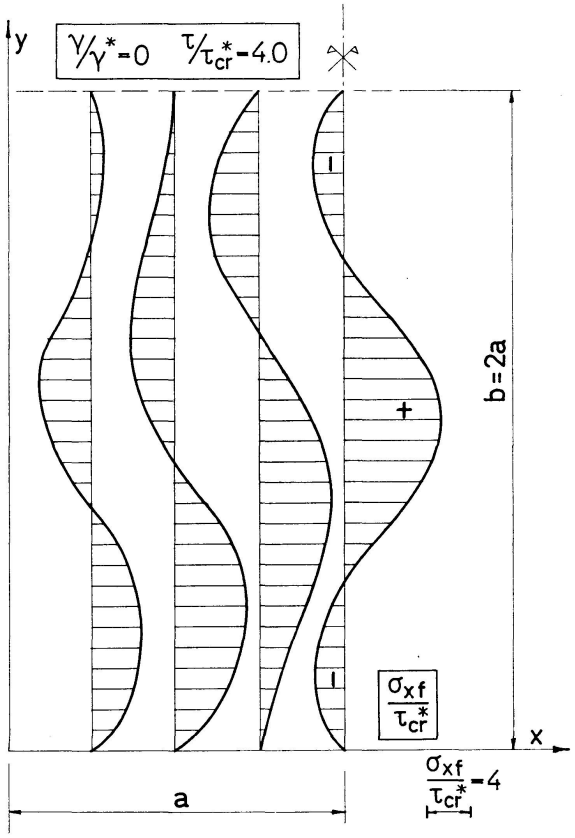


Fig. 9.

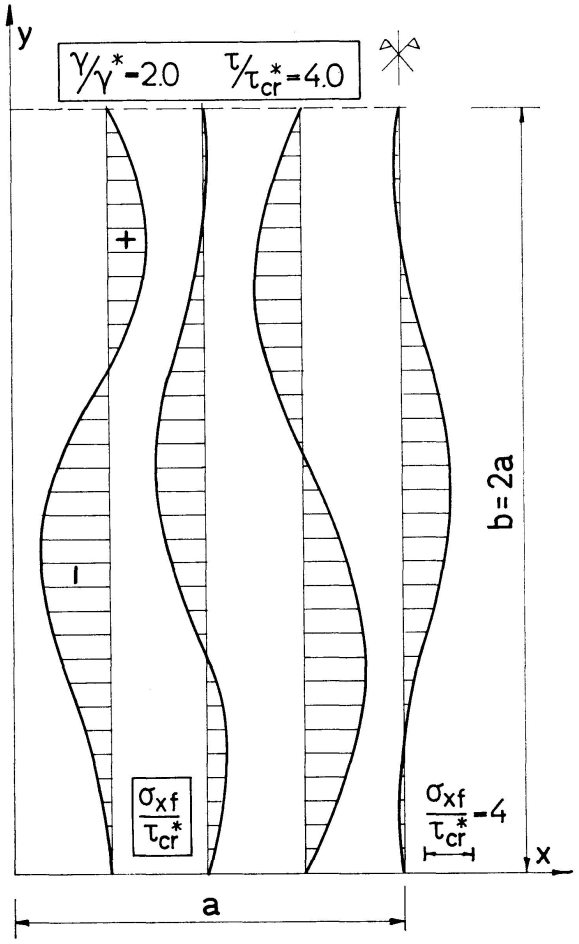


Fig. 11.

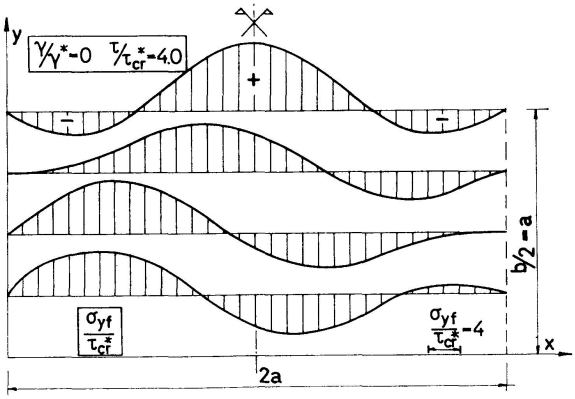


Fig. 10.

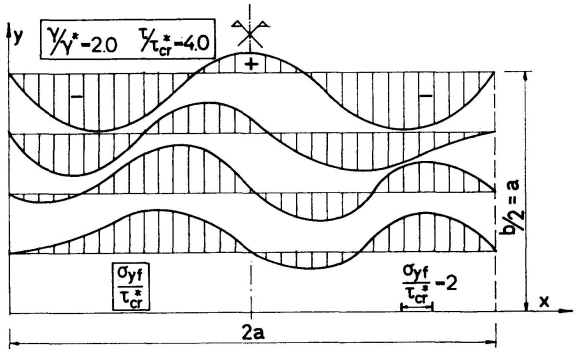


Fig. 12.

4. Contraintes membranaires de comparaison

La contrainte membranaire de comparaison a pour expression:

$$\sigma_{mc} = \sqrt[2]{\sigma_{xm}^2 + \sigma_{ym}^2 - \sigma_{xm}\,\sigma_{ym} + 3\,\tau_m^2}. \tag{4.1}$$

Les valeurs de σ_{mc}/τ^*_{cr} sont données pour $\gamma/\gamma^* = 0, 1, 2, 3$ dans les tableaux I, II, III, et IV en fonction du cisaillement τ/τ^*_{cr}.

Tableau I a

$\gamma/\gamma^* = 0$ $\tau/\tau^*_{cr} = 3{,}5$ σ_{mc}/τ^*_{cr} $\gamma/\gamma^* = 0$ $\tau/\tau^*_{cr} = 4{,}0$

$y/2a$	$x/2a$				
	0	0,125	0,250	0,375	0,500
0	7,308	6,876	7,194	6,823	6,558
0,125	6,901	6,939	6,871	6,665	7,259
0,250	7,116	6,985	6,254	6,018	7,318
0,375	6,755	6,854	6,173	5,871	7,175
0,500	6,542	7,332	7,319	7,122	7,306
0,625	6,357	7,441	7,930	8,030	7,175
0,750	6,138	6,960	7,579	8,086	7,318
0,875	6,070	6,554	7,089	7,610	7,259
1,0	6,063	6,066	6,154	6,432	6,558

$y/2a$	$x/2a$				
	0	0,125	0,250	0,375	0,500
0	9,055	8,334	8,886	8,142	7,737
0,125	8,393	8,202	8,139	7,777	8,664
0,250	8,734	8,326	7,260	6,915	8,790
0,375	8,027	8,101	7,163	6,778	8,691
0,500	7,703	8,782	8,763	8,579	8,948
0,625	7,429	8,872	9,491	9,748	8,691
0,750	7,060	8,147	8,950	9,771	8,790
0,875	6,945	7,618	8,362	9,169	8,664
1,0	6,930	6,935	7,090	7,597	7,737

Tableau I b

$\gamma/\gamma^* = 0$ $\tau/\tau^*_{cr} = 6{,}0$ σ_{mc}/τ^*_{cr} $\gamma/\gamma^* = 0$ $\tau/\tau^*_{cr} = 8{,}0$

$y/2a$	$x/2a$				
	0	0,125	0,250	0,375	0,500
0	16,690	14,699	16,342	13,588	12,670
0,125	14,966	13,272	13,344	12,163	14,271
0,250	15,890	13,825	11,388	10,565	14,655
0,375	13,307	13,034	11,076	10,376	14,809
0,500	12,487	14,498	14,323	14,327	15,623
0,625	11,881	14,490	15,392	16,381	14,809
0,750	10,796	12,798	14,121	16,267	14,655
0,875	10,471	11,877	13,365	15,412	14,271
1,0	10,410	10,414	10,872	12,633	12,670

$y/2a$	$x/2a$				
	0	0,125	0,250	0,375	0,500
0	24,784	21,475	24,296	19,235	17 819
0,125	21,998	18,353	18,637	16,570	19,924
0,250	23,545	19,426	15,583	14,308	20,569
0,375	18,783	17,988	15,022	13,975	21,029
0,500	17,425	20,229	19,832	20,093	22,429
0,625	16,485	20,110	21,174	22,964	21,029
0,750	14,581	17,437	19,187	22,720	20,569
0,875	14,022	16,172	18,372	21,749	19,924
1,0	13,898	13,895	14,690	17,996	17,819

Tableau II a

$\gamma/\gamma^* = 1{,}0$ $\tau/\tau^*_{cr} = 3{,}5$ σ_{mc}/τ^*_{cr} $\gamma/\gamma^* = 1{,}0$ $\tau/\tau^*_{cr} = 4{,}0$

$y/2a$	$x/2a$				
	0	0,125	0,250	0,375	0,500
0	6,077	6,077	6,087	6,102	6,077
0,125	6,076	6,066	6,098	6,154	6,197
0,250	6,072	6,221	6,482	6,339	6,137
0,375	6,084	6,306	6,670	6,504	6,168
0,500	6,126	6,212	6,290	6,277	6,253
0,625	6,072	6,157	6,024	5,993	6,168
0,750	6,062	6,234	6,144	6,074	6,137
0,875	6,064	6,182	6,155	6,178	6,197
1,0	6,069	6,073	6,070	6,072	6,077

$y/2a$	$x/2a$				
	0	0,125	0,250	0,375	0,500
0	6,980	6,981	7,020	7,080	6,982
0,125	6,977	6,947	6,995	7,135	7,233
0,250	6,962	7,261	7,752	7,467	7,110
0,375	7,003	7,446	8,138	7,765	7,128
0,500	7,115	7,278	7,414	7,336	7,267
0,625	6,954	7,138	6,917	6,836	7,128
0,750	6,928	7,280	7,155	7,028	7,110
0,875	6,931	7,169	7,143	7,211	7,233
1,0	6,949	6,965	6,954	6,961	6,982

Tableau IIb

$\gamma/\gamma^* = 1{,}0$ $\tau/\tau_{cr}^* = 6{,}0$ σ_{mc}/τ_{cr}^* $\gamma/\gamma^* = 1{,}0$ $\tau/\tau_{cr}^* = 8{,}0$

$y/2a$	$x/2a$				
	0	0,125	0,250	0,375	0,500
0	10,884	10,818	11,235	11,659	10,801
0,125	10,803	10,627	10,584	11,199	11,578
0,250	10,749	11,666	12,730	11,742	11,053
0,375	10,856	12,475	14,331	12,649	10,838
0,500	11,377	12,198	12,556	11,722	11,205
0,625	10,589	11,412	10,951	10,454	10,838
0,750	10,396	11,517	11,419	11,143	11,053
0,875	10,406	11,123	11,254	11,656	11,578
1,0	10,499	10,599	10,538	10,611	10,801

$y/2a$	$x/2a$				
	0	0,125	0,250	0,375	0,500
0	15,476	15,015	16,312	16,830	14,813
0,125	15,188	14,726	14,572	15,414	16,020
0,250	15,090	16,360	17,233	15,504	14,969
0,375	14,948	17,716	19,988	16,778	14,291
0,500	15,644	17,533	17,996	16,003	14,791
0,625	14,418	16,075	15,495	14,430	14,291
0,750	13,878	15,691	15,803	15,557	14,969
0,875	13,881	15,036	15,541	16,354	16,020
1,0	14,025	14,175	14,149	14,359	14,813

Tableau IIIa

$\gamma/\gamma^* = 2{,}0$ $\tau/\tau_{cr}^* = 3{,}5$ σ_{mc}/τ_{cr}^* $\gamma/\gamma^* = 2{,}0$ $\tau/\tau_{cr}^* = 4{,}0$

$y/2a$	$x/2a$				
	0	0,125	0,250	0,375	0,500
0	6,072	6,072	6,078	6,086	6,072
0,125	6,073	6,076	6,119	6,156	6,166
0,250	6,068	6,197	6,438	6,326	6,129
0,375	6,082	6,234	6,535	6,428	6,151
0,500	6,107	6,123	6,174	6,198	6,209
0,625	6,067	6,115	5,990	5,973	6,151
0,750	6,063	6,212	6,127	6,055	6,129
0,875	6,063	6,169	6,132	6,137	6,166
1,0	6,067	6,070	6,068	6,069	6,072

$y/2a$	$x/2a$				
	0	0,125	0,250	0,375	0,500
0	6,969	6,970	6,998	7,036	6,969
0,125	6,970	6,965	7,041	7,141	7,172
0,250	6,952	7,239	7,749	7,493	7,087
0,375	7,007	7,343	7,993	7,726	7,133
0,500	7,096	7,133	7,220	7,243	7,266
0,625	6,945	7,064	6,815	6,763	7,133
0,750	6,929	7,273	7,114	6,948	7,087
0,875	6,930	7,172	7,102	7,119	7,172
1,0	6,947	6,963	6,951	6,956	6,969

Tableau IIIb

$\gamma/\gamma^* = 2{,}0$ $\tau/\tau_{cr}^* = 6{,}0$ σ_{mc}/τ_{cr}^* $\gamma/\gamma^* = 2{,}0$ $\tau/\tau_{cr}^* = 8{,}0$

$y/2a$	$x/2a$				
	0	0,125	0,250	0,375	0,500
0	10,694	10,697	10,958	11,310	10,708
0,125	10,685	10,553	10,670	11,179	11,355
0,250	10,601	11,554	13,087	12,153	11,053
0,375	10,890	12,099	14,192	12,978	11,099
0,500	11,371	11,507	11,742	11,511	11,531
0,625	10,489	11,026	10,380	10,056	11,099
0,750	10,398	11,633	11,317	10,765	11,053
0,875	10,401	11,244	11,097	11,252	11,355
1,0	10,516	10,667	10,541	10,589	10,708

$y/2a$	$x/2a$				
	0	0,125	0,250	0,375	0,500
0	14,598	14,563	15,273	16,057	14,579
0,125	14,539	14,198	14,249	15,293	15,692
0,250	14,421	16,022	18,351	16,657	15,113
0,375	14,854	17,158	20,627	18,095	14,946
0,500	15,796	16,271	16,662	15,820	15,659
0,625	14,068	15,182	14,234	13,476	14,946
0,750	13,874	15,993	15,667	14,814	15,113
0,875	13,878	15,284	14,152	15,585	15,692
1,0	14,107	14,455	14,162	14,276	14,579

Tableau IV a

$\gamma/\gamma^* = 3{,}0$ $\tau/\tau_{cr}^* = 3{,}5$ σ_{mc}/τ_{cr}^* $\gamma/\gamma^* = 3{,}0$ $\tau/\tau_{cr}^* = 4{,}0$

$y/2a$	$x/2a$				
	0	0,125	0,250	0,375	0,500
0	6,071	6,071	6,077	6,083	6,070
0,125	6,072	6,078	6,121	6,154	6,157
0,250	6,067	6,191	6,423	6,317	6,124
0,375	6,081	6,219	6,504	6,408	6,146
0,500	6,103	6,115	6,154	6,183	6,200
0,625	6,066	6,109	5,986	5,970	6,146
0,750	6,063	6,206	6,123	6,050	6,124
0,875	6,063	6,165	6,127	6,127	6,157
1,0	6,066	6,070	6,067	6,068	6,070

$y/2a$	$x/2a$				
	0	0,125	0,250	0,375	0,500
0	6,968	6,969	6,995	7,029	6,967
0,125	6,970	6,972	7,056	7,146	7,160
0,250	6,950	7,237	7,754	7,501	7,081
0,375	7,010	7,324	7,964	7,718	7,133
0,500	7,095	7,103	7,177	7,220	7,264
0,625	6,944	7,053	6,796	6,746	7,133
0,750	6,929	7,278	7,112	6,933	7,081
0,875	6,930	7,175	7,095	7,099	7,160
1,0	6,946	6,964	6,950	6,955	6,967

Tableau IV b

$\gamma/\gamma^* = 3{,}0$ $\tau/\tau_{cr}^* = 6{,}0$ σ_{mc}/τ_{cr}^* $\gamma/\gamma^* = 3{,}0$ $\tau/\tau_{cr}^* = 8{,}0$

$y/2a$	$x/2a$				
	0	0,125	0,250	0,375	0,500
0	10,678	10,682	10,922	11,238	10,689
0,125	10,680	10,577	10,735	11,187	11,290
0,250	10,581	11,547	13,160	12,223	11,030
0,375	10,929	12,008	14,097	12,999	11,143
0,500	11,365	11,331	11,517	11,429	11,594
0,625	10,477	10,968	10,281	9,970	11,143
0,750	10,400	11,689	11,331	10,682	11,030
0,875	10,400	11,284	11,065	11,145	11,290
1,0	10,520	10,688	10,544	10,585	10,689

$y/2a$	$x/2a$				
	0	0,125	0,250	0,375	0,500
0	14,493	14,491	15,088	15,817	14,521
0,125	14,479	14,197	14,344	15,276	15,523
0,250	14,322	15,949	18,528	16,868	15,092
0,375	14,927	16,892	20,410	18,222	15,119
0,500	15,752	15,791	16,104	15,669	15,874
0,625	14,024	15,002	13,969	13,292	15,119
0,750	13,882	16,116	15,686	14,617	15,092
0,875	13,879	15,390	15,080	15,322	15,553
1,0	14,123	14,521	14,171	14,269	14,521

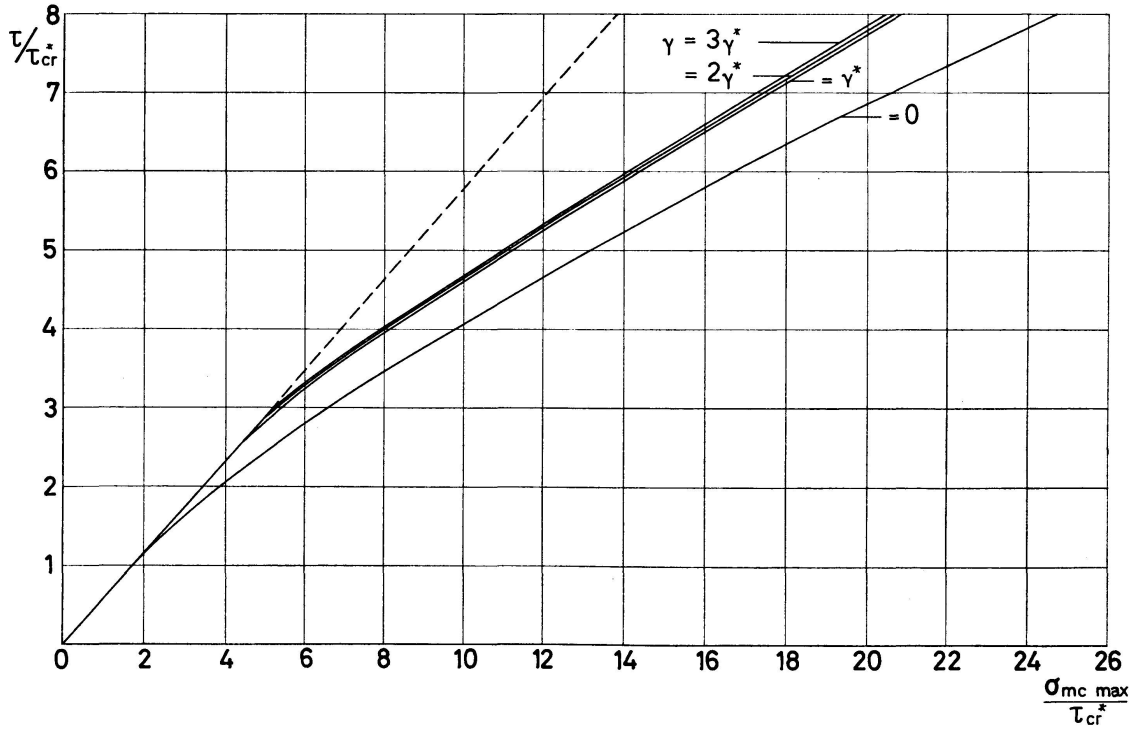


Fig. 13.

On constatera que, quel que soit le raidissage, l'écart entre les valeurs maximum et minimum de σ_{mc} pour une charge donnée est d'environ 25%.

La figure 13 montre la variation en fonction de la sollicitation τ/τ_{cr}^* de la contrainte membranaire de comparaison maximum $(\sigma_{mc})_{max}/\tau_{cr}^*$.

La ligne hachurée montre les valeurs de $\sigma_{cm\,max}$ pour une plaque qui ne voile pas. En ce cas,

$$\frac{\sigma_{cm\,max}}{\tau_{cr}^*} = \sqrt{3}\,\frac{\tau}{\tau_{cr}^*}. \tag{4.2}$$

5. Etat limite de la plaque

En attendant d'avoir une théorie analytique du comportement post-critique dans le domaine plastique, on peut se baser dans une analyse approximative de l'état limite des plaques sur la solution des équations correspondant au comportement parfaitement élastique (voir les équations (1) de la première partie de ce mémoire [1]).

En vue de définir l'état limite des plaques en acier, on peut accepter les points de vue suivants:

a) Tenons compte d'abord à la fois des contraintes de membrane et des contraintes de flexion.

Mesurons l'intensité de l'état de contrainte par la contrainte de comparaison σ_c calculée selon l'hypothèse de HUBER-MISES-HENCKY:

$$\sigma_c = \sqrt{\sigma_x^2 + \sigma_y^2 - \sigma_x\,\sigma_y + 3\,\tau^2}, \tag{5.1}$$

où σ_x, σ_y, τ désignent les sommes des contraintes de membrane et de flexion.

L'état limite dans ce cas est déterminé par la condition

$$\sigma_{c\,max} = R_e, \tag{5.2.}$$

indiquant que la contrainte maximum de comparaison $\sigma_{c\,max}$ atteint la limite élastique R_e.

En ce cas, l'état limite des âmes est donné par le début de plastification à la surface à l'endroit de la plaque le plus sollicité. Le début de plastification ne correspond pas à la ruine de la plaque; c'est pourquoi cette définition est assez conservatrice.

b) On peut ensuite considérer les contraintes de membrane uniquement.

De manière analogue, l'état limite est déterminé par la condition

$$\sigma_{cm\,max} = R_e. \tag{5.3).}$$

On suppose ainsi que les pointes de contrainte de flexion s'annulent dans le domaine plastique.

Il est vrai que même la sollicitation limite déterminée par la définition (b) ne correspond pas à la charge ultime. Mais, en tous cas, elle est moins conser-

vatrice que la contrainte limite déterminée par (a), parce qu'elle correspond déjà à un certain degré de plastification de l'âme.

C'est pourquoi nous avons utilisé ce concept dans l'analyse de l'effet de la rigidité flexionnelle d'un raidisseur vertical médian sur l'état limite d'une plaque carrée cisaillée.

Les sollicitations limites résultantes $\bar{\tau}$ sont données pour l'acier doux A 37 ($R_e = 2400$ kg/cm^2, par conséquent $R_e^\tau = 1385$ kg/cm^2) et pour $\gamma = 0$ (âme non raidie), $\gamma = \gamma^*$, $\gamma = 2\gamma^*$, $\gamma = 3\gamma^*$ à la figure 14.

Les contraintes critiques τ_{cr}, déterminées dans la première partie [1] de ce mémoire, sont également indiquées sur cette figure à titre de comparaison.

Il apparaît clairement que la sollicitation limite $\bar{\tau}$ est (sauf pour les minceurs faibles) substantiellement plus élevée que la contrainte critique τ_{cr}, ce qui indique l'effet bienfaisant du comportement hypercritique des plaques minces. Par exemple, pour $\gamma = 0$, $\bar{\tau}$ est, pour $\lambda = 200$, supérieur de 159%, et, pour $\lambda = 400$, de 626% à τ_{cr}; tandis que pour $\gamma = 3\gamma^*$: $\bar{\tau}$ est pour $\lambda = 200$, de 13,8% et pour $\lambda = 400$ de 183% plus élevé que τ_{cr}.

L'analyse de la sollicitation limite $\bar{\tau}$ montre que cette grandeur est considérablement influencée par la rigidité flexionnelle γ du raidisseur vertical. Par exemple, $\bar{\tau}(\gamma = 3\gamma^*)$ est, pour $\lambda = 200$, de 20,5%, et, pour $\lambda = 400$, de 15,6% plus élevé que $\bar{\tau}(\gamma = 0)$.

Il résulte en outre de la fig. 14 que la contrainte limite $\bar{\tau}$ continue à croître si la rigidité γ dépasse la valeur optimum théorique γ^*, ce qui est en accord avec les conclusions de la première partie [1] de ce mémoire, où l'on a montré,

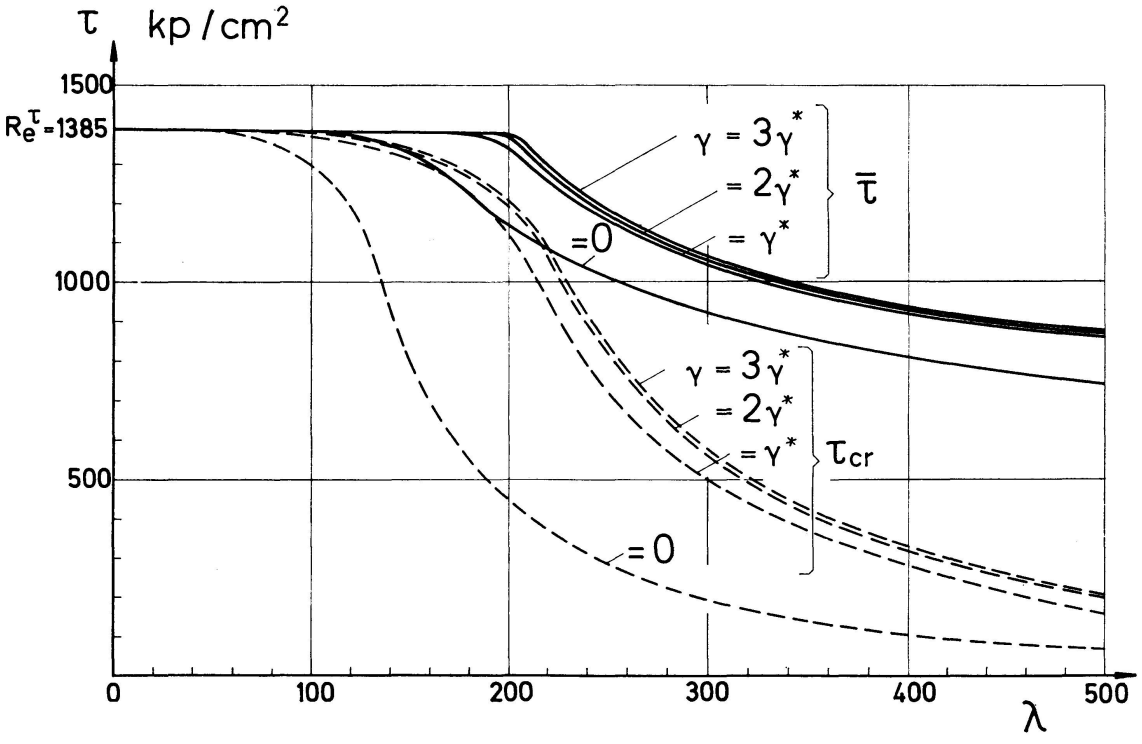


Fig. 14.

entre autre, que l'efficacité du raidisseur de rigidité relative $\gamma = \gamma^*$, est limitée dans le domaine post-critique.

Il faut souligner toutefois qu'en donnant à la rigidité flexionnelle γ du raidisseur la valeur $\gamma = 3\gamma^*$, on réduit certes considérablement la déformée du raidisseur et de la plaque, mais le bénéfice en sollicitation limite (dans le cas considéré d'une plaque carrée, cisaillée, renforcée par un raidisseur vertical médian) est assez faible.

Bibliographie

[1] CH. MASSONNET, M. SKALOUD et J. DONEA: Comportement postcritique d'une plaque carrée raidie cisaillée uniformément. Mémoires de l'A.I.P.C., Vol. 27, 1967, p. 187 à 210.

Résumé

Le présent mémoire constitue la seconde partie d'une étude sur le comportement postcritique des plaques raidies cisaillées uniformément, dont la première partie a été publiée dans le Volume 27 des Mémoires A.I.P.C., p. 187 à 210. Son objet est l'étude de la répartition des contraintes et l'analyse de *l'état limite* dans le cas particulier d'une plaque carrée.

Deux définitions différentes de l'état limite de la plaque sont examinées successivement. En adoptant la moins conservatrice des deux, qui définit l'état limite par la condition $\sigma_{cm\,max} = R_e$, où $\sigma_{cm\,max}$ est la plus grande contrainte membranaire et R_e la limite d'élasticité du métal, on montre numériquement que la *contrainte limite* $\bar{\tau}$ est substantiellement plus élevée que la contrainte critique τ_{cr}, le gain allant jusqu'à 626% pour une plaque non raidie de minceur $b/e = 400$. On montre aussi qu'en donnant au raidisseur la rigidité relative $\gamma = 3\gamma^*$, on réduit considérablement la déformée du raidisseur et de la plaque dans le domaine postcritique, mais le bénéfice sur la contrainte limite $\bar{\tau}$ est par contre assez faible.

Zusammenfassung

Diese Abhandlung bildet den zweiten Teil einer Studie über das überkritische Verhalten einer gleichmäßig durch Schub beanspruchten, versteiften Platte, deren erster Teil in den Abhandlungen der IVBH, Band 27, auf den Seiten 187 bis 210 abgedruckt ist. Die Verteilung der Spannungen sowie die Berechnung des Grenzzustandes für die Quadratplatte sollen behandelt werden.

Zwei Definitionen für den Grenzzustand werden nacheinander betrachtet: Wenn man die weniger konservative der beiden anwendet, dieselbe den Grenzzustand durch die Bedingung $\sigma_{cm\,max} = R_e$, wo $\sigma_{cm\,max}$ die größte Membran-

spannung und R_e die Streckgrenze des Metalles bedeuten, gibt, kann man numerisch zeigen, daß die Grenzschubspannung $\bar{\tau}$ wesentlich über der kritischen Schubspannung τ_{kr} liegt; für eine unversteifte Platte der Dicke $b/e = 400$ steigt der Gewinn bis zu 626%. Ebenso wird gezeigt, wenn man der Steife die relative Steifigkeit von $\gamma = 3\gamma^*$ zuweist, daß sich dann die Verformungen derselben und der Platte im überkritischen Bereich beträchtlich verringern, jedoch der Gewinn für die Grenzschubspannung $\bar{\tau}$ im Gegensatz dazu gering bleibt.

Summary

Present paper constitutes the second part of a study on the postbuckling behaviour of stiffened plates subjected to pure shear, whose first part has been published in the IABSE Publications, Vol. 27, p. 187 to 210. Its aim is the study of the distribution of stress and the analysis of the limit state in the particular case of a square plate.

Two different definitions of the limit state of the plate are examined in turn. Adopting the less conservative of the two, which defines the limit state by the condition $\sigma_{cm\,max} = R_e$, where $\sigma_{cm\,max}$ is the largest membrane stress and R_e the yield point of the metal, it is shown numerically that the limit stress $\bar{\tau}$ is substantially higher than the critical stress τ_{cr}, the benefit amounting to 626% for an unstiffened plate with a "thinness" $b/e = 400$. It is also shown that, by giving to the stiffener a relative rigidity $\gamma = 3\gamma^*$, the transverse displacements of the stiffener and the plate are considerably reduced in the postbuckling range; on the other hand, the increase in limit stress $\bar{\tau}$ is relatively small.

Nonlinear Inelastic Dynamics of Multi-Story Buildings

Dynamique non-linéaire inélastique de bâtiments à multiples étages

Nichtlineare, unelastische Dynamik von Hochhäusern

WILLIAM E. SAUL
Ph. D., Associate Professor

JAAFAR K. AL-ABDULLA
Graduate Student

Department of Civil Engineering, The University of Wisconsin,
Madison, Wisconsin, U.S.A.

Introduction

It is of interest to explore further and elaborate on the General Report on "Dynamic Effects of Wind and Earthquake" by D. SFINTESCO in the *Preliminary Publication* of the Eighth Congress of IABSE on the effects of nonlinear and inelastic deformation of multi-story buildings due to strong-motion earthquake [1].

In the general report, plastic deformation is correctly stated to act as a damping mechanism under high intensity earthquakes. In addition, damage is incurred whenever yielding takes place and the damage is accumulative. The damage may be assessed by integrating the area under the hysteresis loops of the moment-curvature diagram for each member since the method of analysis discussed herein accounts for the columns in flexure as continuous members, including the nonlinear and inelastic effects, instead of lumping the inelastic strain at discrete points as plastic hinges or bilinear hinges.

In this discussion a method of shear building analysis by direct stiffness presented by SAUL, FLEMING and LEE [2] for a bilinear hysteretic strain hardening moment-curvature material law is solved numerically by the fourth order Runge-Kutta formulation for a 10-story building subjected to an interval of the ground acceleration record of the north-south component of the 1940 El Centro, California earthquake to obtain very accurate response records of lateral deflection, column end moments, and other parameters of interest. In a shear building, the floor systems act as rigid diaphrams and the columns, which are rigidly attached to the floor systems, resist all lateral forces and

thereby undergo relative displacement between floors. In the analyses, the column segments are massless and continuous; the mass of each story is concentrated at the floor levels.

The nonlinear set of coupled differential equations of motion are numerically integrated over variable steps of time which, in this situation, are governed by either the pulse duration of the seismogram or a smaller interval used to pinpoint phase transitions in the bilinear hysteretic moment-curvature relationship. The response curves obtained, which are the histories of deflection, moment, etc., contain all the effects inherent in the assumptions including nonlinearities, inelastic deformations, and vibration in higher modes. It is notable that the response over the short time increment of integration is not assumed to be linear, but, in fact, follows the material law for shear-deflection which, integrated from the assumed bilinear moment-curvature relationship, is linear when elastic but otherwise nonlinear.

From the response data obtained, illustrative response curves for lateral deflection and column end moments are presented as well as moment-curvature diagrams and envelopes of maximum deflection and moment. Deflected shapes at particular times are also shown. Three values of the strain hardening coefficient were used in the analyses which define an elastic structure, an elasto-plastic structure, and a moderately strain hardened structure. Although damping was neglected in the problem solutions, it is available in the formulation and can be easily included. Since damping restricts vibration, it may be instructive to include it.

A frame building with flexible girders may be sized so that yielding must primarily take place in the girders. However, structures in which the floor beams are composite with reinforced concrete floors or are otherwise more rigid with respect to the columns, will force the inelastic deformation into the columns. Inelastic strains of increasing magnitude, accompanied with large deflections, may indicate that the structure is collapsing since stiffness in the inelastic material regime is a function of relative lateral deflection.

All equations herein are based on an n-story building with n-degrees of freedom in the plane. Thus, summation over repeated indices are understood to be from 1 to n and free indices identify a particular element.

Theoretical Background of the Inelastic Analysis

The complete derivation of the analysis is somewhat lengthy and given elsewhere [2] so only high points of the theory are repeated here. The material law and the resistance function of the structure are reviewed as items of principal interest.

The material represented by a bilinear strain-hardening hysteretic moment-curvature relationship can be given as

$$M_i = N_i + K_{ij}(\Phi_j - \Psi_j). \tag{1}$$

where M_i is the bending moment, Φ_j is the curvature, N_i and Ψ_j are the moment and curvature values at a material phase change and are constant throughout a phase, and the stiffness is

$$K_{ij} = \begin{cases} EI & \text{if } i=j \text{ and the phase is elastic,} \\ \alpha EI & \text{if } i=j \text{ and the phase is plastic,} \\ 0 & \text{if } i \neq j, \end{cases} \tag{2}$$

in which α is the coefficient of strain hardening. When $\alpha = 1$ the material remains elastic and as $\alpha \to 0$ an elastic-perfectly plastic material is represented. In addition, variable values of moment and curvature within a material phase, zero at each phase change, are defined as

$$L_i = M_i - N_i, \tag{3}$$

$$\Omega_i = \Phi_i - \Psi_i \tag{4}$$

so that

$$L_i = K_{ij}\Omega_j. \tag{5}$$

Thus, the material law is defined.

The equations of motion of an n-story multiple bay shear building with framed columns of an elastic-linear strain hardening inelastic material subjected to seismic motion are given as

$$m_{ij}\ddot{u}_j + C_{ij}\dot{u}_j + A_{ij}(u)\,u_j + B_i(u) = W_i\,G\,f(t), \tag{6}$$

where m_{ii} is the mass of the i-th story, the C_{ij} are viscous damping coefficients, W_i is the weight of story i, G is the magnitude factor of the earthquake (maximum fraction of acceleration due to gravity), $f(t)$ represents the unitized time variation of the earthquake; u_j, $\dot{u}_j$, and $\ddot{u}_j$ are the relative displacement, velocity, and acceleration, respectively, of the j-th floor, with respect to the base, the $A_{ij}(u)$ are stiffness influence coefficients, and $B_i(u)$ is a residual vector proportional to the accumulated inelastic strain in the columns. Furthermore, the resistance function of the structure, R_i for the i-th floor, is variable and may be represented as a function of relative displacement by

$$R_i(u) = A_{ij}(u)\,u_j + B_i(u), \tag{7}$$

where

$$A_{ij}(u) = S_{ik}K_{kr}\Gamma_{rj}(u), \tag{8}$$

$$B_i(u) = S_{ik}(N_k - K_{kr}\Gamma_{rj}(u)\,T_{jp}\Lambda_p), \tag{9}$$

in which T_{jp} and S_{ik} are constant for a particular structure, their being defined by geometry, Λ_p accounts for residual strain at phase changes, N_k is the bending moment at a phase change, and $\Gamma_{rj}(u)$ is a nonlinear function of $\Omega_i(u)$ the phase variable curvature which is a function of relative displacement. When $\alpha \to 0$ $\Gamma_{rj}(u)$ is singular so a very small value of α, say $\alpha = 0.0001$, is used in calculations for the elastic-perfectly plastic case.

A detailed derivation of the analysis which includes complete definitions of all the tensors given herein is given in reference [2].

The Method of Computation

Numerical Integration

The equations of motion, Eq. (6), without damping, were integrated numerically using the Runge-Kutta fourth-order method [3]. The equations of motion are written

$$\ddot{u}_i = F(t, u_i, \dot{u}_i) = \frac{1}{m_{(ii)}} [G W_i f(t) - A_{ij}(u) u_j - B_i(u)] \tag{10}$$

and the solution at time $t+\tau$, where $\tau = \Delta t$, is

$$u_i(t_1+\tau) = u_i(t_1) + \tau \dot{u}_i(t_1) + \tfrac{1}{6}\tau(a_i + b_i + c_i), \tag{11A}$$

$$\dot{u}_i(t_1+\tau) = \dot{u}_i(t_1) + \tfrac{1}{6}(a_i + 2b_i + 2c_i + d_i), \tag{11B}$$

in which

$$a_i = \tau F[t_1, u_i(t_1), \dot{u}_i(t_1)], \tag{12A}$$

$$b_i = \tau F[t_1 + \tfrac{1}{2}\tau, u_i(t_1) + \tfrac{1}{2}\tau \dot{u}_i(t_1), \dot{u}_i(t_1) + \tfrac{1}{2}a_i], \tag{12B}$$

$$c_i = \tau F[t_1 + \tfrac{1}{2}\tau, u_i(t_1) + \tfrac{1}{2}\tau \dot{u}_i(t_1) + \tfrac{1}{4}\tau a_i, \dot{u}_i(t_1) + \tfrac{1}{2}b_i], \tag{12C}$$

$$d_i = \tau F[t_1 + \tau, u_i(t_1) + \tau \dot{u}_i(t_1) + \tfrac{1}{2}\tau b_i, \dot{u}_i(t_1) + c_i]. \tag{12D}$$

Note that the $A_{ij}(u)$ and $B_i(u)$ are functions of displacement and are recalculated for each of the values in Eqs. (12) using the extrapolation values of the displacement function in the formulation.

The duration of the time increment $\Delta t = \tau$ should be as large as possible to conserve computation time and retain a valid solution. However, it may have to be decreased to pinpoint the coordinates of a material phase transition or the characteristics of the forcing function. Since the duration of Δt may be changed with each integration and the time between pulse changes of an earthquake accelerogram is considerably smaller than the period of a tall building, a larger time increment well within the duration of pulse change coordinates of the seismogram and a smaller time increment of 1/20 to 1/4 of the larger to locate the material phase transitions should be chosen for the integration.

Computer Program

A program was written to perform the computation with a digital computer. Once the story heights, weights, and column stiffnesses and yield moments are processed to obtain the physical parameters describing the structure, seismogram cards are read which give the coordinates of acceleration and time

delineating peak values. As each seismogram card is read integration proceeds, linearly interpolating seismogram values, at the larger time increment until a material phase transition has been passed. At that time, the last set of calculations are rejected and integration proceeds from the former time with the smaller time increment until the material phase transition is established. Control then returns to the larger time increment until a material phase transition is again detected, at which time the process is repeated.

Each cycle of integration required the reestablishment of the variable matrices, a number of matrix operations, and a check on each column for possible material phase transitions. Lateral floor deflections; column moments, shears, curvature, and angle change moments; residual values of column moments, curvature, and angle change moments; as well as the stiffness influence coefficients and the residual force vector are obtained and printed with each integration cycle.

The procedure is essentially a direct stiffness method and, therefore, matrix operations of multiplication or addition only are required.

The Design Building

For purposes of this study, a 10-story shear building was designed for which the parameters of a column segment are given in Table 1. The funda-

Table 1. 10-story column segment of design building

Story	Height (ft.)	Weight (kips)	I (in.^{4})
1	15	58.5	1166
2	12	58.5	1166
3	12	58.5	1166
4	12	56.5	1166
5	12	56.5	583
6	12	56.5	583
7	12	49.5	583
8	12	49.5	389
9	12	49.5	389
10 (Roof)	12	44.0	389

mental period of the elastic structure is 1.5 seconds using $E = 30{,}000$ ksi for the material. The first column of 4 stories length extends through the first story although this obviously decreases its stiffness. This built in defect not only sensed response effects more rapidly than the rest of the structure as expected but also appears to provide a probable collapse mechanism, especially in the elasto-plastic case.

The initial yield moment for a column is reduced because of the presence of axial force and is given, arbitarily, by

$$N_i' = \epsilon I_i, \tag{13}$$

where ϵ is a factor defined by

$$\epsilon = 1.076 \frac{F_y}{d}. \tag{14}$$

F_y is the yield stress of the material, and d is the depth of the section. Eq. (14) is derived as follows: From AISC formula 21 [4]:

$$\frac{N_i'}{M_{pi}} = 1.18\left(1 - \frac{P}{P_y}\right), \tag{15}$$

where $P_y = F_y A$, P is the axial force, and

$$M_{pi} \cong 1.14 \frac{2 F_y I}{d}. \tag{16}$$

Since maximum $P = 0.6 P_y$ (Section 2.3 of [4]) substitution of Eq. (16) into Eq. (15) yields Eq. (14). Thus, for the A 36 steel 12 inch columns used in the problem $\epsilon = 0.269$ ft.-kips/in.^{4}. In addition, the yield moment of column 1 was further reduced by a ratio of the story heights of adjacent columns cubed to account for its lesser stiffness. This factor is empirical and may prove to be excessive or unnecessary, however, results of analyses without it were not significantly different.

The building is tapered in stiffness and mass. It is representative of a commonplace type of rectangular design although the analysis can handle buildings which decrease in the number of bays with height.

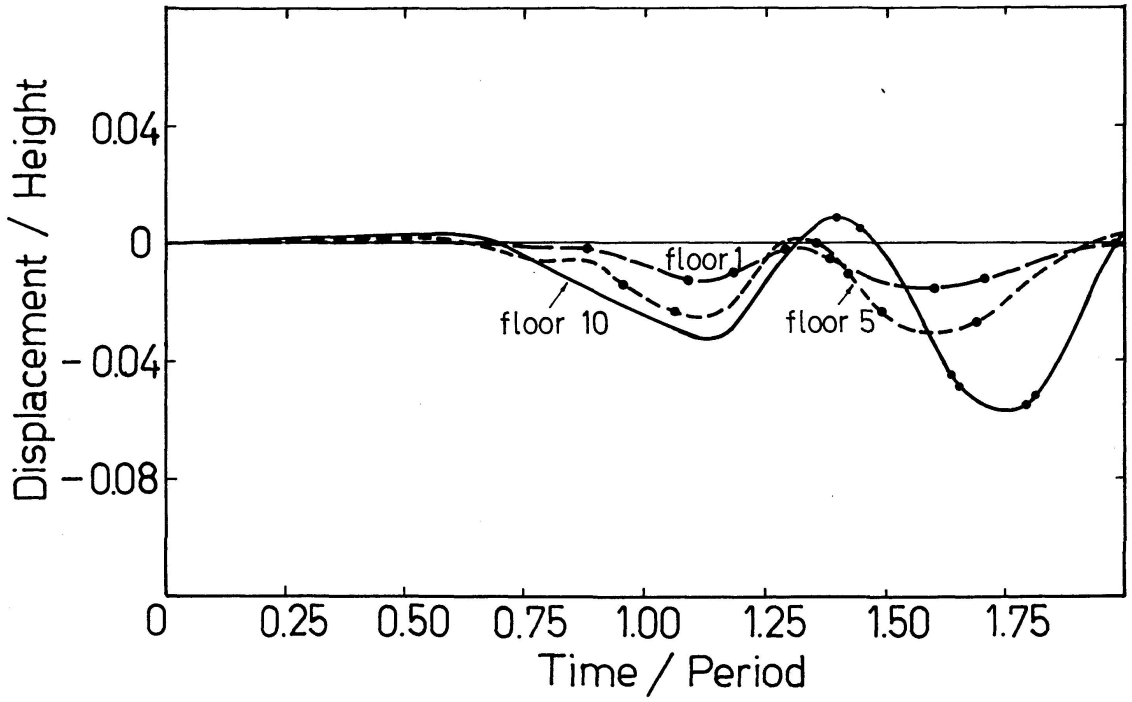


Fig. 1. Deflection response curves for floors 1, 5 an 10 ($\alpha = 0.10$).

Response Calculations

The north-south component of the May 18, 1940 El Centro, California ground acceleration, which is well known and somewhat of a standard in earthquake engineering studies, was used as the dynamic excitation in this study. It is representative of a moderately strong earthquake. The maximum pulse has an acceleration of about 32% of gravity. The most intensive portion of the earthquake was in the second through fifth seconds of its duration although intensive ground movement continued for a half minute. To conserve computer time the problem calculations were generally for 3 seconds of earthquake duration although several solutions were for more extensive periods of time. The

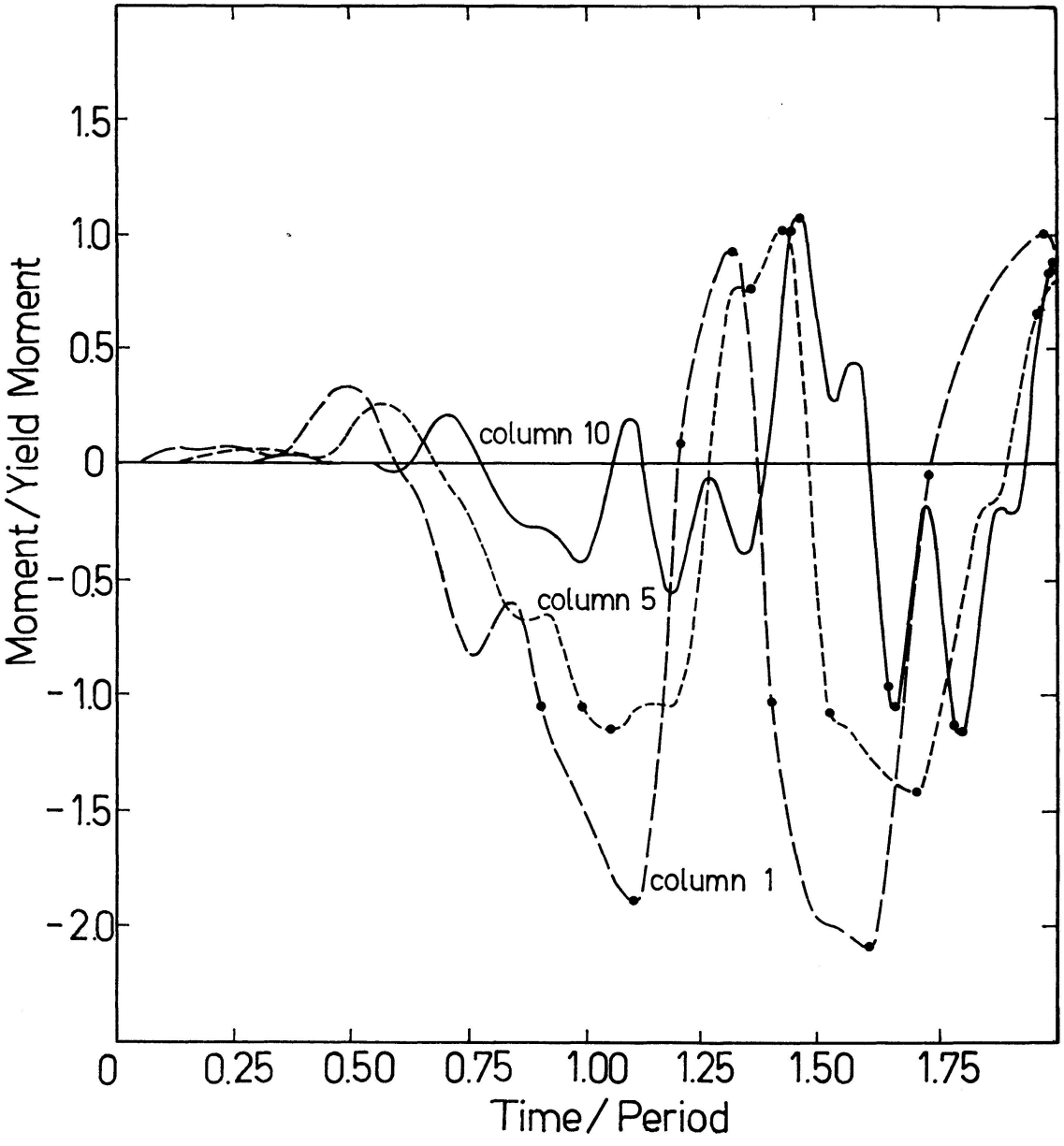


Fig. 2. End moment response Curves for columns 1, 5 and 10 ($\alpha = 0.10$).

results obtained for this particular excitation are only indicative of earthquake response in general since each has its own characteristics.

The design building, with strain-hardening coefficients of $\alpha = 0.00001$ (elasto-plastic), $\alpha = 0.10$ (moderate strain-hardening) and $\alpha = 1.0$ (elastic) was subjected to 3 seconds of excitation. Stress resultants of moment, deflection, curvature, influence coefficients, the resistance forces including residuals, and the excitation were recorded at each time interval of integration, as well as other parameters. From the data representative curves were plotted.

Results of the Analysis

Histories of the deflections and column end moments of floors 1, 5 and 10 with a strain hardening coefficient of $\alpha = 0.10$ are shown in Figs. 1 and 2. The response of floor 10 for the elasto-plastic case, $\alpha = 0.00001$, a strainhardened case in which $\alpha = 0.10$, and the elastic case in which $\alpha = 1.00$ are shown in Figs. 3 and 4. Material regime changes are marked on the curves indicating when excursions take place into the plastic phase. Although excessive deflections were noted for the elasto-plastic case, which may indicate incipient collapse, the bending moment is, of course, contained. However, in the presence of strain

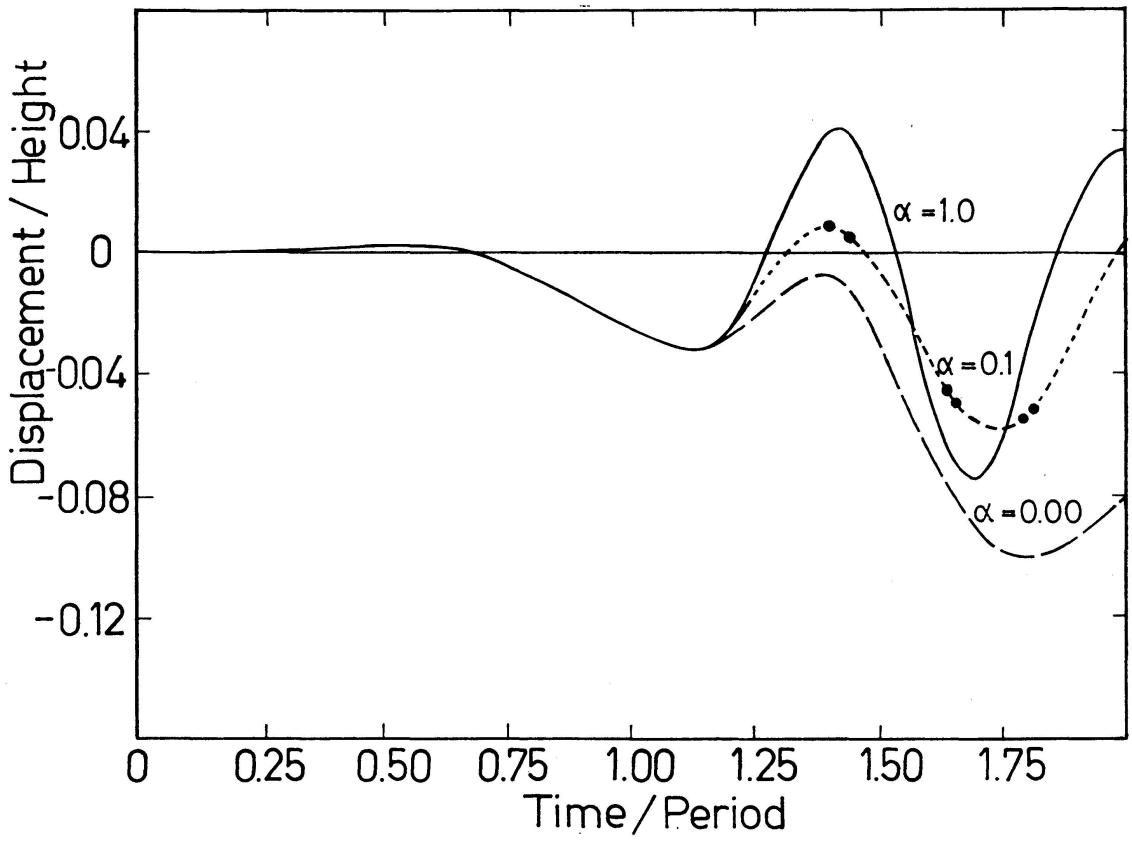


Fig. 3. Deflection response curves for floor 10 for $\alpha = 0.0$, $\alpha = 0.1$ and $\alpha = 1.0$.

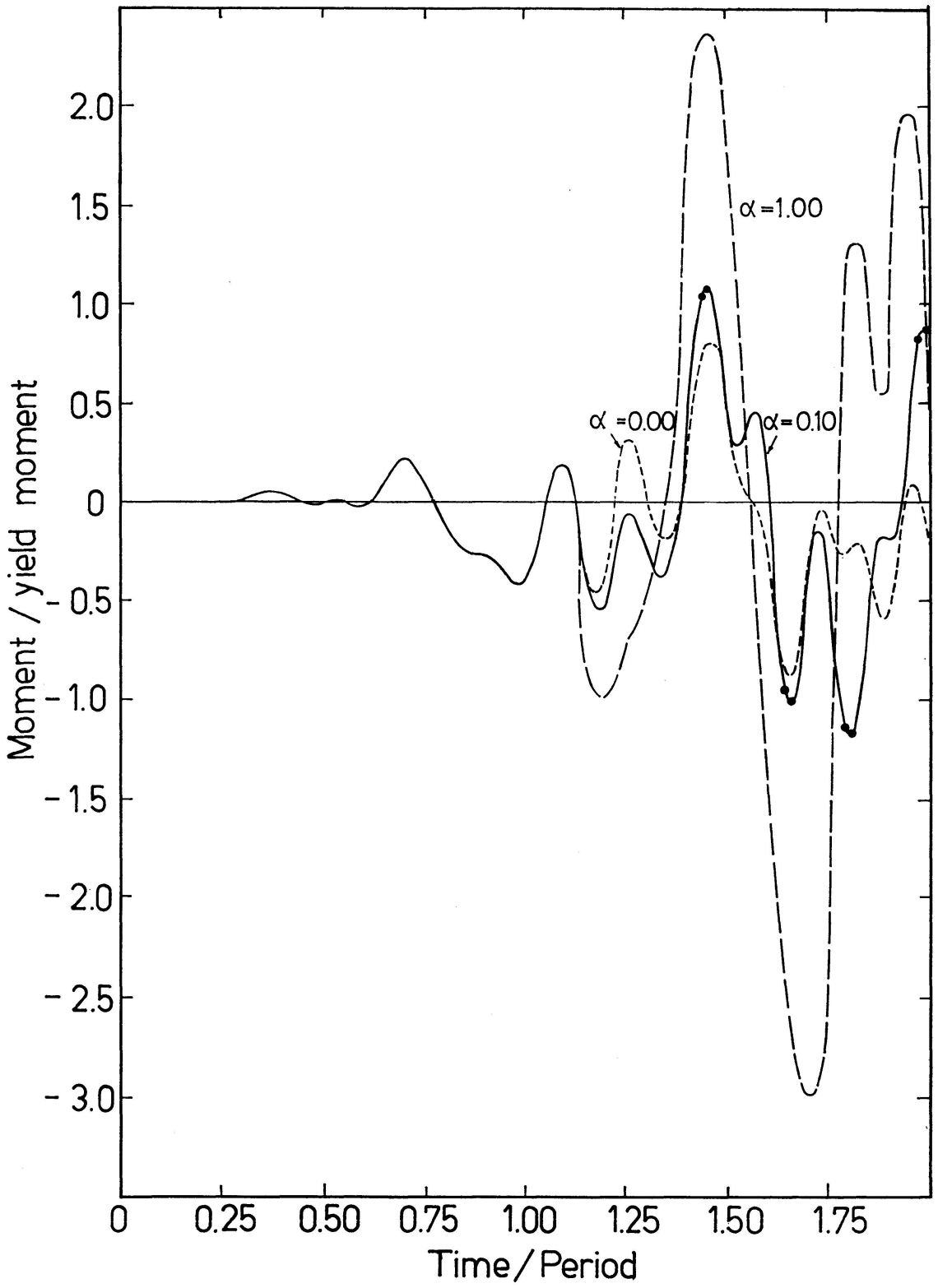


Fig. 4. End moment response curve of the 10th story column for $\alpha=0.00$, $\alpha=0.10$ and $\alpha=1.00$.

hardening, although deflections are considerably decreased with respect to the elasto-plastic case, the magnitude of bending moment in the first story column indicates that it is undergoing excessive deformation although the higher columns are not.

The moment-curvature excursions for columns 1 and 10 with a strain hardening coefficient of $\alpha = 0.10$ are shown in Fig. 5. The amount of plastic deformation can be easily seen from this type of diagram. The limbs of the curves are either positive velocity or negative velocity and their directions are marked. The area under this diagram is a measure of energy and so constitutes a record of cumulative damage. After the ground acceleration has died out

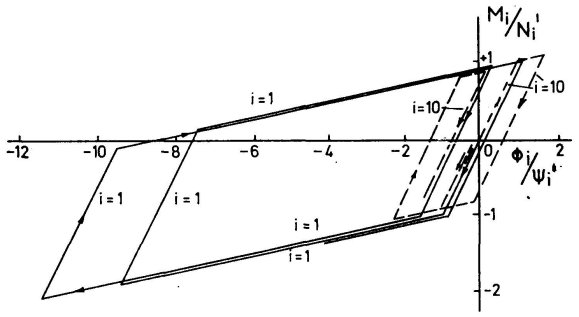


Fig. 5. End moment-curvature history of columns 1 and 10 for $\alpha = 0.1$,

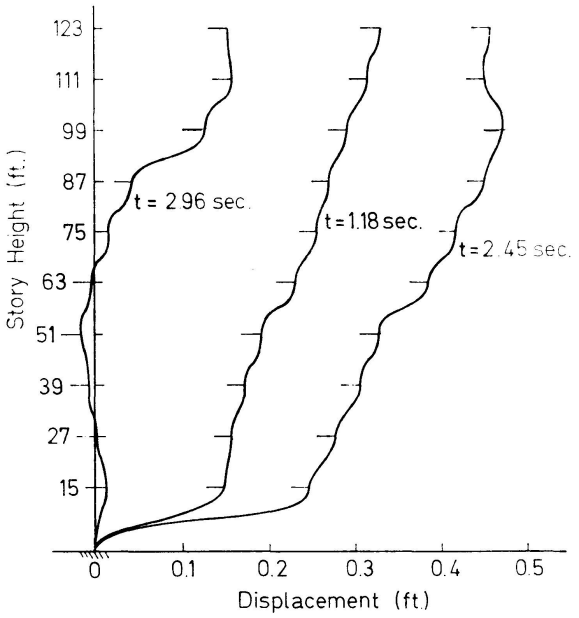


Fig. 6. Defiected position of 10-story column at selected times ($\alpha = 0.10$).

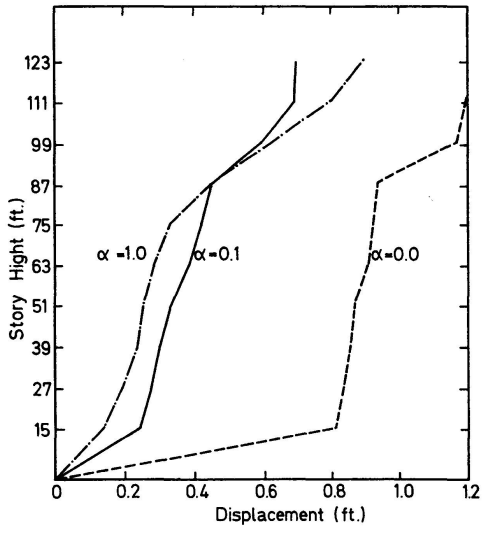


Fig. 7. Envelope of maximum story deflections for $\alpha = 0.00$, $\alpha = 0.10$ and $\alpha = 1.00$ with 3 second duration.

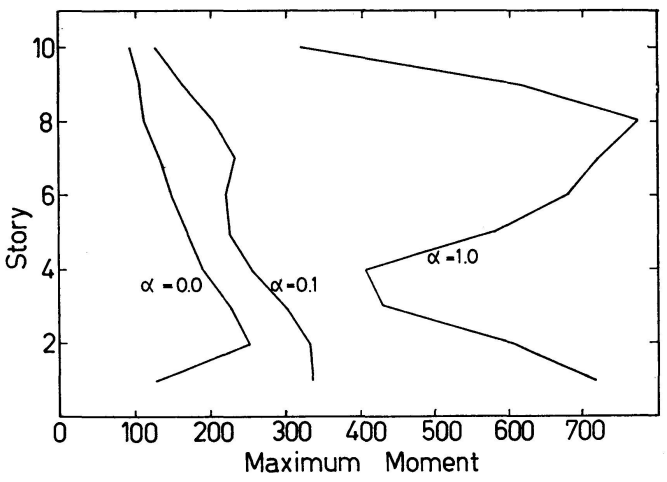


Fig. 8. Envelope of maximum column moments of each story for $\alpha = 0.0$, $\alpha = 0.1$ and $\alpha = 1.0$ within a 3 second duration. (Moments in ft.-kips.)

the structure, if it has not collapsed, will vibrate elastically about a new axis where the offset in curvature is the permanent set.

The deflected position of the 10-story column segment at three randomly selected times is of illustrative interest in that it depicts a physical view of the vibration. Of particular interest is the behavior of the first story column due to its greater relative flexibility to the columns immediately above. The reduced stiffness and yield moment of column 1 is immediately evident in Figs. 5 and 6.

Of major interest to the analyst are the maximum values of deflection and stress resultants at each story which occured during the earthquake. Maximum values can be taken from the response curves and plotted as an envelope as is shown in Fig. 7 for maximum deflections and in Fig. 8 for maximum bending moments for the three levels of strain hardening used in the solution. Maximum shears are directly proportional to the end moments and are given by

$$V_i = \frac{2}{h_{(i)}} M_i. \tag{17}$$

The moment in a column is related to the difference in lateral deflection of its adjoining floors. Thus, the change in deflection between stories in Fig. 7 relates to the moment in Fig. 8, but only in a general sense since the relationship is not linear.

Conclusions

It is shown that a structure idealized as a shear building can be very precisely, within the framework of prior assumptions, analyzed for its response under seismic loading by numerically integrating the nonlinear equations of motion. The columns are treated as continuous members and so inelastic strains also have continuity. No conclusions can be drawn with respect to the behavior of shear buildings in general from the limited analyses in this paper. However, the behavior of the structure analyzed is studied in depth. It is immediately apparent that the lesser stiffness of column 1 and its reduced yield moment has a pronounced adverse effect on the structure. It is felt that a more accurate method of yield moment reduction due to axial force should be used.

Acknowledgment

The research upon which this paper is based was supported in part by the National Science Foundation under Grant No. GK-951 and the University of Wisconsin Computing Center, which is partially supported by the Wisconsin Alumni Research Foundation and the National Science Foundation.

References

1. D. Sfintesco: "Dynamic Effects of Wind and Earthquake". International Association for Bridge and Structural Engineering, Eighth Congress, New York, Preliminary Publication (1968), p. 345—367.
2. W. E. Saul, J. E. Fleming, S. L. Lee: "Dynamic Analysis of Bilinear Inelastic Multiple Story Shear Buildings". Proceedings — Third World Conference on Earthquake Engineering, New Zealand, 1965, Vol. II, p. II—533—551.
3. F. B. Hildebrand: Introduction to Numerical Analysis. McGraw-Hill Book Co., New York, 1956, p. 236—239.
4. Anon.: Manual of Steel Construction, AISC, Sixth Ed., 1967.

Summary

A direct stiffness method of analysis of multi-story shear buildings of a bilinear hysteretic material is used to find their response to ground motion. The nonlinear coupled equations of motion of a building are precisely integrated with the Runge-Kutta Method of numerical integration to obtain their deformation and stress resultant history due to ground acceleration records of the 1940 El Centro earthquake. A 10-story structure is analyzed at three levels of strain hardening in the post-elastic material regime. It is shown how damage may be assessed.

Résumé

Une méthode de rigidité directe permet l'analyse des réactions aux mouvements du sol d'une construction à plusieurs étages, assemblée avec des matériaux à histérésie bilinéaire. Les équations de mouvement d'une construction, non-linéaires, couplées, sont résolues avec précision par l'intégration numérique de la méthode Runge-Kutta, ce qui donne les déformations et les contraintes dues aux accélérations du sol lors du séisme d'El Centro en 1940. Un bâtiment à 10 étages est analysé dans le domaine post-élastique du matériau, à trois échelons de durcissement. Il est démontré comment des dégâts peuvent être évités.

Zusammenfassung

Um die Wirkung der Bodenbewegung (infolge Erdbebens) auf ein Hochhaus aus Material, welches bilineare Hysteresis aufweist, beschreiben zu können, wird ein direktes Drehwinkelverfahren angewandt. Die nichtlinearen, gekoppelten Bewegungsgleichungen sind genau nach Runge-Kutta integriert worden, um den Verlauf der Verformungen und Spannungen infolge der Beschleunigungen des El-Centro-Erdbebens zu erhalten, welches 1940 stattfand. Ein zehnstöckiges Tragwerk ist für drei Stufen innerhalb des Verfestigungsbereiches untersucht worden. Es folgt daraus, wie Schaden abgewendet werden kann.

Maximum Loads for Eccentrically Loaded Thin-walled Channel Struts

Charges maximales pour piles à parois minces en U, comprimées excentriquement

Höchstlasten für dünnwandige U-Stützen unter ausmittiger Belastung

A. C. WALKER
Department of Civil Engineering, University College, London

Introduction

The use of thin-walled open sections as load-bearing members in civil engineering structures has increased considerably in the last few years. This has given rise to a greater need to understand the mechanics of the behaviour of these sections and also to obtain design information in a simple and comprehensible manner. Although considerable research effort [1–3] has been applied to the testing and analysis of uniformly-compressed channel-columns, relatively little attention has been given to the more general condition in which the load is applied offset from the centroid of the cross-section. This paper reports on work carried out on this problem both from an experimental and theoretical standpoint.

The paper is concerned with channel columns having one axis of symmetry in the cross-section, and in the analysis it is assumed that the compressive

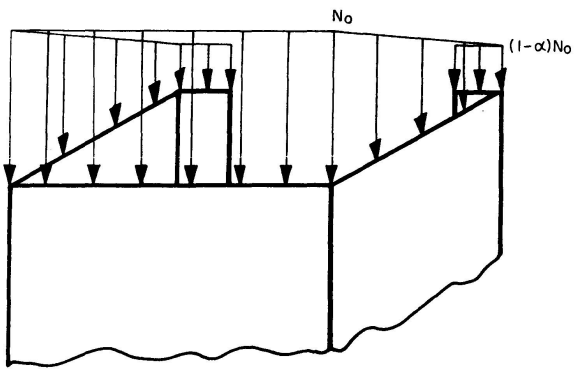


Fig. 1. Channel loading geometry.

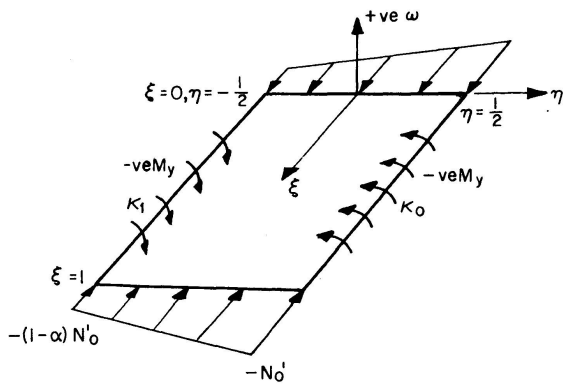


Fig. 2. Non-dimensional representation of plate geometry edge-loading and edge restraints.

load is applied along this axis; then the web of the channel is compressed uniformly, while a linearly varying stress is applied to the flanges, as in Fig. 2. It is also assumed that open thin-walled channel-sections, in which the length is of the same order of magnitude as the flange or web widths, may be considered from a theoretical viewpoint to be composed of individual plates that are connected in a certain manner on their common longitudinal edges. The determination of the channel load-bearing characteristics then becomes one of obtaining the corresponding plate properties and combining these to obtain compatible conditions along the adjoining edge.

We first consider the behaviour of thin, initially flat, plates loaded by a linearly varying edge stress. It has been shown [4] that such plates may sustain load considerably in excess of the theoretical buckling loads before collapse occurs. Also, good engineering estimates of these maximum loads may be obtained analytically by assuming that collapse takes place when the direct stress at the edge reaches the material compressive yield stress. Since the unloaded edge conditions were taken to be rotationally restrained the calculated plate instability loads may be synthesise to provide the theoretical buckling loads [5] of open sections considered to be composed of such plates. In practice, no plate is perfectly flat, and deflections will grow from the beginning of load application; for this reason, the theoretically predicted buckling behaviour is never experienced in practice. However, such a buckling analysis will indicate to a designer the loads for maximum growth of deformation and maximum rate of decrease of stiffness. Like their constituitive plates, compressed sections may sustain loads in excess of the theoretical buckling loads. In this paper an approximate method of analysis is presented which combines the plate collapse estimates to give the corresponding estimate for lipped sections. Test results are described which show that the estimates are good; these results are used as a basis for an empirical approach, by which the actual collapse loads may be predicted from the corresponding theoretical instability loads.

1. Analysis of Single Plates

a) Mathematical Formulation

Ref. [4] presents fully the analysis of the buckling and post-buckling behaviour of initially-flat, rectangular plates compressed by a linear-varying load action. The loaded edges were taken to be simply-supported whilst the longitudinal edges have equal or unequal rotational restraint; this is shown in Fg. 2. For the sake of completeness the above analysis is summarised in this paper. We put,

$$\xi = \frac{x}{a}, \quad \eta = \frac{y}{b}, \quad \phi = \frac{a}{b}, \quad \omega = \frac{w}{t}, \quad F' = \frac{F}{E t^2}, \tag{1}$$

where a is the length of the plate in the x direction and b is the breadth in the y direction; the VON KÁRMÁN [6] large deflection equations may be written in the nondimensional forms

$$\frac{1}{\phi^2}\frac{\partial^4\omega}{\partial\xi^4}+2\frac{\partial^4\omega}{\partial\xi^2\partial\eta^2}+\phi^2\frac{\partial^4\omega}{\partial\eta^4}=12(1-\nu^2)\left(\frac{\partial^2F'}{\partial\xi^2}\frac{\partial^2\omega}{\partial\eta^2}+\frac{\partial^2F'}{\partial\eta^2}\frac{\partial^2\omega}{\partial\xi^2}-2\frac{\partial^2F'}{\partial\xi\,\partial\eta}\frac{\partial^2\omega}{\partial\xi\,\partial\eta}\right), \tag{2a}$$

$$\frac{1}{\phi^2}\frac{\partial^4F'}{\partial\xi^4}+2\frac{\partial^4F'}{\partial\xi^2\partial\eta^2}+\phi^2\frac{\partial^4F'}{\partial\eta^4}=\left(\frac{\partial^2\omega}{\partial\xi\,\partial\eta}\right)+\frac{\partial^2\omega}{\partial\xi^2}\frac{\partial^2\omega}{\partial\eta^2}, \tag{2b}$$

where F' is the non-dimensional form of the Airy stress function, which is related to the direct and shear stresses by

$$\sigma_\xi=\frac{\sigma_x a^2}{\phi^2 E t^2}=\frac{\partial^2F'}{\partial\eta^2},\qquad \sigma_\eta=\frac{\sigma_y a^2}{E t^2}=\frac{\partial^2F'}{\partial\xi^2},\qquad \tau_{\xi\eta}=\frac{\tau_{xy}a^2}{\phi E t^2}=-\frac{\partial^2F'}{\partial\xi\,\partial\eta}.$$

The in-plane boundary conditions for the loaded edges, $\xi=0$ and $\xi=1$, with the imposed loading and for zero shearing stress, are

$$[\sigma_\xi]_{\xi=0,1}=\left[\frac{\partial^2F'}{\partial\eta^2}\right]_{\xi=0,1}=N_0'\left[\left(1-\frac{\alpha}{2}\right)+\alpha\eta\right], \tag{3a}$$

$$[\tau_{\xi\eta}]_{\xi=0,1}=\left[-\frac{\partial^2F'}{\partial\xi\,\partial\eta}\right]_{\xi=0,1}=0, \tag{3b}$$

where $N_0'=\frac{N_0 a^2}{\phi^2 E t^3}$ and α is the eccentricity parameter.

Along the unloaded edges there is considered to be no direct stress acting in the η direction nor any shearing stress, so that

$$[\sigma_\eta]_{\eta=+1/2,-1/2}=\left[\frac{\partial^2F'}{\partial\xi^2}\right]_{\eta=+1/2,-1/2}=0, \tag{4a}$$

$$[\tau_{\eta\xi}]_{\eta=+1/2,-1/2}=\left[\frac{\partial^2F'}{\partial\xi\,\partial\eta}\right]_{\eta=+1/2,-1/2}=0. \tag{4b}$$

The out-of-plane boundary conditions along the loaded edges were those of simple support, i.e. if M_ξ is the linear intensity of bending moment about an axis parallel to the η axis, then

$$[M_\xi]_{\xi=0,1}=\left[\frac{\partial^2\omega}{\partial\xi^2}+\nu\phi^2\frac{\partial^2\omega}{\partial\phi^2}\right]_{\xi=0,1}=0, \tag{5a}$$

$$[\omega]_{\xi=0,1}=0. \tag{5b}$$

The unloaded edges are fully restrained against lateral deflection and elastically restrained against rotation, i.e.

$$[\omega]_{\eta=+1/2,-1/2} = 0, \tag{6a}$$

$$\left[\frac{\partial^2\omega}{\partial\eta^2} + \frac{\nu}{\phi^2}\frac{\partial^2\omega}{\partial\xi^2} - \kappa_1\frac{\partial\omega}{\partial\eta}\right]_{\eta=+1/2,-1/2} = 0, \tag{6b}$$

$$\left[\frac{\partial^2\omega}{\partial\eta^2} + \frac{\nu}{\phi^2}\frac{\partial^2\omega}{\partial\xi^2} + \kappa_0\frac{\partial\omega}{\partial\eta}\right]_{\eta=+1/2} = 0, \tag{6c}$$

where $\kappa_1 = -b r_1/D$, $\kappa_0 = -b r_0/D$ and r_1, r_0 are the degrees of rotation restraint.

An approximate solution of Eq. (2), together with the appropriate boundary conditions (Eq. (3–6)), is obtained using Galerkin's method and employing a digital computer to perform the necessary arithmetic. The trial series for F' is

$$F' = A\left[\left(1-\frac{\alpha}{2}\right)+\frac{\alpha}{3}\eta\right]\eta^2 + \sum_r\sum_s b_{rs} f_r(\xi)\, g_s(\eta), \tag{7}$$

where A is a constant, b_{rs} are constant coefficients, $f_r(\xi)$ and $g_s(\eta)$ are functions of ξ and η only, respectively. After consideration if Eqs. (3) and (4), Eq. (7) besomes

$$F' = \frac{N_0'}{2}\left[\left(1-\frac{\alpha}{2}\right)+\frac{\alpha}{3}\eta\right]\eta^2 + \sum_{r=1,2,\ldots}\ \sum_{s=0,1,\ldots} b_{rs}\sin^2 r\pi\xi\left(\eta^{s+4} - \frac{1}{2}\eta^{s+2} + \frac{1}{16}\eta^s\right). \tag{8}$$

Similarly a trial series for ω may be obtained which satisfies the appropriate boundary conditions (Eqs. (5) and (6)). This series may be written

$$\omega = \sum_{m=1,2,\ldots}\ \sum_{n=0,1,\ldots} q_{mn}\sin m\pi\xi\,[\eta^{n+4} + A_n\eta^{n+3} + B_n\eta^{n+2} + C_n\eta^{n+1} + D_n\eta^n], \tag{9}$$

where the coefficients A_n, B_n, etc., may be obtained from the solution of the matrix equation

$$\begin{bmatrix} 1 & 2 & 4 & 8 \\ 1 & -2 & 4 & -8 \\ 2(n+3)\left[(n+2)+\frac{\kappa_0}{2}\right] & 4(n+2)\left[(n+1)+\frac{\kappa_0}{2}\right] & 8(n+1)\left[n+\frac{\kappa_0}{2}\right] & 16n\left[(n-1)+\frac{\kappa_0}{2}\right] \\ 2(n+3)\left[(n+2)+\frac{\kappa_1}{2}\right] & -4(n+2)\left[(n+1)+\frac{\kappa_1}{2}\right] & 8(n+1)\left[n+\frac{\kappa_1}{2}\right] & -16n\left[(n-1)+\frac{\kappa_1}{2}\right] \end{bmatrix} \cdot \begin{bmatrix} A_n \\ B_n \\ C_n \\ D_n \end{bmatrix} = \begin{bmatrix} -\frac{1}{2} \\ \frac{1}{2} \\ -(n+4)\left[(n+3)+\frac{\kappa_0}{2}\right] \\ (n+4)\left[(n+3)+\frac{\kappa_1}{2}\right] \end{bmatrix}.$$

b) Buckling

Theoretically buckling occurs when the flat plate becomes unstable at a particular value of the applied stress distribution. Thus, in Eq. (8) we have

$b_{rs} \equiv 0$, and, if the plate is considered to buckle in a unique sinewave form in the longitudinal direction, we may write Eq. (9) in the form

$$\omega = \sum_{n=0,1,\ldots}^{n=L} q_n \sin m\pi\xi \, Y_n, \tag{10}$$

where $$Y_n = [\eta^{n+4} + A_n \eta^{n+3} + B_n \eta^{n+2} + C_n \eta^{n+1} + D_n \eta^n].$$

Thus Galerkin's method when applied to Eq. (2) using $b_{rs} = 0$ and Eq. (10), gives

$$\sum_{n=0,1,\ldots}^{n=L} q_n \int_{-1/2}^{1/2} \left\{ \frac{d^4 Y_n}{d\eta^4} - 2\frac{m^2\pi^2}{\phi^2}\frac{d^2 Y_n}{d\eta^2} + \frac{m^4\pi^4}{\phi^4} Y_n - k\frac{m^2\pi^2}{\phi^2}\left[\left(1-\frac{\alpha}{2}\right) + \alpha\eta\right] Y_n \right\} Y_j \, d\eta = 0 \qquad (0 \leqq j \leqq L), \tag{11}$$

where $$k = -\frac{N_0 b^2}{D}.$$

Evaluation of Eq. (11) leads to an algebraic eigenvalue problem for k, the buckling coefficient. This is very easily programmed for solution on a digital computer, and it has been shown [5] that the buckling coefficient converges rapidly for increasing number of terms (L). The buckling load is obtained from

$$P_{crit.} = -\frac{k D}{b}\left(1 - \frac{\alpha}{2}\right).$$

c) Post-buckling Behaviour

It is assumed here that there is no change of buckle pattern as the load is increased beyond the buckling load. Thus, if Eq. (9) is written

$$\omega = \sin m\pi\xi \sum_{n=0,1,\ldots}^{n=L} q_n [\eta^{n+4} + A_n \eta^{n+3} + B_n \eta^{n+2} + C_n \eta^{n+1} + D_n \eta^n],$$

and, if in Eq. (8) the summations are given the limits $1 \leqq r \leqq T$, $0 \leqq s \leqq u$, then Galerkin's method for Eq. (2) gives

$$\sum_{n=0,1,\ldots}^{n=L} \sum_{r=1,2,\ldots}^{r=T} \sum_{s=0,1,\ldots}^{s=U} \int_0^1 \int_{-1/2}^{1/2} \left[\frac{1}{\phi^2}\frac{\partial^4 F'}{\partial\xi^4} + 2\frac{\partial^4 F'}{\partial\xi^2\partial\eta^2} + \phi^2\frac{\partial^4 F'}{\partial\eta^4} - \left(\frac{\partial^2\omega}{\partial\xi\,\partial\eta}\right)^2 + \frac{\partial^2\omega}{\partial\xi^2}\frac{\partial^2\omega}{\partial\eta^2}\right]\frac{dF_{pq}}{db_{pq}} d\eta\, d\xi = 0, \tag{12a}$$

$$\sum_{n=0,1,\ldots}^{n=L} \sum_{r=1,2,\ldots}^{r=T} \sum_{s=0,1,\ldots}^{s=U} \int_0^1 \int_{-1/2}^{1/2} \left\{ \frac{1}{\phi^2}\frac{\partial^4\omega}{\partial\xi^4} + 2\frac{\partial^4\omega}{\partial\xi^2\partial\eta^2} + \phi^2\frac{\partial^4\omega}{\partial\eta^4} - 12(1-\nu^2)\left[\frac{\partial^2 F'}{d\xi^2}\frac{\partial^2\omega}{\partial\eta^2} + \frac{\partial^2 F'}{\partial\eta^2}\frac{\partial^2\omega}{\partial\xi^2} - 2\frac{\partial^2 F'}{\partial\xi\,\partial\eta}\frac{\partial^2\omega}{\partial\xi\,\partial\eta}\right]\right\}\frac{d\omega_i}{dq_i} d\eta\, d\xi = 0, \tag{12b}$$

where

$$1 \leqq p \leqq T, \quad 0 \leqq q \leqq U, \quad 0 \leqq i \leqq L.$$

Evaluation of Eq. (12) gives

$$[A][b_{rs}] = [B][q_i q_j], \tag{13}$$

$$\{[C_1'] - N_0'[C_2]\}[q_k] = [D][b_{rs} q_k], \quad (0 \leqq i, j, k \leqq L) \tag{14}$$

where the coefficients of the matrices $[A], [B]$ etc., are constants. Substitution of $[b_{rs}]$, from Eq. (13) into Eq. (14), gives the simultaneous cubic equations

$$\{[C_1] - N_0'[C_2]\}[q_k] = [D'][q_i q_j q_k]. \tag{15}$$

This system of equations is solved by successive approximation on a digital computer for various values of $N_0' > N_{0crit.}'$

One result of this approximate solution is shown in Fig. 3; the direct longitudinal stress at the cross-section corresponding to the crest of a buckle

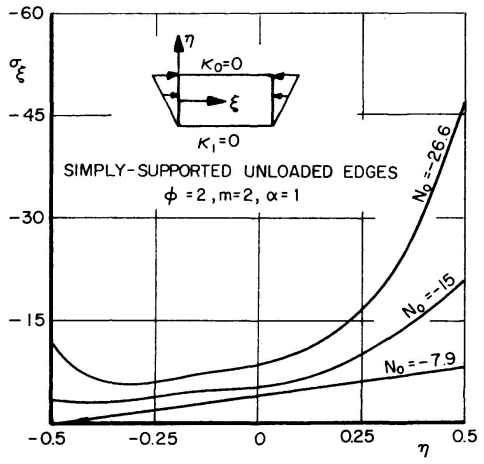


Fig. 3. Middle surface direct longitudinal stress at the crest of a buckle.

is plotted for various values of N_0'. It is seen that the stresses at the edges grow more rapidly than those in the middle, and this gives rise to the formulation of the collapse criterion. Results of tests given in Ref. [4] show that good agreement is obtained using the above analysis for buckling and maximum loads.

2. Collapse Loads for Channel Struts Reinforced with "Lips"

Fig. 4 shows how the section is considered to be subdivided into its constituent plates. The web is thus treated as a uniformly-loaded plate with equal amounts of rotational restraint along the unloaded edge. The flanges are taken to be eccentrically loaded plates elastically restrained against rotation along the unloaded edge common to itself and the web; the lip along the other unloaded edge is assumed to provide a simple support type of condition [7]. The matching at the common longitudinal edges is required to fulfill the following conditions.

a) The degree of edge restraint, r, for the flange and web is equal but opposite in sign, i.e. moment reactions are equal and the original corner geometry is maintained.
b) The value and distribution of the longitudinal direct stress, and therefore the unit shortening, were to be the same for the flange and web.

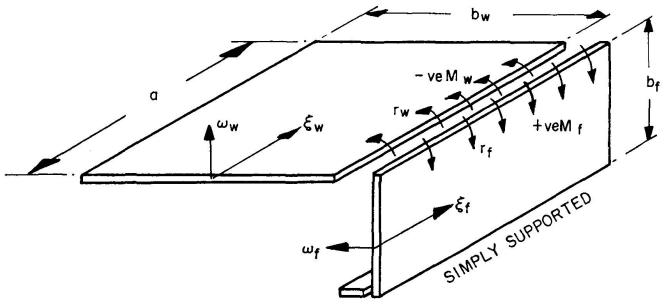


Fig. 4. Geometry and edge restraint representation of component plates of a lipped channel.

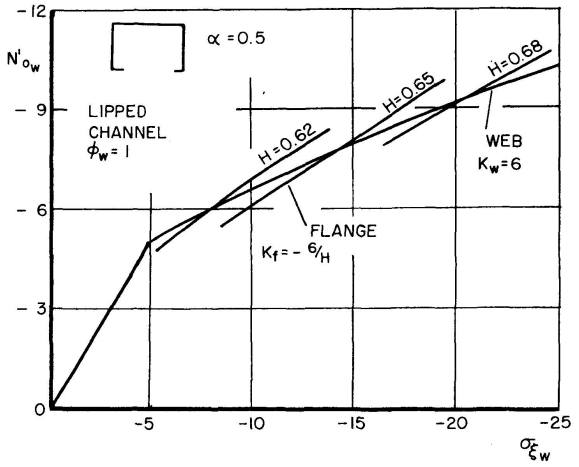


Fig. 5. Variation of load with longitudinal direct stress at $\eta = \frac{1}{2}$.

The simultaneous application of these requirements results in a very complex problem. This is simplified by assuming the stress distribution to be defined to sufficient accuracy by taking only one term in the ξ direction in the series Eq. (8). Now, taking a specific web geometry (ϕ_w, κ_w) we may, from the solution of the appropriate non-linear Eq. (15), obtain a plot of non-dimensionalised maximum edge stress against non-dimensional load parameter, as shown in fig. 5. Now

$$\kappa_w = -\frac{b_w r_w}{D_w} \quad \text{and} \quad \kappa_f = -\frac{b_f r_f}{D_f},$$

but by assumption, above we have, $r_f = -r_w$, and since we are considering only sections with uniform thickness, $D_f = D_w$. Thus, with $H = b_f/b_w$ we have

$$\kappa_f = \frac{b_w r_w}{D_w}\frac{b_f}{b_w} = -H\kappa_w.$$

Similarly, $\phi_f = 1/H\phi_w$, so that we may obtain corresponding plots on Fig. 5 for various values of H, and by using

$$\sigma_{\xi_w} = \frac{1}{H^2}\sigma_{\xi_f} \quad \text{and} \quad N'_{0_w} = \frac{1}{H^2}N'_{0_f},$$

they may be superposed on to the web plot as shown in Fig. 5. The intersections of these curves are valid geometries in that all the specified boundary matching conditions are fulfilled at the particular intersection load. Now, these particular geometries are considered to be sections at the point of collapse, i.e. the maximum direct longitudinal stress is equal to the material yield stress. Thus, using $\sigma_{xw}=\sigma_y$, where $\sigma_{xw}=\sigma_{\xi w}\phi_w^2 E h^2/a^2$, and prescribing a value for σ_y, we can obtain the thickness for the sections.

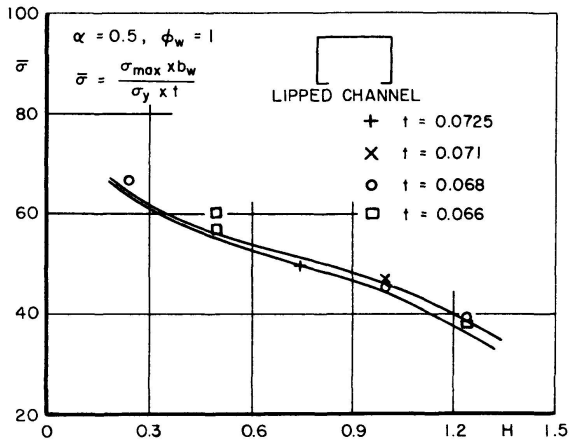


Fig. 6. Variation of non-dimensional maximum stress with shape factor $\alpha=0.5$.

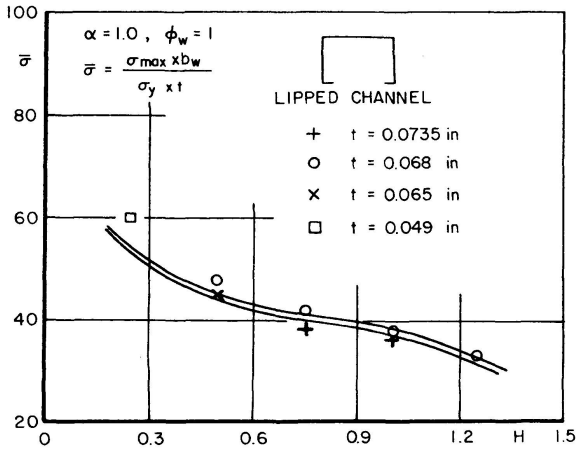


Fig. 7. Variation of non-dimensional maximum stress with shape factor $\alpha=1.0$.

In this study, $\sigma_y = -35\times10^3$ lb. f/in^2, $\phi_w=1$, $E=33\times10^6$ lb. f/in^2, $a=8$ in, and by limiting the thickness range to 0.050 in -0.090 in the plots of collapse load against section geometry shown in Figs. 6 and 7 were calculated; in these, $\sigma=\frac{\sigma_{max}b_w}{\sigma_y h}$ and the lip width is 1 in. The procedure is shown in the following example, with

$$H = 0.62, \qquad \sigma_{\xi_w} = -8.35, \qquad N'_{0_w} = -6.02.$$

$$h = \left[\frac{\sigma_{x_w}a^2}{\phi_w^2 E\,\sigma_{\xi_w}}\right]^{1/2} = \left[\frac{-35\times10^3\times64}{1\times33\times10^6\times-8.35}\right]^{1/2} = 0.0902 \text{ in.},$$

$$P_{max} = \frac{N'_0 h^3 E b_w(1+1.5H+0.125)}{b_w^2} = 3.75\times10^3 \text{ tbf.},$$

$$\bar{\sigma} = \frac{\sigma_{max}}{\sigma_y}\frac{b_w}{h} = 52.9.$$

Similarly, with $H=0.65$, $h=0.0705$, $\sigma=52.0$,
$H=0.68$, $h=0.0582$, $\sigma=51.7$.

In this way Figs. 6 and 7 were constructed; due to the approximate nature of the solution of the plate differential equations there is some scatter in the theoretical results; this is contained in the enclosed area shown in these plots.

The most common design curve is that which enables the designer to calculate the maximum load for a section from the corresponding theoretical buckling load. Examples of this type of curve are given in Ref. [1] and [2] for uniformly compressed sections. The usefulness of this curve lies in the fact that the buckling load is relatively simple to calculate for even complex

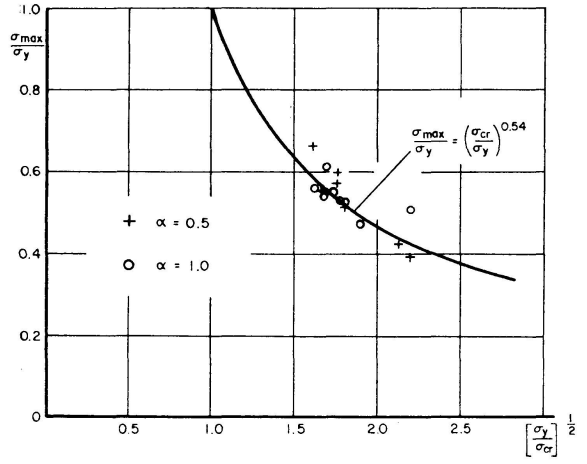


Fig. 8. Maximum strength of eccentrically loaded short lipped channel struts.

sections. If the curves in Figs. 6 and 7 are recast in this manner it is seen that on a plot of (σ_{max}/σ_y) against $(\sigma_y/\sigma_{cr})^{1/2}$ (Fig. 8), these quantities may be related by

$$\frac{\sigma_{max}}{\sigma_y} = \left(\frac{\sigma_{cr}}{\sigma_y}\right)^{0.54}.$$

Here

$$\sigma_{max} = \frac{P_{max}}{b_w h\left[1+2H\left(1-\frac{\alpha}{2}\right)+H_L(1-\alpha)\right]},$$

$$\sigma_{cr} = \frac{P_{cr}}{b_w h\left[1+2H\left(1-\frac{\alpha}{2}\right)+H_L(1-\alpha)\right]},$$

where H_L is the ratio of lip width to web width.

3. Experimental Investigation of Lipped Section Maximum Load

The special loading rig designed for this investigation is shown in Fig. 9. It consisted of two relatively massive plattens opposed to each other and individually mounted on four arms for vertical restraint and on two trunnions for restraint in the horizontal plane. The trunnions fitted over two heavy steel bars, one above the plattens and one below, which ran the length of the frame and were firmly attached to it. Rotation of the serrated hand wheels caused the end assemblies to approach each other thus inducing a load in the specimen channel, placed accurately in position in the grooved case-hardened face plates provided. Eccentric loading was obtained by the differential

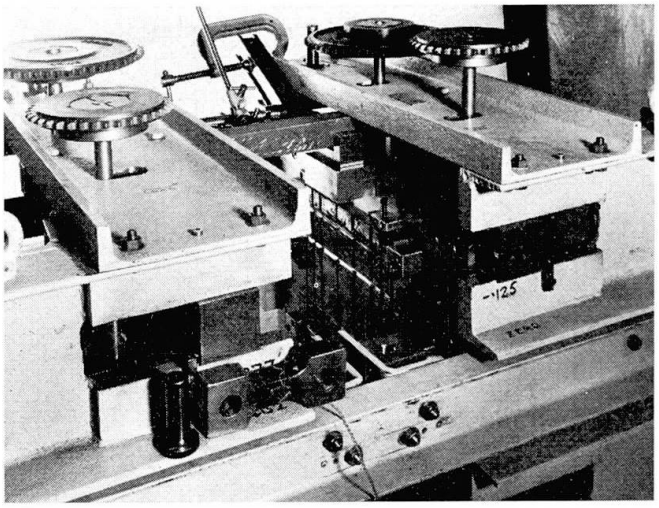


Fig. 9. View of experimental loading rig.

loading of one side from the other. The magnitude of the load was indicated by electrical resistance foil strain gauges bonded to the link bars and connected to a Huggenberger switch box and strain bridge. Each link bar was previously calibrated and was found to give a linear reading over the required load range. Collapse was indicated by a reduction of the load for an inward movement of the loading plattens. Results of this series of tests are plotted in Fig. 6 and 7.

Conclusions

An approximate method of analysis has been presented which assumes that a short channel column may be treated as a collection of individual plates connected appropriately along their common edges. The analysis combines the large deflection behaviour of these constituitive plates to provide an engineering estimate of the maximum load capacity of the channel.

The analysis is shown to give good predictions when applied to short columns subjected to eccentric loading. It is also found that the experimental results may be described adequately by a single curve relating the column theoretical buckling stress, the corresponding or maximum stress and the material yield stress. The test programme reported here was of limited range but the good agreement obtained promises hope for a coherent design formulation for open channel columns subjected to a variety of eccentric load actions.

Notation

a	plate, or channel, length.
b	plate breadth.
b_f, b_w	flange and web widths respectively of a channel section.
b_{01}, b_{11}, etc.	Galerkin coefficients in stress function series.

i, j, k, n	integers used in Galerkin deflection series.
k	buckling constant.
p, q, r, s	integers used in stress function series.
q_0, q_1, etc.	Galerkin coefficients in deflection function series.
r_1, r_0	degrees of rotational restraint per unit distance in x direction at plate edges $y=-b/2$ and $y=+b/2$ respectively.
t	plate thickness.
w	displacement of a point of the plate middle surface in a direction normal to the undeformed middle surface.
x, y	cartesian coordinates.
D	flexural stiffness of the plate, defined by $D=E t^3/12(1-\nu^2)$.
E	Young's modulus of the plate material.
F	Airy's stress function.
F'	non-dimensional form of Airy's stress function, $F'=F/E t^2$.
H	Channel shape factor, $H=b_f/b_w$.
H_L	ratio of lip width to flange width.
L	limit of deflection series.
N_x	normal force per unit length in the middle surface of the plate in the x direction.
N_0	value of N_x at $x=0$, $y=b/2$ and $x=a$, $y=b/2$.
N_0'	non-dimensional form of N_0, $N_0'=N_0 a^2/\phi^2 E t^2$.
N_{0cr}	critical value of N_0 at initial buckling.
P	total compressive load applied to plate.
P_{cr}	critical value of P at initial buckling.
P_{max}	maximum plate load.
T, U	limits of stress function series.
α	load eccentricity parameter.
κ_1, κ_0	non-dimensional forms of the degrees of rotational restraint per unit length in x direction at plate edges $y=-b/2$ and $y=+b/2$ respectively, $\kappa_1=-\frac{r_1 b}{D}$, $\kappa_0=-\frac{r_0 b}{D}$.
κ_f, κ_w	values of κ_1 at common edges for flange and web, respectively.
ν	Poisson's ratio of the plate material.
ξ, η	cartesian coordinates in non-dimensional form, $\xi=x/a$, $\eta=y/b$.
ϕ	aspect ratio of plate, $\phi=a/b$.
ϕ_f, ϕ_w	aspect ratio of flange and web, respectively, of a channel section.
σ_x, σ_y	direct stresses in the x and y direction, respectively.
σ_ξ, σ_η	non-dimensional forms of σ_x and σ_y, $\sigma_\xi=\frac{\sigma_x a^2}{\phi^2 E t^2}$, $\sigma_\eta=\frac{\sigma_y a^2}{E t^2}$.
τ_{xy}	shearing stress in the xy plane.
$\tau_{\xi\eta}$	non-dimensional form of τ_{xy}, $\tau_{\xi\eta}=\frac{\tau_{xy} a^2}{\phi^2 E t}$.
ω	non-dimensional form of w, $\omega=w/t$.

References

1. GERARD, G.: Handbook of Structural Stability, Pt. IV Failure of Plates and Composite Elements, N.A.C.A., T.N. 3784, 1957.
2. CHILVER, A. H.: The stability and strength of thin-walled steel struts. The Engineer, p. 180, 1953.
3. CHILVER, A. H.: The maximum strength of the thin-walled channel strut. Civil Engineering, vol. 48, p. 1143, p. 1953.
4. WALKER, A. C.: Flat rectangular plates subjected to linearly-varying edge compressive loading. Thin walled Structures, Chatto and Windus, 1967.
5. WALKER, A. C.: Local stability in plates and channel struts. Journ. of the Struct. Div., Proc. A.S.C.E., vol. 92, No. ST 3, p. 39, 1966.
6. KARMAN, T. VON: Enzyklopädie der mathematischen Wissenschaften, vol. IV, p. 349, 1910.
7. PFLÜGER, A. VON: Thin walled compression members, Report No. 2, Institut für Statik der Technischen Hochschule Hannover, 1959.

Summary

An analytical and experimental investigation is made of the maximum load-carrying capacity of thin-walled open channel columns under eccentric compression. The channels are treated as being composed of individual plates connected appropriately along their common edges. The large deflection behaviour of these plates is analysed approximately using Galerkin's method and the results are synthesised to give an engineering estimate of the maximum load of the short columns.

The results of the experimental investigation show these estimates to be of good engineering accuracy and it is also shown that the results may be described adequately by a single curve relating the column buckling stress, the corresponding maximum stress and the material yield stress.

Résumé

Ce rapport présente une étude théorique et expérimentale sur la capacité de charge de piliers à section en U. On considère la section comme composée de parois individuelles, liées conformément. Les grandes déformations propres à ces plaques ont été analysées à l'aide de la méthode Galerkin. A partir des résultats obtenus, on réussit une estimation très générale de la capacité de charge de piliers courts, estimation qui se montre en bon accord avec les valeurs expérimentales. En plus on voit que les résultats peuvent être représentés par une seule courbe reliant la tension de flambage, la tension maximale correspondante et la limite d'écoulement du matériau.

Zusammenfassung

Es wird eine theoretische und experimentelle Studie über die Höchstlast dünnwandiger U-Stützen dargelegt. Man nimmt an, der Querschnitt sei aus einzelnen Platten zusammengesetzt, die an ihren Ecken entsprechend verbunden sind. Die diesen Platten eigenen großen Verformungen werden näherungsweise nach dem Galerkin-Verfahren untersucht. Die Synthese der Ergebnisse dient der praktischen Schätzung der Maximallast kurzer Stützen.

Die Versuchsergebnisse zeigen, daß diese Schätzung für praktische Zwecke genügend genau ist. Es wird ferner gezeigt, daß die Ergebnisse zweckmäßig durch eine einzige Kurve dargestellt werden können: Diese Kurve verbindet die Beulspannung, die entsprechende Maximalspannung und die Fließgrenze des Materials.

Leere Seite
Blank page
Page vide